Northumbria Research Link

Citation: Popoola, Wasiu Oyewole (2009) Subcarrier intensity modulated free-space optical communication systems. Doctoral thesis, Northumbria University.

This version was downloaded from Northumbria Research Link: https://nrl.northumbria.ac.uk/id/eprint/1939/

Northumbria University has developed Northumbria Research Link (NRL) to enable users to access the University's research output. Copyright © and moral rights for items on NRL are retained by the individual author(s) and/or other copyright owners. Single copies of full items can be reproduced, displayed or performed, and given to third parties in any format or medium for personal research or study, educational, or not-for-profit purposes without prior permission or charge, provided the authors, title and full bibliographic details are given, as well as a hyperlink and/or URL to the original metadata page. The content must not be changed in any way. Full items must not be sold commercially in any format or medium without formal permission of the copyright holder. The full policy is available online: http://nrl.northumbria.ac.uk/policies.html

Northumbria University NEWCASTLE

University Library

SUBCARRIER INTENSITY MODULATED FREE-SPACE OPTICAL COMMUNICATION SYSTEMS

WASIU OYEWOLE POPOOLA

A thesis submitted in partial fulfilment
of the requirements of the
University of Northumbria at Newcastle
for the degree of
Doctor of Philosophy

Research undertaken in the
School of Computing, Engineering and Information Sciences

September 2009

Abstract

This thesis investigates and analyses the performance of terrestrial free-space optical communication (FSO) system based on the phase shift keying pre-modulated subcarrier intensity modulation (SIM). The results are theoretically and experimentally compared with the classical On-Off keying (OOK) modulated FSO system in the presence of atmospheric turbulence. The performance analysis is based on the bit error rate (BER) and outage probability metrics. Optical signal traversing the atmospheric channel suffers attenuation due to scattering and absorption of the signal by aerosols, fog, atmospheric gases and precipitation. In the event of thick fog, the atmospheric attenuation coefficient exceeds 100 dB/km, this potentially limits the achievable FSO link length to less than 1 kilometre. But even in clear atmospheric conditions when signal absorption and scattering are less severe with a combined attenuation coefficient of less than 1 dB/km, the atmospheric turbulence significantly impairs the achievable error rate, the outage probability and the available link margin of a terrestrial FSO communication system.

The effect of atmospheric turbulence on the symbol detection of an OOK based terrestrial FSO system is presented analytically and experimentally verified. It was found that atmospheric turbulence induced channel fading will require the OOK threshold detector to have the knowledge of the channel fading strength and noise levels if the detection error is to be reduced to its barest minimum. This poses a serious design difficulty that can be circumvented by employing phase shift keying (PSK) pre-modulated SIM. The results of the analysis and experiments showed that for a binary PSK-SIM based FSO system, the symbol detection threshold level does not require the knowledge of the channel fading strength or noise level. As such, the threshold level is fixed at the zero mark in the presence or absence of atmospheric turbulence. Also for the full and seamless integration of FSO into the access network, a study of SIM-FSO performance becomes compelling because existing networks already contain subcarrier-like signals such as radio over fibre and cable television signals. The use of multiple subcarrier signals as a means of increasing the throughput/capacity is also investigated and the effect of optical source nonlinearity is found to result in intermodulation distortion. The intermodulation distortion can impose a BER floor of up to 10^{-4} on the system error performance.

In addition, spatial diversity and subcarrier delay diversity techniques are studied as means of ameliorating the effect of atmospheric turbulence on the error and outage performance of SIM-FSO systems. The three spatial diversity linear combining techniques analysed are maximum ratio combining, equal gain combining and selection combining. The system performance based on each of these combining techniques is presented and compared under different strengths of atmospheric turbulence. The results predicted that achieving a 4 km SIM-FSO link length with no diversity technique will require about 12 dB of power more than using a 4 × 4 transmitter/receiver array system with the same data rate in a weak turbulent atmospheric channel. On the other hand, retransmitting the delayed copy of the data once on a different subcarrier frequency was found to result in a gain of up to 4.5 dB in weak atmospheric turbulence channel.

Contents

Abstract ii

List of Figures viii

List of Tables xiv

Glossary of Abbreviations xv

Glossary of Symbol xviii

Dedication xxiv

Acknowledgements xxv

Declaration xxvi

Chapter One

Introduction 1

1.1 Background 1

1.2 Research Motivation and Justification 5

1.3 Research Objectives 11

1.4 Thesis Organisation 13

1.5 Original Contributions 15

1.6 List of Publications and Awards 18

Chapter Two

Fundamentals of FSO 21

2.1 Introduction 21

2.2 Overview of FSO Technology 22

2.3 Features of FSO 23

2.3.1 Areas of application 26

2.4 FSO Block Diagram 27

2.4.1 The transmitter 28
2.4.2 The atmospheric channel 30
2.4.3 The receiver 33
2.5 Eye Safety and Standards 36
2.5.1 Maximum Permissible Exposures (MPE) 40
2.6 Summary 41
Chapter Three
Optical Detection Theory 42
3.1 Introduction 42
3.2 Photodetectors 43
3.2.1 PIN photodetector 44
3.2.2 APD photodetector 46
3.3 Photodetection Techniques 47
3.3.1 Direct detection 47
3.3.2 Coherent detection 48
3.4 Photodetection Noise 51
3.4.1 Photon fluctuation noise 52
3.4.2 Dark current and excess noise 52
3.4.3 Background radiation 54
3.4.4 Thermal noise 55
3.5 Optical Detection Statistics 55
3.6 Summary 58
Chapter Four
The Atmospheric Turbulence Models 59
4.1 Introduction 59
4.2 Turbulent Atmospheric Channel 60
4.3 Log-normal Turbulence Model 64
4.3.1 Spatial coherence in weak turbulence 70

4.3.2 Limit of log-normal turbulence model 73
4.4 The Gamma-Gamma Turbulence Model 73
4.5 The Negative Exponential Turbulence Model 78
4.6 Summary 80
Chapter Five
FSO Modulation Techniques 81
5.1 Introduction 81
5.2 On-Off Keying 83
5.2.1 OOK in a Poisson atmospheric optical channel 84
5.2.2 OOK in a Gaussian atmospheric optical channel 87
5.3 Pulse Position Modulation 93
5.4 Subcarrier Intensity Modulation 97
5.4.1 SIM generation and detection 99
5.5 Summary 104
Chapter Six
Subcarrier Intensity Modulated FSO in Atmospheric Turbulence Channels 105
6.1 Introduction 105
6.2 SIM-FSO Performance in Log-normal Atmospheric Channels 106
6.2.1 Bit error probability analysis of SIM-FSO 109
6.2.2 Outage probability in log-normal atmospheric channels 121
6.3 SIM-FSO Performance in Gamma-Gamma and Negative Exponential Atmospheric Channels 123
6.3.1 Outage probability in negative exponential model atmospheric channels 127
6.4 Atmospheric Turbulence Induced Penalty 129
6.5 Intermodulation Distortion Due to Laser Non-linearity 132
6.6 Summary 144
Chapter Seven
SIM-FSO with Spatial and Temporal Diversity Techniques 145

7.1 Introduction 145

7.2 Receiver Diversity in Log-normal Atmospheric Channels 148

7.2.1 Maximum ratio combining (MRC) 150

7.2.2 Equal gain combining (EGC) 153

7.2.3 Selection combining (SelC) 155

7.2.4 Effect of received signal correlation on error performance 157

7.2.5 Outage probability with receiver diversity in a log-normal atmospheric channel 159

7.3 Transmitter Diversity in a Log-normal Atmospheric Channel 160

7.4 Transmitter-Receiver Diversity in a Log-normal Atmospheric Channel 162

7.5 Results and Discussions of SIM-FSO with Spatial Diversity in a Log-normal Atmospheric Channel 163

7.6 SIM-FSO with Receiver Diversity in Gamma-gamma and Negative Exponential Atmospheric Channels 170

7.6.1 BER and outage probability of BPSK-SIM with spatial diversity 171

7.6.2 BER and outage probability of DPSK-SIM in negative exponential channels 177

7.7 SIM-FSO with Subcarrier Time Delay Diversity 184

7.7.1 Error performance with the subcarrier TDD 187

7.7.2 Performance of multiple-SIM with TDD and intermodulation distortion 189

7.7.3 Subcarrier TDD results and discussions 191

7.8 Summary 195

Chapter Eight

Link Budget Analysis 197

8.1 Introduction 197

8.2 Power Loss 198

8.2.1 Atmospheric channel loss 198

8.2.2 Beam divergence 205

8.2.3 Optical and window loss 209

8.2.4 Pointing loss 210

8.3 The Link Budget 210

8.4 Summary 214

Chapter Nine

Experimental Demonstration of Scintillation Effect 215

9.1 Introduction 215

9.2 Experimental Set-up 216

9.2.1 The transmitter 217

9.2.2 Turbulence simulation chamber 219

9.2.3 The receiver 220

9.3 Characterisation of Simulated Turbulence 225

9.4 Experimental Results 228

9.4.1 Scintillation effect on OOK signalling 228

9.4.2 Scintillation effect on BPSK-SIM modulation 233

9.5 Summary 239

Chapter Ten

Conclusions and Future work 240

10.1 Conclusions 240

10.2 Recommendations for Future Work 247

Appendix A: Zeros and weights of Gauss Hermite integration 250

Appendix B: Mean and variance of the sum of log-normal distribution 251

Appendix C: Probability density function of $I_{\max} = \max\{I_i\}_{i=1}^{N}$ for log-normal distributed variables 253

Appendix D: Probability density function of $I_{\max} = \max\{I_i\}_{i=1}^{N}$ for negative exponential distributed variables 255

References 257

List of Figures

Fig.1.1 Summary of thesis contributions.

Fig. 2.1 Conventional FSO system block diagram.

Fig. 2.2 Modulated retro-reflector based FSO system block diagram.

Fig. 2.3 Block diagram of a terrestrial FSO link.

Fig. 2.4 Response/absorption of the human eye at various wavelengths.

Fig. 3.1 PIN photodetector schematic diagram.

Fig. 3.2 Responsivity and quantum efficiency as a function of wavelength for PIN photodetectors.

Fig. 3.3 Block diagram of a direct detection optical receiver.

Fig. 3.4 Block diagram of a coherent detection optical receiver.

Fig. 4.1 Atmospheric channel with turbulent eddies.

Fig. 4.2 Log-normal probability density function with $E[I] = 1$ for a range of log irradiance variance σ_l^2.

Fig. 4.3 Plane wave transverse coherence length for $\lambda = 850$nm and a range of C_n^2.

Fig. 4.4 Plane wave transverse coherence length for $\lambda = 1550$nm and a range of C_n^2.

Fig. 4.5 Gamma-gamma probability density function for three different turbulence regimes, namely weak, moderate and strong.

Fig. 4.6 *S.I.* against log intensity variance for $C_n^2 = 10^{-15}$ $m^{-2/3}$ and $\lambda = 850$nm.

Fig. 4.7 Values of α and β under different turbulence regimes: weak, moderate to strong and saturation.

Fig. 4.8 Negative exponential probability density function for different values of I_0.

Fig. 5.1 Modulation tree.

Fig. 5.2 BER against the average photoelectron count per bit for OOK-FSO in a Poisson atmospheric turbulence channel for $\sigma_l^2 = [0, 0.1, 0.2, 0.5]$.

Fig. 5.3 The likelihood ratio against the received signal for different turbulence levels and noise variance of 10^{-2}.

Fig. 5.4 OOK threshold level against the log intensity standard deviation for various noise levels.

Fig. 5.5 BER of OOK based FSO in atmospheric turbulence with σ_l^2 = 0.2 considering fixed and adaptive threshold levels.

Fig. 5.6 BER of OOK-FSO with fixed and adaptive threshold at various levels of scintillation, $\sigma_l = [0.2, 0.5, 0.7]$ and I_0 = 1.

Fig. 5.7 Time waveforms for 4-bit OOK and 16-PPM.

Fig. 5.8 Binary PPM BER as a function of scintillation index for K_{Bg} = 10; T_e = 300 K, ζ = 0.028, R_b = 155 Mbps and g = 150.

Fig. 5.9 Block diagram of SIM-FSO: (a) transmitter, and (b) receiver.

Fig. 5.10 Output characteristic of an optical source driven by a subcarrier signal showing optical modulation index.

Fig. 6.1 QPSK constellation of the input subcarrier signal without noise and channel fading.

Fig. 6.2 Received constellation of QPSK pre-modulated SIM-FSO with noise and channel fading for SNR = 2 dB and $\sigma_l^2 = 0.001$.

Fig. 6.3 Received constellation of QPSK pre-modulated SIM-FSO with noise and channel fading for SNR = 2 dB and $\sigma_l^2 = 0.5$.

Fig. 6.4 BER against the normalised SNR using numerical and 20th order Gauss-Hermite integration methods in weak atmospheric turbulence for $\sigma_l^2 = 0.12$.

Fig. 6.5 The BER against the average received irradiance in weak turbulence under different noise limiting conditions for R_b = 155 Mpbs and σ_l^2 = 0.3.

Fig. 6.6 Block diagram of an FSO link employing DPSK modulated SIM; (a) transmitter and (b) receiver.

Fig. 6.7 BER against the received irradiance for SIM-FSO with different subcarrier modulation techniques in weak atmospheric turbulence for σ_l^2 = 0.3, $\lambda = 850$ nm and link range = 1 km.

Fig. 6.8 BER against the normalised SNR for multiple subcarriers FSO system in weak atmospheric turbulence for $N = [1,2,5,10]$ and σ_l^2 = 0.3.

Fig. 6.9 SNR required to attain a BER of 10^{-6} against the number of subcarriers for BPSK modulated SIM-FSO system with $\sigma_l = [0.1, 0.2, 0.5, 0.7]$.

Fig. 6.10 Outage probability against the power margin for a log-normal turbulent atmospheric channel for $\sigma_l^2 = [0.1, 0.3, 0.5, 1]$.

Fig. 6.11 BER performance against the normalised electrical SNR across all of turbulence regimes based on gamma-gamma and negative exponential modes.

Fig. 6.12 Error performance of BPSK SIM and OOK with fixed and adaptive threshold based FSO in weak turbulence regime modeled using gamma-gamma distribution.

Fig. 6.13 The outage probability against the power margin in saturation and weak turbulence regimes for $\sigma_l^2 = 0.5$.

Fig. 6.14 Error rate performance against normalised SNR for BPSK-SIM based FSO in weak atmospheric turbulence channel for $\sigma_l^2 = [0, 0.1, 0.3, 0.5, 0.7]$.

Fig. 6.15 Turbulence induced SNR penalty as function of log irradiance variance for BPSK-SIM based FSO for BER = [10^{-3}, 10^{-6}, 10^{-9}].

Fig. 6.16 BER of BPSK-SIM against the turbulence strength in weak atmospheric turbulence for normalised SNR (dB) = [5, 20, 25, 30].

Fig. 6.17 P_{Out} of BPSK-SIM against the turbulence strength in weak atmospheric turbulence for m (dBm) = [30, 35, 38, 40].

Fig. 6.18 In-band intermodulation products against number of subcarriers for $k = \ell = 1$.

Fig. 6.19 Modulation index against the irradiance in the absence of atmospheric turbulence for N = [10, 15, 25].

Fig. 6.20 $CINR_{ave}$ (dB) against the modulation depth in atmospheric turbulence for $\sigma^2 = 10^{-2}$, $\sigma_l^2 = 0.25$, $a_3 = 0.3$, $\ell = k = 1$ and $N = 12$.

Fig. 6.21 Unconditional BER against the modulation depth in atmospheric turbulence for $\sigma^2 = 10^{-2}$, $\sigma_l^2 = 0.25$, $a_3 = 0.3$, $\ell = k = 1$ and $N = 12$.

Fig. 6.22 Optimum modulation index based on minimum BER and maximum $CINR_{ave}$ against I_0 for $N = 12$, $a_3 = 0.3$, $\ell = k = 1$, $\sigma^2 = 10^{-3}$ and $\sigma_l^2 = 0.1$.

Fig. 6.23 BER of multiple SIM-FSO against I_0 in atmospheric turbulence for $N = 12$, $a_3 = 0.3$, $\ell = k = 1$, $\sigma^2 = 10^{-3}$ and $\sigma_l^2 = 0.1$ using optimum and suboptimum modulation index.

Fig. 7.1 Block diagram of a spatial diversity receiver with $\mathcal{N}$ detectors.

Fig. 7.2 Correlation coefficient for a weak turbulent field as a function of transverse separation.

Fig. 7.3 The exact outage probability and its upper bound against the power margin with EGC spatial diversity in weak turbulent atmospheric channel for $\sigma_l^2 = 0.22$ and $\mathcal{N} = [1, 4]$.

Fig. 7.4 BPSK-SIM link margin with EGC and SelC against number of photodetectors for various turbulence levels and a BER of 10^{-6}.

Fig. 7.5 DPSK-SIM with SelC spatial diversity link margin against turbulence strength for $\mathcal{N} = [2, 4, 6, 8, 10]$.

Fig. 7.6 BPSK-SIM diversity link margin with EGC and MRC against number of photodetectors for various turbulence levels and a BER of 10^{-6}.

Fig. 7.7 EGC diversity gain in log-normal atmospheric channel against the number of photodetectors at P_{Out} of 10^{-6} and $\sigma_l^2 = [0.22, 0.52, 0.72, 1]$.

Fig. 7.8 Error performance of BPSK-SIM at different values of correlation coefficient for $\mathcal{N} = [2, 3]$ and $\sigma_l^2 = 0.52$.

Fig. 7.9 Error performance of BPSK-SIM with MIMO configuration in turbulent atmospheric channel for $\sigma_l^2 = 0.3$.

Fig. 7.10 BPSK-SIM error rate against the normalised SNR in gamma-gamma and negative exponential channels for two photodetectors.

Fig. 7.11 The outage probability as a function of power margin m_{EGC} (dBm) for $\mathcal{N} = [1, 2, 4]$ in negative exponential channel.

Fig. 7.12 Diversity gain against number of independent photodetectors at BER and P_{Out} of 10^{-6} in negative exponential atmospheric channel.

Fig. 7.13 The pdf, $p\left(max\{I_i\}_{i=1}^{\mathcal{N}}\right)$ for $\mathcal{N} = [1, 4, 10]$, and I_0 = 1 in a negative exponential channel.

Fig. 7.14 Error rate of DPSK-SIM against the average received irradiance with spatial diversity in negative exponential channel for $\mathcal{N} = [2, 4, 6, 8, 10]$.

Fig. 7.15 Outage probability against the average irradiance with SelC spatial diversity in negative exponential channel for I^* = 0 dBm and $\mathcal{N} = [1, 2, 4, 6, 10]$.

Fig. 7.16 Predicted SelC diversity gain per photodetector against P_{out} in saturation regime for $\mathcal{N} = [1, 2, 4, 6, 10]$.

Fig. 7.17 Predicted SelC diversity gain (dB) per photodetector for $P_{Out} = [10^{-6}, 10^{-3}, 10^{-2}]$ in saturation regime.

Fig. 7.18 Proposed subcarrier TDD block diagram: (a) transmitter, and (b) receiver.

Fig. 7.19 Performance of 12-subcarrier FSO link with and without TDD (a) average CINR and BER as a function of modulation index at 14 dB SNR, and (b) optimum BER against I_0 for σ_l^2 = 0.3, a_3 = 0.3, and $\ell = k = 1$.

Fig. 7.20 Error performance of BPSK-SIM against I_0 at 155 Mbps and $\sigma_l^2 = 0.3$ with no fading and with/without TDD.

Fig. 7.21 Average irradiance and 1-TDD gain for different turbulence strength, $Rb = [155, 625]$ Mbps and $N = 1$.

Fig. 7.22 Error performance against the normalised SNR for N = 12, $a3 = [0.3, 0.7]$, $\sigma_l^2 = 0.3$ and $\xi = 0.3$ (a) with 1-TDD, and (b) with no TDD.

Fig. 8.1 Atmospheric absorption transmittance over a sea level 1820 m horizontal path.

Fig. 8.2 Measured attenuation coefficient as a function of visibility range at λ = 830 nm in early 2008, Prague, Czech Republic.

Fig. 8.3 Beam divergence.

Fig. 8.4 Typical beam expander.

Fig. 8.5 Link length against the available link margin for OOK-FSO in a channel with visibility values 5, 30 and 50 km.

Fig. 8.6 Link length against the available link margin for SIM-FSO considering 1-TDD, 4×4-MIMO configuration and no diversity in clear turbulent atmospheric channel.

Fig. 9.1 An FSO experimental system block diagram to evaluate the turbulence effect.

Fig. 9.2 Schematic diagram of the BPSK subcarrier modulator.

Fig. 9.3 Impedance matching network.

Fig. 9.4 Schematic diagram of the turbulence simulation chamber.

Fig. 9.5 LT6202 trans-impedance amplifier schematic diagram.

Fig. 9.6 10^{th} order low-pass filter with root raised cosine response.

Fig. 9.7 OOK modulated laser input and received signal waveforms without turbulence, input signal 100 mV p-p, 40 kHz.

Fig. 9.8 BPSK subcarrier modulated laser: (a) input and received signal waveforms before demodulation in the absence of turbulence (b)

received signals after demodulation. Carrier signal input: 150 mV p-p, 1MHz, modulating signal: 100 mVp-p, 40 kHz.

Fig. 9.9 Turbulence simulation set-up picture.

Fig. 9.10 Received mean signal distribution in the absence of turbulence

Fig. 9.11 Received mean signal distribution with simulated turbulence and photodetection noise.

Fig. 9.12 OOK modulated laser received signal waveform and its distribution for 50 mV p-p input signal: (a) without turbulence, and (b) with turbulence.

Fig. 9.13 OOK modulated laser received signal waveform and its distribution for 100 mV p-p input signal: (a) without turbulence and (b) with turbulence.

Fig. 9.14 OOK modulated laser received signal waveform and its distribution for 200 mV p-p input signal: (a) without turbulence, and (b) with turbulence.

Fig. 9.15 Received signal waveform for BPSK-SIM modulated laser and its distribution for 50 mV p-p modulating signal: (a) without turbulence, and (b) with turbulence.

Fig. 9.16 BPSK-SIM modulated laser received signal waveform and its distribution for 100 mV p-p modulating signal: (a) without turbulence, and (b) with turbulence.

Fig. 9.17 Received signal waveform for BPSK-SIM modulated laser and its distribution for 200 mV p-p modulating signal: (a) without turbulence, and (b) with turbulence.

List of Tables

Table 2.1 Optical sources.

Table 2.2 The gas constituents of the atmosphere.

Table 2.3 FSO Photodetectors.

Table 2.4 Classification of lasers according to the IEC 60825-1 standard.

Table 2.5 Accessible emission limits for two wavelengths, 850 and 1550 nm.

Table 2.6 Example of MPE values (W/m^2) of the eye (cornea) at 850 nm and 1550 nm wavelengths.

Table 3.1 Operating wavelength ranges for different photodetector materials.

Table 3.2 Dark current values for different materials.

Table 3.3 Statistical parameters of Poisson random distribution.

Table 5.1 Comparison of FSO modulation techniques.

Table 6.1 Values of K_1 and K_0 for different noise limiting conditions.

Table 6.2 Simulation parameters.

Table 6.3 Fading strength parameters for gamma-gamma turbulence model.

Table 6.4 Third order intermodulation products.

Table 6.5 Number of in-band intermodulation products for $N = 12$.

Table 7.1 Diversity gain at a BER of 10^{-6} in gamma-gamma and negative exponential channels.

Table 7.2 Numerical simulation parameters.

Table 7.3 Gain per photodetector at a BER of 10^{-6}.

Table 7.4 Fading penalty and TDD gain at BER = 10^{-9}, $\sigma_l^2 = 0.3$, $N = \xi = 1$.

Table 8.1 Typical atmospheric scattering particles with their radii and scattering process at $\lambda = 850$ nm.

Table 8.2 International visibility range and attenuation coefficient in the visible waveband for various weather conditions.

Table 8.3 Typical link budget parameters.

Table 8.4 Required irradiance to achieve a BER of 10^{-9} based on BPSK-SIM, $R_b = 155$ Mbps and $\sigma_l^2 = 0.3$.

Table 9.1 Parameters for the OOK and BPSK subcarrier modulation experiment.

Table 9.2 Turbulence simulation chamber temperature at four different positions.

Table 9.3 Challenges in optical wireless communications.

Glossary of Abbreviations

3G	Third generation
4G	Fourth generation
ADSL	Asynchronous digital subscriber loop
AEL	Accessible emission limits
AM	Amplitude modulation
ANSI	American national standards institute
APD	Avalanche photodetector
AWGN	Additive white Gaussian noise
BER	Bit error rate
BPF	Band pass filter
bps	Bits per second
BPSK	Binary phase shift keying
CDMA	Code division multiple access
CDRH	Centre for devices and radiological health
CENELEC	European committee for electrotechnical standardization
CNIR	Carrier-to-noise-and-interference ratio
$CNIR_{ave}$	Average carrier-to-noise-and-interference ratio
CW	Continuous wave
DC	Direct current
DPIM	Digital pulse interval modulation
DPSK	Differential phase shift keying
DSL	Digital subscriber loop
EGC	Equal gain combining
FCC	Federal communications commission
FEC	Forward error control
FM	Frequency modulation
FOV	Field of view
FSO	Free-space optics
FTTH	Fibre to the home
GaAs	Gallium arsenide

Ge	Germanium
H-V	Hufnagel-Valley model of index of refraction structure parameter
IEC	International electrotechnical commission
IMD	Inter-modulation distortion
IMD2	Second order inter-modulation distortion
IMD3	Third order inter-modulation distortion
IMP	Inter-modulation product
InP	Indium phosphide
ISI	Inter symbol interference
LED	Light emitting diode
LIA	Laser Institute of America
LMDS	Local multipoint distribution service
LOS	Line of sight
M-ASK	M-level amplitude shift keying
M-FSK	M-level frequency shift keying
MIMO	Multi-input multi-output
MLCD	Mars laser communication demonstration
MPE	Maximum permissible exposure
M-PSK	M-level phase shift keying
MRC	Maximum ratio combining
MRR	Modulated retro-reflector
NRZ	Non-return-to-zero
OBPF	Optical band pass filter
Ofcom	Office of communications
OOK	On-off keying
PAM	Pulse amplitude modulation
PAT	Pointing, acquisition and tracking
pdf	Probability density function
PFM	Pulse frequency modulation
PIN	*p*-type-intrinsic-*n*-type photodetector
P_{Out}	Outage probability
PPM	Pulse position modulation
PSD	Power spectral density
PWM	Pulse width modulation

QAM	Quadrature amplitude modulation
QPSK	Quadrature phase shift keying
RF	Radio frequency
RoFSO	Radio over free-space optics
RT	Receiver telescope
RZ	Return to zero
S.I.	Scintillation index
SelC	Selection combining
SILEX	Semiconductor-laser inter-satellite link experiment
SIM	Subcarrier intensity modulation
SNR	Signal to noise ratio
TDD	Time delay diversity
TIA	Trans-impedance amplifier
TT	Transmitter telescope
UWB	Ultra wide band
WDM	Wavelength division multiplexing

Glossary of Symbols

$\Re$	Photodetector responsivity
A_p	Cross-sectional area of scattering
$\{a_{ci}\}_{i=1}^{\mathcal{N}}$	Linear combining gain factor
$\{a_i\}_{i=2}^{\infty}$	Degree of laser nonlinearity coefficient
$\{a_{ic}, a_{is}\}_{i=1}^{N}$	Signal constellation symbol amplitude for N subcarriers
$[w_i]_i^n$	Weight factors of the n^{th} order Hermite polynomial
$[x_i]_i^n$	Zeros of the n^{th} order Hermite polynomial
$\langle g^2 \rangle$	Mean square current gain of an APD
$\langle i_d \rangle$	Mean photodetector dark current
$\alpha_a(\lambda)$	Wavelength dependent aerosol absorption coefficient
$\alpha_m(\lambda)$	Wavelength dependent molecular absorption coefficient
$\beta_a(\lambda)$	Wavelength dependent aerosol scattering coefficient
$\beta_m(\lambda)$	Wavelength dependent molecular scattering coefficient
$\tilde{\gamma}$	Average electrical SNR
$\gamma_T(\lambda)$	Total attenuation coefficient in m^{-1} as function of wavelength
$\Gamma_x(\rho)$	Spatial coherence as a function of spatial distance
θ_L	Optical local oscillator field phase
θ_b	Diffraction limited beam divergence angle in radians
θ_c	Incoming optical carrier field phase
θ_s	Optical source divergence angle in milliradians
$\mu_{\mathcal{U}}$	Mean of sum of log-normal variables
ξ_{opt}	Optimum optical modulation index
ξ_{subopt}	Suboptimum optical modulation index
ρ_0	Spatial coherence distance of a field traversing a turbulent channel
σ^2	Total noise variance
σ^2_{IMD3}	Third order inter-modulation distortion variance
σ^2_{Bg}	Background radiation noise variance
σ^2_{Dk}	Dark current noise variance
σ_I^2	Irradiance fluctuation variance

σ_N^2	Normalised irradiance fluctuation variance
σ_{Qtm}^2	Quantum noise variance
σ_{Sh}^2	Shot noise variance
σ_{Th}^2	Thermal noise variance
σ_k^2	Variance of $\ln(K_s)$
σ_l^2	Log irradiance variance
σ_x^2	Log field amplitude fluctuation variance
σ_U^2	Variance of sum of log-normal variables
τ_0	Temporal coherence time of a turbulent channel
$\phi_0(r)$	Field phase as a function of position without atmospheric turbulence
$\Phi_n(K)$	Refractive index fluctuation power spectral density as a function of *K*
ω_L	Local oscillator field angular frequency in radian per second
Ω_b	Radiating solid angle of an optical source
ω_c	Carrier field angular frequency in radian per second
ω_{co}	Incoming optical carrier angular frequency in radians
$A_0(r)$	Field amplitude as a function of position without atmospheric turbulence
A_D	Receiver aperture area without spatial diversity
A_L	Local oscillator field amplitude
A_T	Transmitter aperture area
A_c	Carrier field amplitude
A_d	Photodetector area
A_s	Optical source area
$\vec{E}$	Electric field
$E_L(t)$	Local oscillator field as a function of time
$E_c(t)$	Carrier field as a function of time
G_R	Receiver effective antenna gain
G_T	Transmitter effective antenna gain
K_{Bg}	Average photon count due to the background radiation
N_p	Number of particles per unit volume along the propagation path
R_F	Fresnel zone
d_s	Optical source diameter
f'	Effective focal length
$\bar{g}$	Average APD gain

$\langle i \rangle$	Mean generated electric current over a given period of time
i_B	Laser bias current
$i_D(t)$	Subcarrier signal coherent demodulator output as a function of time
i_d	Photodetector dark current
$i_p(t)$	Instantaneous generated current during optical coherent detection
i_{th}	Received signal threshold level
m_k	Mean of $\ln(K_s)$
$\langle n \rangle$	Mean received photoelectron count
$\langle x \rangle$	Mean value of variable *x*
x_0	Particle size parameter
n_0	Atmospheric channel refractive index in the absence of turbulence
α_e	Extinction ratio
$\Delta\omega$	Subcarrier frequency separation
B	Bandwidth in Hz
b_0	DC bias level
c	Speed of light in vacuum
C_n^2	Index of refraction structure parameter
d	Photodetector diameter
D	Receiver telescope aperture
d_{im}	Image diameter
E[.]	Expectation
E_g	Energy band gap in (eV)
F	Photodetector excess noise
f	Frequency in Hz
F#	f-number
g	Photodetector gain/multiplication factor
g(t)	Pulse shaping function
h	Planck's constant
I	Received irradiance at the receiver plane.
i(*t*)	Instantaneous current generated by a photodetector
I_0	Mean received irradiance without atmospheric turbulence
I_{sky}	Background irradiance from the sky
I_{sun}	Background irradiance from the Sun
i_{Th}	Laser source threshold level

K	Spatial wave number
k	Wavenumber
$\mathrm{K}_n(.)$	Modified Bessel function of the 2nd kind of order n
K_s	Average photoelectron count per unit pulse position modulation time slot
L	Link range
$\mathcal{L}$	Free space path loss
l_0	Inner scale of turbulence
L_0	Outer scale of turbulence
L_{Geom}	Geometric loss
L_M	Link margin
L_{op}	Optical/window loss
L_P	Pointing loss
m	Power margin needed to achieve a given outage probability in dB
M	Number of signal levels or symbols
$\mathcal{M}$	Number of optical sources in a multiple source system
$m(t)$	Subcarrier signal
n	Number of photo-electron count
N	Number of subcarriers
$N(\lambda)$	Spectral irradiance of the sky
n_b	Photoelectron count due to background radiation of power P_{Bg}
n_{th}	Threshold photo-electron count
P	Atmospheric pressure
$p(.)$	Probability density function
$P(t)$	Instantaneous received optical power
P_0	Received average optical power in the absence of scintillation
P_{Bg}	Background radiation power
P_e	Unconditional bit error rate
P_e^*	Threshold or reference bit error rate
P_{ec}	Bit error rate conditioned on the received optical power/irradiance
P_R	Received optical power over a period of time
P_T	Transmitted peak optical power over a period of time
q	Electronic charge
$\mathrm{Q}(.)$	Q-function
r	Position vector

R_b	Data symbol rate
R_L	Equivalent load resistance
T	Pulse duration/symbol duration
t	Instantaneous time
T_e	Temperature in Kelvin
T_s	Pulse position modulation slot duration
V	Visibility
$v(r)$	Local wind velocity as function of position, r
$W(\lambda)$	Spectral radiant emittance of the sun
Z	Sum of received irradiance in a system with receiver diversity
α	Effective number of atmospheric turbulence large scale eddies
β	Effective number of atmospheric turbulence small scale eddies
$\Gamma(.)$	Gamma function
$\gamma(a, x)$	Incomplete gamma function with variables a and x
$\gamma(I)$	Electrical SNR as a function of received irradiance
γ^*	Threshold or reference signal to noise ratio
$\Delta\lambda$	Optical band pass filter bandwidth
ζ	APD ionisation factor
η	Quantum efficiency of a photodetector
κ	Boltzmann's constant
λ	Radiation wavelength
Λ	Likelihood function
λ_c	Cut-off wavelength in micrometres (μm)
ξ	Optical modulation index
τ	Temporal diversity delay time
$\phi(r)$	Field phase as a function of position in atmospheric turbulence channel
$\Psi(r)$	Natural logarithm of the propagating field $E(r)$
Ω	Photodetector field of view angle in radians
$A(r)$	Field amplitude as a function of position in a turbulent channel
F	Noise factor of an APD
$He_n(.)$	n^{th} order Hermite polynomial
U	Number of time delay diversity paths per subcarrier channel
$n(t)$	Time varying additive white noise
$\mathcal{N}$	Number of photodetectors in a multi-detector system

$\mathcal{S}$	Gaussian distributed phase fluctuation
$\mathcal{X}$	Gaussian distributed log-amplitude fluctuation
$\mathcal{h}$	Altitude in metres
$\mathcal{n}$	Atmospheric channel refractive index
$\mathcal{r}$	Atmospheric scattering particle radius
$\mathcal{s}$	Photodetector separation in a multi-detector system
η	Photodetector quantum efficiency
κ	Boltzmann's constant
$\tau(\lambda, L)$	Transmittance of the atmosphere at wavelength, λ and distance, L
φ	Subcarrier signal phase

Dedication

To the memory of my darling mum Mrs Falilat Adetoro Popoola.

Acknowledgements

The work presented in this thesis was carried out in the Optical Communications Research Group within the School of Computing, Engineering and Information Sciences at Northumbria University, Newcastle upon Tyne. The work was part funded by Northumbria University and through the Overseas Research Students Award organised by the UK Government, both which are gratefully acknowledged.

I would like to thank my director of studies, Professor Z. Ghassemlooy, for his advice, guidance, support and constant enthusiasm throughout this work. I would also like to thank him for proof reading this thesis, and for giving me the opportunity to undertake my studies within his research group in the first place.

Sincere thanks also go to Mr. Joseph Allen and Dr. Erich Leitgeb of Graz University of Technology, who are my first and second supervisors in that order, for providing invaluable help and advice throughout this work. A word of thanks must also go to Dr. G. Brooks and the entire academic and technical members of Northumbria Communication Research Laboratory for helping me out from time to time.

I would also like to thank my colleagues in the Optical Communications Research Group, both past and present, for sharing a few laughs with me and generally making my time in Newcastle a very enjoyable experience.

I specially thank my family, especially my wife - Aisha, for their constant support, patience, understanding and encouragement throughout the duration of this work. Finally, I would like to acknowledge the unique joy I enjoy from my little angel – Widad – right from the very moment she arrived in the family some eight months ago.

Declaration

I declare that the work contained in this thesis is entirely mine and that no portion of it has been submitted in support of an application for another degree or qualification in this, or any other university, or institute of learning, or industrial organisation.

Popoola, Wasiu Oyewole

September 2009

Chapter One

Introduction

1.1 Background

Free-space optical communication (FSO) or better still, laser communication is an age long technology that entails the transmission of information laden optical radiation through the atmosphere from one point to the other. Around 800 BC, ancients Greeks and Romans used fire beacons for signalling and by 150 BC the American Indians were using smoke signals for the same purpose of signalling. Other optical signalling techniques such as the semaphore were used the French sea navigators in the 1790s; but what can be termed the first optical communication in an unguided channel was the

Photophone experiment by Alexander Graham Bell in 1880 [1, 2]. In his experiment, Bell modulated the Sun radiation with voice signal and transmitted it over a distance of about 200 metres. The receiver was made of a parabolic mirror with a selenium cell at its focal point. However, the experiment did not go very well because of the crudity of the devices used and the intermittent nature of the sun radiation.

The fortune of FSO changed in the 1960s with the discovery of optical sources, most importantly, the laser. A flurry of FSO demonstrations was recorded in the early 1960s into 1970s. Some of these included the: spectacular transmission of television signal over a 30 mile (48 km) distance using a GaAs light emitting diode by researchers working in the MIT Lincolns Laboratory in 1962 [3]; a record 118 miles (190 km) transmission of voice modulated He-Ne laser between Panamint Ridge and San Gabriel Mountain, USA in May 1963 [3]; and the first TV-over-laser demonstration in March 1963 by a group of researchers working in the North American Aviation [3]. The first laser link to handle commercial traffic was built in Japan by the Nippon Electric Company (NEC) around 1970. The link was a full duplex 0.6328 μm He-Ne laser FSO between Yokohama and Tamagawa, a distance of 14 km [3].

From this time on, FSO has continued to be researched and used chiefly by the military for covert communications. FSO has also been heavily researched for deep space applications by NASA and ESA with programmes such as the then Mars Laser Communication Demonstration (MLCD) and the Semiconductor-laser Inter-satellite Link Experiment (SILEX) respectively [4, 5]. Although, deep space FSO lies outside the scope of our discussion here, it is worth mentioning that over the past decade, near Earth FSO were successfully demonstrated in space between satellites at data rates of up to 10 Gbps [6]. In spite of early knowledge of the necessary techniques to build an

operational laser communication system, the usefulness and practicality of a laser communication system was until recently questionable for many reasons [3]. First, existing communications systems were adequate to handle the demands of the time. Second, considerable research and development were required to improve the reliability of components to assure reliable system operation. Third, a system in the atmosphere would always be subject to interruption in the presence of heavy fog. Fourth, use of the system in space where atmospheric effects could be neglected required accurate pointing and tracking optical systems which were not then available. In view of these problems, it is not surprising that until now, FSO had to endure a slow penetration into the access network.

With the rapid development and maturity of optoelectronic devices, FSO has now witnessed a re-birth. Also, the increasing demand for more bandwidth in the face of new and emerging applications implies that the old practice of relying on just one access technology to connect with the end users has to give way. These forces coupled with the recorded success of FSO in military applications have rejuvenated interest in its civil applications within the access network. Several successful field trials have been recorded in the last few years in various parts of the world which have further encouraged investments in the field [7-14]. This has now culminated into the increased commercialisation and the deployment of FSO in today's communication infrastructures.

FSO has now emerged as a commercially viable complementary technology to radio frequency (RF) and millimetre wave wireless systems for reliable and rapid deployment of data, voice and video within the access networks. RF and millimetre wave based wireless networks can offer data rates from tens of Mbps (point-to-multipoint) up to

several hundred Mbps (point-to-point) [15]. However, there is a limitation to their market penetration due to spectrum congestion, licensing issues and interference from unlicensed bands. The future emerging license-free bands are promising [16], but still have certain bandwidth and range limitations compared to the FSO. The short-range FSO links are used as an alternative to the RF links for the last or first mile to provide broadband access network to homes and offices as well as a high bandwidth bridge between the local and wide area networks [17]. Full duplex FSO systems running at 1.25 Gbps between two static nodes are now common sights in today's market just like FSO systems that operate reliably in all weather conditions over a range of up to 3.5 km. In 2008, the first 10 Gbps FSO system was introduced to the market, making it the highest-speed commercially available wireless technology [18]. Efforts are continuing to further increase the capacity via integrated FSO/fibre communication systems and wavelength division multiplexed (WDM) FSO systems which are currently at experimental stages [19].

The earlier scepticism about FSO's efficacy, its dwindling acceptability by service providers and slow market penetration that bedevilled it in the 1980s are now rapidly fading away judging by the number of service providers, organisations, government and private establishments that now incorporate FSO into their network infrastructure [7, 20]. Terrestrial FSO has now proven to be a viable complementary technology in addressing the contemporary communication challenges, most especially the bandwidth/high data rate requirements of end users at an affordable cost. The fact that FSO is transparent to traffic type and data protocol makes its integration into the existing access network far more rapid. Nonetheless, the atmospheric channel effects such as thick fog, smoke and turbulence as well as the attainment of 99.999% availability still pose the greatest challenges to long range terrestrial FSO.

1.2 Research Motivation and Justification

The ever increasing bandwidth requirement of present and emerging communication systems is the driving force behind research in optical communications (both fibre optics and optical wireless). Optical communication guarantees abundant bandwidth, which translates into high data rate capabilities. The huge bandwidth available on the fibre ring networks that form the backbone of modern communication technology is still not available to end users within the access network. This is mainly due to the bandwidth limitations of the copper wire based technologies that, in most places, connect the end users to the backbone. This places a restrictive limit on the data rate/download rate available to end users. This problem is termed 'access network bottleneck' and a number of approaches, including fibre to the home (FTTH), Digital subscriber loop (DSL) or cable modems, power-line communication, local multipoint distribution service (LMDS), ultra-wide band technologies (UWB) and terrestrial free space optics (FSO), have been proposed to tackle this bottleneck.

The FTTH technology would be an ideal solution to the access network bottleneck, and it continues to be deployed with Japan and South Korea being the world leaders in terms of FTTH deployment and penetration rates [21]. FTTH technology can conveniently deliver up top 10 Gbps to the end users and with the implementations of schemes such as dense wavelength division multiplexing, higher data rates of up to 10 Tbps are feasible [15, 22, 23]. The most prominent obstacle inhibiting a wider deployment of FTTH is its prohibitive cost of implementation. Also, the fact that both DSL and power-line communication systems are copper-based make them less attractive [20]. The LMDS is a fixed broadband, line of sight, wireless radio access system using a range of frequencies around 27.5 - 31.3 GHz and 40.5 - 42.5 GHz in the US and Europe,

respectively [24]. It has bandwidth capabilities of several hundreds of Mbps, but the fact that its carrier frequencies are within the licensed bands makes it less attractive [15], it also surfers severe signal attenuation and outage during rainfall [24].

The UWB is another wireless radio solution whose spectrum is unlicensed just like the FSO technology; the Federal Communications Commission in 2002 approved it for unlicensed operation in the 3.1-10.6 GHz band [16]. UWB can potentially deliver several Mbps data rate over a short range. The technology is appealing but just as copper wire based solutions, its potential data rate is a far cry from the several Gbps available in the backbone. Moreover, being a wideband technology, there are serious concerns regarding the interference of UWB signals with other systems/gadgets operating within the same frequency spectrum [25].

Terrestrial FSO is now receiving an increasing interest as a very promising complementary technology in this regard. The capacity of FSO is comparable with that of optical fibre and at a fraction of FTTH deployment cost; it requires less time to deploy, is re-deployable (no sunk cost), and is requires no digging of trenches and rights of way [26, 27]. FSO is transparent to traffic type and protocol, making its integration into the access network almost hitch free. To further enhance its seamless integration, an understanding of the capabilities, limitations and performance analysis of an optical wireless system that is based on some of the existing access network traffic types, modulation techniques, is therefore highly desirable.

The greatest challenges facing FSO result from the atmospheric channel, resulting in signal scattering, absorption and fluctuation [28-33]. The presence of aerosols (fog, smoke and other suspended particles) and gases in the atmosphere cause attenuation of

the traversing optical signal. Thick fog presents the highest attenuation, and in experimental results for: Prague, Graz, Italy, United Kingdom, America and other parts of the World, atmospheric attenuation of over 100 dB have been recorded [9, 15, 34-37]. Fog distribution, its different types and characterisation are well reported in literature [36, 38-40]; during thick fog, the atmospheric attenuation is independent of wavelength [15, 31, 34].

Atmospheric attenuation, due to fog, places an additional requirement on the design of an FSO system in that, more optical power will have to be transmitted to cater for the loss without exceeding the safety limits stipulated by regulatory bodies or the link range be shortened [15]. In the study reported in [15, 34], the authors argued that it is impossible to achieve a reliable FSO link of over 500 metres in the presence of thick fog without exceeding the regulatory limits on the amount of optical power that can be transmitted through the atmosphere. Since the occurrence of thick fog is localised, short lived and not experienced in all locations, FSO links longer than 1 km are viable. In regions prune to thick fog, an RF back-up link can be incorporated to have an FSO-RF hybrid system which is capable of delivering 99.999% availability in all weather conditions as reported in [34, 41]. The use of this hybrid system however means that a reduced data rate will be in operation whenever the RF back-up link is in action [15]. Some of the challenges of the hybrid system include loss of data during switch over from FSO to RF or vice versa and/or loss of real time operation due to temporary storage of data when switching. Preventing data loss during switching will require the use of buffers. In addition, the change over switch is expected to be fast and quite clever to avoid any false trigger.

Apart from attenuation, another important channel effect is the atmospheric scintillation. It is caused by atmospheric turbulence, which is a direct product of atmospheric temperature inhomogeneity [28-30, 40, 42]. The scintillation effect results in signal fading, due to constructive and destructive interference of the optical beam traversing the atmosphere. For FSO links spanning 500 meters or less, typical scintillation fade margins are 2 to 5 dB, which is less than the margins for atmospheric attenuation [43], making scintillation insignificant for short range FSO systems. However, in clear air when the atmospheric channel attenuation is less than 1 dB/km and most especially when the link range is in excess of 1 km, scintillation impairs the FSO link availability, attainable error performance and the available link margin significantly [29, 31, 42, 44].

The most commonly reported model for describing the atmospheric turbulence induced scintillation is the log-normal model [30, 45-47]. This model is valid only in weak atmospheric turbulence and as the strength of turbulence increases, multiple scattering effects, not accounted for by the log-normal model, must be taken into account. Beyond the weak turbulence regime, the log-normal model exhibit large deviations compared to experimental data [28-30] and its probability density function (pdf) also underestimates the signal distribution behaviour in the tails as compared with measurements results [9]. Since bit error and fade probabilities are primarily based on the tails of the pdf, underestimating this region will significantly affect the accuracy of any error performance analysis carried out with it [45]. For longer range FSO systems (> 1km), the atmospheric turbulence strength increases from weak to strong and ultimately to saturation regime as the link range increases. The gamma-gamma and negative exponential models [30, 48-50], which will be discussed in details in Chapter Four, are other models for describing the signal fluctuation under a wide range of atmospheric turbulence conditions.

In evaluating the performance of FSO systems in turbulent atmospheric channels, researchers [48, 51, 52] have analysed the bit error probabilities, based on on-off keying (OOK) modulated FSO systems, across all turbulence regimes. Also, an alternative modulation technique - the pulse position modulation (PPM) technique - which has a superior power efficiency compared to OOK has also been studied in atmospheric turbulence channels [53-56]. The low peak-to-average power requirement of the PPM makes it a prime candidate in deep space laser communications, where it is being used predominantly [4, 6]. PPM however suffers from poor bandwidth efficiency due to its short duration pulses, stringent slot and symbol synchronisation requirements and as such, is not used in commercial terrestrial FSO systems at the moment.

Typical scintillation fades last between 1 μs and 100 μs, and when the link is operated at multi-gigabits per second data rate, the loss of potentially up to 10^9 consecutive bits may occur, thus causing devastating effect on the throughput of the network due to interactions with the upper layer protocols [44]. Therefore, the turbulence induced fading duration and strength has to be mitigated. To achieve this goal, the use of forward error control mechanisms with OOK-FSO have been reported in [48, 51, 57-60]. Invoking error control coding introduces huge processing delays and efficiency degradation in view of the number of redundant bits that will be required [61, 62]. To this end, the use of receiver array with OOK-FSO has been proposed and analysed in [61, 63-65] while [66] reported on the error performance analysis of PPM-FSO with photo-counting array receivers used to lessen the atmospheric turbulence induced channel fading. In the work reported in [67], semiconductor amplifiers operated in saturation mode have been proposed to reduce the channel fading. The study of adaptive optics to correct the wavefront deformation caused by atmospheric turbulence has also

been investigated in [68], but this technique is very expensive and complex to implement on terrestrial FSO systems.

The OOK modulation technique is very simple to implement and is therefore the modulation technique of choice in all commercially available terrestrial FSO systems at the moment [20, 29, 31, 34, 40]. In the standard OOK-FSO, the threshold level/point in the decision circuitry used to distinguish between bits zero and one is always fixed midway between the expected levels of data bits one and zero [69]. This works fine and gives the optimum error performance in non-fading channels. In the presence of turbulence induced channel fading, the received signal level fluctuates, this means that the threshold detector has to track this fluctuation in order to determine the optimum decision point [70]. This poses a great design challenge, as the channel noise and fading will have to be continually tracked for the OOK-FSO to perform optimally. Ignoring the signal fluctuation and operating the OOK-FSO system with a fixed threshold level however will result in increased detection error as reported in [71].

In order to address the symbol detection challenges of OOK-FSO in atmospheric turbulence induced channels and the poor bandwidth efficiency of PPM; this research will be investigating the phase shift keying pre-modulated subcarrier intensity modulation (SIM) as an alternative modulation technique. Moreover for the full and seamless integration of FSO into existing networks, some of which already contain subcarrier/multicarrier signals, such as, cable television signals, multi carrier and radio over fibre signals, the understanding and error performance analysis of subcarrier modulated FSO becomes imperative. In this thesis, the error and outage performance of SIM-FSO will be broadly investigated in the following atmospheric turbulence regimes, weak, moderate, strong and saturation. In order to ameliorate the fading effect of

turbulent atmospheric channels on SIM-FSO systems and avoid the huge processing delays associated with forward error control, the cost and complexity of adaptive optics, this research will be considering spatial and temporal diversity techniques. The following research objectives have been formulated in order to achieve these goals.

1.3 Research Objectives

This research work is aimed at investigating the performance of a subcarrier intensity modulated FSO system with the view to understanding its benefits and limitations. The research is also aimed at comparing the error performance of SIM-FSO with that of OOK-FSO. The results of the analysis will be useful in determining the power required to achieve a desired level of performance and consequently, the achievable link margin and possible link range. To achieve this, a number of research objectives have been outlined as follows:

- Review the fundamental properties of terrestrial FSO and understand the characteristics properties of the atmospheric channel and the challenges imposed on the system performance.

- Review the models for describing the channel fading induced by a turbulent atmosphere. To understand the limits and range of validity of each of the models.

- Review the performance of terrestrial FSO based on OOK and PPM in a turbulent atmospheric channel.

- Investigate the performance of SIM free-space optical communication systems in terms of the bit error rate and outage probability in all atmospheric turbulence conditions – weak, moderate, strong and saturation turbulence regimes – based on the following atmospheric turbulence models:

    - Log-normal
    - Gamma-gamma
    - Negative exponential

- Investigate the spatial diversity as a technique for ameliorating the fading effect of atmospheric turbulence on the performance of terrestrial SIM-FSO systems.

- Investigate the temporal diversity as an alternative or complementary technique for ameliorating the effect of atmospheric turbulence on the performance of SIM-FSO systems.

- Investigate the effect of optical source (transmitter) inherent non-linearity on the system error performance.

- To develop an experimental test-bed to validate the atmospheric turbulence fading effect on an FSO system. Verify experimentally the turbulence induced fading effect on the threshold level of OOK-FSO and compare with SIM-FSO.

1.4 Thesis Organisation

This thesis is arranged into ten chapters, following the introduction chapter, Chapter Two examines the basic fundamentals of FSO. In the chapter, an overview of the FSO technology is presented with its distinguishing features. The three main building blocks of FSO are also introduced in this chapter and the functions of each block highlighted. The chapter mentions areas where terrestrial FSO currently finds application and atmospheric channel effects are introduced in the remainder of the chapter. The methods and process of recovering information from an incoming optical radiation is discussed in Chapter Three. The chapter discusses photodetectors used for converting optical radiation to an electrical signal and the properties of the two classes of photodetectors. A review of both direct and coherent optical detection theory as well as various sources of noise encountered in terrestrial FSO is presented. The chapter is concluded with a review of optical detection statistics, this provides the required background for the analysis presented in later chapters.

In Chapter Four, a review of atmospheric turbulence is presented and its effect on optical radiation traversing the atmosphere highlighted. Three different statistical distributions for modelling the irradiance fluctuation of optical radiation travelling through a turbulent atmosphere are discussed. The discussion of these models is vital as they will be used in later chapters to model the statistical behaviour of the received signal in a short, long and very long range FSO link. Also in this chapter, the spatial coherence of a field travelling through a turbulent channel is discussed; this will be later used in determining the spacing of detectors in a receiver array of Chapter Seven.

The error performance of a terrestrial FSO system based on OOK and PPM signalling techniques is the subject of discussion in Chapter Five. The error performance of PPM modulated FSO is reviewed and its pros and cons highlighted and same is done for OOK-FSO. This chapter highlights the performance limitation of OOK-FSO operating in turbulent atmospheric channel and proposes SIM as an alternative modulation technique. Chapter Six presents the performance of an SIM-FSO link, based on the bit error and the probability of outage performance metrics. The turbulent atmospheric channel is described by the models reviewed in Chapter Four and closed form expressions are derived for the system performance under different turbulence strength and noise conditions. The chapter is concluded by investigating intermodulation distortion due to non linearity of the optical source and its implication on the modulation index and system performance.

The use of two methods, namely, spatial and temporal diversity techniques, to mitigate the power penalty induced by the channel fading is investigated in Chapter Seven. The chapter discusses and contains the process of deriving both the error rate and outage probabilities of a SIM-FSO employing spatial diversity. Three different ways of linearly combining the signals from the multiple photodetectors are investigated and the error rate equations derived for each one of them. The chapter goes on to consider the impact of signal correlation on the predicted gain of using multiple photodetectors. Other spatial diversity configurations, such as multiple sources with or without multiple photodetectors, are also analysed in this chapter with the view to obtaining the optimum number of sources/photodetectors.

In Chapter Eight, the different types of loss mechanisms encountered in the design of an FSO system, including but not limited to the channel absorption and scattering, are

examined and the link budget expression derived. Based on the results of previous chapters, an estimate of achievable link ranges and margins are also presented in this chapter. Chapter Nine gives a detailed description of the experiment used to demonstrate the effect of atmospheric turbulence on the threshold level of an OOK-FSO system along with its SIM-FSO counterpart. In the experiment, optical beam is passed through a 'turbulence chamber' to create the turbulence induced scintillation effect. Finally in Chapter Ten, keys findings of this research are summarised, concluding comments made and recommendations for future are outlined.

1.5 Original Contributions

During the course of this research, the author has:

1. Investigated the performance limit imposed on a terrestrial FSO system based on the OOK signalling technique. Expression for the error performance of OOK-SIM has been derived in turbulence induced fading channel and the difficulty of estimating the optimum threshold level highlighted, as detailed in Chapter Five.

2. Derived closed form expressions for the bit error rate and the outage probabilities of phase shift keying pre-modulated SIM-FSO in turbulent atmosphere, covering weak, moderate, strong and saturation atmospheric turbulence regimes. Compared the error performance of SIM-FSO with its OOK-FSO counterpart operating under the same channel conditions. Investigated in Chapter Six, the use of multiple subcarrier systems to increase the capacity/throughput and its accompanying penalty.

3. Investigated the atmospheric turbulence induced power penalty, impact of optical source inherent non linearity on the error performance of SIM-FSO and analytical method of determining optimum modulation index in the presence of intermodulation distortion, these are all detailed in Chapter Six.

4. Derived closed form expressions for the error performance of SIM-FSO with linearly combined multiple sources and/or receivers in Chapter Seven. Considered and investigated the impact of signal correlation on the error performance and compared three different ways of combining the signals received by an array of detectors.

5. Introduced subcarrier time delay diversity as a channel fading mitigating technique in Chapter Seven and investigated its performance with and without intermodulation distortion.

6. Experimentally verified the difficulty imposed on the determination of the threshold level of an OOK modulated FSO operating in turbulent atmosphere and compared that with a binary phase shift keying pre-modulated SIM-FSO as detailed in Chapter Nine.

These contributions are summarised in Fig.1.1 and have led to the following publications and awards:

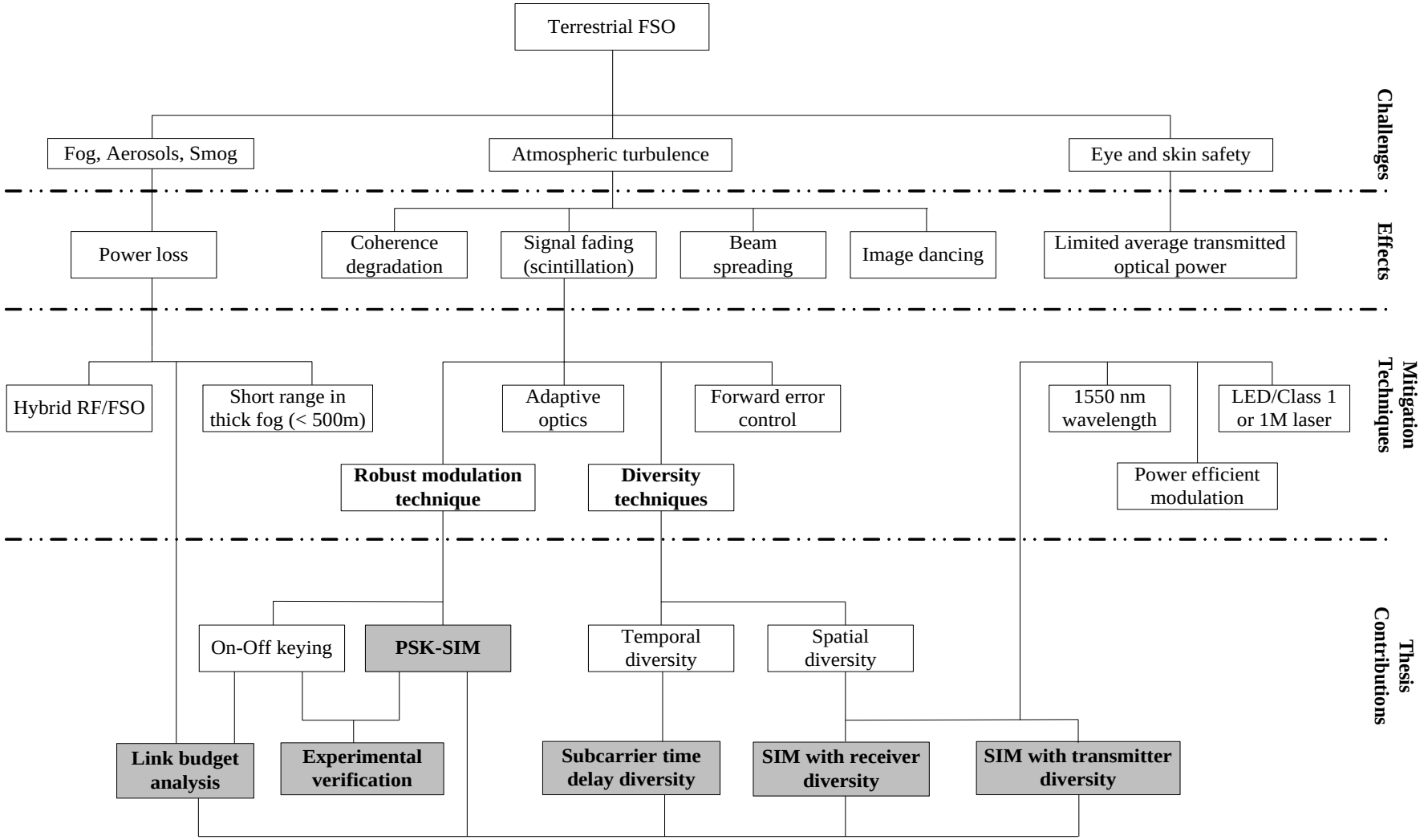

Fig.1.1: Summary of thesis contributions

1.6 List of Publications and Awards

Book Chapter

1. Terrestrial Free-Space Optical Communications in "Mobile and Wireless Communications: Key Technologies and Future Applications" ISBN 978-3-902613-47-9" (In print).

Refereed Journal Papers

2. W. Popoola, Z. Ghassemlooy, C. G. Lee, and A. C. Boucouvalas,: "*Scintillation Effect on Intensity Modulated Laser Communication Systems - A Laboratory Demonstration*", Elsevier's Optics and Laser Technology Journal (In print)

3. W. O. Popoola, Z. Ghassemlooy,: "*BER and Outage Probability of DPSK Subcarrier Intensity Modulated Free Space Optics in Fully Developed Speckle*" Journal of Communications (In print).

4. W. O. Popoola, and Z. Ghassemlooy,: *"BPSK Subcarrier Modulated Free-Space Optical Communications in Atmospheric Turbulence"* IEEE-Journal of Lightwave Technology, Vol. 27. No 8, pp. 967-973, April 15 2009.

5. W. O. Popoola, Z. Ghassemlooy, and V. Ahmadi,: "*Performance of sub-carrier modulated Free-Space optical communication link in negative exponential atmospheric turbulence environment*," International Journal of Autonomous and Adaptive Communications Systems, Vol. 1, No. 3, pp.342–355, 2008.

6. *W. O. Popoola, Z Ghassemlooy, J I H Allen, E Leitgeb, S Gao: " *Free-Space Optical Communication employing Subcarrier Modulation and Spatial Diversity in Atmospheric Turbulence Channel*" IET Optoelectronics, Vol. 2, Issue 1, pp.16 – 23, Feb. 2008.

7. Ghassemlooy, Z., Popoola, W. O., and Aldibbiat, N. M.: "*Equalised Dual Header Pulse Interval modulation for diffuse optical wireless communication system*", Mediterranean J. of Electronics and Communications, Vol. 2, No. 1, pp. 56-61, 2006.

**According to IET, this paper ranked No. 2 in terms of the number of full text downloads within IEEE Xplore in 2008, from the hundreds of papers published by IET Optoelectronics since 1980.*

Conference Papers

8. Ijaz, M., Wu, S., Fan, Z., Popoola, W. O., and Ghassemlooy, Z.: "*Study of the atmospheric turbulence in free space optical communications*," 10th Annual Postgraduate Symposium On the Convergence of Telecommunications, Networking and Broadcasting, Liverpool, UK, pp. 88-91, 22-23 June 2009.

9. Z. Ghassemlooy, W. O. Popoola, V. Ahmadi, and E Leitgeb: "*MIMO Free-Space Optical Communication Employing Subcarrier Intensity Modulation in Atmospheric Turbulence Channels*" **Invited paper.** The First International ICST Conference on Communications Infrastructure, Systems and Applications in Europe (EuropeComm), London, UK, 11-13 August 2009.

10. W. Popoola, Z. Ghassemlooy, M. S. Awan, and E. Leitgeb: "*Atmospheric Channel Effects on Terrestrial Free Space Optical Communication Links*" **Invited paper**. 3rd International Conference on Computers and Artificial Intelligence (ECAI 2009), 3-5, Piteşti, Romania, July, 2009.

11. W. O. Popoola, Z. Ghassemlooy and E. Leitgeb "*BER Performance of DPSK Subcarrier Modulated Free Space Optics in fully Developed Speckle*", IEEE - CSNDSP, Graz, Austria, pp. 273-277, 23-25 July 2008.

12. Z. Ghassemlooy, W.O. Popoola, S. Rajbhandari, M. Amiri, S. Hashemi,: "*A synopsis of modulation techniques for wireless infrared communication*", **Invited paper**. IEEE - International Conference on Transparent Optical Networks, Mediterranean Winter (ICTON-MW), Sousse, Tunisia, pp. 1-6. 6-8 Dec. 2007.

13. W.O. Popoola and Z. Ghassemlooy.: *"Free-Space optical communication in atmospheric turbulence using DPSK subcarrier modulation*", Ninth International Symposium on Communication Theory and Applications, ISCTA'07, Ambleside, Lake District, UK, 16-20 July 2007.

14. Z. Ghassemlooy, W.O. Popoola, and E. Leitgeb. "*Free-Space optical communication using subcarrier modulation in Gamma-Gamma atmospheric turbulence*" **Invited paper**. IEEE - 9th International Conference on Transparent Optical Networks, Rome, Italy, 1-5 July 2007.

15. W. O. Popoola, Z. Ghassemlooy and J. I. H. Allen. "*Performance of subcarrier modulated Free-Space optical communications*", 8th Annual Post Graduate Symposium on the Convergence of Telecommunications, Networking and Broadcasting (PGNET), Liverpool, UK, 28-29 June 2007.

16. S. Rajbhandari, Z. Ghassemlooy, N. M. Aldibbiat, M. Amiri, and W. O. Popoola.: "*Convolutional coded DPIM for indoor non-diffuse optical wireless link*", 7th

IASTED International Conferences on Wireless and Optical Communications (WOC 2007), Montreal, Canada, pp. 286-290, May-Jun. 2007.

17. Popoola, W. O., Ghassemlooy, Z., and Amiri, M.: "*Coded-DPIM for non-diffuse indoor optical wireless communications*", PG Net 2006, ISBN: 1-9025-6013-9, Liverpool, UK, pp. 209-212, 26-27 June 2006.

18. W. O. Popoola, Z Ghassemlooy, and N. M. Aldibbiat,: "*DH-PIM employing LMSE equalisation for indoor infrared diffuse systems*", 14th ICEE, Tehran, Iran, 2006.

19. W. O. Popoola, Z. Ghassemlooy and N. M. Aldibbiat: "*Performance of DH-PIM employing equalisation for diffused infrared communications*", LCS 2005, London, pp. 207-210, Sept. 2005.

Posters

20. Popoola, W. O., and Ghassemlooy, Z.: "Free space optical communication", UK GRAD Programme Yorkshire & North East Hub, Poster Competition & Network Event, Leeds, Poster No. 52, 9 May 2007.

21. Burton, A, Ghassemlooy, Z, Popoola, W.O., Simulation software for the evaluation of free space optical communications links, 19th International Scientific Conference, Mittweida, Germany, July 2008.

Research Related Awards

- **2009**: 2nd most downloaded paper in terms of the number of full text downloads within IEEE Xplore in 2008, from the hundreds of papers published by IET Optoelectronics since 1980.
- **2008**: C. R. Barber Conference Grant awarded by the Institute of Physics (IoP) to attend CSNDSP international conference in Graz, Austria.
- **2008 – 2009**: Best performing PhD student for two consecutive academic sessions, 2007/2008 and 2008/2009.
- **2006 – 2009**: Northumbria University PhD Studentship.
- **2006 – 2009**: Overseas Research Student Award (ORSA) by the UK Government.

Chapter Two

Fundamentals of FSO

2.1 Introduction

An overview of the FSO technology is presented in this chapter alongside its salient features that make it a viable complementary access network technology. The fundamental challenges facing FSO are also introduced and areas where FSO presently find application are highlighted. The chapter looks into the optoelectronic devices used in FSO and concludes with a discussion on eye/skin safety from optical radiation.

2.2 Overview of FSO Technology

In basic terms, FSO involves the transfer of data/information between two points using optical radiation as the carrier signal through unguided channels. The data to be transported could be modulated on the intensity, phase or frequency of the optical carrier. An FSO link is essentially based on line-of sight (LOS), thus to ensure a successful exchange of information requires that both the transmitter and the receiver directly 'see' one another without any obstruction in their path. The unguided channels could be any, or a combination, of space, sea-water, or atmosphere. The emphasis in this work is however on terrestrial FSO and, as such, the channel of interest is the atmosphere.

An FSO communication system can be implemented in two variants. The conventional FSO, shown in Fig. 2.1, is for point-to-point communication with two similar transceivers, one at each end of the link. This configuration allows for a full-duplex communication, in which information can be exchanged simultaneously between the two link heads in both directions. The second variant uses a modulated retro-reflector (MRR). Laser communication links with MRRs are composed of two different terminals and hence are asymmetric links. On one end of the link there is the MRR, while the other hosts the interrogator as shown in Fig. 2.2. The interrogator projects a continuous wave (CW) laser beam out to the retro-reflector. The modulated retro-reflector then modulates the CW beam with the input data stream. The beam is then retro-reflected back to the interrogator. The interrogator receiver collects the return beam and recovers the data stream from it. The system just described permits only simplex communication. A two-way communication can also be achieved with the MRR by adding a photodetector to the MRR terminal and the interrogator beam is then

shared in a half-duplex manner. Unless otherwise stated however, the conventional FSO link is assumed throughout this work.

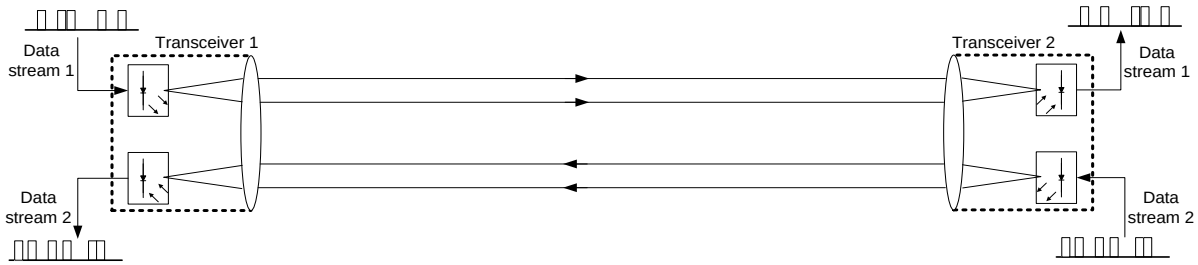

Fig. 2.1: Conventional FSO system block diagram

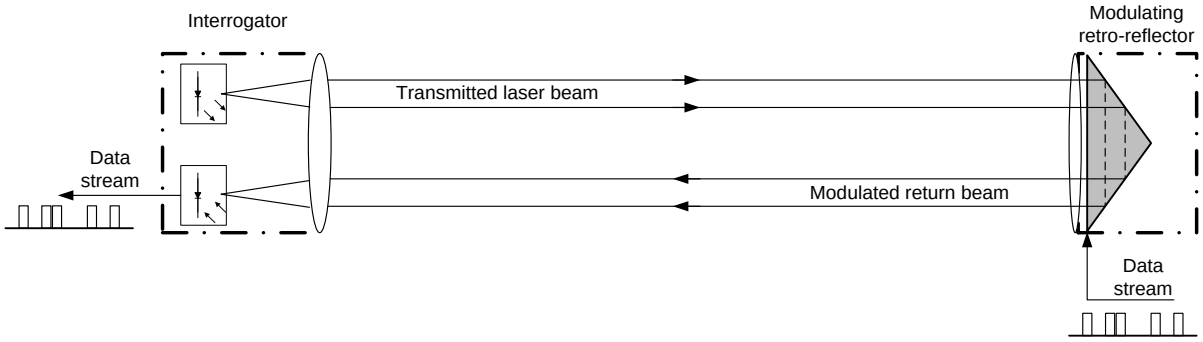

Fig. 2.2: Modulated retro-reflector based FSO system block diagram

The basic features, areas of application and the description of each fundamental block of an FSO system are further discussed in the following sections.

2.3 Features of FSO

Given below are the basic features of FSO technology:

Huge modulation bandwidth – In any communication system, the amount of data transported is directly related to the bandwidth of the modulated carrier. The allowable data bandwidth can be up to 20 % of the carrier frequency. Using an optical carrier whose frequency ranges from 10^{12} – 10^{16} Hz could thus permit up to 2000 THz data

bandwidth. Optical communication therefore guarantees an increased information capacity compared to radio frequency based communication systems. This is simply because on the electromagnetic spectrum, the optical carrier frequency, which includes infrared, visible and ultra violet frequencies, is far greater than the radio frequency. The usable frequency bandwidth in RF range is comparatively lower by a factor of 10^5.

Narrow beam size – The optical radiation is known for its extremely narrow beam, a typical laser beam has a diffraction limited divergence of between 0.01 – 0.1 mrad [1]. This implies that the transmitted power is only concentrated within a very narrow area, thus providing an FSO link with adequate spatial isolation from its potential interferers. The tight spatial confinement also allows for the laser beams to operate nearly independently, providing virtually unlimited degrees of frequency reuse in many environments and makes data interception by unintended users difficult. Conversely, the narrowness of the beam implies a tighter alignment requirement.

Unlicensed spectrum – Due to the congestion of the RF spectrum, interference from adjacent carriers is a major problem facing wireless RF communication. To minimise this interference, regulatory authorities, such as the Federal Communication Commission (FCC) in US and Office of Communication (Ofcom) in the UK, put stringent regulations in place. To be allocated a slice of the RF spectrum therefore requires a huge fee and several months of bureaucracy. At present, the optical frequencies are free from all of this. The absence of a license fee and its bureaucratic time delay implies that the return on investments in FSO technology begins to trickle in far more quickly since the initial set-up cost is lower and the deployment time shorter.

Cheap – The cost of deploying FSO is lower than that of an RF with a comparable data rate. FSO can deliver the same bandwidth as optical fibre but without the extra cost of right of way and trenching. Based on a recent findings by 'fSONA', an FSO company based in Canada, the cost per Mbps per month based on FSO is about half that of RF based systems [72].

Quick to deploy and redeploy – The time it takes for an FSO link to become fully operational, starting from installation down to link alignment, could be as low as four hours. The key requirement is the establishment of an unimpeded line of sight between the transmitter and the receiver. It can also be taken down and redeployed to another location quite easily.

Weather dependent – The performance of terrestrial FSO is tied to the atmospheric conditions. The 'unfixed' properties of the FSO channel undoubtedly pose the greatest challenge. However this is not peculiar to FSO, as RF and satellite communication links also experience link outages during heavy rainfall and in stormy weather.

In addition to the above points, other secondary features of FSO include:

- It leverages on existing fibre optics communications optoelectronics
- It is free from, and does not cause, electromagnetic interference
- Unlike wired systems, FSO is a non-fixed recoverable asset
- The optical radiation power must be within the stipulated safety limits
- It has light weight and is very compact
- It consumes low power
- It requires line of sight and strict alignment as a result of its beam narrowness.

2.3.1 Areas of application

The characteristic features of FSO discussed above make it very attractive for various applications within the access and the metro networks. It can conveniently complement other technologies, such as wired and wireless radio frequency communications, fibre-to-the-X technologies and hybrid fibre coaxial among others, in making the huge bandwidth that resides in an optical fibre backbone available to the end users. The point that most end users are within a short distance from the backbone – one mile or less – makes FSO very attractive as a data bridge between the backbone and the end-users. Among other emerging areas of application, terrestrial FSO has been found suitable for use in the following areas:

Last mile access – FSO is used to bridge the bandwidth gap (last mile bottleneck) that exists between the end-users and the fibre optic backbone. Links ranging from 50 m up to a few km are readily available in the market with data rates covering 1 Mbps to 10 Gbps [18, 20].

Optical fibre back up link – Used to provide back-up against loss of data or communication breakdown in the event of damage or unavailability of the main optical fibre link [20].

Cellular communication back-haul – Can be used to back-haul traffic between base stations and switching centres in the $3^{rd}/4^{th}$ generation (3G/4G) networks, as well as transporting IS-95 code division multiple access (CDMA) signals from macro and micro-cell sites to the base stations [20].

Disaster recovery/Temporary links – The technology finds application where a temporary link is needed, be it for a conference or ad-hoc connectivity in the event of a collapse of an existing communication network [73].

Multi-campus communication network – FSO has found applications in interconnecting campus networks and providing back-up links at Fast-Ethernet or Gigabit-Ethernet speeds [73].

Difficult terrains – FSO is an attractive data bridge in such instances as across a river, a very busy street, rail tracks or where right of way is not available or too expensive to pursue.

High definition television – In view of the huge bandwidth requirement of high definition cameras and television signals, FSO is increasingly being used in the broadcast industry to transport live signals from high definition cameras in remote locations to a central office [18].

2.4 FSO Block Diagram

The block diagram of a typical terrestrial FSO link is shown in Fig. 2.3. Like any other communication technology, an FSO system essentially comprises the following three parts: transmitter, channel and receiver. Further discussion of each of these blocks is presented in the following sections.

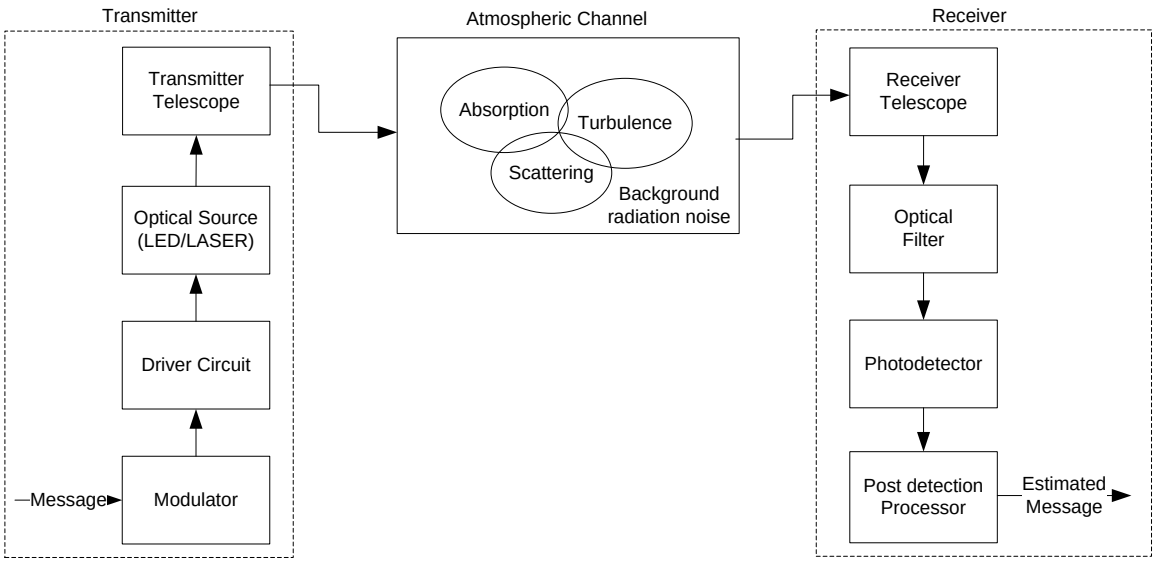

Fig. 2.3: Block diagram of a terrestrial FSO link

2.4.1 The transmitter

This functional block has the primary duty of modulating the source data onto the optical carrier, which is then propagated through the atmosphere to the receiver. The most widely used modulation type is the intensity modulation (IM), in which the source data is modulated onto the irradiance of the optical radiation. This is achieved by varying the driving current of the optical source directly in sympathy with the data to be transmitted or via an external modulator, such as the symmetric Mach-Zehnder interferometer. The use of an external modulator guarantees a higher data rate than direct modulation, but an external modulator has a nonlinear response. Other properties of the radiated optical field such as its phase, frequency and state of polarisation can also be modulated with data/information through the use of an external modulator. The transmitter telescope collects, collimates and directs the optical radiation towards the receiver telescope at the other end of the channel. Table 2.1 contains the summary of commonly used sources in FSO systems.

Table 2.1: Optical sources

Wavelength (nm)	Type	Remark
~850	Vertical cavity surface emitting laser	Cheap and readily available (CD lasers) No active cooling Lower power density Reliable up to ~10Gbps Typical power: 6 mW
~1300/~1550	Fabry-Perot lasers	Long life Lower eye safety criteria 50 times higher power density (100 mW/cm^2) Typical power: 28 mW
	Distributed-feedback lasers	Compatible with Erbium doped fibre amplifier High speed, up to 40 Gbps A slope efficiency of 0.03-0.2 W/A Typical power can reach 1 - 2 W when combined with Erbium doped fibre amplifier [31]
~10,000	Quantum cascade laser	Expensive and relative new Very fast and highly sensitive Better thin fog transmission characteristics [74]. Components not readily available No penetration through glass Output power up to 100 mW
Near Infrared	LED	Cheaper Non coherent Lower power density, hence safer [75] Simpler driver circuit Lower data rates: < 200 Mbps [76, 77] Typically low power: < 10 mW

Within the 700 – 10,000 nm wavelength band, there are a number of transmission windows that are almost transparent with an attenuation of < 0.2 dB/km. The majority of FSO systems are however designed to operate in the 780 – 850 nm and 1520 – 1600 nm spectral windows. The former is the most widely used spectrum, because devices and components are readily available and at a low cost at these wavelengths [20]. The 1550 nm band is attractive for a number reasons including: i) compatibility with the 3rd window wavelength-division multiplexing networks; ii) eye safety (more power can be transmitted than in the 780 nm band); and iii) reduced solar background and scattering

in light haze/fog. Consequently at 1550 nm significantly more power can be transmitted to overcome attenuation by fog [78]. However, the drawbacks of the 1550 nm band are slightly reduced detector sensitivity, higher component cost and stricter alignment requirements.

2.4.2 The atmospheric channel

An optical communications channel differs from the conventional Gaussian-noise channel in that the signal $x(t)$ represents power rather than amplitude. This leads to two constraints on the transmitted signal: i) $x(t)$ must be non-negative; and ii) the average value of $x(t)$ must not exceed a specified maximum power $P_{\max}$, that is $P_{\max} \geq \lim_{T\to\infty} \frac{1}{2T}\int_{-T}^{T} x(t)dt$. In contrast to the conventional channels, where the signal-to-noise ratio (SNR) is proportional to the power, in optical systems the received electrical power and the variance of the shot noise are proportional to A_d^2 and A_d, respectively, where A_d is the receiver detector area. Thus, for a shot noise limited optical system, the SNR is proportional to A_d. This implies that for a given transmitted power, a higher SNR can be attained by using a large area detector. However, as A_d increases so does its capacitance, which has a limiting effect on the receiver bandwidth.

The atmospheric channel consists of gases, listed in Table 2.2, and aerosols – tiny particles suspended in the atmosphere. Also present in the atmosphere are rain, haze, fog and other forms of precipitation. The amount of precipitation present in the atmosphere depends on the location (longitude and latitude) and the season. The highest concentration of particles is obviously near the Earth surface within the troposphere and this decreases with increasing altitude up through to the ionosphere [79]. With the size distribution of the atmospheric constituents ranging from sub-micrometres to

centimetres, an optical field that traverses the atmosphere is scattered and/or absorbed resulting in power loss.

Table 2.2: The gas constituents of the atmosphere [80].

Constituent	**Volume Ratio (%)**	**Parts Per Million (ppm)**
Nitrogen (N_2)	78.09	
Oxygen (O_2)	20.95	
Argon (Ar)	0.93	
Carbon dioxide (CO_2)	0.03	
Water vapour (H_2O)		40 – 40,000
Neon (Ne)		20
Helium (He)		5.2
Methane (CH_4)		1.5
Krypton (Kr)		1.1
Hydrogen (H_2)		1
Nitrous oxide (N_2O)		0.6
Carbon monoxide (CO)		0.2
Ozone (O_3)		0.05
Xenon (Xe)		0.09

For an optical radiation traversing the atmosphere, some of the photons are extinguished (absorbed) by the molecular constituents (water vapour, CO_2, fog, ozone etc) and their energy converted into heat, while others experience no loss of energy but their initial directions of propagation are changed (scattering). The beam also spreads out while traversing the channel causing the size of the received beam to be greater than the receiver aperture. The Beer - Lambert law describes the transmittance of an optical field through the atmosphere as [20]:

$$\tau(\lambda, L) = \frac{P_R}{P_T} = \exp[-\gamma_T(\lambda)L] \tag{2.1}$$

where $\gamma_T(\lambda)$ and $\tau(\lambda, L)$ represent the total attenuation/extinction coefficient (m^{-1}) and the transmittance of the atmosphere at wavelength λ, respectively. P_T is the transmitted

optical power and P_R the received optical power after distance, L. This process of optical transmission power loss will be further discussed in Chapter Eight.

Another feature of interest is the atmospheric turbulence. When radiation strikes the Earth from the Sun, some of the radiation is absorbed by the Earth's surface thereby heating up its (Earth's) surface air mass. The resulting mass of warm and lighter air then rises up to mix turbulently with the surrounding cooler air mass. This culminates in small (in the range of 0.01 to 0.1 degrees) but spatially and temporally fluctuating atmospheric temperature [1]. The temperature inhomogeneity of the atmosphere causes corresponding changes in the index of refraction of the atmosphere, resulting in eddies, cells or air packets having varying sizes from ~0.1 cm to ~10 m. These air packets act like refractive prisms of varying indices of refraction. The propagating optical radiation is therefore fully or partially deviated depending on the relative size of the beam and the degree of temperature inhomogeneity along its path. Consequently the optical radiation traversing the turbulent atmosphere experiences random variation/fading in its irradiance (scintillation) and phase. Familiar effects of turbulence are the twinkling of stars caused by random fluctuations of stars' irradiance, and the shimmer of the horizon on a hot day caused by random changes in the optical phase of the light beam resulting in reduced image resolution [1]. Atmospheric turbulence depends on i) atmospheric pressure/altitude, ii) wind speed, and iii) variation of index of refraction due to temperature inhomogeneity. Known effects of atmospheric turbulence include [32]:

a) *Beam steering* – Angular deviation of the beam from its original LOS causing the beam to miss the receiver.

b) *Image dancing* – The received beam focus moves in the image plane due to variations in the beam's angle of arrival.

c) *Beam spreading* – Increased beam divergence due to scattering. This leads to a reduction in received power density.

d) *Beam scintillation* – Variations in the spatial power density at the receiver plane caused by small scale destructive interference within the optical beam.

e) *Spatial coherence degradation* – Turbulence also induces losses in phase coherence across the beam phase fronts. This is particularly deleterious for photomixing (e.g. in coherent receiver) [45].

f) *Polarisation fluctuation* – This results from changes in the state of polarisation of the received optical field after passing through a turbulent medium. However for a horizontally travelling optical radiation, the amount of polarisation fluctuation is negligible [30].

The modelling of the fluctuation of an optical radiation traversing a turbulent atmosphere will be examined in Chapter Four, with the view to understanding the statistical behaviour of the signal received at the receiver plane.

2.4.3 The receiver

This essentially helps recover the transmitted data from the incident optical field. The receiver is composed of the following:

a) *Receiver telescope* – collects and focuses the incoming optical radiation onto the photodetector. It should be noted that a large receiver telescope aperture is desirable as it collects multiple uncorrelated radiations and focuses their average on the photodetector. This is referred to as aperture averaging but a wide aperture also means more background radiation/noise.

b) *Optical bandpass filter* – to reduce the amount of background radiation.

c) *Photodetector* – p-i-n diode (PIN) or avalanche photodiode (APD) that converts the incident optical field into an electrical signal. The commonly used photodetectors in contemporary laser communication systems are summarised in Table 2.3. Germanium only detectors are generally not used in FSO because of their high dark current [31].

d) *Post-detection processor/decision circuit* – this is where the required amplification, filtering and signal processing necessary to guarantee a high fidelity data recovery are carried out.

Due to detector capacitance effect, higher speed detectors are inherently smaller in size (70 µm and 30 µm for 2.5 Gbps and 10 Gbps, respectively) with a limited field-of-view (FOV) that requires accurate alignment. The FOV of the receiver is the ratio of the detector size to the focal length [81]: $FOV = d/f' = dF\#/D$, where d is the detector diameter, f' is the effective focal length, and D is the receiver aperture. The quantity $F\#$ is the f-number. For a 75 µm size detector, with $F\# = 1$ and $D = 150$ mm telescope, the FOV = ~0.5 mrad.

Table 2.3: FSO Photodetectors

Material/Structure	**Wavelength (nm)**	**Responsivity**	**Typical Sensitivity**	**Gain**
Silicon PIN	300 – 1100	0.5	-34dBm@155Mbps	1
Silicon PIN, with transimpedance amplifier	300 – 1100	0.5	-26dBm@1.25 Gbps	1
InGaAs PIN	1000 – 1700	0.9	-46dBm@155Mbps	1
Silicon APD	400 – 1000	77	-52dBm@155Mbps	150
InGaAs APD	1000 – 1700	9	-33dBm @ 1.25 Gbps	10
Quantum–well and quatum-dot detectors	~10,000			

The receiver detection process can be classified into:

Direct detection receiver – This type of receiver detects the instantaneous intensity or power of the optical radiation impinging on the photodetector. Hence the output of the photodetector is proportional to the power of the incident field. Its implementation is very simple and most suitable for intensity modulated optical systems [32, 79].

Coherent detection receiver – The coherent receiver works on the photo-mixing phenomenon. The incoming optical field is mixed with another locally generated optical field on the surface of the photodetector. The coherent receiver can be further divided into homodyne and heterodyne receivers. In homodyne receivers the frequency/wavelength of the local (optical) oscillator is exactly the same as that of the incoming radiation [32], while in heterodyne detection the incoming radiation and the local oscillator frequencies are different [82]. In contrast to RF coherent detection, the output of the local oscillator in an optical coherent detection is not required to have the same phase as the incoming radiation. The principal advantages of a coherent receiver are: relative ease of amplification at an intermediate frequency and the fact that the signal-to-noise ratio can be significantly improved by simply raising the local oscillator power.

These receiver structures and the detection process are discussed in more details in the next chapter.

2.5 Eye Safety and Standards

In the design of optical communication systems, efforts must be made to ensure that the optical radiation is safe and does not cause any damage to the people that might come in contact with it. The optical beams can cause injury to both the skin and eye, but the damage to the eye is far more significant because of the eye's ability to focus and concentrate optical energy. The eye can focus light covering the wavelengths around 0.4 – 1.4 μm on to the retina, other wavelengths tend to be absorbed by the front part of the eye (the cornea) before the energy is focused. Fig. 2.4 shows the absorption of the eye at different wavelengths.

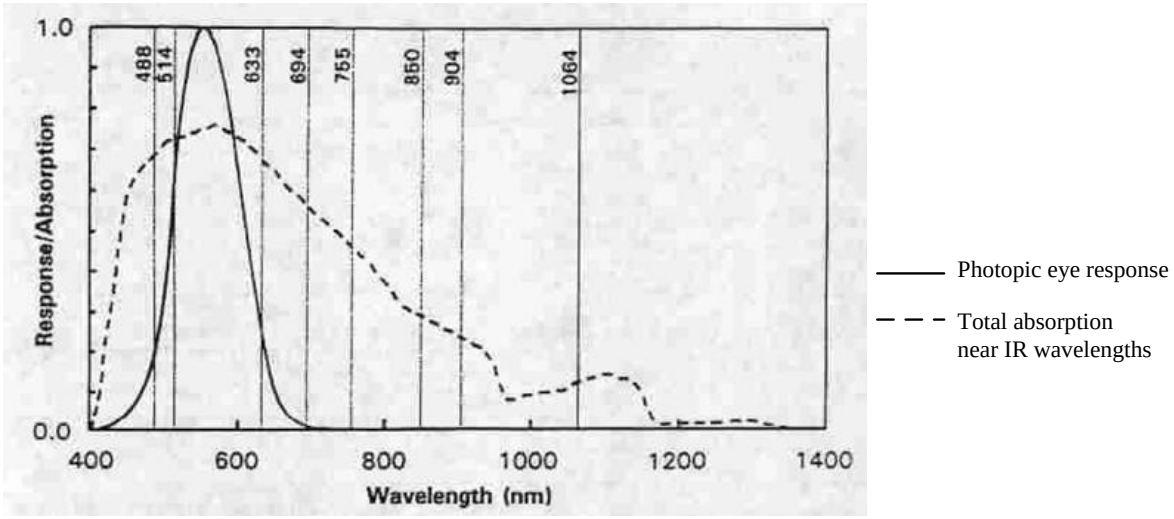

Fig. 2.4: Response/absorption of the human eye at various wavelengths [31].

There are a number of international standard bodies which provide guidelines on safety of optical beams, notable among these are [31]:

Center for Devices and Radiological Health (CDRH) - An agency within the United States (U.S.) Food and Drug Administration (FDA). It establishes regulatory standards for lasers and laser equipment that are enforceable by law (21 CFR 1040).

International Electrotechnical Commission (IEC) - Publishes international standards related to all electrical equipment, including lasers and laser equipment (IEC60825-1). These standards are not automatically enforceable by law, and the decision to adopt and enforce IEC standards is at the discretion of individual countries.

American National Standards Institute (ANSI) - Publishes standards for laser use (ANSI Z136.1). ANSI standards are not enforceable by law but do form the basis for the U.S. Occupational Safety and Health Administration (OSHA) legal standards, as well as comparable legal standards that have been adopted by various state regulatory agencies.

European Committee for Electrotechnical Standardization (CENELEC) - An organisation that establishes electrotechnical standards based on recommendations made by 19 European member nations. CENELEC standards are not directly enforceable by law but, as with IEC standards, are often integrated into the legal requirements developed by individual countries.

Laser Institute of America (LIA). LIA is an organization that promotes the safe use of lasers, provides laser safety information, and sponsors laser conferences, symposia, publications, and training courses.

Each of these organisation have developed ways of classifying lasers, the specific criteria vary slightly from one body to the other but the IEC classifications will be considered in this section. Lasers are generally divided into four groups, Class 1 to Class 4, with Class 1 being the least powerful and Class 4 being the most powerful. Each class is defined by the accessible emission limits (AEL) metric, this depends on the wavelength of the optical source, the geometry of the emitter and the intensity of the source [83].

Table 2.4 presents, the main characteristics and requirements for the classification system as specified by the revised IEC 60825-1 standard [78, 84]. In addition, classes 2 and higher must have the triangular warning label and other labels are required in specific cases indicating laser emission, laser apertures, skin hazards, and invisible wavelengths.

Table 2.4: Classification of lasers according to the IEC 60825-1 standard

Category	**Description**
Class 1	Low power device emitting radiation at a wavelength in the band 302.5−4000 nm. Device intrinsically without danger from its technical design under all reasonably foreseeable usage conditions, including vision using optical instruments (binoculars, microscope, monocular)
Class 1M	Same as Class 1 but there is possibility of danger when viewed with optical instruments such as binoculars, telescope, etc. Class 1M lasers produce large-diameter beams, or beams that are divergent.
Class 2	Low power device emitting visible radiation (in the band 400−700 nm). Eye protection is normally ensured by the defence reflexes including the palpebral reflex (closing of the eyelid). The palpebral reflex provides effective protection under all reasonably foreseeable usage conditions, including vision using optical instruments (binoculars, microscope, monocular).
Class 2M	Low power device emitting visible radiation (in the band 400−700 nm). Eye protection is normally ensured by the defence reflexes including the palpebral reflex (closing of the eyelid). The palpebral reflex provides an effective protection under all reasonably foreseeable usage conditions, with the exception of vision using optical instruments (binoculars, microscope, monocular).
Class 3R	Average power device emitting a radiation in the band 302.5−4000 nm. Direct vision is potentially dangerous
Class 3B	Average power device emitting a radiation in the band 302.5−4000 nm. Direct vision of the beam is always dangerous. Medical checks and specific training required before installation or maintenance is carried out.
Class 4	High power device There is always danger to the eye and for the skin, fire risk exists. Must be equipped with a key switch and a safety interlock. Medical checks and specific training required before installation or maintenance is carried out.

The AEL values at two wavelength mostly used for FSO are presented in Table 2.5. Lasers classified as Class 1 are most desirable for optical wireless communication systems since their radiation are safe under all conditions and circumstances. Class 1 lasers require no warning labels and can be used without any special safety precautions. As shown in Table 2.5 the power available to Class 1 lasers is limited. Most commercial terrestrial FSO links operating at up to 1.5 Gbps use Class 1M lasers, these are inherently safe except when viewed with optical instruments, such as binoculars. On certain instances, higher class lasers are used for FSO, the safety of these systems is maintained by installing the optical beams on rooftops with safety labels and warning or on towers to prevent inadvertent interruption [85].

Table 2.5: Accessible emission limits for two wavelengths, 850 and 1550 nm [78].

Class	**Average optical power output (mW)**	
	$\lambda = 850$ nm	$\lambda = 1550$ nm
1	< 0.22	< 10
2	Category reserved for the range 400–700 nm – same AEL as for Class 1	
3R	0.22 – 2.2	10 – 50
3B	2.2 – 500	50 – 500
4	> 500	> 500

As shown in Table 2.5, a Class 1 laser system operating at 1550 nm is allowed to transmit approximately 50 times more power than a system operating in the shorter IR wavelength range, such as 850 nm, when both have the same size aperture lens. It should however be noted that no wavelength is inherently dangerous or eye-safe, it is the output power that determines the laser classification. It is therefore possible to design eye-safe FSO systems that operate at any wavelength of choice. It also is important to understand that the regulation addresses the power density in front of the transmit aperture rather than the absolute power created by a laser diode inside the

equipment. For example, the laser diode inside the FSO equipment can actually be Class 3B even though the system itself is considered to be a Class 1 or 1M laser product if the light is launched from a large-diameter lens that spreads out the radiation over a large area before it enters the space in front of the aperture [31]. In order to maintain the Class 1 or 1M safety classifications, it is possible to use higher power laser with increased lens aperture or to use multiple large transmission apertures [31].

2.5.1 Maximum Permissible Exposures (MPE)

To provide a better protection to the eye or skin of anybody that might come in contact with the radiation of laser equipments, the maximum permissible exposure limits have been stipulated by standard organisations. It is the highest radiation power or energy, measured in W/cm^2 or J/cm^2 that is considered safe with a negligible probability of causing damage. The MPE is measured at the cornea of the human eye or at the skin, for a given wavelength and exposure time. It is usually about 10 % of the dose that has a 50 % chance of creating damage under worst-case conditions [86]. In Table 2.6, the MPE values for the eye at two commonly used wavelengths for FSO are presented; the values for the skin are much lower since the skin is usually less sensitive to laser radiation.

Table 2.6: Example of MPE values (W/m^2) of the eye (cornea) at 850 nm and 1550 nm wavelengths [78].

Exposure duration (s)	1	2	4	10	100	1000	10000
MPE (W/m^2) at 850 nm	36	30	25	20	11	6.5	3.6
MPE (W/m^2) at 1550 nm	5600	3300	1900	1000	1000	1000	1000

As shown in Table 2.6, the MPE is higher for brief exposure durations than for high exposures times. The MPE for the eye is much higher at 1550 nm than at 850 nm, this is related to the laser radiation absorption at the level of the various eye components. This difference in MPE values can be explained by the fact that at 850 nm approximately 50% of the signal can reach the retina whereas at 1550 nm the signal is almost completely absorbed by the cornea and aqueous humour [78].

2.6 Summary

A review of the FSO technology has been carried out in this chapter. Key features that make FSO suitable for use within the access network have been highlighted while the challenges posed by the atmospheric channel to an optical beam travelling though it have also been introduced. Areas where FSO systems have been found suitable to provide a data bridge have equally been mentioned and the issue of laser safety and classification has also been discussed.

Chapter Three

Optical Detection Theory

3.1 Introduction

This chapter discusses the process of converting optical radiation into an electrical signal used in the decision-making and other signal processing that takes place in an optical communication receiver. The primary aim of optical detection in communication engineering is to recover the information embedded on the intensity, phase or frequency of the incoming optical radiation. The different types of transducers used in this process and the commonly used optical detection processes (direct and coherent detection) are also explained in this chapter. In addition, the various sources of noise in an FSO

system are discussed with a view to understanding the limit they imposed on the system performance. The chapter is concluded with a discussion on the Poisson optical detection statistics and its Gaussian approximation.

3.2 Photodetectors

The photodetector is a square law optoelectronic transducer that generates an electrical signal which is proportional to the square of the instantaneous optical field impinging on its surface. Thus, the signal generated by a photodetector is always proportional to the instantaneous (received) optical power. Since the optical signal is generally weak, having travelled through the communication channel, the photodetector must therefore meet stringent performance requirements such as high sensitivity within its operational range of wavelengths, low noise level and adequate bandwidth to accommodate the desired data rate. The effect of temperature fluctuations on the response of the photodetector is required to be minimal and the device must equally have a long operating life.

The ratio of the number of electron-hole pairs generated by a photodetector to the incident photons in a given time is termed the quantum efficiency and has the symbol η. This is often used as a metric to characterise a photodetector. Consider an incoming optical radiation with an average power P_{R} impinging on a photodetector over a period T, then the electric current (quantity of charge per unit time) generated by the detector is given by [87]:

$$\langle i \rangle = \frac{\eta q \lambda P_R}{hc} = \Re P_R \tag{3.1}$$

where q is the electronic charge, λ is the wavelength of the radiation, and the physical constants c and h represent the speed of light in vacuum and Planck's constants, respectively. The parameter $\Re = \frac{\eta q \lambda}{hc}$, termed the photodetector responsivity, is very useful as it specifies the generated photocurrent per unit optical power impinging on the photodetector.

3.2.1 PIN photodetector

The PIN photodetector consists of *p*- and *n*- type semiconductor materials separated by a very lightly *n*-doped intrinsic region [88]. In normal operating conditions, a sufficiently large reverse bias voltage is applied across the device as shown in the schematic of Fig. 3.1. The reverse bias ensures that the intrinsic region is depleted of any charge carriers.

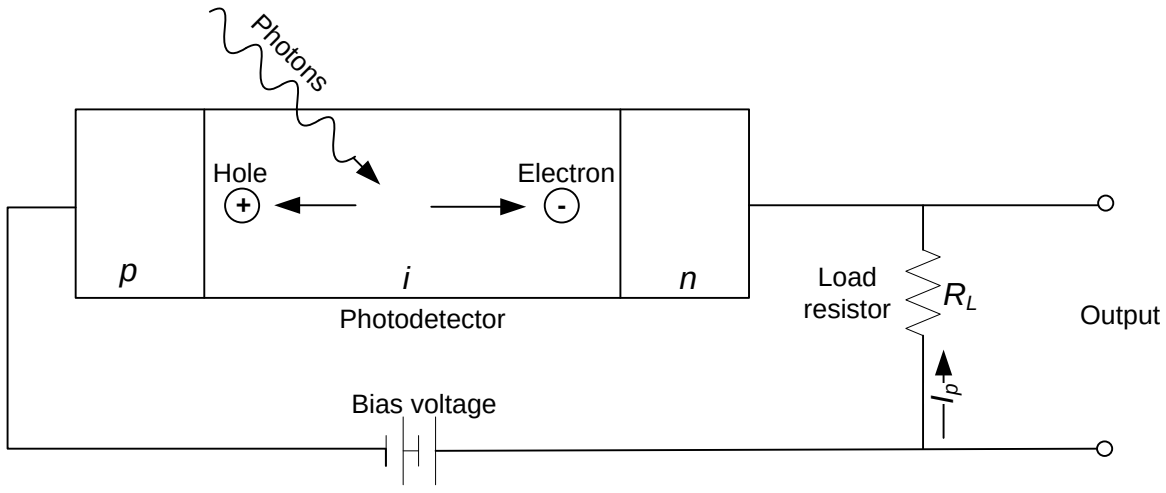

Fig. 3.1: PIN photodetector schematic diagram.

For the device to convert an incident photon into an electron/electric current, the energy of the incoming photon must not be less than the band-gap energy of the semiconductor material. The incident photon uses its energy to excite an electron from the valence

band to the conduction band, thereby generating a free electron-hole pair in the process. Normally the incident light is concentrated on the depleted intrinsic region. The high electric field present in this depleted region causes the generated charge carriers to separate and be collected across the reverse biased junction. This gives rise to a current flow in an external circuit as shown in Fig. 3.1, there is one electron flowing for every carrier pair generated.

The semiconductor material of the photodetector determines over what wavelength range the device can be used. The upper cut-off wavelength, λ_c, in micrometres (μm) is generally given by (3.2), where E_g is the energy band-gap of the semiconductor material in electron-volt (eV).

$$\lambda_c(\mu\text{m}) = \frac{hc}{E_g} = \frac{1.24}{E_g} \tag{3.2}$$

The operating wavelength ranges for different photodetector material are summarised in Table 3.1.

Table 3.1: Operating wavelength ranges for different photodetector materials [88].

Material	**Energy gap (eV)**	**Cut-off λ (nm)**	**Wavelength range (nm)**
Silicon	1.17	1060	400–1060
Germanium	0.775	1600	600–1600
GaAs	1.424	870	650–870
InGaAs	0.73	1700	900–1700
InGaAsP	0.75–1.35	1650–920	800–1650

The responsivity of a PIN photodetector is always less than unity and a graph showing typical responsivity values for different PIN photodetectors is depicted in Fig. 3.2.

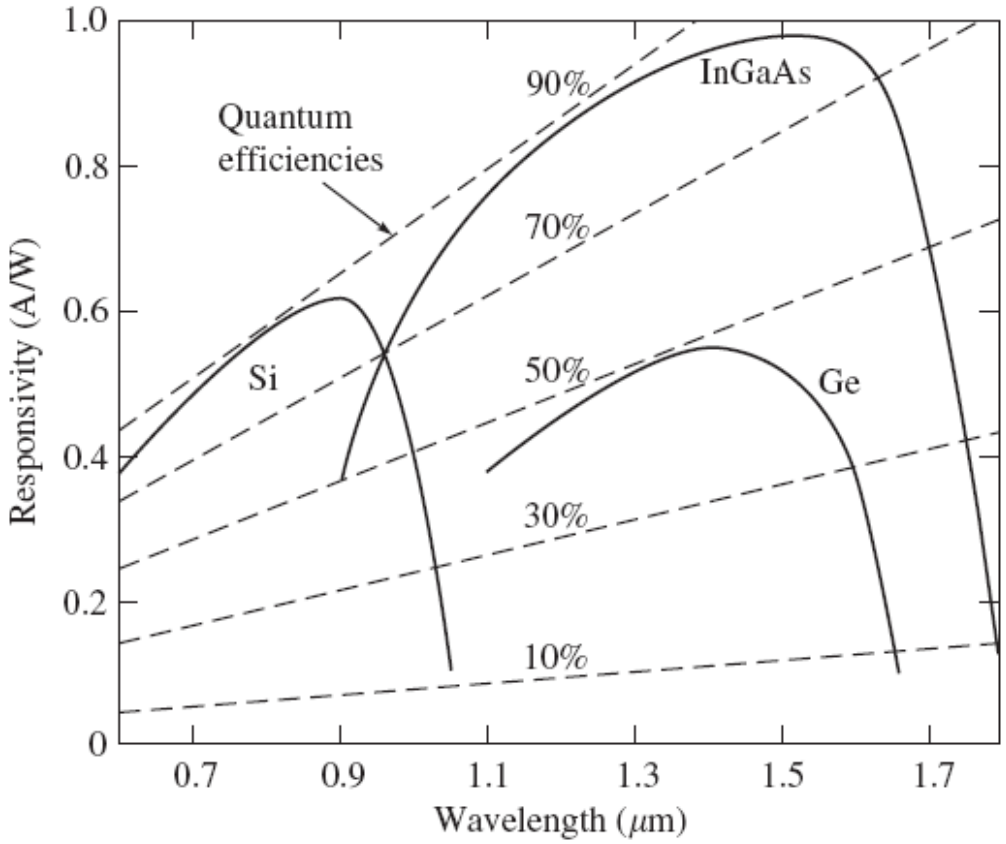

Fig. 3.2: Responsivity and quantum efficiency as a function of wavelength for PIN photodetectors. Reproduced from [88].

3.2.2 APD photodetector

The avalanche photodiode (APD) is different from the PIN photodetector in that it provides an inherent current gain through the process called repeated electron ionisation. This culminates in increased sensitivity since the photocurrent is now multiplied before encountering the thermal noise associated with the receiver circuit. Hence the expression for the responsivity of an APD includes a multiplication (or gain) factor *g*. Typical gain values lie in the range 50 to 300 [79], thus the responsivity value of an APD can be greater than unity. The APD offers a higher sensitivity than the PIN detector but the statistical nature of the ionisation/avalanche process means that there is always a multiplication noise associated with the APD. The avalanche process is also

very temperature-sensitive. These factors are very important and must always be taken into account whenever an APD is used in an optical communication system.

3.3 Photodetection Techniques

Photodetection is the process of converting information-bearing optical radiation into its equivalent electrical signal with the aim of recovering the transmitted information. At the transmitter, the information can be encoded on the frequency, phase or the intensity of the radiation from an optical source. This encoded radiation is then transmitted to the receiver via the free-space channel or the optical fibre. The receiver front-end devices (telescope and optical filter) focus the filtered radiation onto the photodetecting surface in the focal plane. Depending on whether a local oscillator is used during the detection process or not, the following photodetection techniques are possible.

3.3.1 Direct detection

Here, a local oscillator is not used in the detection process and for this type of receiver to recover the encoded information, it is essential that the transmitted information be associated with the intensity variation of the transmitted field [79]. Hence this type of detection is also called envelope detection. For an instantaneous incident power $P(t)$, the instantaneous photodetector current $i(t)$ is given by:

$$i(t) = \frac{\eta q \lambda}{hc} g P(t) \tag{3.3}$$

where g is the photodetector gain factor whose value is unity for a PIN photodetector. The block diagram of the direct detection receiver is illustrated in Fig. 3.3.

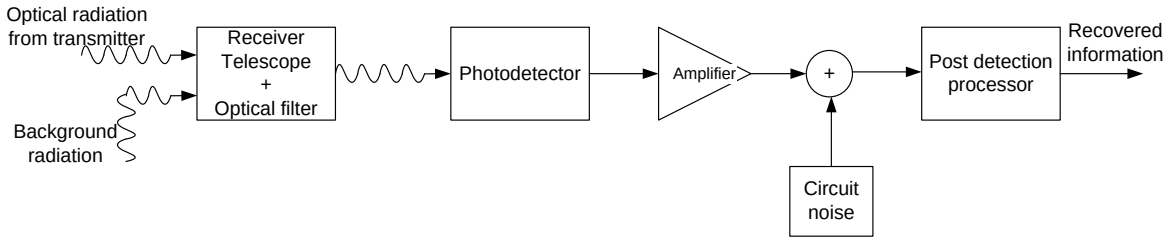

Fig. 3.3: Block diagram of a direct detection optical receiver.

3.3.2 Coherent detection

An optical local oscillator is used here to generate optical radiation at a certain wavelength/frequency [32]. The frequency of the local oscillator does not have to be the same as that of the incoming information-bearing radiation. This possibility is thus responsible for the two variants of coherent detection discussed below. The block diagram of a coherent receiver is shown in Fig. 3.4. It is pertinent to clarify that the term coherent detection in optical detection is not synonymous with coherent detection in radio frequency (RF) parlance. In contrast to RF coherent detection, the output of the local oscillator in optical coherent detection is not required to have the same phase as the incoming radiation.

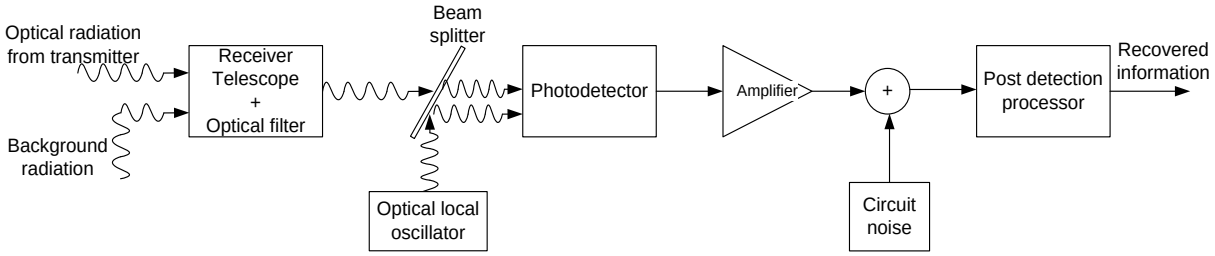

Fig. 3.4: Block diagram of a coherent detection optical receiver.

3.3.2.1 *Heterodyne detection*

In a heterodyne detection optical receiver, the incoming radiation (carrier) is combined with a reference wave from a local laser on the photodetector surface as shown in Fig. 3.4. This optical mixing process produces another wave at an intermediate frequency (IF) which is the difference between the incoming laser carrier and the reference signal frequencies [32]. This IF signal passes through a band-pass filter to an electrical second detector (the post detection processor in Fig. 3.4) for the final demodulation. Assuming that the electric fields of the carrier of frequency ω_{co}, and that of the reference (local) radiation of frequency ω_L are respectively given by:

$$E_c(t) = A_c \cos(\omega_{co} t + \theta_c) \tag{3.4a}$$

$$E_L(t) = A_L \cos(\omega_L t + \theta_L) \tag{3.4b}$$

where A_c and θ_c are the amplitude and phase of the carrier field respectively while the local oscillator amplitude and phase are A_L and θ_L in that order. When the instantaneous field amplitudes, $E_c(t)$ and $E_L(t)$ combine on the photodetector surface, they produce an instantaneous signal whose intensity is given by:

$$C(t) = \big(E_c(t) + E_L(t)\big)^2 \tag{3.5}$$

The time average of $C(t)$ multiplied by the responsivity gives the resultant instantaneous carrier and local oscillator current, $i_p(t)$, at the photodetector output.

Hence:

$$\begin{aligned} i_p(t) = \Re\{&\langle A_L^2 \cos^2(\omega_L t + \theta_L)\rangle + \langle A_c^2 \cos^2(\omega_{co} t + \theta_c)\rangle \\ &+ \langle A_L A_c \cos[(\omega_L - \omega_{co})t + (\theta_L - \theta_c)]\rangle \\ &+ \langle A_L A_c \cos[(\omega_L + \omega_{co})t + (\theta_L + \theta_c)]\rangle\} \end{aligned} \tag{3.6}$$

The first two terms are time invariant, the 3rd term is very slowly varying with respect to the short time over which the average is taken, while the 4th term is out of the IF band [32]. Equation 3.6 is now reduced to:

$$i_p(t) = \Re\left\{\frac{A_L^2}{2} + \frac{A_c^2}{2} + 3^{rd}\ term + 4^{th}\ term\right\} \tag{3.7}$$

Therefore the IF filter, which is an integral part of the post detection processor of Fig. 3.4, only allows the 3rd term to go through while the others are suppressed resulting in the following expression for the instantaneous current:

$$i_p(t) = \Re A_L A_c \cos[(\omega_L - \omega_{co})t + (\theta_L - \theta_c)] \tag{3.8}$$

The above result makes it possible to recover any information impressed on the carrier field amplitude, frequency or even phase. The following points can therefore be deduced from this, that heterodyne detection offers:

1) A relatively easy means of amplifying the photocurrent by simply increasing the local oscillator power.
2) Improved signal-to-noise ratio. This is achieved by increasing the local oscillator power so much that its inherent shot noise dwarfs the thermal and the shot noise from other sources.

However the frequency of an optical source is known to drift over time. Therefore the IF frequency needs to be continually monitored at the input of the electrical detector and the local oscillator frequency varied accordingly to keep the IF centre frequency constant. Also the optical source, particularly a laser, does suffer from phase noise which means that θ_c and θ_L in (3.8) are not absolutely fixed, they fluctuate. These factors contribute to the challenges of implementing a coherent optical communication system.

3.3.2.2 *Homodyne detection*

This is similar to the heterodyne detection process discussed above except that the local oscillator has the same frequency as the incoming optical radiation/carrier [32]. The resultant photocurrent thus contains the information signal at the baseband. Following the same step as in heterodyne detection, the instantaneous photocurrent is obtained thus:

$$i_p(t) = \Re\left\{\frac{A_L^2}{2} + \frac{A_c^2}{2} + \langle A_L A_c \cos(\theta_L - \theta_c)\rangle + \langle A_L A_c \cos(2\omega_{co}t + \theta_L + \theta_c)\rangle\right\} \quad (3.9)$$

The 3rd term is time invariant and the 4th term is suppressible via filtering to obtain:

$$i_p = \Re\left\{\frac{A_L^2}{2} + \frac{A_c^2}{2} + A_L A_c \cos(\theta_L - \theta_c)\right\} \quad (3.10)$$

By increasing the locally generated radiation power such that $A_cA_L >> 0.5A_c$ [32], expression (3.10) reduces to:

$$i_p = \Re[A_L A_c \cos(\theta_L - \theta_c)] \quad (3.11)$$

3.4 Photodetection Noise

The types of noise encountered in optical communications can be broadly stratified into shot noise and thermal noise. The various sources of noise in optical communications are discussed below. For FSO systems, the noise from the background radiation can be significant, while in fibre optics communication the background radiation noise is negligible.

3.4.1 Photon fluctuation noise

For an ideal photodetector, the only significant noise that affects its performance is that associated with the quantum nature of light itself, the by-product of which is that the number of photons emitted by a coherent optical source in a given time is never constant. Although for a constant power optical source the mean number of photons generated per second is constant, the actual number of photons per second follows the Poisson distribution. This results in photon fluctuation or quantum noise.

The quantum fluctuation is also important because it is dominates over the thermal fluctuations within the photodetector, since $hf > \kappa T_e$ where h and f are the Planck's constant and radiation frequency respectively while κ and T_e represent the Boltzmann's constant and temperature. The quantum noise is a shot noise with variance:

$$\sigma_{Qtm}^2 = 2q\langle i \rangle B \tag{3.12}$$

where the bandwidth of the electrical filter that follows the photodetector is represented by B Hz.

3.4.2 Dark current and excess noise

The dark current is the photocurrent generated when no photon is impinging on the photodetector. It is produced by the transition of electrons from the valence to the conduction band due to causes other than photon-induced excitation; its magnitude is closely related to the energy band-gap of the photodetector material(s). Large band-gap materials, such as Silicon (Si), Indium phosphide (InP) and Gallium arsenide (GaAs) show very low values of mean dark current, $\langle i_d \rangle$, while for Germanium (Ge), the value could be significant when they are operated at room temperature [82]. The dark current

consists of diffusion, tunnel, leakage currents and generation-recombination taking place in the space-charge region and is proportional to the volume of the depletion region [82].

Photodetectors that employ internal avalanche gain mechanism to boost the signal above the thermal noise of amplifier stages on the receiver exhibit what is referred to as excess noise [45]. According to [45], the excess noise in an APD is due to the multiplication process in the high-field region of the detector where each primary electron hole can generate an additional electron through impact ionisation of bound electrons. These additional carriers can then create still additional carriers in a cascading process.

If all primary carriers were to be multiplied equally in an APD, the mean-square current gain $\langle g^2 \rangle$ would be equal to the mean gain, g, and the excess noise, defined as $F = \langle g^2 \rangle / g$ would be equal to 1. This is the case for PIN photodetectors [45]. However, due to the statistical nature of the avalanche process, *F* is always greater than 1 in an APD and other avalanche devices. Typical dark current values for some photodetector materials are shown in Table 3.2.

Table 3.2: Dark current values for different materials [77].

Photodetector material	**Dark current (nA)**	
	PIN	**APD**
Silicon	1 – 10	0.1 – 1
Germanium	50 – 500	50 – 500
InGaAs	0.5 – 2.0	10 – 50 @ g =10

The dark current carries no useful information and thereby constitutes a shot noise whose variance is given by the following:

$$\sigma_{Dk}^2 = 2q\langle i \rangle B \tag{3.13}$$

3.4.3 Background radiation

This type of noise is due to the detection of photons generated by the environment. Two types of sources contribute to background radiation noise, these are: localised point sources (e.g. the Sun) and extended sources (e.g. the sky). Background radiation from other celestial bodies such as stars and reflected background radiation are assumed to be too weak to be considered for a terrestrial FSO link; however they contribute significantly to background noise in deep space FSO. The following are the irradiance (power per unit area) expressions for both the extended and localised background sources [32, 46, 89]:

$$I_{sky} = N(\lambda)\Delta\lambda\pi\,\Omega^2/4 \tag{3.14a}$$

$$I_{sun} = W(\lambda)\Delta\lambda \tag{3.14b}$$

where $N(\lambda)$ and $W(\lambda)$ are the spectral radiance of the sky and spectral radiant emittance of the sun, respectively, $\Delta\lambda$ is the bandwidth of the optical band pass filter (OBPF) that precedes the photodetector, and Ω is the photodetector's field of view angle (FOV) in radians. By carefully choosing a receiver with a very narrow FOV and $\Delta\lambda$, the impact of background noise can be greatly reduced. Optical BPF in the form of coatings on the receiver optics/telescope with $\Delta\lambda < 1$ nm are now readily available. Empirical values of $N(\lambda)$ and $W(\lambda)$ under different observation conditions are also available in literature [32, 79, 89]. The background radiation is a shot noise with variance [32]:

$$\sigma_{Bg}^2 = 2qB\Re\left(I_{sky} + I_{sun}\right) \tag{3.15}$$

Combining these noise processes together results in the total shot noise whose variance, σ_{Sh}^2, is the sum of the individual noise variances. This is however dominated by the background radiation as the other two are usually smaller.

3.4.4 Thermal noise

This is the noise caused by the thermal fluctuation of electrons in any receiver circuit of equivalent resistance R_L, and temperature T_e. The thermal noise is regarded as a 'white' noise. This is because the power spectral density (PSD) is independent of frequency. Moreover, the thermal noise obeys the Gaussian distribution with mean zero and has a variance defined by [77]:

$$\sigma_{Th}^2 = \frac{4\kappa T_e B}{R_L} \tag{3.16}$$

where κ is the Boltzmann's constant.

3.5 Optical Detection Statistics

According to the semi-classical approach, which treats an optical radiation as a wave and prescribes a probabilistic relation to account for its interaction with the atomic structure of the detector surface [79], the probability of a detector with an aperture area A_D, emitting n number of electrons from impinging photons during a period T obeys the Poisson distribution given as:

$$p(n) = \frac{\langle n \rangle^n \exp(-\langle n \rangle)}{n!} \tag{3.17}$$

The mean count is related to the aperture area and the received irradiance $I(t,r)$ by the following expression:

$$\langle n \rangle = \frac{\eta\lambda}{hc} \iint I(t,r)\, dtdr \tag{3.18}$$

The process of counting the number of electrons generated by the impinging photons is often referred to as photon or photoelectron counting.

Table 3.3 summarises some basic statistical parameters of the Poisson random variable. It is worth noting that both the mean and variance of a Poisson random distribution are the same and are given by the mean count in this instance.

Table 3.3: Statistical parameters of Poisson random distribution [79]

Parameter	**Definition**	
Mean	$\sum_n np(n)$	$\langle n \rangle$
Mean-square value	$\sum_n n^2 p(n)$	$\langle n \rangle^2 + \langle n \rangle$
Characteristic function	$\sum_n e^{j\omega n} p(n)$	$\exp\left[\left(e^{j\omega} - 1\right)\langle n \rangle\right]$
Moment generating function	$\sum_n (1-z)^n p(n)$	$\exp[-z\langle n \rangle]$
q^{th} moment	$\sum_n n^q p(n)$	$\frac{\partial^q}{\partial z^q}[\exp(-z\langle n \rangle)]_{z=1}$

The mean current generated from the $\langle n \rangle$ electrons is $\langle i \rangle = q\langle n \rangle / T$ and its variance is given by:

$$\sigma^2 = \left(\frac{q}{T}\right)^2 \sigma_n^2 \tag{3.19}$$

Since for a Poisson distribution the mean and variance are equal, and by choosing the electrical bandwidth of the post detection filter as $1/2T$ (which is the Nyquist minimum bandwidth requirement), the expression (3.19) becomes:

$$\begin{aligned}\sigma^2 &= \left(\frac{q}{T}\right)^2 \langle n \rangle = \left(\frac{q}{T}\right)^2 \frac{\langle i \rangle T}{q} \\ &= \frac{q}{T}\langle i \rangle = 2q\langle i \rangle B\end{aligned} \tag{3.20}$$

This is the general expression for the variance of any shot noise process associated with photodetection. It should be mentioned that the photon counts from the desired incoming optical radiation, background radiation and that due to dark current are independent Poisson random variables. Hence, the pdf of the photoelectron emission due to all of these processes occurring together is also a Poisson distribution whose mean is the sum of the means of the individual processes.

With large signal photoelectron counts the generated signal current probability distribution can be approximated to be Gaussian [32]. That is:

$$p(i) = \frac{1}{\sqrt{2\pi\sigma_{Sh}^2}} \exp\left\{-\frac{(i - \langle i \rangle)^2}{2\sigma_{Sh}^2}\right\} \tag{3.21}$$

By taking the AWGN into account, this expression is modified to become:

$$p(i) = \frac{1}{\sqrt{2\pi\left(\sigma_{Sh}^2 + \sigma_{Bg}^2\right)}} \exp\left\{-\frac{(i - \langle i \rangle)^2}{2\left(\sigma_{Sh}^2 + \sigma_{Bg}^2\right)}\right\} \tag{3.22}$$

These expressions (3.17), (3.21) and (3.22) are only valid for a non-varying received optical field. However, if the incoming field is randomly varying, then the received irradiance and $\langle i \rangle$ also vary accordingly. Assuming the randomly varying field has a pdf given by $p(\langle i \rangle)$, it follows therefore that the generated photocurrent is now doubly

stochastic and its pdf given by (3.23) is obtained by averaging (3.22) over the statistics of the varying field.

$$p(i) = \int_0^{\infty} \frac{1}{\sqrt{2\pi\left(\sigma_{Sh}^2 + \sigma_{Bg}^2\right)}} \exp\left\{-\frac{(i - \langle i\rangle)^2}{2\left(\sigma_{Sh}^2 + \sigma_{Bg}^2\right)}\right\} P(\langle i\rangle)\, d\langle i\rangle \tag{3.23}$$

In free-space optical communications, atmospheric turbulence is the principal source of random fluctuations in the received optical radiation irradiance. This source of fluctuation is therefore the subject of discussion in the next chapter.

3.6 Summary

This chapter has discussed the process of optical detection by first reviewing the transducers used for converting optical radiation to their equivalent electrical signals. When using direct detection, it is essential that the transmitted information is associated with the intensity variation of the optical beam. While in coherent detection, the information can be encoded on the phase, field amplitude or frequency of the optical radiation. The different types of noise encountered in optical detection have also been reviewed and the statistics of the optical detection process discussed.

Chapter Four

The Atmospheric Turbulence Models

4.1 Introduction

Solar radiation absorbed by the Earth's surface causes air around the earth surface to be warmer than that at higher altitude. This layer of warmer air becomes less dense and rises to mix turbulently with the surrounding cooler air causing the air temperature to fluctuate randomly [32]. Inhomogeneities caused by turbulence can be viewed as discrete cells, or eddies of different temperature, acting like refractive prisms of different sizes and indices of refraction. The interaction between the laser beam and the turbulent medium results in random phase and amplitude variations (scintillation) of the

information-bearing optical beam which ultimately results in performance degradation of FSO links. Of all the effects of atmospheric turbulence introduced in Chapter Two, only the modelling of the atmospheric turbulence induced fluctuation of the received optical power (or irradiance) will be discussed in this chapter, since in the intensity modulated, direct detection FSO system under consideration, it is only the received power/irradiance that matters. Atmospheric turbulence is usually categorised in regimes depending on the magnitude of index of refraction variation and inhomogeneities. These regimes are a function of the distance travelled by the optical radiation through the atmosphere and are classified as weak, moderate, strong and saturation.

In this chapter, models describing the probability density function (pdf) statistics of the irradiance fluctuation will be described. Unfortunately, due to the extreme complexity involved in mathematically modelling of atmospheric turbulence, a universal model valid for all the turbulence regimes does not currently exist. As such, this chapter will review three most reported models for irradiance fluctuation in a turbulent channel. These are log-normal, gamma-gamma and negative exponential models. Their respective ranges of validity, as reported in literature [30, 45, 47, 49, 50], are in the weak, weak-to-strong and saturate regimes.

4.2 Turbulent Atmospheric Channel

Atmospheric turbulence results in random fluctuation of the atmospheric refractive index, n along the path of the optical field/radiation traversing the atmosphere. This refractive index fluctuation is the direct end product of random variations in atmospheric temperature from point to point [32]. These random temperature changes are a function of the atmospheric pressure, altitude and wind speed. The smallest and

the largest of the turbulence eddies are termed the inner scale, l_0, and the outer scale, L_0, of turbulence respectively. l_0 is typically on the order of a few millimetres while L_0 is typically on the order of several metres [29, 49]. These weak lens-like eddies shown graphically in Fig. 4.1 result in a randomised interference effect between different regions of the propagating beam causing the wavefront to be distorted in the process.

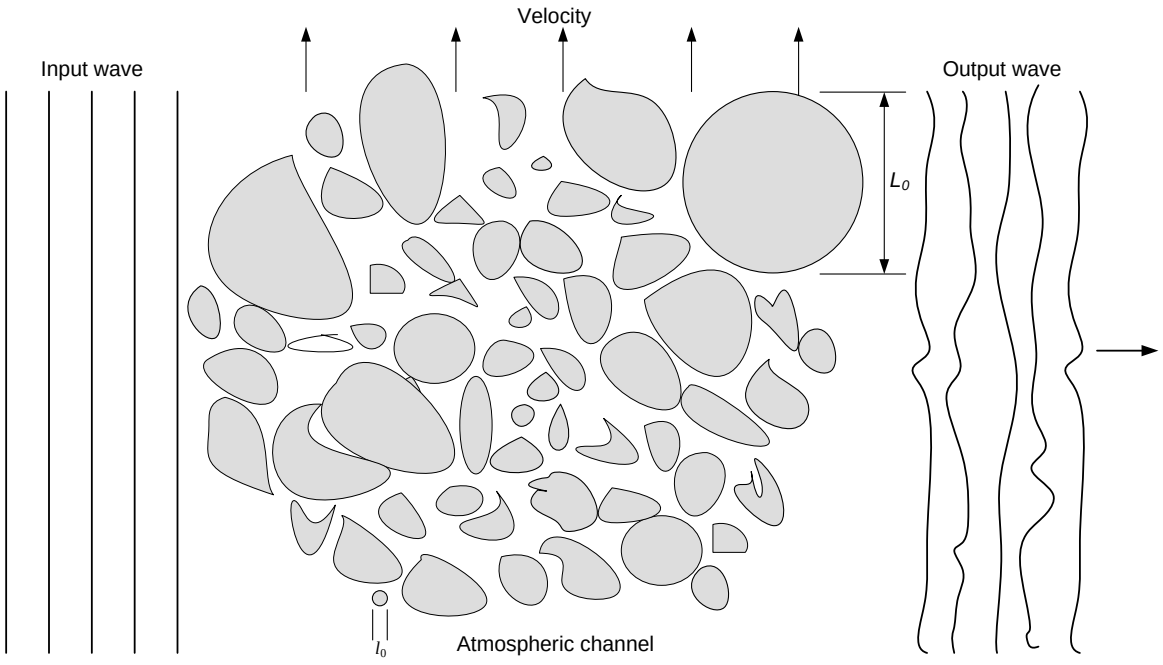

Fig. 4.1: Atmospheric channel with turbulent eddies

In an attempt to model the turbulent atmospheric channel, the widely accepted 'Taylor hypothesis' [30], which says that the turbulent eddies are fixed or frozen and can only move in their frozen form with the transverse component of the mean local wind will be followed. This hypothesis means that the temporal variations in the beam pattern or its statistical properties are caused by the component of the local wind that is perpendicular to the beam direction of propagation. In addition, the temporal coherence time, τ_o, of atmospheric turbulence is reported to be in the order of milliseconds [45]. This value is very large compared to the duration of a typical data symbol, thus the turbulent

atmospheric channel can be described as a 'slow fading channel' since it is static over the duration of a data symbol.

The relationship between the temperature of the atmosphere and its refractive index is given by (4.1) [90] while for most engineering applications, the rate of change of the refractive with respect to channel temperature is represented by equation (4.2) [30].

$$n = 1 + 77.6(1 + 7.52 \times 10^{-3}\lambda^{-2})\frac{P}{T_e} \times 10^{-6} \tag{4.1}$$

$$-dn/dT_e = 7.8 \times 10^{-5}\, P/T_e^2 \tag{4.2}$$

where P is the atmospheric pressure in millibars, T_e is the temperature in Kelvin and λ the wavelength in microns. Near sea level, $-dn/dT_e \cong 10^{-6}$ K^{-1} [30]. The contribution of humidity to the refractive index fluctuation is not accounted for in (4.1) because this is negligible at optical wavelengths [45].

The position and time dependent index of refraction denoted by $n(r,t)$ can be expressed as the sum of its free-space (no turbulence) value, n_0, and a turbulence induced random fluctuation component $n_1(r,t)$. Thus:

$$n(r,t) = n_0 + n_1(r,t) \tag{4.3}$$

In accordance with the Taylor's 'frozen-flow' hypothesis, which implies that the temporal variations of the index of refraction of the channel are mainly due to the transverse component of the atmospheric wind, the randomly fluctuating part of equation (4.3) can then be written as:

$$n_1(r,t) = n_1(r - vt) \tag{4.4}$$

where $v(r)$ is the local wind velocity perpendicular to the field direction of travel. In atmospheric turbulence, an important parameter for characterising the amount refractive index fluctuation is the index of refraction structure parameter, C_n^2, introduced by Kolmogorov [91]. The value of C_n^2 varies with altitude and a commonly used model to describe it is the Hufnagel-Valley (H-V) model given below as [49]:

$$C_n^2(\hbar) = 0.00594(v/27)^2(10^{-5}\hbar)^{10}\exp(-\hbar/1000) + 2.7 \times 10^{-16}\exp(-\hbar/1500) + \hat{A}\exp(-\hbar/100) \tag{4.5}$$

where $\hat{A}$ is taken as the nominal value of $C_n^2(0)$ at the ground in $m^{-2/3}$ and $\hbar$ is the altitude in metres. The value of the index of refraction structure parameter varies with altitude, but for a horizontally propagating field it is usually assumed constant. C_n^2 typically ranges from 10^{-12} $m^{-2/3}$ for strong turbulence to 10^{-17} $m^{-2/3}$ for weak turbulence with a typical average value being 10^{-15} $m^{-2/3}$ [47].

A similar parameter for temperature variations is the temperature structure parameter and it is related to C_n^2 by (4.6) [30].

$$C_n^2 = \left(\frac{dn}{dT_e}\right)^2 C_T^2 \tag{4.6}$$

In the spectral domain, the power spectral density of the refractive index fluctuation is related to C_n^2 by the following expression [91, 92]:

$$\Phi_n(K) = 0.033C_n^2K^{-11/3}; \qquad 2\pi/L_0 \ll K \ll 2\pi/l_0 \tag{4.7}$$

where K is the spatial wave number. For a wider range of K however, this expression has been modified by Tatarski and von Karman and reported in the following references [47, 93, 94].

By their very nature, turbulent media are extremely difficult to describe mathematically, the difficulty, according to [45], is primarily due to the presence of non-linear mixing of observable quantities which is fundamental to the process. In order to derive expressions for the statistical properties, namely the pdf and variance, of an optical beam travelling through the turbulent atmosphere; the following simplifying but valid assumptions will be used to reduce the mathematics to a manageable level [45]:

1) The atmosphere is a non-dissipative channel for the propagating wave. This assumption can be explained thus, in the event of absorption of the propagating wave or radiation by the atmosphere, the heat so generated is insignificant compared to diurnal contributions.
2) The process of scattering by the turbulent eddies does not result in loss of energy from the beam. Hence the mean energy in the presence of turbulence is assumed equal to the mean energy in the absence of turbulence. This assumption is valid for plane and spherical waves. The plane wave, is generally applicable to laser beams propagating over a long distance [45, 79].

4.3 Log-normal Turbulence Model

In describing the pdf of the irradiance fluctuation in a turbulent atmosphere, the beam is first represented by its constituent electric field $\vec{E}$. By employing Maxwell's electro-magnetic equations for the case of a spatially variant dielectric like the atmosphere, the

following expression is derived [45]:

$$\nabla^2\vec{E} + k^2 n^2\vec{E} + 2\nabla[\vec{E}.\vec{\nabla}\ln(n)] = 0 \tag{4.8}$$

where the wave number $k = 2\pi/\lambda$, and the vector gradient operator $\vec{\nabla} = \left(\frac{\partial}{\partial x}\right)\boldsymbol{i} + \left(\frac{\partial}{\partial y}\right)\boldsymbol{j} + \left(\frac{\partial}{\partial z}\right)\boldsymbol{k}$ with $\boldsymbol{i}$, $\boldsymbol{j}$, and $\boldsymbol{k}$ being the unit vectors along the *x*, *y* and *z* axes respectively. The last term on the left hand side of (4.8) represents the turbulence induced depolarisation of the wave. In weak atmospheric turbulence, which is characterised by single scattering event, the wave depolarisation is negligible [30, 95, 96]. In fact, it has been shown both theoretically [97] and experimentally [98] that the depolarisation is insignificant even for strong turbulence conditions. Equation (4.8) then reduces to:

$$\nabla^2\vec{E} + k^2 n^2\vec{E} = 0 \tag{4.9}$$

The position vector will henceforth be denoted by r and $\vec{E}$ represented by $E(r)$ for convenience.

In solving this last equation, Tatarski [93] in his approach introduced a Gaussian complex variable $\Psi(r)$ defined as the natural logarithm of the propagating field $E(r)$, and termed it the Rytov transformation. That is:

$$\Psi(r) = \ln[E(r)] \tag{4.10}$$

The Rytov approach is also based on a fundamental assumption that the turbulence is weak and that it is characterised by single scattering process. By invoking the Rytov transformation (4.10), and equating the mean refractive index of the channel, n_0, to

unity, equation (4.9) transforms to the following Riccati equation whose solution already exists:

$$\nabla^2\Psi + (\nabla\Psi)^2 + k^2(1+n_1)^2 = 0 \tag{4.11}$$

The next stage involves breaking $\Psi(r)$ down to its free-space form, $\Psi_0(r)$, and its turbulence induced departure from it represented by $\Psi_1(r)$. This is done via the smooth perturbing method [45], which in effect implies that $\Psi(r) = \Psi_0(r) + \Psi_1(r)$. Combining this with the Rytov change of variable (4.10), results in the following:

$$\Psi_1(r) = \Psi(r) - \Psi_0(r) \tag{4.12}$$

$$\Psi_1(r) = \ln[E(r)] - \ln[E_0(r)]$$

$$= \ln\left[\frac{E(r)}{E_0(r)}\right] \tag{4.13}$$

Where the electric field and its free-space (without turbulence) form, $E_0(r)$, are by definition given as:

$$E(r) = A(r)\exp(i\phi(r)) \tag{4.14a}$$

$$E_0(r) = A_0(r)\exp(i\phi_0(r)) \tag{4.14b}$$

where $A(r)$ and $\phi(r)$ represent the amplitude and phase of the actual field with atmospheric turbulence, respectively while $A_0(r)$ and $\phi_0(r)$ represent the amplitude and phase of the field without atmospheric turbulence, respectively. These transformations can then be used to arrive at the solution of (4.11) which describes the behaviour of a field in weak atmospheric turbulence. In finding the irradiance fluctuation statistical distribution, first combine equations (4.13) and (4.14) to arrive at the turbulence induced field amplitude fluctuation given below as:

$$\Psi_1(\mathrm{r}) = \ln\left[\frac{A(r)}{A_0(r)}\right] + i[\phi(r) - \phi_0(r)] = \mathcal{X} + i\mathcal{S} \tag{4.15}$$

Since $\Psi_1(\mathrm{r})$ is Gaussian, it follows therefore that, $\mathcal{X}$ is the Gaussian distributed log-amplitude fluctuation, and similarly $\mathcal{S}$ is the Gaussian distributed phase fluctuation of the field. By concentrating only on the field amplitude however, the pdf of $\mathcal{X}$ is thus [45, 47]:

$$p(\mathcal{X}) = \frac{1}{\sqrt{2\pi\sigma_x^2}} \exp\left\{-\frac{(\mathcal{X} - E[\mathcal{X}])^2}{2\sigma_x^2}\right\} \tag{4.16}$$

where $E[\mathcal{X}]$ denotes the expectation of $\mathcal{X}$ and σ_x^2 is the log-amplitude variance, commonly referred to as the Rytov parameter. According to [30], the σ_x^2 which characterises the extent of field amplitude fluctuation in atmospheric turbulence is related to the index of refraction structure parameter, the horizontal distance, L, travelled by the optical field/radiation by the following equations:

$$\sigma_x^2 = 0.56k^{7/6} \int_0^L C_n^2(x)(L-x)^{5/6} dx \qquad \text{for a plane wave} \tag{4.17a}$$

and

$$\sigma_x^2 = 0.563k^{7/6} \int_0^L C_n^2(x)(x/L)^{5/6}(L-x)^{5/6} dx \qquad \text{for a spherical wave} \tag{4.17b}$$

For a field propagating horizontally through the turbulent medium, as is the case in most terrestrial applications, the refractive index structure parameter, C_n^2, is constant, and the log irradiance variance for a plane wave becomes:

$$\sigma_l^2 = 1.23 C_n^2 k^{7/6} L^{11/6} \tag{4.18}$$

The field irradiance (intensity) in the turbulent medium is $I = |A(r)|^2$ while the intensity in free-space (no turbulence) is given by $I_0 = |A_0(r)|^2$, the log-intensity is then given by:

$$l = \log_e \left| \frac{A(r)}{A_0(r)} \right|^2 = 2\mathcal{X} \tag{4.19}$$

Hence,

$$I = I_0 \exp(l) \tag{4.20}$$

To obtain the irradiance pdf, invoke the transformation of variable, $p(I) = p(\mathcal{X}) \left| \frac{d\mathcal{X}}{dI} \right|$, to arrive at the log-normal distribution function given by (4.21) .

$$p(I) = \frac{1}{\sqrt{2\pi\sigma_l^2}} \frac{1}{I} \exp\left\{ - \frac{(\ln(I/I_0) - E[l])^2}{2\sigma_l^2} \right\} \qquad I \geq 0 \tag{4.21}$$

In the region of weak fluctuations, the statistics of the irradiance fluctuations have been experimentally found to obey the log-normal distribution. From (4.19) the log-intensity variance $\sigma_l^2 = 4\sigma_x^2$ and the mean log intensity, $E[l] = 2E[X]$. Based on the second assumption of Section 4.2, it follows that $E[\exp(l)] = E[I/I_0] = 1$ since there is no energy loss during the turbulence induced scattering process and as such $E[I] = I_0$. The expectation, $E[l]$ is obtained by invoking the standard relation (4.22) which is valid for any real-valued Gaussian random variable [47]. An expression for $E[l]$ is then obtained as illustrated in the following steps:

$$E[\exp(az)] = \exp(aE[z] + 0.5a^2\sigma_z^2) \tag{4.22}$$

$$1 = \exp\left(E[l] + 0.5\sigma_l^2\right) \tag{4.23}$$

Hence,

$$E[l] = -\sigma_l^2/2 \tag{4.24}$$

The log-normal pdf is plotted in Fig. 4.2 for different values of log irradiance variance, σ_l^2. As the value of σ_l^2 increases, the distribution becomes more skewed with longer tails in the infinity direction. This denotes the extent of fluctuation of the irradiance as the channel inhomogeneity increases.

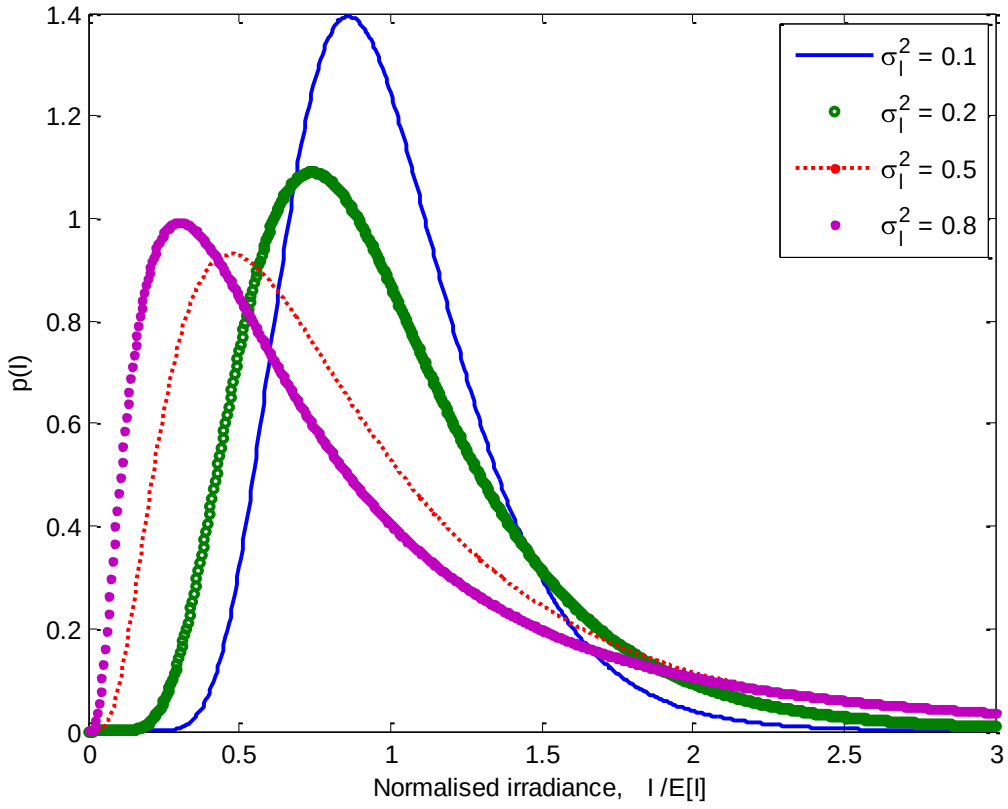

Fig. 4.2: Log-normal probability density function with $E[I]$ = 1 for a range of log irradiance variance σ_l^2 .

After obtaining the pdf of the irradiance fluctuation, it is also paramount to derive an expression for the variance of the irradiance fluctuation, σ_I^2, which characterises the strength of irradiance fluctuation. This is carried out in the following steps:

$$\sigma_I^2 = E[I^2] - E[I]^2 = I_0^2\{E[\exp(2l)] - E[\exp(l)]^2\} \tag{4.25}$$

By applying (4.22) to (4.25) and substituting for $E[l]$, the intensity variance is obtained as:

$$\sigma_I^2 = I_0^2[\exp(\sigma_l^2) - 1] \tag{4.26}$$

The normalised variance of intensity, often referred to as the scintillation index (*S.I.*) is thus:

$$S.I. = \sigma_N^2 = \frac{\sigma_I^2}{I_0^2} = \exp(\sigma_l^2) - 1 \tag{4.27}$$

4.3.1 Spatial coherence in weak turbulence

When a coherent optical radiation propagates through a turbulent medium like the atmosphere, it experiences a decrease in its spatial coherence. The extent of this coherence degradation is, of course, a function of the atmospheric turbulence strength and the propagation distance. In effect, the turbulent channel breaks the coherent radiation up into various fragments whose diameters represent the reduced spatial coherence distance. Following from the Rytov approach used in modelling weak atmospheric turbulence, the spatial coherence of a field travelling through the atmosphere can be derived as [30]:

$$\Gamma_x(\rho) = A^2 \exp\left[-(\rho/\rho_0)^{5/3}\right] \tag{4.28}$$

where ρ_o is the transverse coherence length of the field, this is the transverse distance at

which the coherence of the field is reduced to e^{-1}. Equations 4.29(a-b) give the expressions for the transverse coherence distance, ρ_0 for plane and spherical waves respectively [30].

$$\rho_0 = \left[1.45k^2 \int_0^L C_n^2(x)dx\right]^{-3/5} \tag{4.29a}$$

$$\rho_0 = \left[1.45k^2 \int_0^L C_n^2(x)(x/L)^{5/3}dx\right]^{-3/5} \tag{4.29b}$$

The coherence distance is particularly useful in determining the size of the receiver aperture needed to collect the bulk of the propagating field through the process called aperture averaging, and also to determine the separation distance of detectors in a multiple receiver system. In order for the detectors in the array to receive uncorrelated signals, they must be spaced at a minimum distance ρ_0 apart. Figures 4.3 and 4.4 illustrate the coherence length for a horizontal link at two commonly used FSO wavelengths, λ = 850nm and 1550nm, for typical values of C_n^2. The spatial coherence length is generally longer at longer wavelengths and decreases as both the propagation distance and the atmospheric turbulence increase.

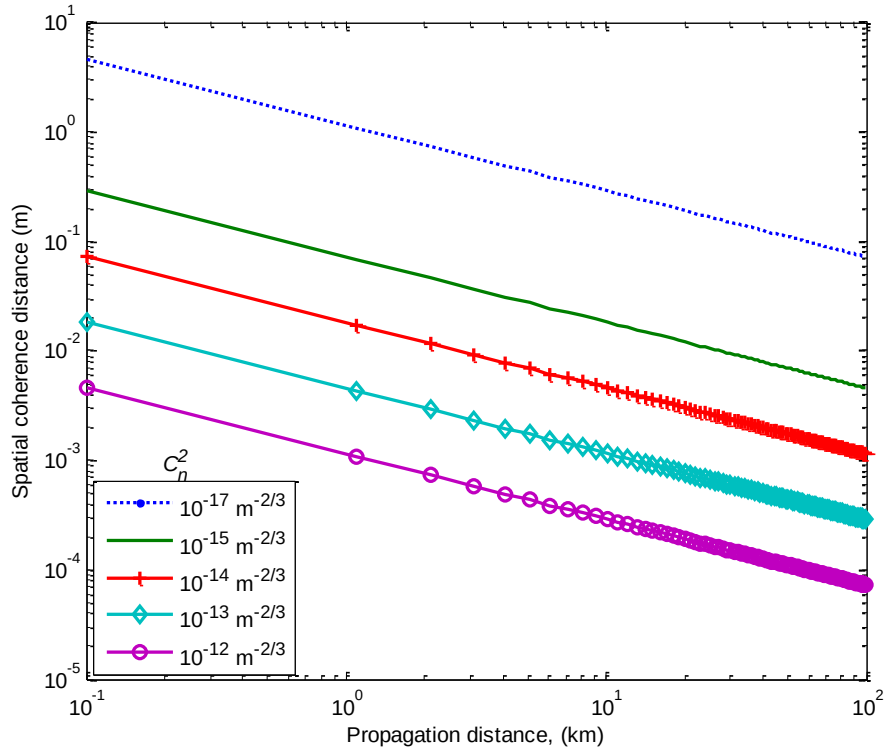

Fig. 4.3: Plane wave transverse coherence length for λ = 850nm and a range of C_n^2.

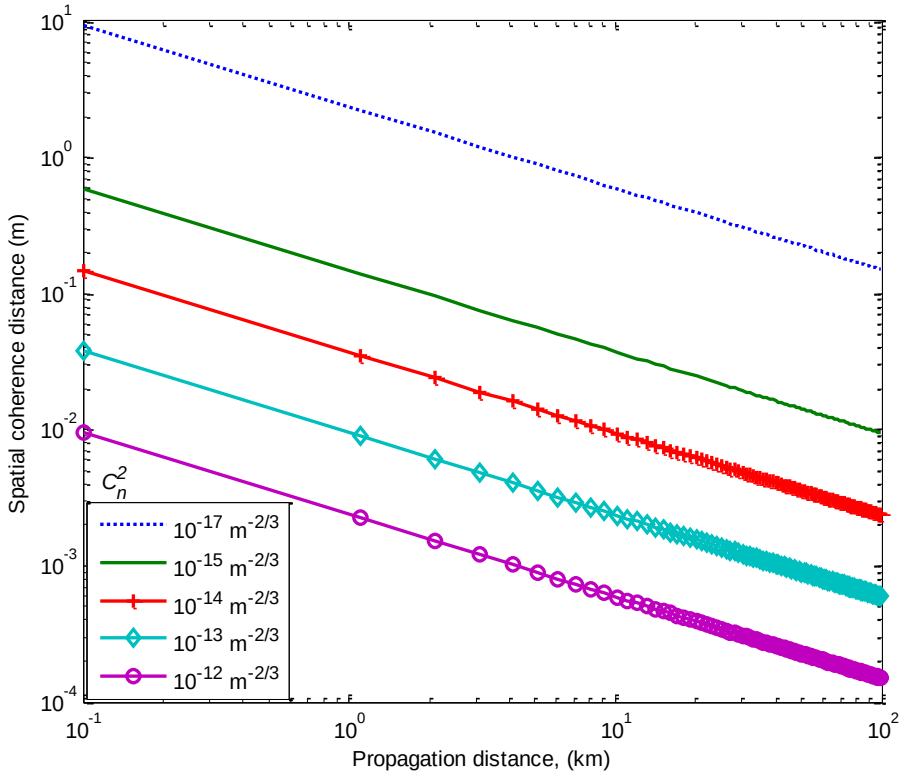

Fig. 4.4: Plane wave transverse coherence length for λ = 1550nm and a range of C_n^2.

4.3.2 Limit of log-normal turbulence model

Thus far, the Rytov approximation has been used to describe atmospheric turbulence and the log-normal turbulence model has been derived. The Rytov approximation predicts that the Rytov parameter increases without limit with the index of refraction structure parameter and/or the path length. However, based on experimental results as reported in [45], this prediction holds only in the weak turbulence regime when $\sigma_x^2 \leq 0.3$. As the turbulence strength increases beyond the weak regime, due to a combination of increased path length and/or increased C_n^2, the turbulent eddies result in multiple scatterings that are not accounted for by Rytov in his approximation [30, 49].

Based on experiments reported in [30, 45] , the scintillation index, *S.I.*, increases linearly with the Rytov parameter within the weak regime and continues to increase to a maximum value greater than unity. The regime in which *S.I.* attains its maximum value characterises the highest strength of inhomogeneity or random focusing. The *S.I.* then starts to decrease due self interference as a result of multiple scattering and approaches unity as the Rytov parameter increases [45]. This observation is in contrast to the prediction of the Rytov approximation beyond the weak atmospheric regime. In the next section, two other irradiance fluctuation models that account for the multiple scatterings will be reviewed and their pdfs will be presented.

4.4 The Gamma-Gamma Turbulence Model

This model proposed by Andrews *et al*. [49] is based on the modulation process where the fluctuation of light radiation traversing a turbulent atmosphere is assumed to consist of small scale (scattering) and large scale (refraction) effects. The former includes contributions due to eddies/cells smaller than the Fresnel zone, $R_F = (L/k)^{1/2}$ or the

coherence radius, ρ_0, whichever is smaller. Large scale fluctuations on the other hand are generated by turbulent eddies larger than that of the first Fresnel zone or the scattering disk $L/k\rho_0$, whichever is larger. The small scale eddies are assumed to be modulated by the large scale eddies. Consequently, the normalised received irradiance I is defined as the product of two statistically independent random processes I_x and I_y:

$$I = I_x I_y \tag{4.30}$$

I_x and I_y arise from the large scale and small scale turbulent eddies respectively and are both proposed to obey the gamma distribution by Andrews et al [49, 50, 57]. Their pdfs are thus given by:

$$p(I_x) = \frac{\alpha(\alpha I_x)^{\alpha-1}}{\Gamma(\alpha)} \exp(-\alpha I_x) \; ; \qquad I_x > 0; \; \alpha > 0 \tag{4.31a}$$

$$p(I_y) = \frac{\beta(\beta I_y)^{\beta-1}}{\Gamma(\beta)} \exp(-\beta I_y) \qquad I_y > 0; \; \beta > 0 \tag{4.31b}$$

By fixing I_x and using the change of variable, $I_y = I/I_x$, the conditional pdf given by (4.32) is obtained in which I_x is the (conditional) mean value of I.

$$p(I/I_x) = \frac{\beta(\beta I/I_x)^{\beta-1}}{I_x \Gamma(\beta)} \exp(-\beta I/I_x) \qquad I > 0 \tag{4.32}$$

To obtain the unconditional irradiance distribution, the conditional probability, $p(I/I_x)$ is averaged over the statistical distribution of I_x given by 4.31(a) to obtain the following gamma-gamma irradiance distribution function.

$$p(I) = \int_0^{\infty} p(I/I_x)p(I_x)dI_x$$

$$p(I) = \frac{2(\alpha\beta)^{(\alpha+\beta)/2}}{\Gamma(\alpha)\Gamma(\beta)} I^{\left(\frac{\alpha+\beta}{2}\right)-1} \mathrm{K}_{\alpha-\beta}\left(2\sqrt{\alpha\beta I}\right); \qquad \mathrm{I} > 0 \tag{4.33}$$

where α and β respectively represent the effective number of large- and small-scale eddies of the scattering process. $K_n(.)$ is the modified Bessel function of the 2nd kind of order *n*, and Γ(.) represents the Gamma function. If the optical radiation at the receiver is assumed to be a plane wave, then the two parameters α and β that characterise the irradiance fluctuation pdf are related to the atmospheric conditions by [99]:

$$\alpha = \left[\exp\left(\frac{0.49\sigma_l^2}{\left(1 + 1.11\sigma_l^{12/5}\right)^{7/6}}\right) - 1\right]^{-1} \tag{4.34a}$$

$$\beta = \left[\exp\left(\frac{0.51\sigma_l^2}{\left(1 + 0.69\sigma_l^{12/5}\right)^{5/6}}\right) - 1\right]^{-1} \tag{4.34b}$$

While the scintillation index is given by:

$$\sigma_N^2 = \exp\left[\frac{0.49\sigma_l^2}{\left(1 + 1.11\sigma_l^{12/5}\right)^{7/6}} + \frac{0.51\sigma_l^2}{\left(1 + 0.69\sigma_l^{12/5}\right)^{5/6}}\right] - 1 \tag{4.35}$$

A plot of this distribution, using equation (4.33), is given in Fig. 4.5 for three different turbulence regimes, namely weak, moderate and strong. The plot shows that as the turbulence increase form weak to strong regime, the distribution spreads out more, with an increase in the range of possible values of the irradiance.

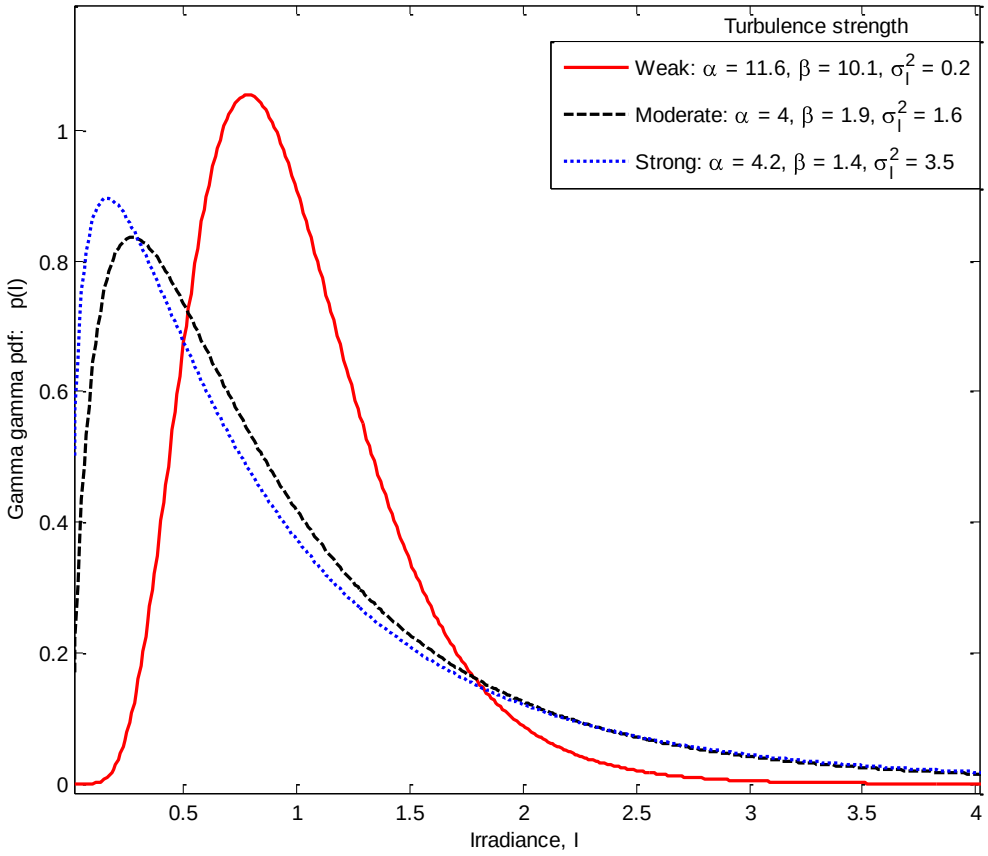

Fig. 4.5: Gamma-gamma probability density function for three different turbulence regimes, namely weak, moderate and strong.

The gamma-gamma turbulence model given by (4.33) is valid for all turbulence scenarios from weak to strong and the values of α and β at any given regime can be obtained from (4.34). Figure 4.6 shows the variation of *S.I.* as a function of the Rytov parameter based on (4.35), this graph shows that as the Rytov parameter increases, the *S.I.* approaches a maximum value greater than one, and then approaches unity as the turbulence induced fading approaches the saturation regime. The values of α and β under different turbulence regimes are depicted in Fig. 4.7.

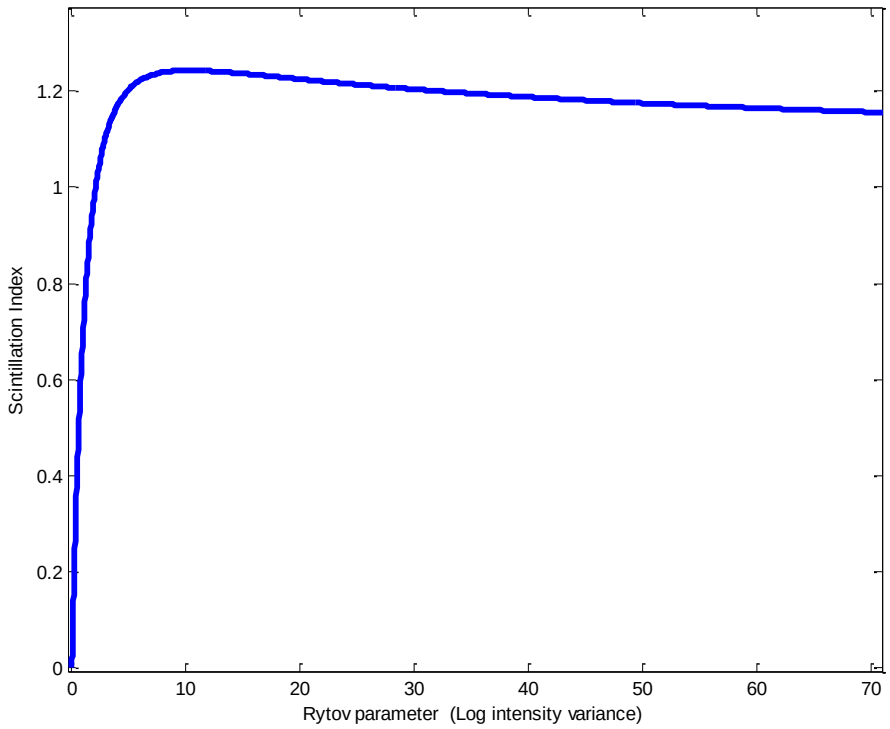

Fig. 4.6: *S.I.* against log intensity variance for $C_n^2 = 10^{-15}$ $m^{-2/3}$ and $\lambda = 850nm$.

In the very weak turbulence regime, $\alpha \gg 1$ and $\beta \gg 1$ as shown in Fig. 4.7, this means that the effective numbers of small and large scale eddies are very large. But, as the irradiance fluctuations increase (beyond $\sigma_l^2 = 0.2$) and the focusing regime is approached, where α and β then decrease substantially as illustrated in Fig. 4.7. Beyond the focussing (moderate to strong) regime and approaching the saturation regime, $\beta \rightarrow 1$. The implication of this according to [57], is that the effective number of small scale cells/eddies ultimately reduces to a value determined by the transverse spatial coherence radius of the optical wave. On the other hand, the effective number of discrete refractive scatterers, α, increases again with increasing turbulence and eventually becomes unbounded in the saturation regime as shown in Fig. 4.7. Under these conditions, the gamma-gamma distribution approaches the negative exponential distribution of Section 4.5.

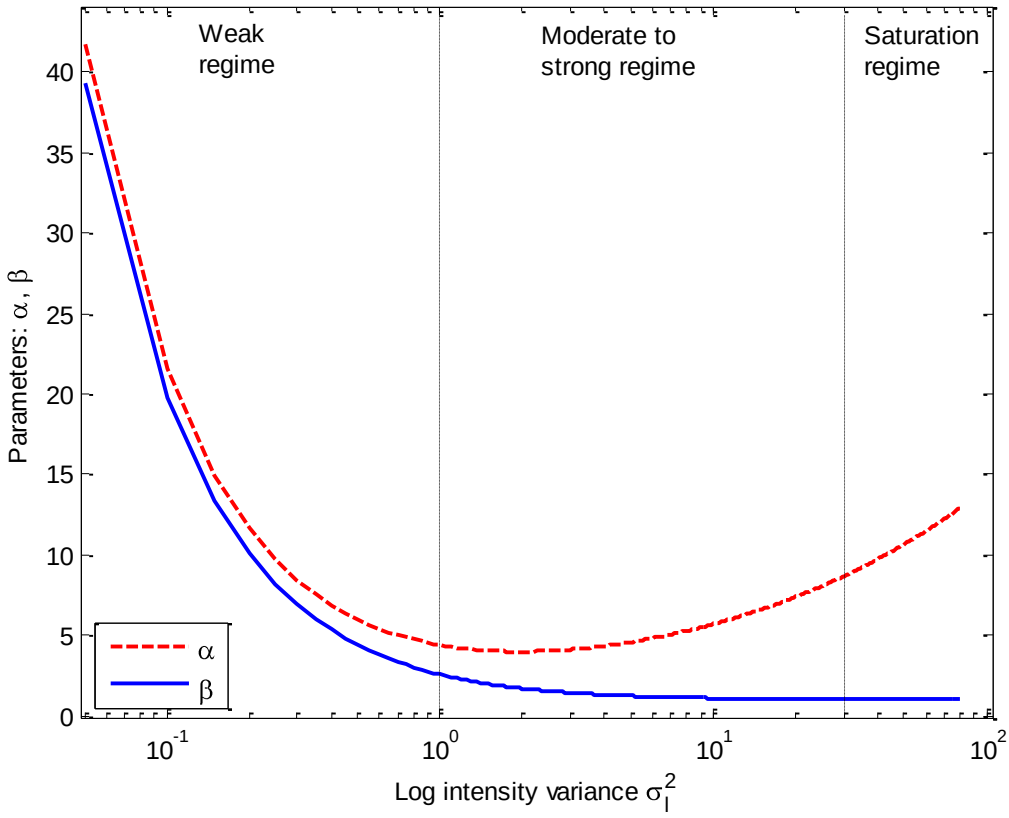

Fig. 4.7: Values of α and β under different turbulence regimes: weak, moderate to strong and saturation.

4.5 The Negative Exponential Turbulence Model

In the limit of strong irradiance fluctuations (i.e. in saturation regime and beyond) where the link length spans several kilometres, the number of independent scatterings becomes large [4] [5]. This saturation regime is also called the fully developed speckle regime. The amplitude fluctuation of the field traversing the turbulent medium in this situation is generally believed and experimentally verified [45, 55, 58] to obey the Rayleigh distribution implying negative exponential statistics for the irradiance. That is:

$$p(I) = \frac{1}{I_0}\exp\left(-\frac{I}{I_0}\right); \qquad I_0 > 0 \tag{4.36}$$

where $E[I] = I_0$ is the mean received irradiance. During the saturation regime, the value of the scintillation index, $S.I. \rightarrow 1$. It is noteworthy that other turbulence models such as the log-normal-Rician [100] and the I–K [101] distributions, which are both valid from weak to strong turbulence regime; the K-model [102, 103], which is only valid for the strong regime, and the gamma–gamma turbulence models all reduce to the negative exponential in the limit of strong turbulence. The negative exponential pdf is shown in Fig. 4.8.

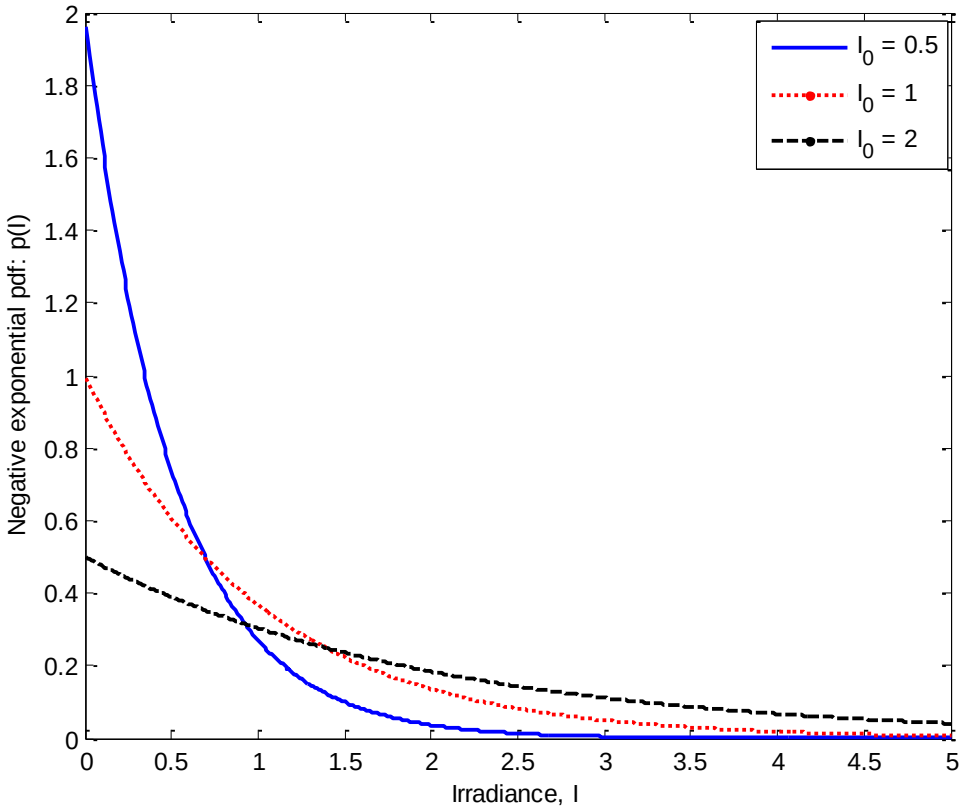

Fig. 4.8: Negative exponential probability density function for different values of I_0

4.6 Summary

In this chapter, different atmospheric turbulence models have been introduced covering short to very long range FSO links. The log-normal is mathematically tractable but only valid in the weak regime. Beyond the weak regime, where multiple scattering needs to be accounted for, the gamma-gamma model is more suitable but lack the mathematical convenience of the log-normal distribution. This model has a validity that covers both the weak and strong turbulence regimes while in the saturation regime, which is otherwise called the fully developed speckle regime, the appropriate model is the negative exponential distribution. These models will then be used in the subsequent chapters to characterise the statistical behaviour of the received signal and in deriving expressions for the error performance of short to very long FSO links.

Chapter Five

FSO Modulation Techniques

5.1 Introduction

This chapter introduces the modulation techniques used in FSO and their performance in the presence of channel impairments such as noise and channel fading induced by atmospheric turbulence. There are many different types of modulation schemes which are suitable for optical wireless communication systems, as shown the modulation tree of Fig. 5.1. The emphasis in this chapter will be on the following digital modulations techniques: OOK, pulse position modulation (PPM) and phase shift keying pre-modulated subcarrier intensity modulation. Since the average emitted optical power is

always limited, the performance of modulation techniques is often compared in terms of the average received optical power required to achieve a desired bit error rate at a given data rate. It is very desirable for the modulation scheme to be power efficient, but this is however not the only deciding factor in the choice of a modulation technique. The design complexity of its transmitter and receiver and the bandwidth requirement of the modulation scheme are all equally important. Though it can be argued that the optical carrier has abundant bandwidth, there exists a constraint on the bandwidth of the optoelectronic devices.

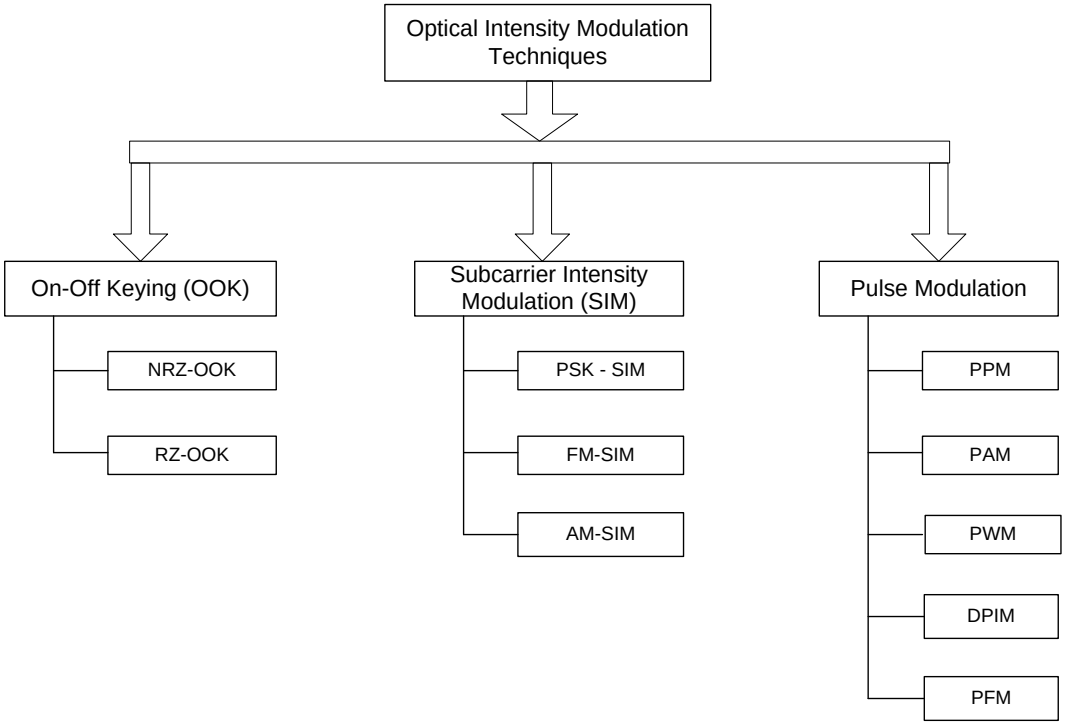

Fig. 5.1: Modulation tree.

The classical modulation technique used for FSO is OOK [20, 31]. This is primarily because of the simplicity of its design and implementation. It is unsurprising therefore that the majority of the work reported in literature [29, 62] is based on this signalling technique. However the performance of a fixed-threshold level OOK in atmospheric turbulence is not optimal, as will be shown in the following section. In atmospheric

turbulence an optimal performing OOK requires the threshold level to vary in sympathy with the prevailing irradiance fluctuation and noise, that is, to be adaptive. The PPM requires no adaptive threshold and is predominantly used for deep space free space optical communication links because of its enhanced power efficiency compared to the OOK signalling [6, 53-55, 61, 104]. The PPM modulation technique, however, requires a complex transceiver design due to tight synchronisation requirements and a higher bandwidth than the OOK.

The performance analysis of these modulation schemes and that of the SIM will be further discussed in both this chapter and the next. The SIM also requires no adaptive threshold and does not require as much bandwidth as PPM, but suffers from a high peak to average power ratio, which translates into poor power efficiency. Choosing a modulation scheme for a particular application therefore entails trade-offs among these listed factors.

5.2 On-Off Keying

OOK is the dominant modulation scheme employed in commercial terrestrial wireless optical communications systems. This is primarily due to its simplicity and resilience to the innate nonlinearities of the laser and the external modulator. OOK can use either non-return-to-zero (NRZ) or return-to-zero (RZ) pulse formats. In NRZ-OOK, an optical pulse of peak power $\alpha_e P_T$ represents a digital symbol '0' while the transmission of an optical pulse of peak power P_T represents a digital symbol '1'. The optical source extinction ratio, α_e, has the range $0 \leq \alpha_e < 1$. The finite duration of the optical pulse is the same as the symbol duration T. With OOK-RZ, the pulse duration is lower than the bit duration, giving an improvement in power efficiency over NRZ-OOK at the expense

of an increased bandwidth requirement. In all the analyses that follow, the extinction ratio, α_e , is equal to zero and NRZ-OOK, which is the scheme deployed in present commercial FSO systems, is assumed unless otherwise stated.

5.2.1 OOK in a Poisson atmospheric optical channel

If the received average power is given by $P_R = P_T \exp(-\gamma_T L)$, where γ_T represents to overall channel attenuation, then the average received photoelectron count is given by [88]:

$$\langle n \rangle = \frac{\eta \lambda T P_R}{hc} \tag{5.1}$$

where *h* and *c* are Planck's constant and the speed of light in vacuum respectively, η is the quantum efficiency of the photodetector and *T* is the optical pulse duration. However the instantaneous count *n*, unlike the average count, is not constant. As mentioned in Chapter Three, it varies with time due to the following reasons:

i) The quantum nature of the light/photodetection process, which suggests that the instantaneous number of counts *n* follows the discrete Poisson distribution with an associated quantum noise of variance $\langle n \rangle$, (the mean and variance of a Poisson distribution are the same).

ii) The received signal field varies randomly due to the effect of scintillation.

This implies that the number of counts is now doubly stochastic and based on the log normal turbulence model of Section 4.2, the probability of *n* counts is derived as [105]:

$$p_1(n) = \int_0^{\infty} \frac{(\eta\lambda T P_R/hc)^n \exp(-\eta\lambda T P_R/hc)}{n!\sqrt{2\pi\sigma_l^2 P_R}} \exp\left[-\frac{1}{2\sigma_l^2}\left(\ln\frac{P_R}{P_0} + \frac{\sigma_l^2}{2}\right)^2\right] dP_R \tag{5.2}$$

where P_0 is the received average power in the absence of atmospheric turbulence and σ_l^2 is the strength of power fluctuation indicator. When an optical pulse is transmitted (that is bit '1' sent), a decision error occurs when the number of counts, *n*, is less than a pre-determined threshold count, n_{th}. Thus, the probability of detecting bit '0' when bit'1' is transmitted is given by [105]:

$$p_1(n < n_{th}) = \sum_{n=0}^{n_{th}-1}\left[\int_0^{\infty} \frac{\left(\eta\lambda T\left(P_R + P_{Bg}\right)\right)^n \exp(-\eta\lambda T\left(P_R + P_{Bg}\right)/hc)}{(hc)^n n!\sqrt{2\pi\sigma_l^2 P_R}} \times \exp\left(-\frac{1}{2\sigma_l^2}\left(\ln\frac{P_R}{P_0} + \frac{\sigma_l^2}{2}\right)^2\right) dP_R\right] \tag{5.3}$$

where P_{Bg} is the power of the background radiation that falls within the receiver's field of view and $n_b = \eta\lambda T P_{Bg}/hc$.

Similarly, the probability of detecting bit '1' when bit '0' is transmitted is derived as [105]:

$$p_0(n > n_{th}) = \sum_{n=n_{th}}^{\infty} \frac{\left(\eta\lambda T P_{Bg}/hc\right)^n \exp\left(-\eta\lambda T P_{Bg}/hc\right)}{n!}$$

$$= 1 - \sum_{n=0}^{n_{th}-1} \frac{\left(\eta\lambda T P_{Bg}/hc\right)^n \exp\left(-\eta\lambda T P_{Bg}/hc\right)}{n!} \tag{5.4}$$

It should be noted from (5.4) that atmospheric turbulence has no impact when no optical power is transmitted. If the bits '1'and '0' are assumed to be equally likely to be transmitted, then the system theoretical bit error rate, P_e becomes:

$$P_e = 0.5\left[p_0(n > n_{th}) + p_1(n < n_{th})\right] \tag{5.5}$$

For an optimal performance, n_{th} is the value of n that satisfies expression (5.6) obtained by invoking the maximum likelihood symbol-by-symbol detection condition.

$$\left(P_{Bg}\right)^n \exp\left(-\eta\lambda T P_{Bg}/hc\right) = \left\{\int_0^\infty \frac{\left(P_R + P_{Bg}\right)^n \exp\left(-\eta\lambda T\left(P_R + P_{Bg}\right)/hc\right)}{\sqrt{2\pi\sigma_l^2 P_R}} \times \exp\left[-\frac{1}{2\sigma_l^2}\left(\ln\frac{P_R}{P_0} + \frac{\sigma_l^2}{2}\right)^2\right] dP_R\right\} \tag{5.6}$$

The impact of scintillation on the achievable bit error rate (BER) of the system is shown in Fig. 5.2, the figure is obtained by combining equations (5.3), (5.4) and (5.5), while the values of n_{th} used is obtained from the solution of equation (5.6).

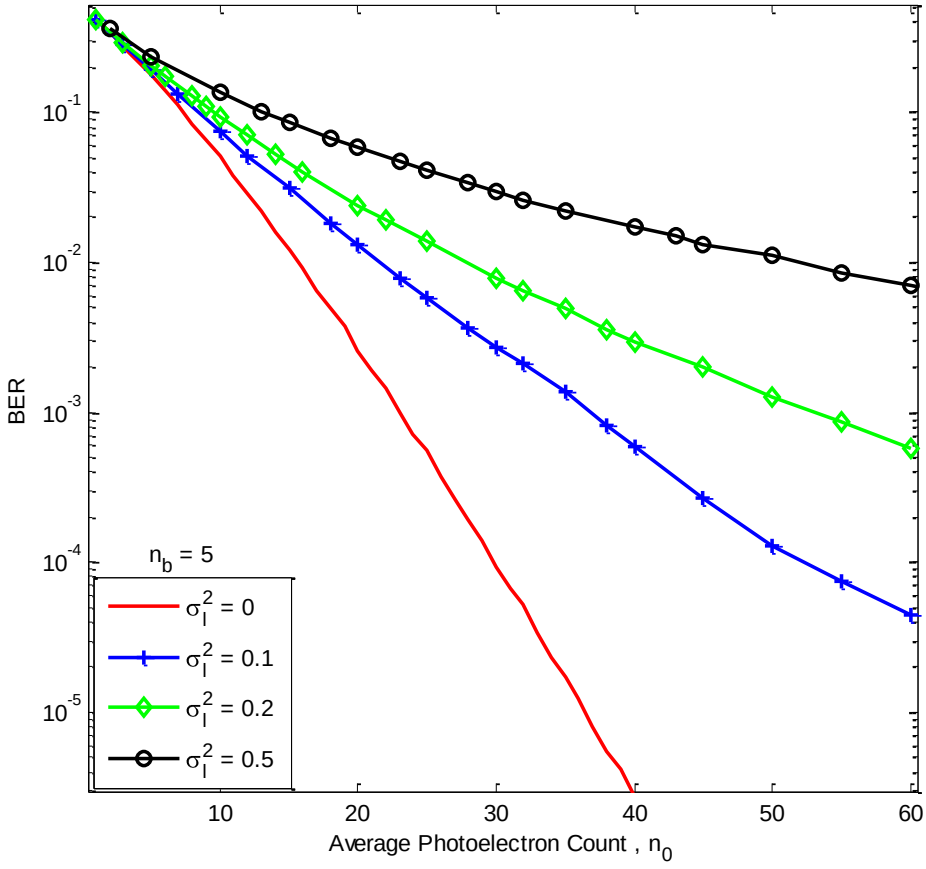

Fig. 5.2: BER against the average photoelectron count per bit for OOK-FSO in a Poisson atmospheric turbulence channel for.$\sigma_l^2 = [0, 0.1, 0.2, 0.5]$.

In the figure, the BER is plotted against the average count $n_0 = \eta\lambda TP_0/hc$. The penalty incurred due to scintillation is quite evident from the plot. For examples, with respect to no scintillation condition, over 20 additional photoelectron counts per bit are needed to maintain the same BER of 10^{-4} in a channel characterised by $\sigma_I^2 > 0.1$. Consequently, when designing a terrestrial laser communication link, an adequate margin, based on the results shown in Fig. 5.2, should be provided to cater for the scintillation effect.

The figure also shows that increasing the average count can help ameliorate the effect of turbulence and result in improved BER in very weak turbulence, but as the strength of turbulence increases, increased average photoelectron count has a less significant impact. For example at $\sigma_I^2 = 0.1$ and $n_0 = 10$, the BER was about 10^{-1} but this decreases to less than 10^{-3} when n_0 is increased to 40. In comparison, when $\sigma_I^2 = 0.5$, the BER is higher than 10^{-1} for $n_0 = 10$ and remains higher than 10^{-2} with n_0 increased to 40. Note that in the absence of turbulence, $n_0 = \langle n \rangle$ and that the result presented in Fig. 5.2 should be viewed as the theoretical performance lower bound since the photo-multiplication process has been assumed ideal.

5.2.2 OOK in a Gaussian atmospheric optical channel

With large signal photoelectron counts, and by taking the detection thermal noise into account, the generated signal current probability distribution can be approximated as the tractable Gaussian distribution. Without any loss of generality, the receiver area may be normalised to unity such that the optical power may be represented by the optical intensity, *I*. If $\Re$ represents the responsivity of the PIN photodetector, the received signal in an OOK system is therefore given by:

$$i(t) = \Re I\left[1 + \sum_{j=-\infty}^{\infty} d_j g(t - jT)\right] + n(t) \tag{5.7}$$

where $n(t) \sim N(0, \sigma^2)$ is the additive white Gaussian noise, $g(t - jT)$ is the pulse shaping function and d_j = [-1, 0]. At the receiver, the received signal is fed into a threshold detector which compares the received signal with a pre-determined threshold level. A digital symbol '1' is assumed to have been received if the received signal is above the threshold level and '0' otherwise.

The probability of error is therefore given as:

$$P_e = p(0)\int_{i_{th}}^{\infty} p(i\ /\ 0)di + p(1)\int_{0}^{i_{th}} p(i\ /\ 1)di \tag{5.8}$$

where i_{th} is the threshold signal level and the marginal probabilities are defined as:

$$p(i\ /\ 0) = \frac{1}{\sqrt{2\pi\sigma^2}}\exp(-i^2/2\sigma^2) \tag{5.9a}$$

$$p(i/\ 1) = \frac{1}{\sqrt{2\pi\sigma^2}}\exp\left[\frac{-(i - \Re I)^2}{2\sigma^2}\right] \tag{5.9b}$$

For equiprobable symbols, $p(0) = p(1) = 0.5$, hence the optimum threshold point is at $i_{th} = 0.5\Re I$ and the conditional probability of error reduces to:

$$P_{ec} = \mathrm{Q}\left(\frac{i_{th}}{\sigma}\right) \tag{5.10}$$

where $\mathrm{Q}(x) = 0.5\mathrm{erfc}\left(x/\sqrt{2}\right)$. In the presence of atmospheric turbulence, the threshold level is no longer fixed midway between the signal levels representing symbols '1' and '0'. The marginal probability $p(i/\ 1)$ is then modified by averaging the conditional pdf

of $i(t)$ over the scintillation statistics. Note that scintillation does not occur when no pulse is transmitted.

$$p(i/1) = \int_0^\infty p(i/1, I)p(I)dI \tag{5.11}$$

Assuming equiprobable symbol transmission and invoking the maximum a posteriori symbol-by-symbol detection, the likelihood function Λ, becomes [106]:

$$\Lambda = \int_0^\infty \exp\left[\frac{-(i - \Re I)^2 - i^2}{2\sigma^2}\right] p(I)dI \tag{5.12}$$

Fig. 5.3 below shows the plot of log (Λ) against the average photocurrent *i*, at various levels of scintillation and noise variance of 10^{-2}. The threshold level, as would be expected, is at the point where Λ = 1 (i.e. when log (Λ) = 0).

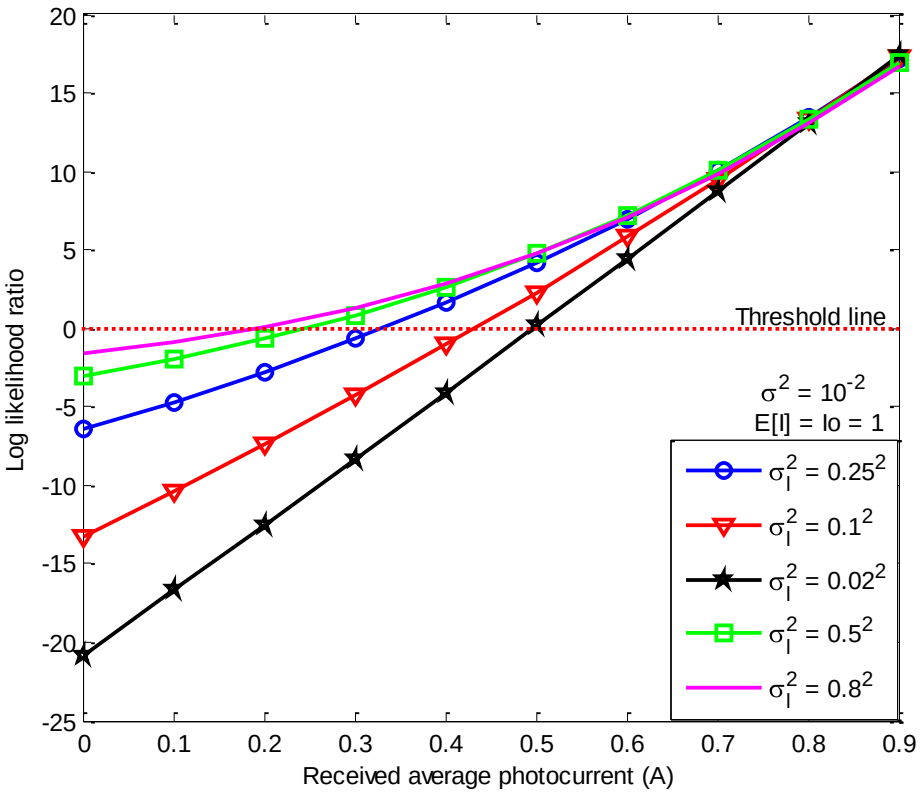

Fig. 5.3: The likelihood ratio against the received signal for different turbulence levels and noise variance of 10^{-2}.

Based on the log-normal turbulence model, the plot of i_{th} against the log intensity standard deviation for different noise levels is depicted in Fig. 5.4 for different noise levels. The threshold is observed to approach the expected value of 0.5 as the scintillation level approaches zero. As an illustration, at a turbulence level $\sigma_l^2 = 0.2$, the probability of bit error P_e, obtained from the combination of (5.8), (5.9) and (5.11) is plotted against the normalised SNR = $(\Re E[I])^2/\sigma^2$ in Fig. 5.5, the value of i_{th} used for the adaptive threshold level graph is obtained from the solution of equation (5.12). From this figure, the effect of using a fixed threshold level in fading channels results in a BER floor. The values of which depend on the fixed threshold level and turbulence induced fading strength. With an adaptive threshold, there is no such BER floor and any desired level of BER can thus be realised.

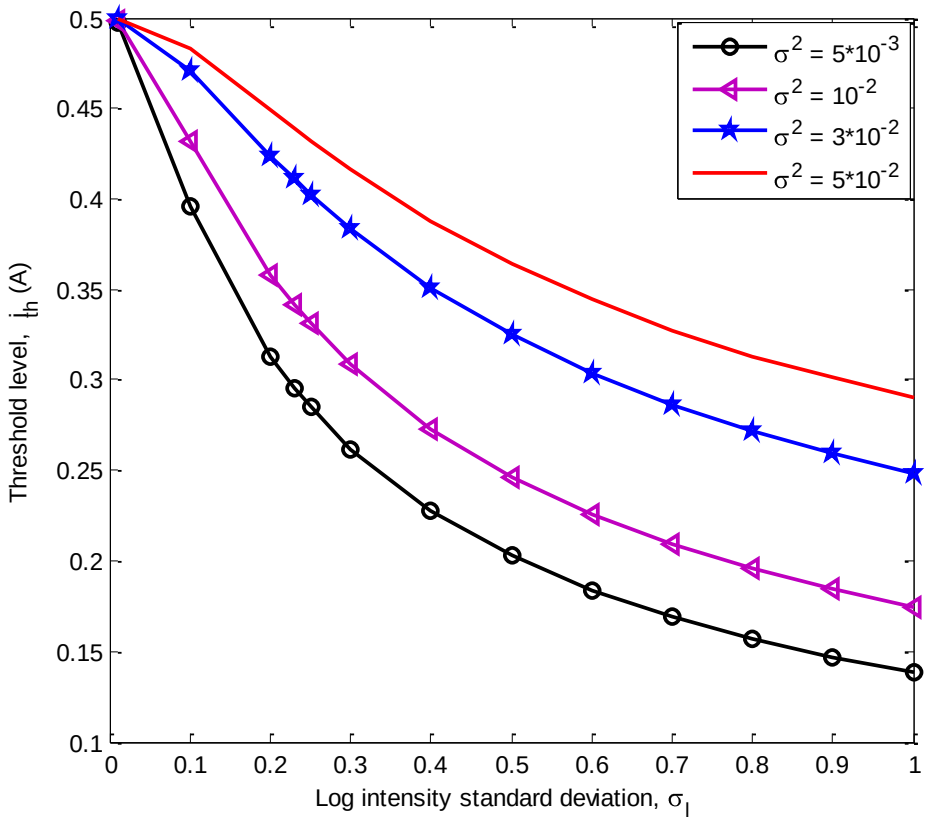

Fig. 5.4: OOK threshold level against the log intensity standard deviation for various noise levels.

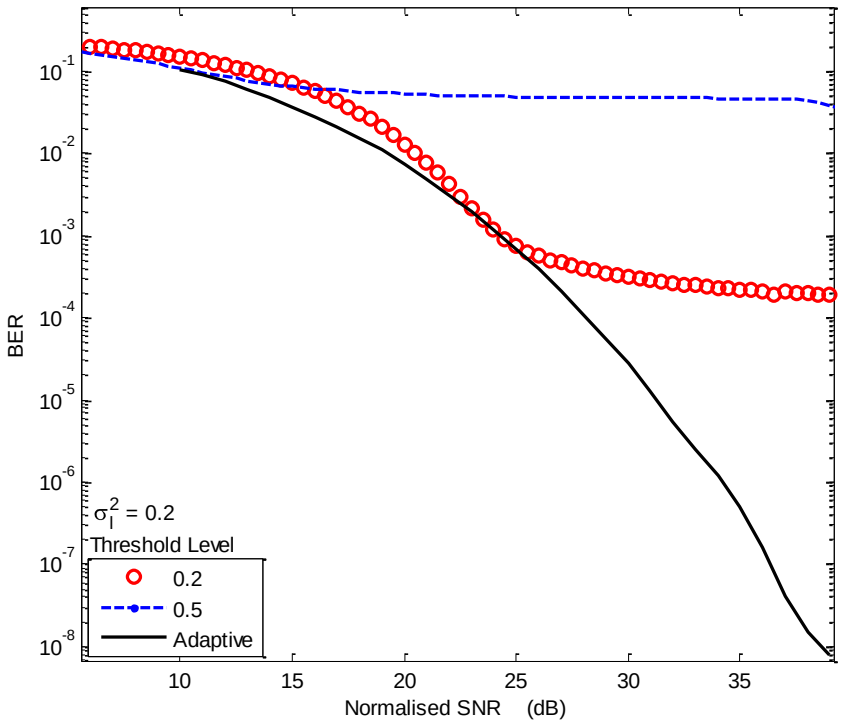

Fig. 5.5: BER of OOK based FSO in atmospheric turbulence with $\sigma_l^2 = 0.2$ considering fixed and adaptive threshold levels.

In Fig. 5.6, the BER is again plotted against the normalised SNR at various levels of scintillation including when the threshold is fixed at 0.5. This is intended to show the effect of turbulence strength on the amount of SNR required to maintain a given error performance level. With a fixed threshold, the BER reaches a floor at a BER that is greater than 10^{-4}, meaning that a lower BER is not achievable at the specified low scintillation level. From this graph, it can be inferred that atmospheric turbulence: i) causes SNR penalty, for example ~26 dB of SNR is needed to achieve a BER of 10^{-6} due to a very weak scintillation of strength $\sigma_l^2 = 0.25^2$, this however increases by over 20 dB as the scintillation strength increases to $\sigma_l^2 = 0.7^2$; and ii) implies that adaptive threshold will be required to avoid a BER floor in the system performance.

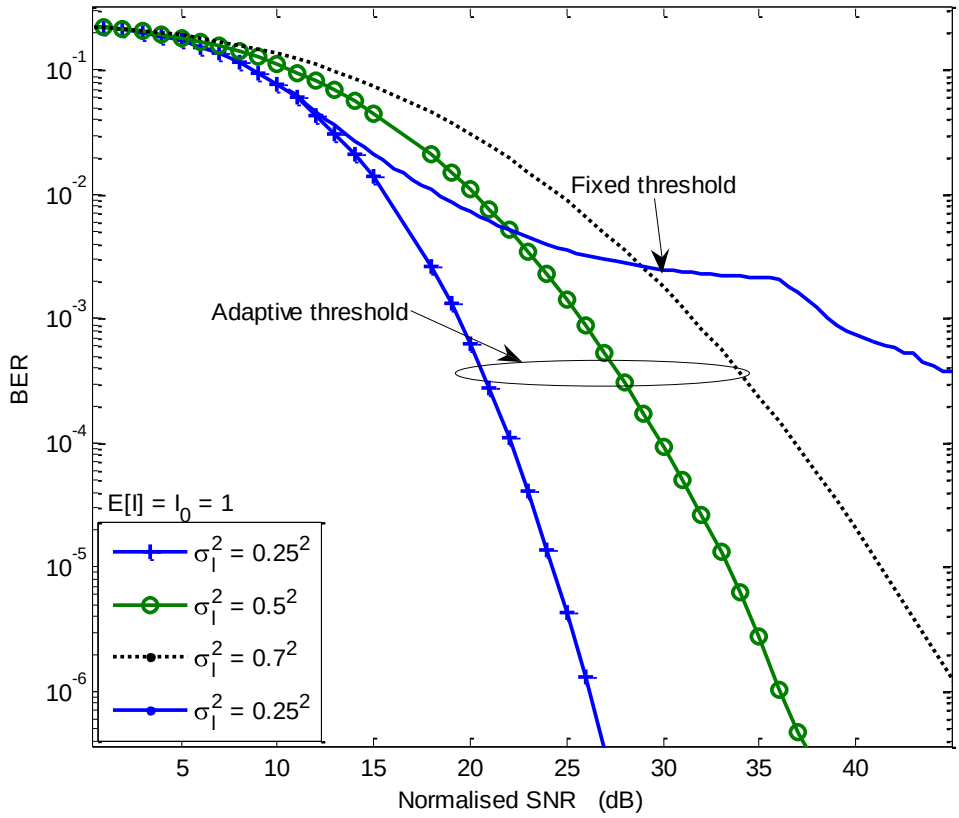

Fig. 5.6: BER of OOK-FSO with fixed and adaptive threshold at various levels of scintillation, $\sigma_l = [0.2, 0.5, 0.7]$ and $I_0 = 1$.

The above results illustrate that for the OOK modulated FSO system to perform at its best, the receiver will require knowledge of both the fading strength and the noise level. This can be resolved by integrating into the system an intensity estimation network which can predict the scintillation level based on past events. The implementation of this is not trivial, and as such, commercial FSO designers tend to adopt the fixed threshold approach and include a sufficiently large link margin in the link budget to cater for turbulence induced fading [20].

5.3 Pulse Position Modulation

This is an orthogonal modulation technique and a member of the pulse modulation family (see Fig. 5.1). The PPM modulation technique improves on the power efficiency of OOK but at the expense of an increased bandwidth requirement and greater complexity. In PPM, each block of $\log_2 M$ data bits is mapped to one of M possible symbols. Generally the notation M-PPM is used to indicate the order. Each symbol consists of a pulse of constant power, P_T, occupying one slot, along with M-1 empty slots. The position of the pulse corresponds to the decimal value of the $\log_2 M$ data bits. Hence, the information is encoded by the position of the pulse within the symbol. The slot duration, T_s, is related to the bit duration by the following expression:

$$T_s = \frac{T \log_2 M}{M} \tag{5.13}$$

The transmitted waveforms for 16-PPM and OOK are shown in Fig. 5.7.

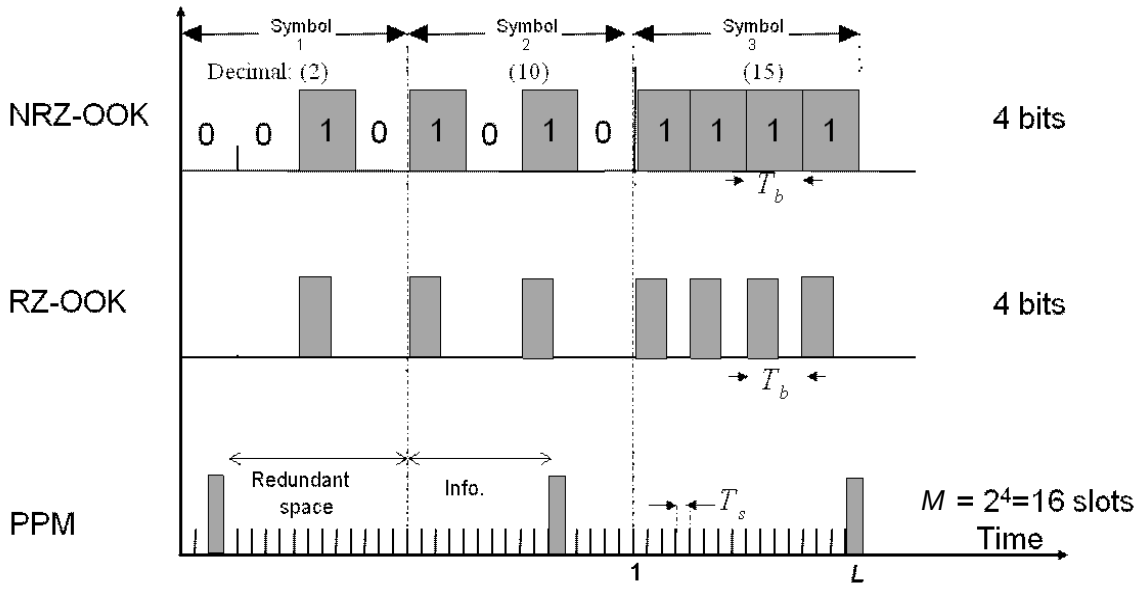

Fig. 5.7: Time waveforms for 4-bit OOK and 16-PPM

A PPM receiver will require both slot and symbol synchronisation in order to demodulate the information encoded on the pulse position. Nevertheless, because of its superior power efficiency, PPM is an attractive modulation technique for optical wireless communication systems particularly in deep space laser communication applications [4]. Assuming that complete synchronisation is maintained between the transmitter and receiver at all times, the optical receiver detects the transmitted signal by attempting to determine the energy in each possible time slot. It then selects the signal which corresponds to the maximal energy. In direct photodetection, this is equivalent to "counting" the number of released electrons in each T_s interval. The photo count per PPM slot can be obtained from:

$$K_s = \frac{\eta \lambda P_R T_s}{hc} \tag{5.14}$$

where P_R is the received optical power during a slot duration. An APD could be used to give an increase in the number of photon counts per PPM slot but, unfortunately, the photo-multiplication process that governs the generation of the secondary electrons is a random process. This implies that a large photo-multiplication gain will eventually lead to a large noise factor and an error prone performance. For a moderately high received signal, as is the case in commercial and short range FSO systems, the BER conditioned on K_s is given by [79]:

$$P_{ec} = Q\left(\sqrt{\frac{(\bar{g}q)^2 K_s^2}{(\bar{g}q)^2 F\left(K_s + 2K_{Bg}\right) + 2\sigma_{Th}^2}}\right) \tag{5.15}$$

where the parameters are defined as:

$K_{Bg} = \eta\lambda P_{Bg} T_s/hc$	Average photon count per PPM slot due to the background Radiation of power P_{Bg}
$\bar{g}$	Average APD gain
q	Electronic charge
$F \approx 2 + \zeta\bar{g}$	Noise factor of the APD
ζ	APD ionisation factor
$\sigma_{Th}^2 = (2\kappa T_e q/R_L)(T_s)$	Equivalent thermal noise count within a PPM slot duration [79]
$R_b = 1/T$	Bit rate.
κ	Boltzmann's constant
R_L	Equivalent load resistance

In the presence of log normal atmospheric turbulence, the unconditional BER for a binary PPM modulated FSO obtained by averaging (5.15) over the scintillation statistics can be approximated as [54]:

$$P_e \approx \frac{1}{\sqrt{\pi}} \sum_{i=1}^{n} w_i \mathrm{Q}\left(\frac{\exp\left(2\left(\sqrt{2}\sigma_k x_i + m_k\right)\right)}{F\exp\left(\sqrt{2}\sigma_k x_i + m_k\right) + K_n} \right) \tag{5.16}$$

where $[w_i]_{i=1}^n$ and $[x_i]_{i=1}^n$ are the weight factors and the zeros of an n^{th} order Hermite polynomial. These values are contained in Appendix A for a 20^{th} order Hermite polynomial. m_k represents the mean of $\ln(K_s)$, $K_n = (2\sigma_{Th}^2/(\bar{g}q)^2) + 2FK_{Bg}$ and $\sigma_k^2 = \ln(\sigma_N^2 + 1)$. It is noteworthy that the fluctuation of the mean count, K_s, is brought about by the atmospheric turbulence and its ensemble average is given by the following [54]:

$$E[K_s] = \exp\left(\frac{\sigma_k^2}{2} + m_k\right) \tag{5.17}$$

For an *M*-PPM system, the BER denoted by P_e^M has an upper bound given by [54]:

$$P_e^M \leq \frac{M}{2\sqrt{\pi}} \sum_{i=1}^{n} w_i \mathrm{Q}\left(\frac{\exp\left(2\left(\sqrt{2}\sigma_k x_i + m_k\right)\right)}{F\exp\left(\sqrt{2}\sigma_k x_i + m_k\right) + K_n}\right) \tag{5.18}$$

The BER of a binary PPM modulated FSO is shown in Fig. 5.8 at different levels of scintillation. The extension of the result is straight forward from (5.18) and hence not presented here.

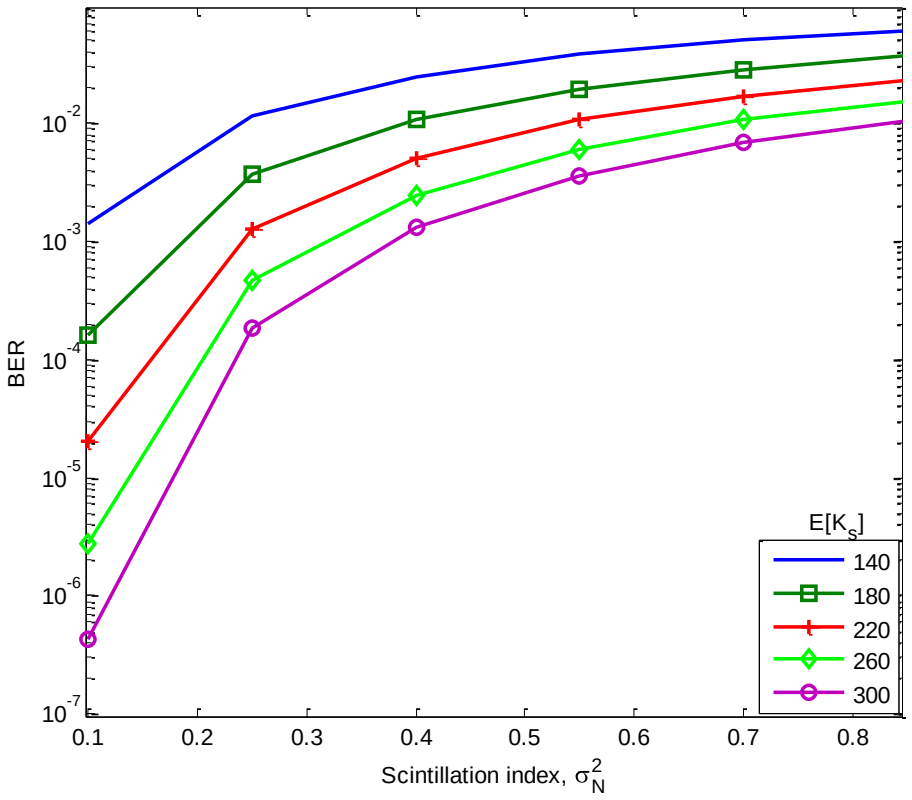

Fig. 5.8: Binary PPM BER as a function of scintillation index for K_{Bg} = 10; T_e = 300 K, ζ = 0.028, R_b = 155 Mbps and $\bar{g}$ = 150.

As expected, an increase in the atmospheric scintillation results in an increase in the required signal level to achieve a given BER. Increasing the signal strength can be used to minimise the scintillation effect at a low scintillation index, but as turbulence strength increases, it is observed that the BERs all tend towards a high BER asymptotic value.

5.4 Subcarrier Intensity Modulation

Subcarrier intensity modulation is a technique borrowed from the very successful multiple carrier radio frequency (RF) communications already deployed in applications such as digital television, local area networks (LANs), asymmetric digital subscriber line (ADSL), 4G communication systems and optical fibre communications [107, 108]. In optical fibre communication networks for example, the subcarrier modulation techniques have been commercially adopted in transmitting cable television signals and have also been used in conjunction with wavelength division multiplexing [109]. For the seamless integration of FSO systems into present and future networks, which already harbour subcarrier modulated (or multiple carrier) signals, the study of subcarrier modulated FSO is thus imperative. Other reasons for studying the subcarrier intensity modulated FSO systems include:

a) It benefits from already developed and evolved RF communication components such as stable oscillators and narrow filters [110].
b) It avoids the need for an adaptive threshold required by optimum performing OOK modulated FSO [99].
c) It can be used to increase capacity by accommodating data from different users on different subcarriers.

d) It has comparatively lower bandwidth requirement than the PPM.

There are however some challenges in the implementation of SIM, these are:

a) Relatively high average transmitted power due to:

(i) the optical source being ON during the transmission of both binary digits '1' and '0', unlike in OOK where the source is ON during the transmission of bit '1' only.

(ii) the multiple subcarrier composite electrical signal being the sum of the modulated sinusoids (i.e. dealing with both negative and positive values) requires a DC bias. This is to ensure that this composite electrical signal, that will eventually modulate the laser irradiance, is never negative. Increasing the number of subcarriers leads to increased average transmitted power, because the minimum value of the composite electrical signal decreases (becomes more negative) and the required DC bias therefore increases [111]. This factor results in poor power efficiency and places a bound on the number of subcarriers that can be accommodated when using multiple SIM.

b) The possibility of signal distortions due to: inherent laser non-linearity and signal clipping due to over-modulation.

c) Stringent synchronization requirements at the receiver side.

It is therefore worthwhile to mention that multiple-SIM is only recommended when the quest for higher capacity/users outweighs the highlighted challenges or where FSO is to be integrated into existing networks that already contain multiple RF carriers. Several methods have been researched and documented [111-113] to improve the poor power efficiency of SIM but not be considered in this thesis.

5.4.1 SIM generation and detection

In optical SIM links an RF subcarrier signal, $m(t)$, pre-modulated with the source data, $d(t)$, is used to modulate the intensity, P_T, of the optical source - a continuous wave laser diode. Figure 5.9 illustrates the system block diagram of a SIM-FSO with N subcarriers. The serial-to-parallel converter distributes the incoming data across the N-subcarriers. Each subcarrier carries a reduced symbol rate but the aggregate must be equal to the symbol rate of $d(t)$.

Another obvious possibility, not shown in the figure, is to have different users occupying the N different subcarriers. Prior to modulating the laser irradiance, the source data $d(t)$ are modulated onto the RF subcarriers. For the M-PSK subcarrier modulation shown in Fig. 5.9, the encoder maps each subcarrier symbol onto the symbol amplitude $\{a_{ic}, a_{is}\}_{i=1}^{N}$ that corresponds to the constellation in use. Since the subcarrier signal, $m(t)$, is sinusoidal, having both positive and negative values, a DC level b_0 is added to $m(t)$ before it is used to directly drive the laser diode – to avoid any signal clipping.

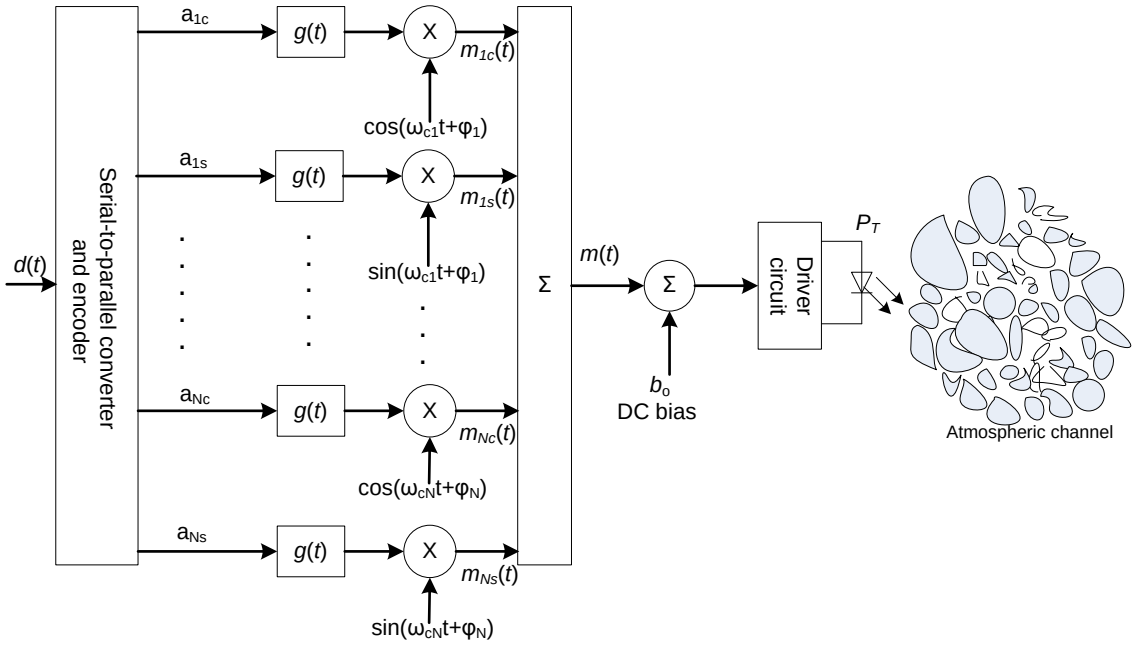

(a)

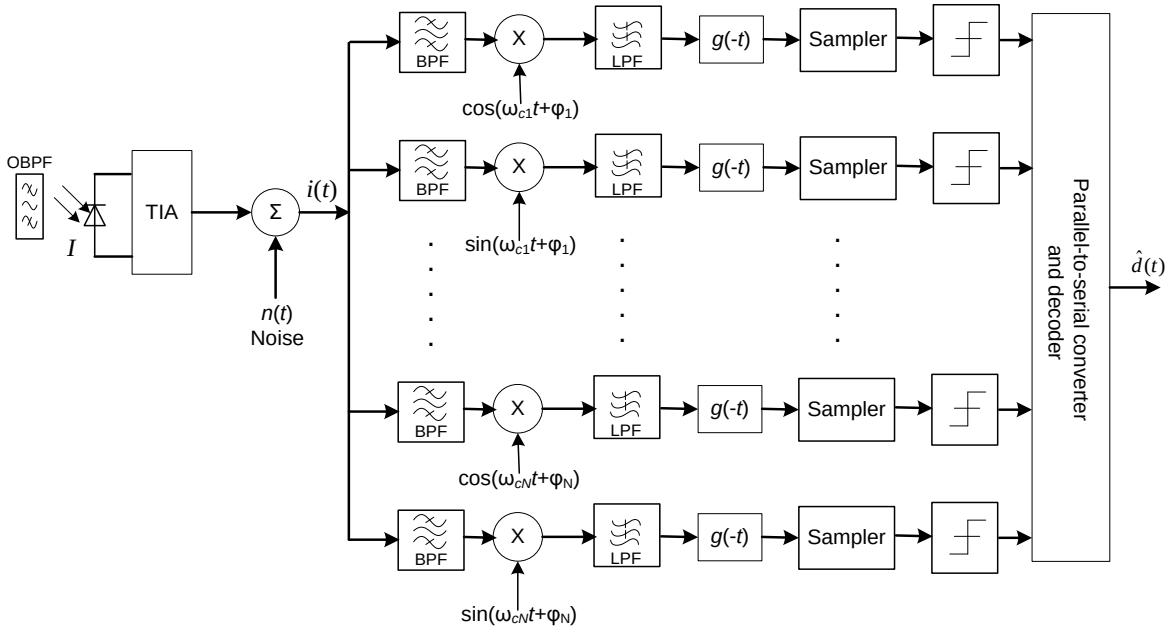

(b)

Fig. 5.9: Block diagram of SIM-FSO: (a) transmitter, and (b) receiver.

TIA – trans-impedance, OBPF – Optical band pass filter.

The following gives the general expression for $m(t)$ in the N-SIM-FSO system:

$$m(t) = \sum_{i=1}^{N} m_i(t) \tag{5.19}$$

During a symbol duration, each RF subcarrier signal is generally represented by:

$$m_i(t) = g(t)a_{ic}\cos(\omega_{ci}t + \varphi_i) + g(t)a_{is}\sin(\omega_{ci}t + \varphi_i) \tag{5.20}$$

where $g(t)$ is the pulse shaping function, and the subcarrier angular frequency and phase are represented by $[\omega_{ci}, \varphi_i]_{i=1}^{N}$. It follows that each subcarrier can be modulated by any standard RF digital/analogue modulation technique, such as QAM, M-PSK, M-FSK and M-ASK. Using direct detection at the receiver, the incoming optical radiation, P_R, is converted into an electrical signal, $i(t)$. This is followed by a standard RF demodulator to recover the transmitted symbol as shown in Fig. 5.9(b). By normalising the receiver area to unity and representing the received power by irradiance, I, the received signal can be modelled as:

$$i(t) = \Re I[1 + \xi m(t)] + n(t) \tag{5.21}$$

where the optical modulation index $\xi = \left|\frac{\mathrm{m(t)}}{i_B - i_{Th}}\right|$, as shown in Fig. 5.10.

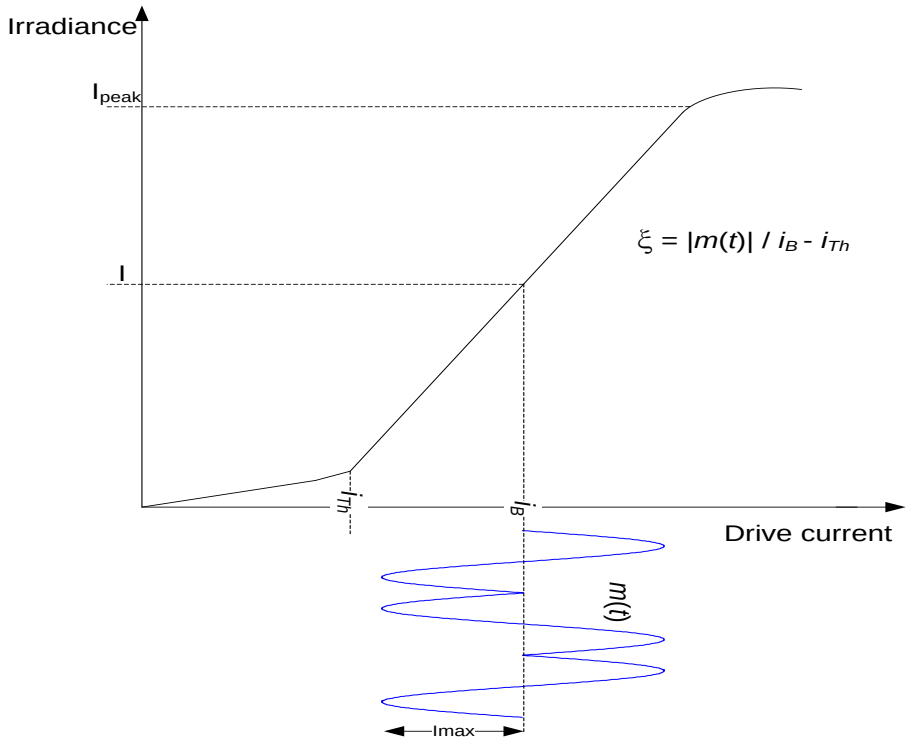

Fig. 5.10: Output characteristic of an optical source driven by a subcarrier signal showing optical modulation index.

The electrical band pass filter (BPF) with a minimum bandwidth of $2R_b$ performs the following functions: selection of the individual subcarrier for demodulation; reduction of the noise power; and suppression of any slow varying $\Re I$ component present in the received signal. For a subcarrier at ω_{ci} the received signal is:

$$i(t) = I_{comp} + Q_{comp} \tag{5.22}$$

where

$$I_{comp} = \Re I \xi g(t) a_{ic} \cos(\omega_{ci} t + \varphi_i) + n_I(t) \tag{5.23a}$$

$$Q_{comp} = -\Re I \xi g(t) a_{is} \sin(\omega_{ci} t + \varphi_i) + n_Q(t) \tag{5.23b}$$

$n_I(t)$ and $n_Q(t)$ are the independent additive white Gaussian noise (AWGN) with a zero mean and a variance σ^2. The quadrature components I_{comp} and Q_{comp} are down converted by the reference signals $\cos\omega_c t$ and $\sin\omega_c t$ respectively, and applied to the standard receiver architecture. The electrical low pass filters, which are part of the standard RF receiver, remove any out of band (unwanted) signals from the down converted signal and then pass it onto the decision circuit. In the case of phase shift keying modulated subcarrier, the decision circuit estimates the phase of the received signal and decides which symbol has been received. By adopting the approach in [114], the conditional BER expressions can be deduced. This error performance analysis is the subject of the next chapter. Table 5.1 presents a comparison of the three modulation techniques discussed in this chapter.

Table 5.1: Comparison of FSO modulation techniques

On-Off Keying	**Pulse Position Modulation**	**Subcarrier Intensity Modulation**
Simple to implement	Power efficient	Power inefficient
Synchronisation not required	Synchronisation required	Higher throughput
Adaptive threshold required in fading channels	Adaptive threshold not required in fading channels	Adaptive threshold not required in fading channels
Component nonlinearity not an issue	Component nonlinearity not an issue	Component nonlinearity an issue with multiple subcarrier
Suboptimal with fixed threshold	High bandwidth requirement	Benefits from advances in digital signal processing and matured RF components

5.5 Summary

The modulation techniques for FSO have been discussed. The error performance of both OOK and PPM techniques have been analysed in the presence of noise and atmospheric turbulence, and the effect of turbulence on the BER highlighted. For instance, an OOK-FSO system will require ~26 dB of SNR is needed to achieve a BER of 10^{-6} due to a very weak scintillation of strength $\sigma_I^2 = 0.25^2$, this however increases by over 20 dB as the scintillation strength increases to $\sigma_I^2 = 0.7^2$. It has also been shown that, in very weak turbulence situations, increased signal strength could be used to combat the channel fading. This approach however does not work beyond the very weak regime and alternative techniques, to be discussed in Chapter Seven, will have to be explored.

The choice of modulation technique involves a balance between simplicity, power efficiency and bandwidth efficiency. In view of the BER floor experienced in OOK, the poor bandwidth efficiency of PPM and the requisite slot and symbol synchronisation requirements, the focus in this work will be on SIM. However, this does suffer from poor power efficiency due to its high peak to average power ratio. In the next chapter, the performance of SIM-FSO in all turbulence regimes is presented.

Chapter Six

Subcarrier Intensity Modulated FSO in Atmospheric Turbulence Channels

6.1 Introduction

In this chapter, the error performance analysis of both single and multiple subcarriers based FSO systems in a turbulent atmospheric channel will be discussed. The chapter will also examine the intermodulation distortion caused by the optical source and ways of choosing the optical modulation in order to optimise the system error performance. The performance analysis in this chapter will be based on the direct detection with a PIN photo-detector. Since the FSO link is a line-of-sight (LOS) system with no

multipath, the inter-symbol interference (ISI) will therefore not be considered. Also the number of photons received is sufficient to justify the use of Gaussian statistics approximation for the detection process. The log normal, gamma-gamma and the negative exponential turbulence models discussed in Chapter Four will be used to describe received irradiance fluctuation for the short, medium to long and the very long span FSO systems, respectively.

Performance metrics are used to characterise, model and predict the behaviour of a system under different channel conditions. In addition to the generic bit-error-rate (BER) metric which models the fraction of bits received incorrectly in a digital communication system, the outage probability due to turbulence induced signal fading will also be considered. The outage probability is a measure of the probability that the instantaneous BER is greater that a pre-determined threshold level. This metric adequately describes the system performance including short duration deep fades, which the generic average BER might not capture.

6.2 SIM-FSO Performance in Log-normal Atmospheric Channels

Prior to the analytical estimation of the effect of scintillation on the system performance, the effect of turbulence and noise on a subcarrier signal constellation will first be presented. The simulation will be based on the block diagram of Fig. 5.9, with a QPSK modulated single subcarrier. The constellation at the input of the transmitter is shown in Fig. 6.1. The signal is then transmitted through the atmospheric channel with turbulence induced fading and noise. For this illustration, the electrical $SNR = (\xi \Re E[I])^2/\sigma^2$ is fixed, for instance, at 2 dB. The received constellation under a very low fading of $\sigma_l^2 = 0.001$ is shown in Fig. 6.2 while the effect of turbulence induced

fading is made evident by displaying in Fig. 6.3 the received constellation with a much higher fading with $\sigma_l^2 = 0.5$.

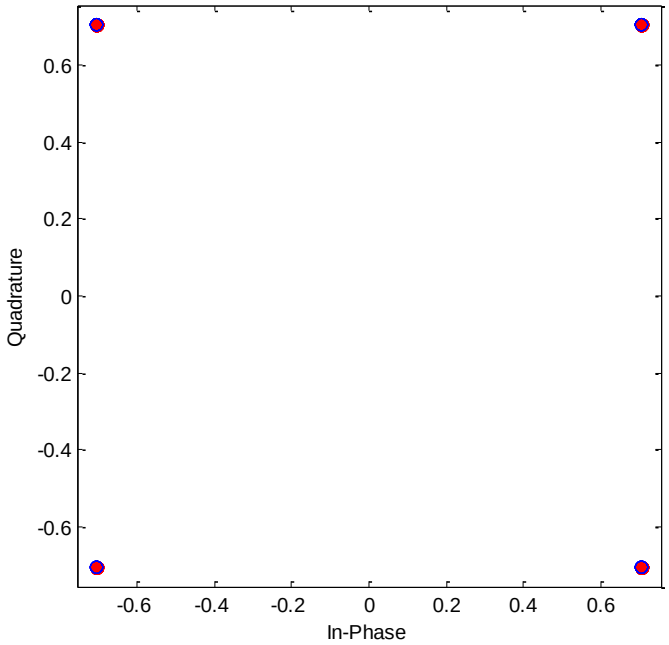

Fig. 6.1: QPSK constellation of the input subcarrier signal without noise and channel fading

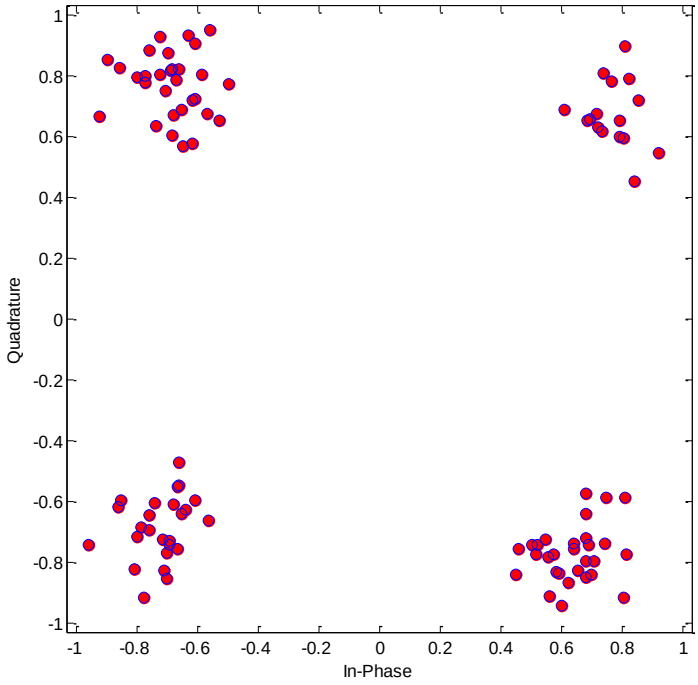

Fig. 6. 2: Received constellation of QPSK pre-modulated SIM-FSO with noise and channel fading for SNR = 2 dB and $\sigma_l^2 = 0.001$

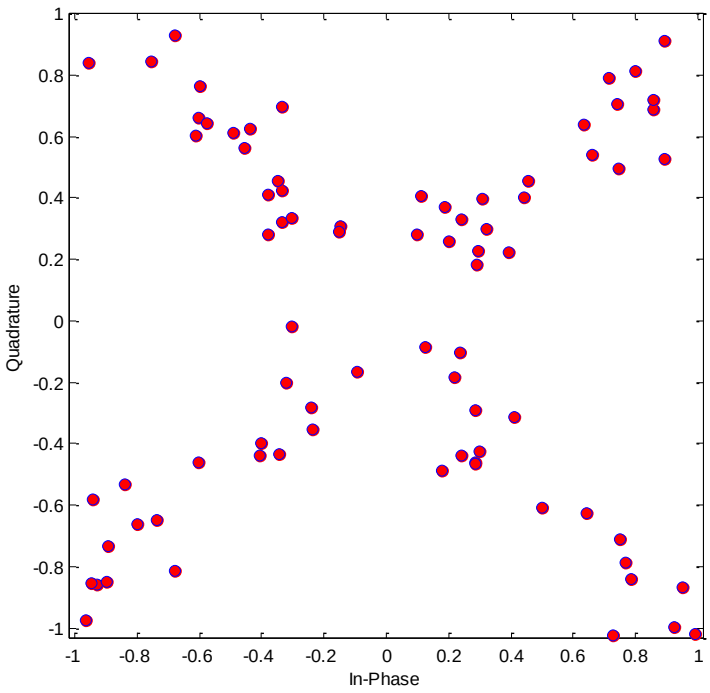

Fig. 6.3: Received constellation of QPSK pre-modulated SIM-FSO with noise and channel fading for SNR = 2 dB and $\sigma_l^2 = 0.5$

With a very low turbulence induced fading strength $\sigma_l^2 = 0.001$, the constellations form clusters that are clearly confined within their respective quadrants and the chance of erroneous demodulation is very low but as the turbulence level increases to $\sigma_l^2 = 0.5$, the confinement is lost and the constellation points become more staggered and move toward the centre of the plot. This apparently increases the chance of demodulation error during the symbol detection process. To quantify this observation, the bit error and the outage probabilities of SIM-FSO in atmospheric turbulence will now be presented.

6.2.1 Bit error probability analysis of SIM-FSO

In this section the BER analysis is presented in a clear but turbulent atmospheric channel, the turbulence induced irradiance fluctuation considered in this section is based on the log normal model of Section 4.2. A single BPSK pre-modulated subcarrier will first be considered and this will be followed by the *M*-PSK and then the DPSK modulated subcarrier.

6.2.1.1 *BPSK modulated subcarrier*

The result of this section will be for a single BPSK pre-modulated subcarrier $m(t) = g(t)a_c \cos(\omega_c t + \varphi)$, over a symbol duration, where $a_c = [-1,1]$ represents the data symbols '0' and '1'. By employing a coherent demodulation at the subcarrier level, the symbol-by-symbol detection is carried out by multiplying the received signal, given by equation 5.23(a), by a locally generated RF signal of the same frequency ω_c, and phase as follows. Without any loss of generality, the subcarrier phase is equated to zero, that is $\varphi = 0$. The coherent demodulator output, $i_D(t)$ is then given by:

$$\begin{aligned} i_D(t) &= I_{comp} \times \cos(\omega_c t) \\ &= \frac{\Re \xi I a_c g(t)}{2}[1 + \cos(2\omega_c t)] + n(t)\cos(\omega_c t) \end{aligned} \tag{6.1}$$

Passing $i_D(t)$ through a low pass filter with a bandwidth of $1/T$ suppresses the $\cos(2\omega_c t)$ term without distorting the information bearing signal. This also reduces the noise variance at the output of the coherent demodulator filter to half its value at the input of the demodulator. Equation (6.1) therefore reduces to:

$$i_D(t) = \frac{\Re \xi I a_c g(t)}{2} + n_D(t) \tag{6.2}$$

where the additive noise $n_D(t) \sim N(0, \sigma^2/2)$. Assuming an equiprobable data transmission such that $p(0) = p(1) = ½$, the probability of error conditioned on the received irradiance becomes:

$$\begin{aligned} P_{ec} &= p(1)p(e/1) + p(0)p(e/0) \\ &= 0.5[p(e/1) + p(e/0)] \end{aligned} \tag{6.3}$$

The marginal probabilities are given by:

$$p(e/1) = \int_{-\infty}^{0} \frac{1}{\sqrt{\pi\sigma^2}} \exp\left\{-\frac{(i_D(t) - \mathcal{K})^2}{\sigma^2}\right\} di_D(t) \tag{6.4a}$$

$$p(e/0) = \int_{0}^{\infty} \frac{1}{\sqrt{\pi\sigma^2}} \exp\left\{-\frac{(i_D(t) + \mathcal{K})^2}{\sigma^2}\right\} di_D(t) \tag{6.4b}$$

Where $\mathcal{K} = I\Re\xi/2$ and $g(t) = 1$ for $0 \leq t \leq T$ and zero elsewhere. Here both binary symbols '1' and '0' are affected by the irradiance fluctuation since the optical source is on during the transmission of both data symbols '1' and '0'. This is in contrast to the OOK signalling technique where irradiance fluctuation only affects the data symbol '1'. Based on the antipodal nature of (6.2), the decision threshold level can hence be fixed at the zero mark. This zero level threshold is irradiance independent and hence not affected by the irradiance fluctuation caused by the atmospheric turbulence. From the foregoing and the apparent symmetry of (6.4), the BER conditioned on the received irradiance can now be written as:

$$\begin{aligned} P_{ec} &= \int_{0}^{\infty} \frac{1}{\sqrt{\pi\sigma^2}} \exp\left\{-\frac{(i_D(t) + \mathcal{K})^2}{\sigma^2}\right\} di_D(t) \\ &= 0.5 \operatorname{erfc}(\mathcal{K}/\sigma) = \mathrm{Q}\left(\frac{\mathcal{K}\sqrt{2}}{\sigma}\right) \end{aligned} \tag{6.5}$$

At the input of the subcarrier coherent demodulator, the electrical SNR per bit is given by:

$$\gamma(I) = \frac{(\xi \Re I)^2 P_m}{\sigma^2} \tag{6.6}$$

where $P_m = \frac{A^2}{2T}\int_0^T g^2(t)dt$, from which $\sqrt{\gamma(I)} = \sqrt{2}\,\mathcal{K}/\sigma$. Equation (6.6) can now be expressed in terms of the SNR at the demodulator input as:

$$P_{ec} = \mathrm{Q}\left(\sqrt{\gamma(I)}\right) \tag{6.7}$$

The unconditional probability P_e, is obtained by averaging (6.7) over the log normal irradiance fluctuation statistics to obtain the following:

$$P_e = \int_0^\infty P_{ec} p(I) dI \tag{6.8a}$$

$$P_e = \int_0^\infty \mathrm{Q}(\gamma(I)) \frac{1}{I\sqrt{2\pi\sigma_l^2}} \exp\left\{-\frac{[\ln I/I_0 + \sigma_l^2/2]^2}{2\sigma_l^2}\right\} dI \tag{6.8b}$$

A closed form solution of equation 6.8(b) does not exist and using the numerical integration could result in truncating its upper limit. Also, the presence of the argument of the Q-function at the lower limit of the Q-function integral always poses analytical problems [115]. By combining an alternative representation of the Q-function given by (6.9) with the Gauss-Hermite quadrature integration approximation of (6.10), the analytical difficulty involved solving (6.8) can be circumvented.

$$\mathrm{Q}(y) = \frac{1}{\pi}\int_0^{\pi/2} \exp\left(-\frac{y^2}{2\sin^2(\theta)}\right) d\theta \qquad \text{for } y > 0 \tag{6.9}$$

$$\int_{-\infty}^{\infty} f(x)\exp(-x^2)dx \cong \sum_{i=1}^{n} w_i f(x_i) \tag{6.10}$$

where $[w_i]_{i=1}^{n}$ and $[x_i]_{i=1}^{n}$, whose values are given in Appendix A, are the weight factors and the zeros of an n^{th} order Hermite polynomial, $He_n(x)$ [116]. The degree of accuracy of (6.10) depends on the order n of the Hermite polynomial. By invoking a change of variable, $y = \frac{\ln(I/I_0)+\sigma_l^2/2}{\sqrt{2}\sigma_l}$ in 6.8(b) and combining this with (6.9) and (6.10), the unconditional BER given by 6.8(b) can be reduced to the following form:

$$P_e \cong \frac{1}{\pi}\int_{0}^{\pi/2} \frac{1}{\sqrt{\pi}}\sum_{i=1}^{n} w_i \exp\left(-\frac{K_0 \exp\left(2K_1\left[\sqrt{2}\sigma_l x_i - \sigma_l^2/2\right]\right)}{2\sin^2(\theta)}\right) d\theta \tag{6.11}$$

$$P_e \cong \frac{1}{\sqrt{\pi}}\sum_{i=1}^{n} w_i \mathrm{Q}\left(\sqrt{K_0}\exp\left(K_1\left[\sqrt{2}\sigma_l x_i - \sigma_l^2/2\right]\right)\right) \tag{6.12}$$

The values of K_1 and K_0 are as given in Table 6.1 for different noise limiting conditions.

Table 6.1: Values of K_1 and K_0 for different noise limiting conditions

	Noise Limiting Conditions			
	Quantum Limit	*Thermal Noise*	*Background Noise*	*Thermal and Background Noise*
K_0	$\frac{\xi^2 \Re I_0 P_m}{2qR_b}$	$\frac{(\xi\Re I_0)^2 P_m R_L}{4kT_e R_b}$	$\frac{(\xi I_0)^2 \Re P_m}{2qR_b(I_{sky}+I_{sun})}$	$\frac{(\xi\Re I_0)^2 P_m}{(\sigma_{Bg}^2+\sigma_{Th}^2)}$
K_1	0.5	1	1	1

In Table 6.1, R_b represents the symbol rate. The BER plots, using both the approximation given by (6.12) and the numerical simulation of the exact solution given by 6.8(b) against the normalised SNR $= (\xi\Re E[I])^2/\sigma^2$ are illustrated in Fig. 6.4. These

results hint that using the 20th order Gauss Hermite approximation gives an accurate representation of the exact BER. The Gauss Hermite integration solution of the BER is however preferred for its simplicity and compactness.

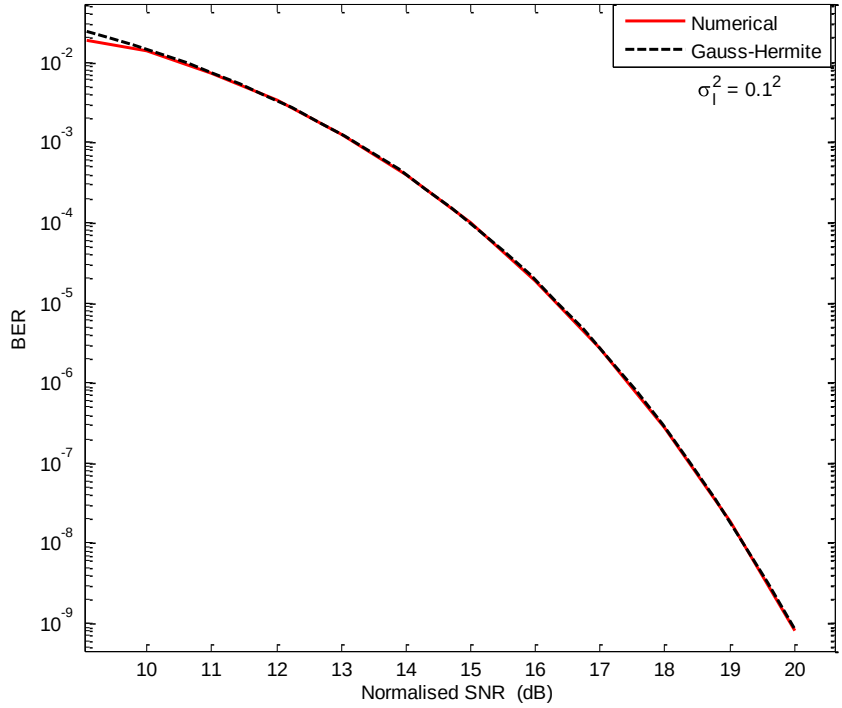

Fig. 6.4: BER against the normalised SNR using numerical and 20th order Gauss-Hermite integration methods in weak atmospheric turbulence for $\sigma_I^2 = 0.1^2$.

In order to keep the optical source (laser) within its linear dynamic range and avoid signal clipping distortion, the condition $|\xi m(t)| \leq 1$ must always hold. For a given value of ξ, this places an upper bound on the amplitude of each subcarrier. The BER given by (6.12) is plotted against the normalised SNR for different noise limiting conditions in Fig. 6.5, based on the simulation parameters given in Table 6.2. The figure illustrates clearly that for an FSO link with a suitable optical BPF and a narrow FOV detector, the system performance is limited by thermal noise. Moreover, under this thermal noise limited condition, the SIM-FSO still requires about additional 30 dB of SNR compared with the theoretical quantum limit.

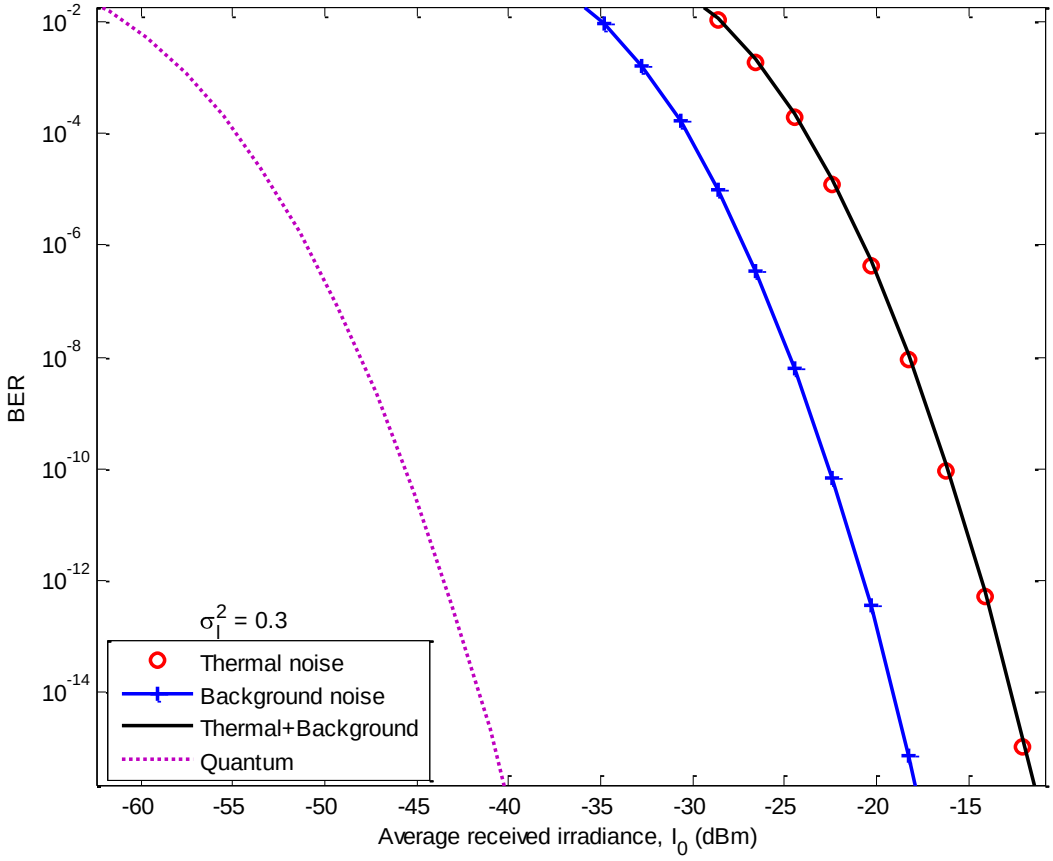

Fig. 6.5: The BER against the average received irradiance in weak turbulence under different noise limiting conditions for R_b = 155 Mpbs and σ_I^2 = 0.3.

Table 6.2: Simulation parameters

Parameter	**Value**
Symbol rate R_b	155 Mbps
Spectral radiance of the sky $N(\lambda)$	10^{-3} W/cm^{2}μmSr
Spectral radiant emittance of the sun $W(\lambda)$	0.055 W/cm^{2}μm
Optical band-pass filter bandwidth $\Delta\lambda$ @ λ = 850 nm	1 nm
PIN photodetector field of view (FOV)	0.6 rad
Radiation wavelength λ	850 nm
Number of subcarriers N	1
Link range L	1 km
Index of refraction structure parameter C_n^2	0.75×10^{-14} m$^{-2/3}$
Load resistance R_L	50 Ω
PIN photodetector responsivity $\Re$	1
Operating temperature T_e	300 K
Optical modulation index ξ	1

6.2.1.2 *M-ary PSK modulated subcarrier*

Here the data symbols which comprise of $\log_2 M$ binary digits are mapped onto one of the M available phases on each subcarrier signal, $m(t)$. Based on the subcarrier coherent demodulation and by following the analytical approach given in [114], the following conditional BER expressions are obtained:

$$P_{ec} \approx \frac{2}{\log_2 M} \mathrm{Q}\left(\sqrt{(\log_2 M)\gamma(I)}\sin(\pi/M)\right) \quad \text{for } M\text{-PSK, } M \geq 4 \tag{6.13a}$$

$$P_{ec} = \frac{2(1-1/\sqrt{M}}{\log_2 M} \mathrm{Q}\left(\sqrt{\frac{3\log_2 M\,\gamma(I)}{2(M-1)}}\right) \quad \text{for } M\text{-QAM, } \log_2 M \text{ even} \tag{6.13b}$$

The unconditional BER, P_e, is thus obtained in a similar fashion, by averaging the conditional bit error rate over the atmospheric turbulence statistics. The resulting BER expression (6.14) for M-PSK has no closed form solution and can only be evaluated numerically.

$$P_e \cong \frac{2}{\log_2 M} \int_0^\infty \mathrm{Q}\left(\sqrt{\gamma(I)\log_2 M}\sin(\pi/M)\right) p(I)dI \tag{6.14}$$

Whenever a subcarrier coherent detection is used, there is always an ambiguity associated with the estimation of the absolute phase of the subcarrier signal [114]. This poses an implementation challenge for the subcarrier coherent demodulation based systems, this can however be solved by considering a differential phase shift keying (DPSK) based SIM-FSO system as discussed below.

6.2.1.3 *DPSK modulated subcarrier*

This modulation scheme is the most suitable when the absolute phase estimation needed for the subcarrier coherent demodulation is not feasible or too complex to realise. The DPSK pre-modulated SIM-FSO is demodulated by comparing the phase of the received signal in any signalling interval with the phase of the signal received in the preceding signalling interval [114], as shown in Fig. 6.6 for a single subcarrier FSO system. Accurate demodulation of the present data symbol thus depends on whether the preceding symbol has been correctly demodulated or not. The demodulation of DPSK based SIM-FSO is feasible during atmospheric turbulence because the turbulence coherence time, which is in the order of milliseconds, is far greater than the typical duration of two consecutive data symbols. This implies that the channel properties are fixed during a minimum of two symbol durations – a pre-requisite for non-coherent demodulation of DPSK subcarrier signal.

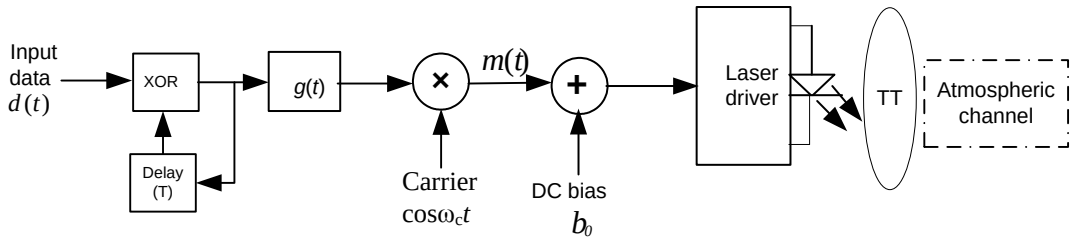

(a)

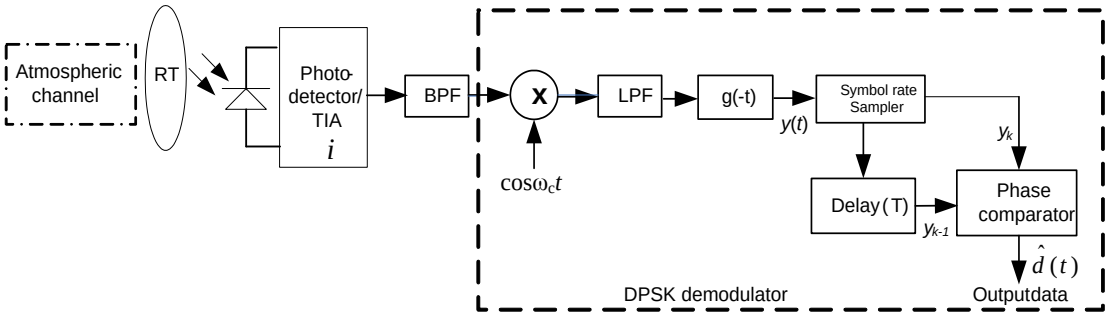

(b)

Fig. 6.6: Block diagram of an FSO link employing DPSK modulated SIM; (a) transmitter and (b) receiver.

TIP-trans-impedance amplifier; TT-Transmitter telescope; RT-Receiver telescope.

The conditional BER of the DPSK pre-modulated subcarrier is given by [114, 117]:

$$P_{ec} = 0.5\exp(-0.5\gamma(I)) \tag{6.15}$$

In the presence of scintillation, the following unconditional BER, P_e, is derived using the Gauss-Hermite quadrature integration approximation of Section 6.2.1.1 as:

$$P_e = \int_0^{\infty} 0.5\exp\big(-\gamma(I)\big)\, p(I) dI \tag{6.16}$$

$$P_e \cong \frac{1}{2\sqrt{\pi}} \sum_{i=1}^{n} w_i \exp\big(-K^2 \exp\big[x_i 2\sqrt{2}\sigma_l - \sigma_l^2\big]\big) \tag{6.17}$$

where $= \Re\xi I_0/2\sqrt{\sigma^2}$. In Fig. 6.7, the BER of SIM-FSO based on different modulation techniques on the subcarrier are compared at a scintillation level of $\sigma_l^2 = 0.5^2$.

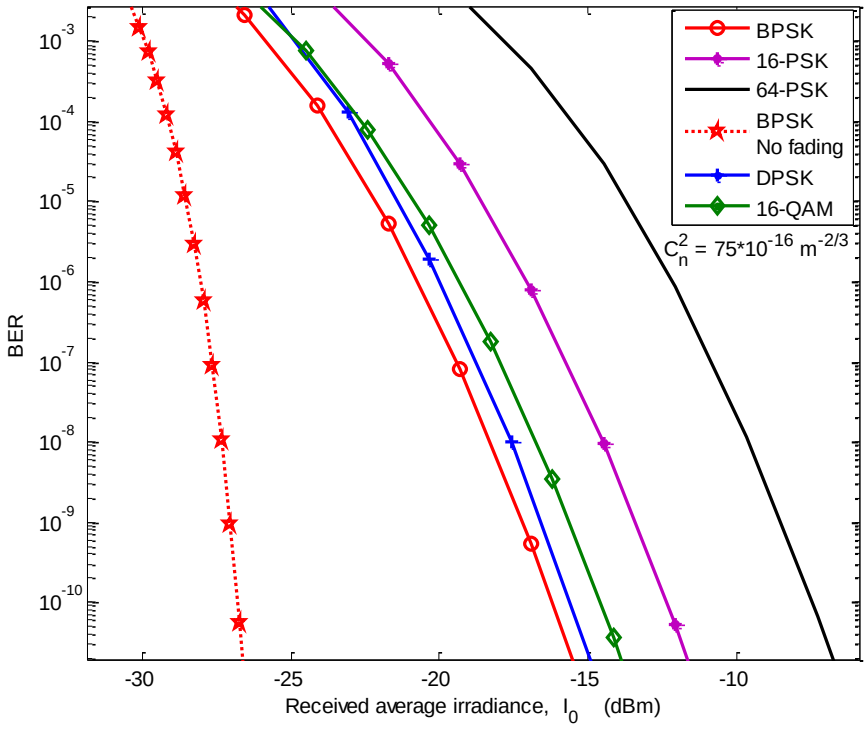

Fig. 6.7: BER against the received irradiance for SIM-FSO with different subcarrier modulation techniques in weak atmospheric turbulence for $\sigma_l^2 = 0.3$, $\lambda = 850$ nm and link range = 1 km.

The performance in a turbulence free channel is included in the figure for the estimation of turbulence induced fading penalty. The figure shows clearly the performance superiority of BPSK modulated SIM in terms of the amount of SNR required to achieve a given BER. Due to atmospheric turbulence induced channel fading, a BPSK pre-modulated SIM-FSO system will incur a power penalty of ~5 dB at a BER of 10^{-6}, the penalty rises to ~10 dB when the error performance level is raised to a BER of 10^{-9}. This penalty is higher for other modulation techniques as shown in the figure. The *M*-PSK (with $M \geq 4$) modulated subcarrier is known to be more bandwidth efficient [114], while the DPSK is advantageous in that it does not require absolute phase estimation but both are not as power efficient as the BPSK-SIM. The choice of modulation technique at the subcarrier level therefore depends on the application at hand and requires a compromise between simplicity, power and bandwidth efficiencies.

6.2.1.4 *Multiple SIM performance analysis*

The use of multiple subcarriers is a viable way of increasing system throughput/capacity. To archive this, different data/users are pre-modulated on different subcarrier frequencies. These are then aggregated and the resulting composite signal used to modulate the intensity of the optical source. For a subcarrier system with N subcarrier signals operating at different frequencies, the inherent non-linearity of the optical source will result in the transfer of energy among the subcarrier frequencies (i.e. the inter-modulation distortion (IMD)). The IMD potentially results in a reduced SNR as it contributes to the amount of unwanted signals within the frequency band of interest. The detailed discussion of the IMD due to optical source non-linearity will be covered in Section 6.5. In the mean time, the multiple subcarriers system will be examined by assuming an ideal optical source with no reference to the IMD and the clipping distortion.

By definition, the modulation index/depth is given by:

$$\xi \triangleq \frac{|m(\mathrm{t})|}{i'_{\mathrm{B}}} = \sum_{j=1}^{N} \frac{\left|A_j g(t) \cos\left(\omega_{cj} + \theta_j\right)\right|}{i'_{\mathrm{B}}} \tag{6.18}$$

where $i'_B = i_B - i_{Th}$ as already shown in Fig. 5.10. The peak value of the composite signal $m(t)$, occurs when all the individual subcarrier amplitudes add up coherently, that is:

$$\xi = \sum_{j=1}^{N} \left|\frac{A_j}{i'_B}\right| = \sum_{j=1}^{N} \xi_j = N\xi_{sc} \tag{6.19}$$

In (6.19), all the subcarrier signals have been assumed to have the same individual modulation depth $\xi_{sc} = \xi/N$. Since the SNR on each subcarrier is proportional to the square of the modulation depth, there exists at least a loss of $20 \log N$ (dB) in electrical SNR (equivalent to $10 \log N$ (dB) optical power reduction) on each subcarrier due to the presence of *N* subcarrier signals with non-overlapping frequencies.

The BER plots of a BPSK pre-modulated subcarrier with different numbers of subcarriers are shown in Fig. 6.8. The graph is obtained by replacing ξ with ξ_{sc} in (6.12). For example, the SNR required to achieve a BER of 10^{-6} with 5 subcarriers is ~40 dB in an atmospheric channel with a fading strength of $\sigma_l^2 = 0.3$. This increases to ~46 dB with 10 subcarriers under the same channel conditions, depicting a $20 \log N$ (dB) increment over the SNR required by a single subcarrier FSO system.

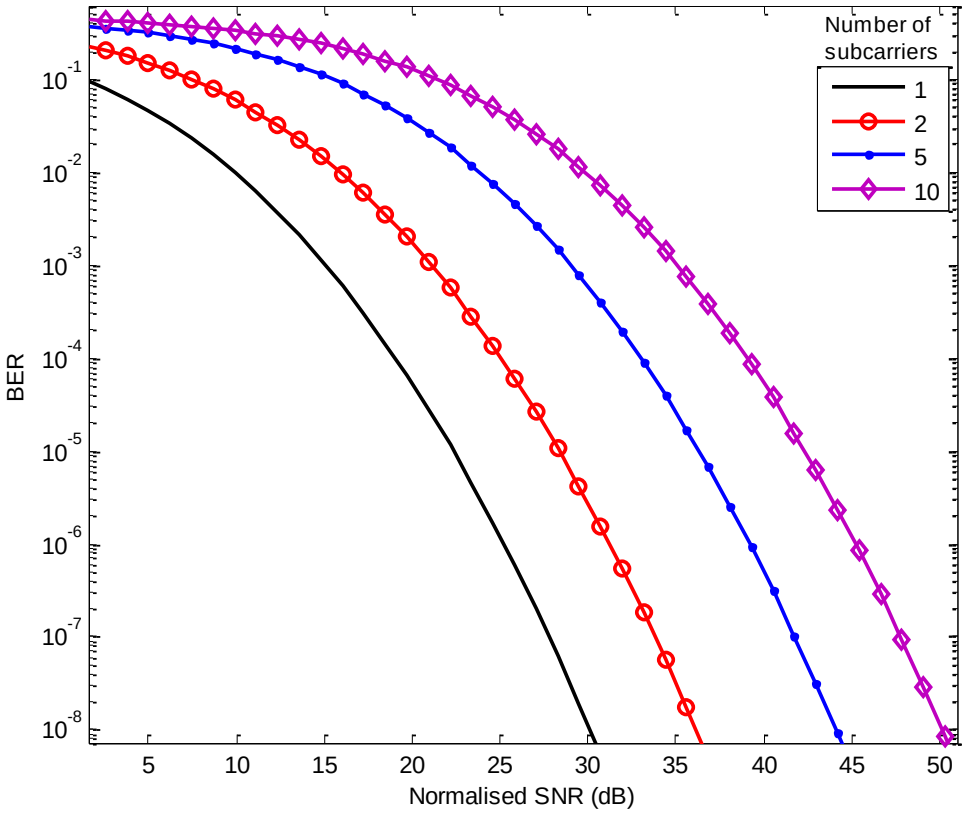

Fig. 6.8: BER against the normalised SNR for multiple subcarriers FSO system in weak atmospheric turbulence for $N = [1,2,5,10]$ and $\sigma_l^2 = 0.3$.

In Fig. 6.9, these SNR values required to attain a BER of 10^{-6} are plotted against the number of subcarriers for turbulent atmospheric channels of different fading strengths. This shows explicitly that for a given BER value, the SNR values increase with an increase in both number of subcarriers and the fading strength. Based on the foregoing therefore, the multiple SIM-FSO is only recommended whenever the quest for increased throughput/capacity outweighs its accompanying power penalty.

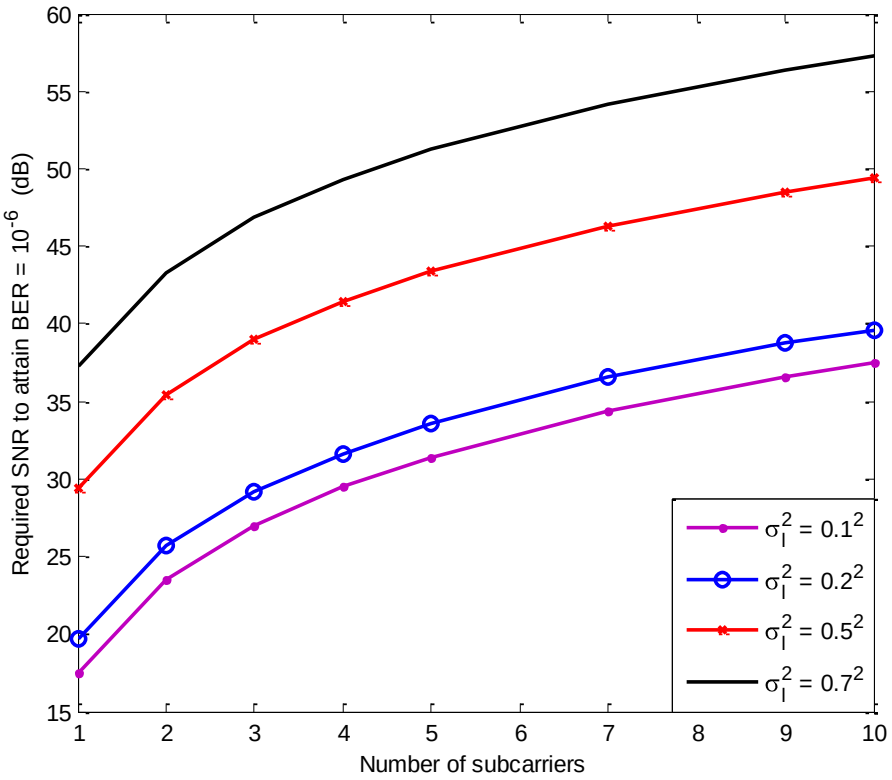

Fig. 6.9: SNR required to attain a BER of 10^{-6} against the number of subcarriers for BPSK modulated SIM-FSO system with $\sigma_l = [0.1, 0.2, 0.5, 0.7]$.

6.2.2 Outage probability in log-normal atmospheric channels

The outage probability is another metric for quantifying the performance of communication systems in fading channels. A system with an adequate average BER can temporarily suffer from increases in error rate due to deep fades and this 'short outages' is not adequately modelled by the average BER [44]. An alternative performance metric therefore is the probability of outage due to the presence of atmospheric turbulence, which is defined as $P_e > P_e^*$, where P_e^* is a predetermined threshold BER. This is akin to finding the probability that the SNR, $\gamma(I)$, that corresponds to P_e is lower than the threshold SNR (denoted by γ^*) that corresponds to P_e^*. That is:

$$P_{Out} = P(P_e > P_e^*) \equiv P(\gamma(I) < \gamma^*) \tag{6.20}$$

where $\gamma^* = (\Re\xi I_0)^2/2\sigma^2$ is the average SNR in the absence of atmospheric turbulence for a given noise level. If a parameter *m*, here called 'power margin', is introduced to account for the extra power needed to cater for turbulence induced signal fading, then, the outage probability is derived as follows:

$$\begin{aligned} P_{Out} = P(m\gamma(I) < \gamma^*) &= \int_0^{I_0/m} \frac{1}{I\sqrt{2\pi\sigma_l^2}} \exp\left\{-\frac{\left(\ln I/I_0 + \sigma_l^2/2\right)^2}{2\sigma_l^2}\right\} dI \\ &= \mathrm{Q}\left(\frac{1}{\sigma_l}\ln m - \frac{\sigma_l}{2}\right) \end{aligned} \tag{6.21}$$

Invoking the Chernoff upper bound, $\mathrm{Q}(x) \leq 0.5\exp(-x^2/2)$, on equation (6.21) gives an upper bound value for the outage probability, from this an approximate power margin, *m*, needed to obtain P_{Out} can be obtained as:

$$m \approx \exp\left(\sqrt{-2\ln 2P_{Out}\sigma_l^2} + \sigma_l^2/2\right) \tag{6.22}$$

This extra power needed to obtain a given outage probability is depicted in Fig. 6.10 at various levels of irradiance fluctuation. For example, to achieve an outage probability of 10^{-6}, about 35 dBm of extra power is needed at $\sigma_l^2 = 0.2^2$. This will rise to ~43 dBm and 48 dBm when the irradiance strength is $\sigma_l^2 = 0.5^2$ and $\sigma_l^2 = 0.7^2$, respectively. The extra margin can also be viewed as the penalty introduced by the atmospheric turbulence and to reduce it, diversity techniques will be considered in Chapter Seven.

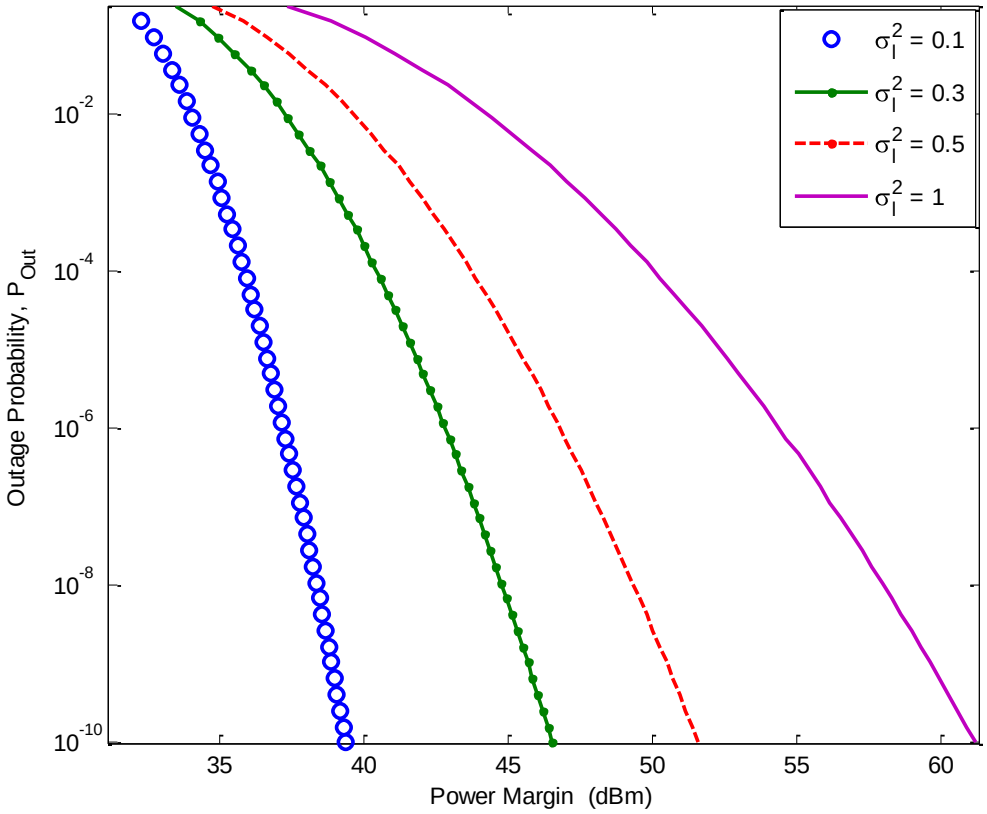

Fig. 6.10: Outage probability against the power margin for a log-normal turbulent atmospheric channel for $\sigma_l^2 = [0.1, 0.3, 0.5, 1]$.

6.3 SIM-FSO Performance in Gamma-Gamma and Negative Exponential Atmospheric Channels

To obtain the unconditional BER in a gamma-gamma turbulent atmospheric channel, the irradiance fluctuation statistics in the previous section is replaced appropriately by the gamma-gamma pdf. For a BPSK pre-modulated subcarrier, the unconditional BER now becomes:

$$P_e = \int_0^\infty \mathrm{Q}\left(\sqrt{\gamma(I)}\right) \frac{2(\alpha\beta)^{(\alpha+\beta)/2}}{\Gamma(\alpha)\Gamma(\beta)} I^{\left(\frac{\alpha+\beta}{2}\right)-1} \mathrm{K}_{\alpha-\beta}\left(2\sqrt{\alpha\beta I}\right) dI \qquad 6.23)$$

This BER expression can only be evaluated numerically as it does not have a closed form solution. The values of the parameters α and β, which are used to describe the turbulence strength, are as given in Table 6.3.

Table 6.3: Fading strength parameters for gamma-gamma turbulence model

	Turbulence Regime		
Parameter	Weak	Moderate	Strong
σ_l^2	0.2	1.6	3.5
α	11.6	4.0	4.2
β	10.1	1.9	1.4

In the limit of strong turbulence, that is, in the saturation regime and beyond, the BER is obtained by replacing the pdf in the conditional BER by the fully developed speckle pdf given by (4.38). By applying the alternative representation of Q(.) given by (6.9) the unconditional BER in the fully developed speckle regime is derived as:

$$P_e = \frac{1}{\pi I_0} \int_0^{\pi/2} \int_0^{\infty} \exp\left(-\frac{(\xi \Re I)^2}{4\sigma^2 \sin^2 \vartheta} - \frac{I}{I_0} \right) dI d\vartheta \tag{6.24}$$

The multiple integration involved in (6.24) can be conveniently circumvented by invoking equation 3.322.2 given in [118]. This reduces the BER expression P_e, to the following:

$$P_e = \frac{1}{\pi} \int_0^{\pi/2} \sqrt{\pi \mathcal{K}_o(\vartheta)} \exp(\mathcal{K}_0(\vartheta)) \operatorname{erfc}\left(\sqrt{\mathcal{K}_0(\vartheta)}\right) d\vartheta \tag{6.25}$$

where $\mathcal{K}_0(\vartheta) = (\sigma \sin(\vartheta)/\xi \Re)^2$ and erfc (.) is the complementary error function. The following upper bound, given by (6.26), is then obtained by maximising the integrand with the substitution of $\vartheta = \pi/2$ in (6.25).

$$P_e \leq \sqrt{\pi \mathcal{K}_0}\, \exp(\mathcal{K}_0)\, \mathrm{Q}\left(\sqrt{2\mathcal{K}_0}\right) \tag{6.26}$$

where $\mathcal{K}_0 = (\sigma / \xi\Re)^2$. From these BER expressions, the error performance of the system can be predicted for any given value of SNR and turbulence strength (or link range). The numerical simulations of the BER expressions (6.23), (6.25) and the upper bound (6.26) are shown in Fig. 6.11, where the P_e is plotted against the normalised SNR under different turbulence regimes.

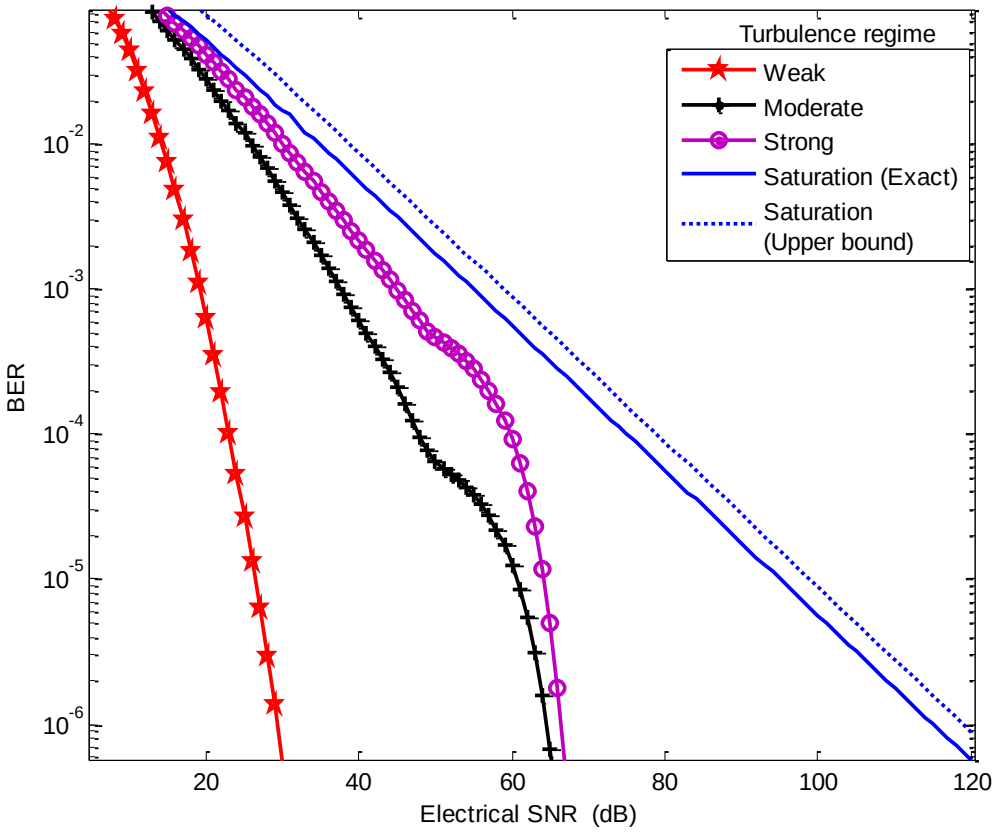

Fig. 6.11: BER performance against the normalised electrical SNR across all of turbulence regimes based on gamma-gamma and negative exponential modes.

For instance, to achieve a BER of 10^{-6} in a weak atmospheric turbulence, the required SNR is ~29 dB and this rises to ~65 dB and ~67 dB, respectively for moderate and intermediate regimes. While in the saturation regime, a staggering ~115 dB (the upper bound value is 4 dB higher) is required to achieve the same level of error performance (i.e. BER of 10^{-6}). Achieving a BER lower than 10^{-6} in the saturation regime requires a phenomenal increase in SNR as seen in Fig. 6.11. It is noteworthy that the normalised SNR is in the electrical domain and it is based on the average received irradiance, $E[I]$. Also the 'kinks' observed in the curves for strong and moderate turbulence are due to the numerical integration process.

On order to compare the error performance BPSK-SIM with an OOK modulated FSO system of the same average transmitted optical power, the unconditional BER of the OOK-FSO is modified to become:

$$P_e = 0.5\left[\int_{i_{th}}^{\infty} \frac{1}{\sqrt{\pi\sigma^2}} \exp(-i^2/\sigma^2)di + \int_0^{\infty}\int_0^{i_{th}} \frac{1}{\sqrt{\pi\sigma^2}} \exp\left[-\frac{(i-2\Re I)^2}{\sigma^2}\right] p(I)didI\right] \qquad (6.27)$$

In Fig. 6.12, the BER performances of the OOK system employing adaptive (optimum) and fixed threshold values of 0.05 and 0.8 are shown alongside that of BPSK-SIM in a weak turbulent atmospheric fading. Although the optimum OOK is marginally superior to BPSK-SIM under the stated conditions, as it requires 1.6 dB electrical SNR less at a BER of 10^{-6}, it does require an accurate knowledge of both the additive noise and fading levels to achieve this performance. With the threshold fixed at say 0.05, the OOK requires about 7 dB electrical SNR more than BPSK-SIM at a BER of 10^{-6}. Also, the BER performance of OOK with a fixed threshold level exhibits a BER floor as shown in Fig. 2(b) for i_{th} = 0.8 and in the previous work by [8]. The SIM is therefore recommended in atmospheric turbulence channels as against the fixed threshold OOK currently used in commercial terrestrial FSO systems.

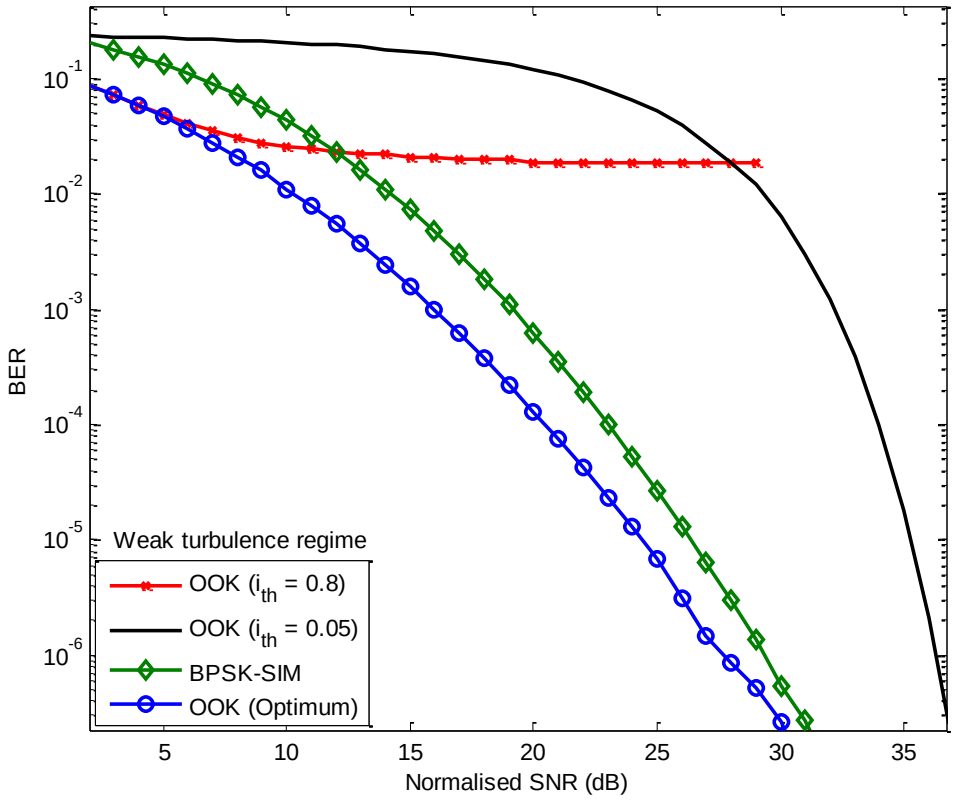

Fig. 6.12: Error performance of BPSK SIM and OOK with fixed and adaptive threshold based FSO in weak turbulence regime modeled using gamma-gamma distribution.

6.3.1 Outage probability in negative exponential model atmospheric channels

By following the approach of Section 6.2.2, the outage probability in the fully developed speckle is obtained as follows:

$$P_{Out} = P(m\gamma(I) < \gamma^*) = \int_0^{I_0/m} \frac{1}{I_0} \exp\left(-\frac{I}{I_0}\right) dI \qquad 6.28)$$

From (6.28) the power margin *m*, needed to achieve a given P_{Out} saturation regime is as given by (6.29). This is plotted in Fig. 6.13, alongside equation (6.22) with $\sigma_l^2 = 0.5$, which represents the outage probability in weak atmospheric turbulence. A comparison

of the results in this figure reveals that, the power margin required to achieve a P_{Out} of 10^{-6} in the fully developed speckle regime is about 40 dB higher than that required in the weak turbulence regime with $\sigma_l^2 = 0.5$, and this will increase as the required outage probability level is reduced to below 10^{-6}.

$$m = [-\ln(1 - P_{Out})]^{-1} \tag{6.29}$$

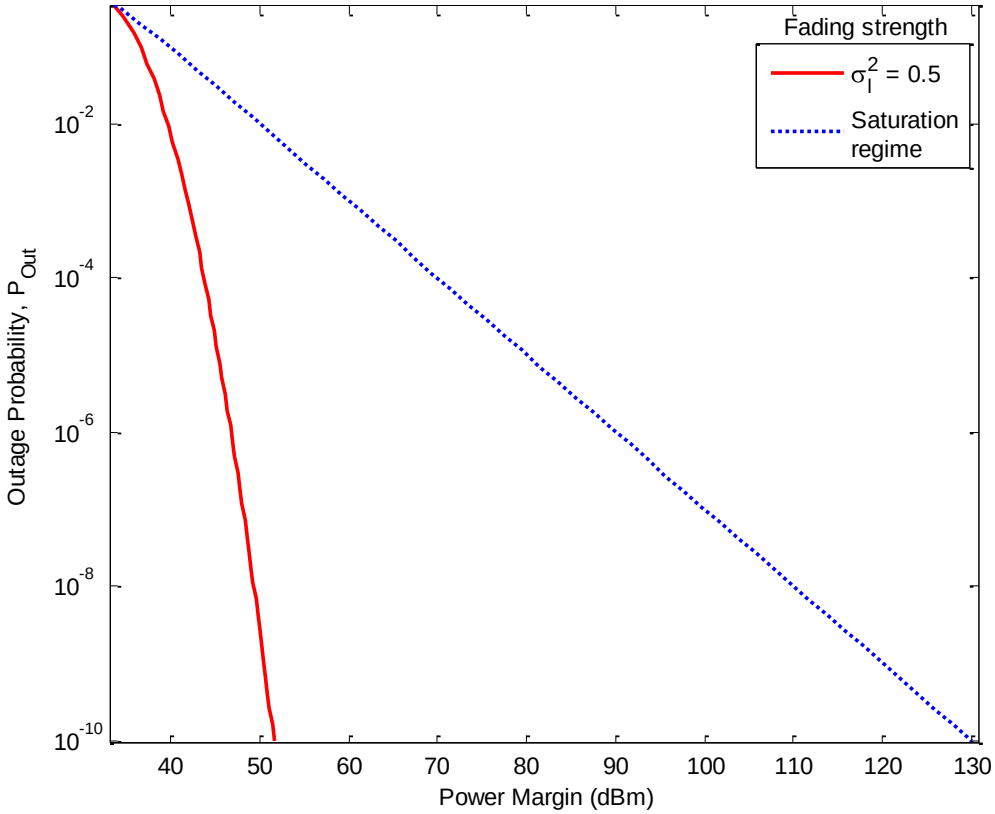

Fig. 6.13: The outage probability against the power margin in saturation and weak turbulence regimes for $\sigma_l^2 = 0.5$.

The prohibitive power required in the saturation regime suggests that the establishment of a reliable communication link in this regime is impossible unless the fading effect due to turbulence is mitigated or compensated for.

6.4 Atmospheric Turbulence Induced Penalty

In this section, the additional power required, due to the presence of turbulence induced channel fading, to achieve a given level of performance will be examined. Without any loss of generality, the result here will be based on the log normal turbulence model, and the BPSK modulated subcarrier. This can however be extended to other turbulence models and modulation schemes in a straight forward manner. In Fig. 6.14, the BER is plotted as a function of normalised for different levels of atmospheric turbulence. As an example, to achieve a BER of 10^{-6} in a channel characterised by $\sigma_l^2 = 0.1$ a SNR of about 24 dB will be required. This increases to ~37 dB as the fading strength increases to $\sigma_l^2 = 0.5$.

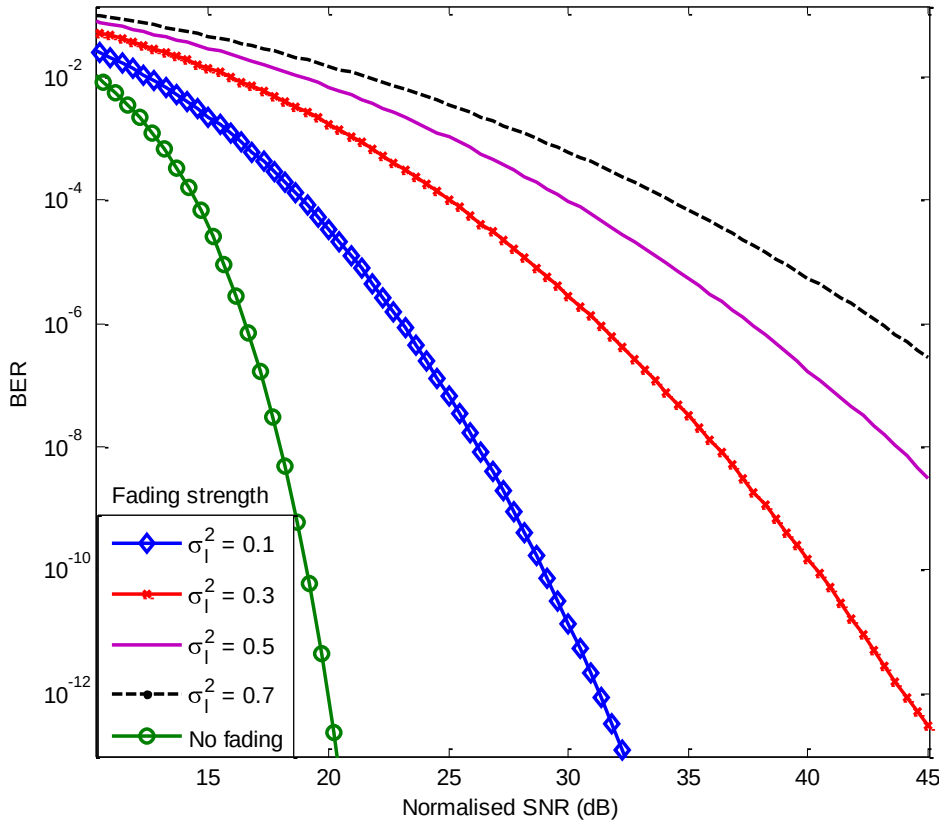

Fig. 6.14: Error rate performance against normalised SNR for BPSK-SIM based FSO in weak atmospheric turbulence channel for $\sigma_l^2 = [0, 0.1,\ 0.3, 0.5, 0.7]$.

Also from this plot, the SNR penalty at any given fading strength and BER can be obtained. The SNR penalty is defined as the difference between the SNR required to achieve a specified BER in the presence and absence of atmospheric turbulence. The SNR penalty is shown in Fig. 6.15 for the following BER levels: 10^{-3}, 10^{-6} and 10^{-9}. Expectedly, the penalty increases as the turbulence strength increases and as the benchmark BER value decreases. Beyond $\sigma_l^2 = 0.1$, the penalty increases very sharply, for instance, at a BER of 10^{-6}, when the fading strength rises by ten folds from $\sigma_l^2 = 0.01$ to $\sigma_l^2 = 0.1$, the penalty only rises from 1 dB to 6.5 dB. But when the fading strength increases to $\sigma_l^2 = 0.3$, the SNR penalty rises to 15 dB.

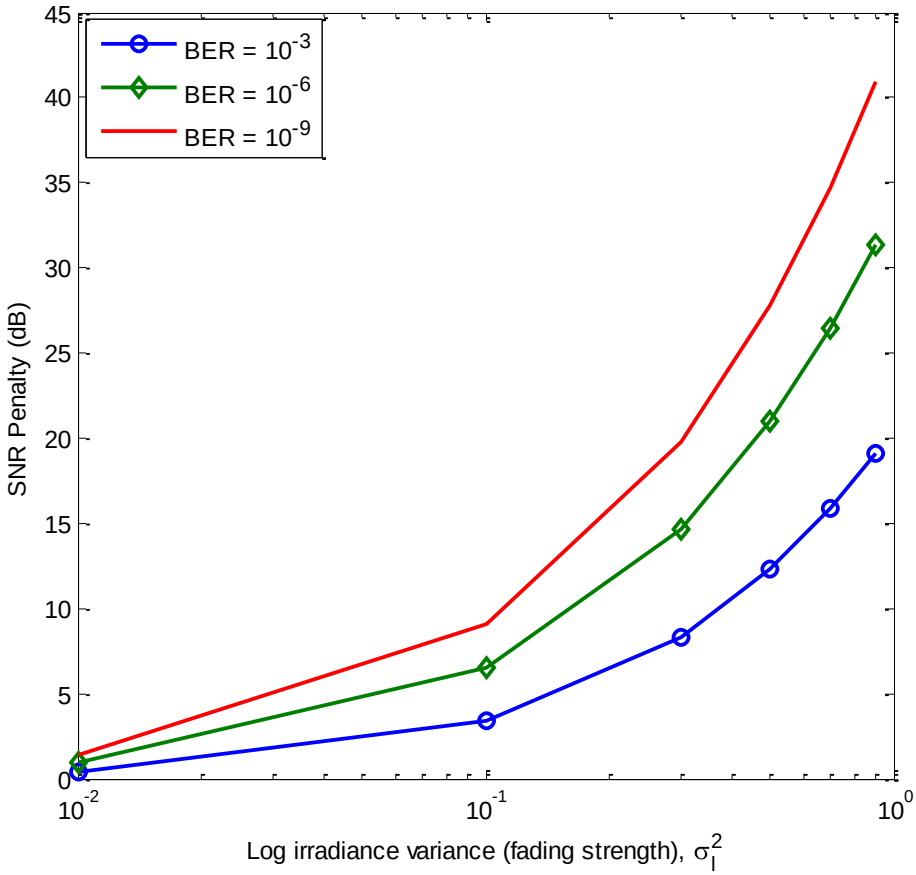

Fig. 6.15: Turbulence induced SNR penalty as function of log irradiance variance for BPSK-SIM based FSO for BER = [10^{-3}, 10^{-6}, 10^{-9}]

Moreover, in Figures 6.16 and 6.17 respectively, the BER and P_{Out} metrics of a BPSK-SIM are plotted against the turbulence strength for different SNR values. These plots show that increasing the signal power can help mitigate the fading caused by the atmospheric turbulence but only in the very weak regime, where $\sigma_l^2 < 0.1$. As the turbulence strength increases beyond this value, the BER and indeed the P_{Out} both tend to high asymptotic values that are too high to guarantee a reliable exchange of information via the link. This implies that techniques other than a mere increase in transmitted power will be required to mitigate atmospheric turbulence beyond the very weak regime. To do just that, diversity techniques will be examined in the next chapter.

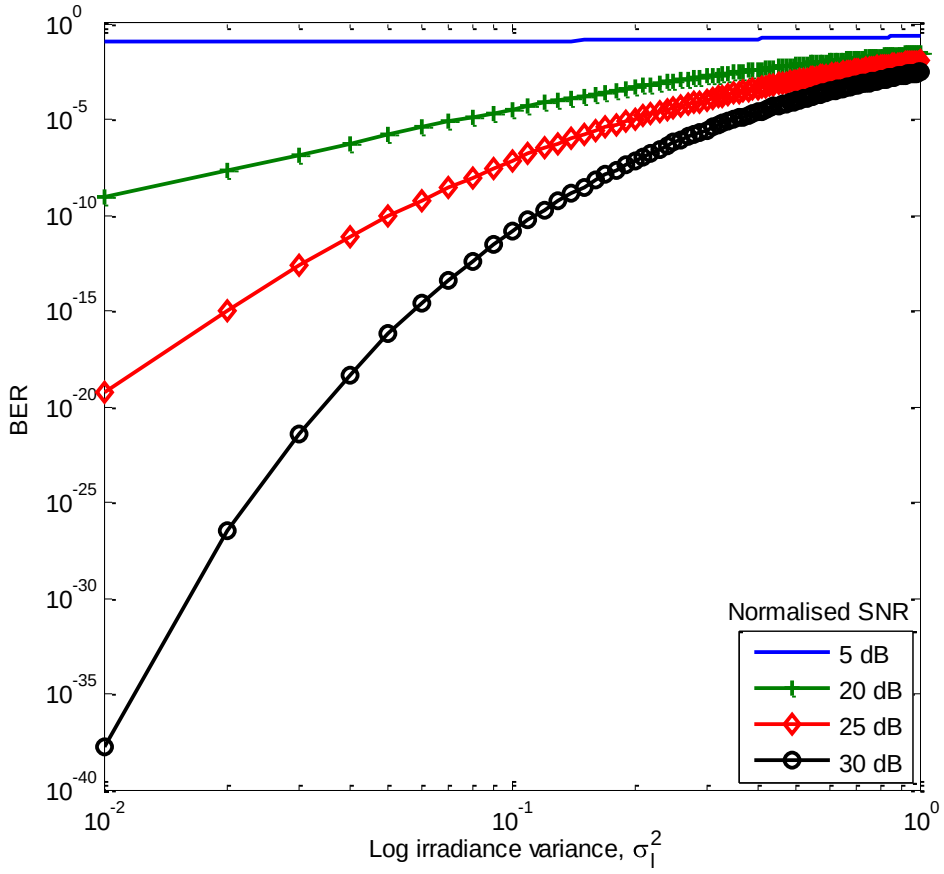

Fig. 6.16: BER of BPSK-SIM against the turbulence strength in weak atmospheric turbulence for normalised SNR (dB) = [5, 20, 25, 30].

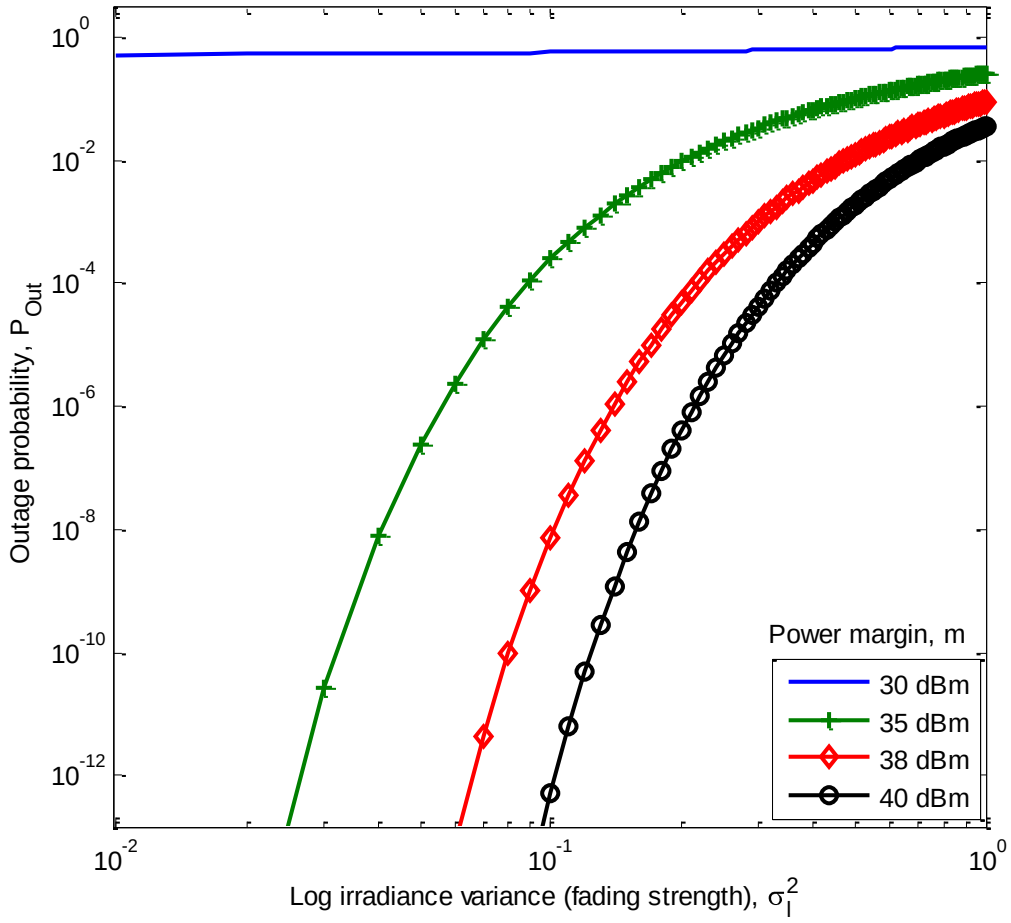

Fig. 6.17: P_{Out} of BPSK-SIM against the turbulence strength in weak atmospheric turbulence for *m* (dBm) = [30, 35, 38, 40].

6.5 Intermodulation Distortion Due to Laser Non-linearity

For a practical optical source with inherent non-linearity, the output power of the source can be expressed in the general form:

$$P(t) = P_T \exp(\xi m(t)) \tag{6.30}$$

By expressing this in a series form and replacing the optical power, without any loss of generality, with irradiance, the following non-memory model for the non-linear laser output is obtained [119, 120].

$$I(t) = I\left[1 + \xi m(t) + a_2\xi^2 m^2(t) + a_3\xi^3 m^3(t) + \cdots + a_i\xi^i m^i(t) + \cdots\right] \qquad (6.31)$$

The output irradiance *I*, and the constants $\{a_i\}_{i=2}^{\infty}$, which describe the degree of optical source on non-linearity are fixed for a given optical source at a specified driving current. These values of $\{a_i\}_{i=2}^{\infty}$ are obtainable from the solution of the rate equation of the particular optical source [121]. For an ideal laser source, the constants $\{a_i\}_{i=2}^{\infty}$ are all equal to zero. The non-memory laser output model is valid for as long as: the difference between the bias current and the modulation current amplitude is higher than the threshold current, that is, no signal clipping; and the modulation frequency is well below the resonance frequency of the laser source. When the laser is operated close to its resonance frequency, the driving signal experiences increased distortion that is not accurately accounted for by the non-memory model [122]. For a laser source, the innate non linearity, which manifests itself as a kink in the output characteristic curve of the optical source, originates from either: (a) the transverse motion of the near field [123] or (b) the guiding properties of the laser [122, 124].

In a single subcarrier frequency system, the terms beyond the second term in (6.31) generate the out-of-band signals, reducing it to the form used in (5.21). Conversely, for multiple subcarriers, these terms result in signals with the in-band frequencies, which then result in IMD. Moreover, for $i > 3$, a_i becomes negligible and will henceforth not be considered. Now, consider the general unity amplitude, PSK modulated multiple subcarrier signals, $m(t) = \sum_{i=\ell}^{N} \cos(\omega_i t + \theta_i)$, in which the subcarriers are separated by an equal frequency $\Delta\omega$. That is, if the first and the last subcarriers are ω_ℓ and ω_N, respectively then $\omega_{\ell+n} = \omega_\ell + n\Delta\omega$. The 2nd and 3rd intermodulation products are generated by $m^2(t)$ and $m^3(t)$ in the following equations:

$$m^2(t) = \frac{1}{2}\sum_{z=\ell}^{N}\sum_{y=\ell}^{N}\cos\left[\left(\omega_y + \omega_z\right)t + \left(\theta_y + \theta_z\right)\right] + \cos\left[\left(\omega_y - \omega_z\right)t + \left(\theta_y - \theta_z\right)\right] \tag{6.32}$$

$$\begin{aligned} m^3(t) = \frac{1}{4}\sum_{x=\ell}^{N}\sum_{y=\ell}^{N}\sum_{z=\ell}^{N}&\cos\left[\left(\omega_x + \omega_y + \omega_z\right)t + \left(\theta_x + \theta_y + \theta_z\right)\right] \\ &+ \cos\left[\left(\omega_x + \omega_y - \omega_z\right)t + \left(\theta_x + \theta_y - \theta_z\right)\right] \\ &+ \cos\left[\left(\omega_x - \omega_y + \omega_z\right)t + \left(\theta_x - \theta_y + \theta_z\right)\right] \\ &+ \cos\left[\left(\omega_x - \omega_y - \omega_z\right)t + \left(\theta_x - \theta_y - \theta_z\right)\right] \end{aligned} \tag{6.33}$$

For a typical subcarrier at frequency ω_k, IMD occurs when the intermodulation products fall within the frequency ω_k. That is when $\omega_x \pm \omega_y = \pm\omega_k$ for the 2nd order intermodulation product (IMP2) and $\omega_x \pm \omega_y \pm \omega_z = \pm\omega_k$ for the 3rd order intermodulation product (IMP3). It should be noted that if the subcarriers are integral multiples of ω_ℓ (orthogonal), then there will be no crosstalk/adjacent channel interference in principle but the bandwidth requirement will be at least $(N-1)\omega_\ell$ and there exists several intermodulation distortion components comprising of both IMP2 and IMP3. However, by considering a single octave operation, in which the upper end subcarrier frequency $\omega_N = 2\omega_\ell$, the bandwidth requirement is reduced to ω_ℓ and all the IMP2 becomes out-of-band. In addition, only two of the possible seven IMP3 shown in Table 6.4 are in-band. These in-band components are $\omega_x + \omega_y - \omega_z$ and $2\omega_x - \omega_y$. The single octave operating condition therefore reduces the amount of IMD to contend with considerably. It also results in negligible harmonic distortion, because the harmonic components will all be out-of-band.

Table 6.4: Third order intermodulation products [120].

Term Type	Number of Components per Term	dB of Term above Harmonic
$3\omega_x$	1	0
$2\omega_x+\omega_y$	3	9.54
$2\omega_x-\omega_y$	3	9.54
$\omega_x-2\omega_y$	3	9.54
$\omega_x+\omega_y-\omega_z$	6	15.56
$\omega_x-\omega_y-\omega_z$	6	15.56
$\omega_x+\omega_y+\omega_z$	6	15.56

In the IMP3, that is the expansion of $m^3(t)$, there are six identical components making up each term, if the indices *x*, *y* and *z* are all different. There are three identical terms in IMP3 if any two of the indices *x*, *y* and *z* are equal in value as shown in Table 6.4. The total third order intermodulation distortion (IMD3) is therefore given by:

$$\begin{aligned}\text{IMD3} = \frac{6}{4}N_{x+y-z}\cos\left[\left(\omega_x+\omega_y-\omega_z\right)t+\left(\theta_x+\theta_y-\theta_z\right)\right] \\ +\frac{3}{4}N_{2x-y}\cos\left[\left(2\omega_x-\omega_y\right)t+\left(2\theta_x-\theta_y\right)\right]\end{aligned} \tag{6.34}$$

where N_{x+y-z} and N_{2x-y} are the numbers of each IMP3 contributing to the IMD3 at ω_k, they can be readily obtained as [120]:

$$\begin{aligned}N_{x+y-z} = \text{int}\lfloor(k-\ell)/2\rfloor\text{int}\lfloor(k-\ell-1)/2\rfloor+(k-\ell)(N-k) \\ +\text{int}\lfloor(N-k)/2\rfloor\text{int}\lfloor(N-k-1)/2\rfloor\end{aligned} \tag{6.35a}$$

$$N_{2x-y} = \text{int}\lfloor(N-k)/2\rfloor+\text{int}\lfloor(N-\ell)/2\rfloor, \quad \ell\le k\le N \tag{6.35b}$$

where $\text{int}\lfloor x\rfloor$ represents the closest integer, smaller than or equal to *x*, for example, $\text{int}\lfloor 3.2\rfloor = 3$. From these equations 6.35(a-b), whenever $\ell = k = 1$ and the total number of subcarrier frequencies *N*, is even, then $N_{x+y-z} = \frac{1}{4}(N-2)^2$ and $N_{2x-y} =$

$(N-2)/2$. When N is odd and $\ell = k = 1$, $N_{x+y-z} = \frac{1}{4}(N-1)(N-3)$ and $N_{2x-y} = (N-1)/2$. In Table 6.5 the values of N_{x+y-z} and N_{2x-y}, for different values of ℓ, k and $N = 12$, are shown as an illustration. This table is useful during frequency planning, as it helps to identify subcarriers with high number of in-band IMD so that they can be avoided.

Table 6.5: Number of in-band intermodulation products for $N = 12$.

k / ℓ	1	2	3	4	5	6	7	8	9	10	11	12
N_{2x-y}												
1	5	5	5	5	5	5	5	5	5	5	5	5
2	-	5	4	5	4	5	4	5	4	5	4	5
3	-	-	4	4	4	4	4	4	4	4	4	4
4	-	-	-	4	3	4	3	4	3	4	3	4
5	-	-	-	-	3	3	3	3	3	3	3	3
6	-	-	-	-	-	3	2	3	2	3	2	3
7	-	-	-	-	-	-	2	2	2	2	2	2
8	-	-	-	-	-	-	-	2	1	2	1	2
9	-	-	-	-	-	-	-	-	1	1	1	1
10	-	-	-	-	-	-	-	-	-	1	0	1
11	-	-	-	-	-	-	-	-	-	-	0	0
12	-	-	-	-	-	-	-	-	-	-	-	0
N_{x+y-z}												
1	25	30	34	37	39	40	40	39	37	34	30	25
2	-	20	25	28	31	32	33	32	31	28	25	20
3	-	-	16	20	23	25	26	26	25	23	20	16
4	-	-	-	12	16	18	20	20	20	18	16	12
5	-	-	-	-	9	12	14	15	15	14	12	9
6	-	-	-	-	-	6	9	10	11	10	9	6
7	-	-	-	-	-	-	4	6	7	7	6	4
8	-	-	-	-	-	-	-	2	4	4	4	2
9	-	-	-	-	-	-	-	-	1	2	2	1
10	-	-	-	-	-	-	-	-	-	0	1	0
11	-	-	-	-	-	-	-	-	-	-	0	0
12	-	-	-	-	-	-	-	-	-	-	-	0

Furthermore in Fig. 6.18, the values of N_{x+y-z} and N_{2x-y} are plotted against the number of subcarriers for $k = \ell = 1$. This graph further illustrates the relationship

between IMD3 and the number of subcarriers. It can thus be concluded that N_{x+y-z} is much greater than N_{2x-y}, and that the IMD3 increases as the square of the number of subcarriers.

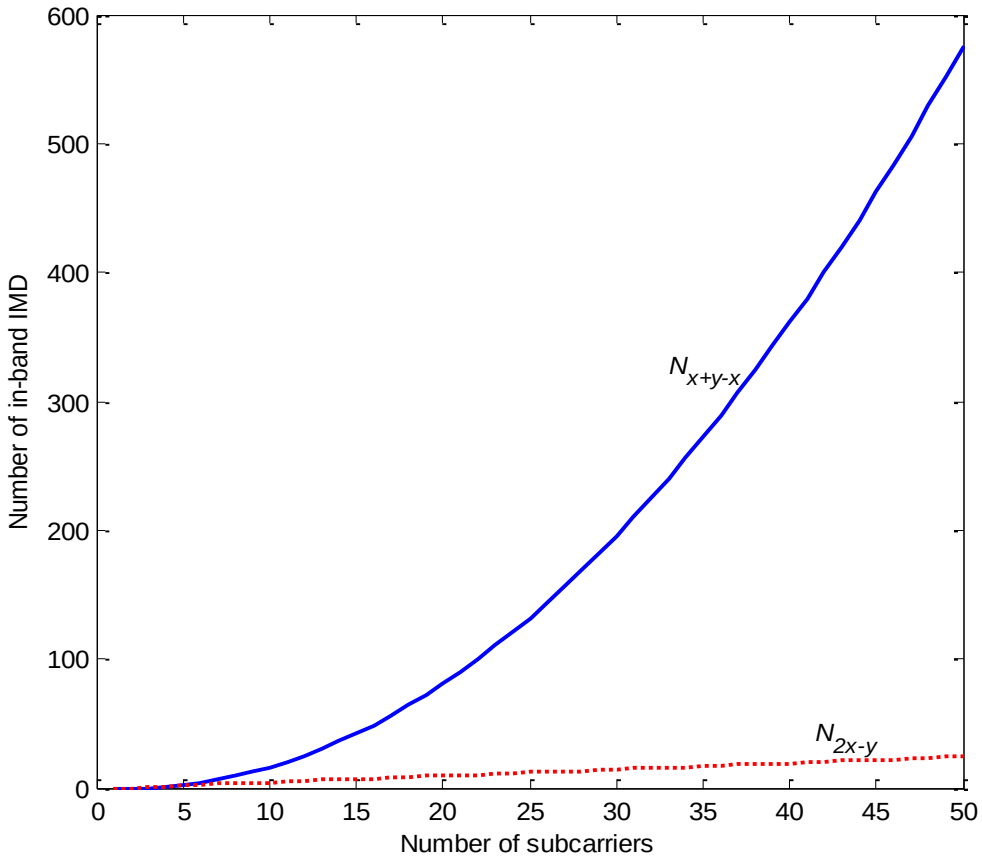

Fig. 6.18: In-band intermodulation products against number of subcarriers for $k = \ell = 1$.

The variance of the IMD3 can thus be obtained as:

$$\sigma^2_{\text{IMD3}} = \frac{1}{2}\left[\left(\frac{6}{4}\right)^2 N^j_{x+y-z} + \left(\frac{3}{4}\right)^2 N^j_{2x-y}\right] \tag{6.36}$$

where $j = 2$ if all the IMP3 add up coherently, this occurs when all the subcarrier are carrying similar symbols, and $j = 1$ otherwise. In the general expansion of $m^3(t)$, there

are always $3\,(2N-1)/4$ terms at the fundamental subcarrier frequency ω_k, of interest. By taking the IMD account, the received signal is now becomes:

$$i(t) = \Re I\left[1 + \xi\cos(\omega_k t + \theta_k) + \frac{3}{4}a_3\xi^3(2N-1)\cos(\omega_k t + \theta_k) + \frac{3}{4}a_3\xi^3(\mathrm{IMD3}) + n(t)\right] \tag{6.37}$$

The DC component can be suppressed via filtering to obtain the signal power (or carrier signal power) per symbol, IMD and noise variances as:

$$S_P = \frac{\Re^2 I^2}{2}\left[\xi + \frac{3}{4}a_3\xi^3(2N-1)\right]^2 \tag{6.38a}$$

$$\sigma^2_{\mathrm{IMD}} = \Re^2 I^2 a_3^2 \xi^6 \sigma^2_{\mathrm{IMD3}} \tag{6.38b}$$

$$\sigma^2 = \sigma^2_{Sh} + \sigma^2_{Th} \tag{6.38c}$$

The subcarrier signal to noise and IMD ratio (CNIR) is thus:

$$\mathrm{CINR}(\xi, I) = \frac{S_P}{\sigma^2 + \sigma^2_{\mathrm{IMD}}} = \frac{\Re^2 I^2\left[\xi + \frac{3}{4}a_3\xi^3(2N-1)\right]^2}{2\sigma^2 + \Re^2 I^2 a_3^2\xi^6\left[\left(\frac{6}{4}\right)^2 N^j_{x+y-z} + \left(\frac{3}{4}\right)^2 N^j_{2x-y}\right]} \tag{6.39}$$

When atmospheric turbulence is negligible or completely absent, the maximum value of the optical modulation depth can be obtained from the solution of $\frac{d(CINR)}{d\xi} = 0$ as:

$$\xi = \left[\frac{16\sigma^2}{9(a_3\Re I)^2\left[4N^j_{x+y-z} + N^j_{2x-y}\right]}\right]^{1/6} \tag{6.40}$$

Equation (6.40) is plotted below in Fig. 6.19 for three different numbers of subcarriers. As expected, as the number of subcarriers and the irradiance increase, the modulation index decreases in order to keep the transmitter within its dynamic range.

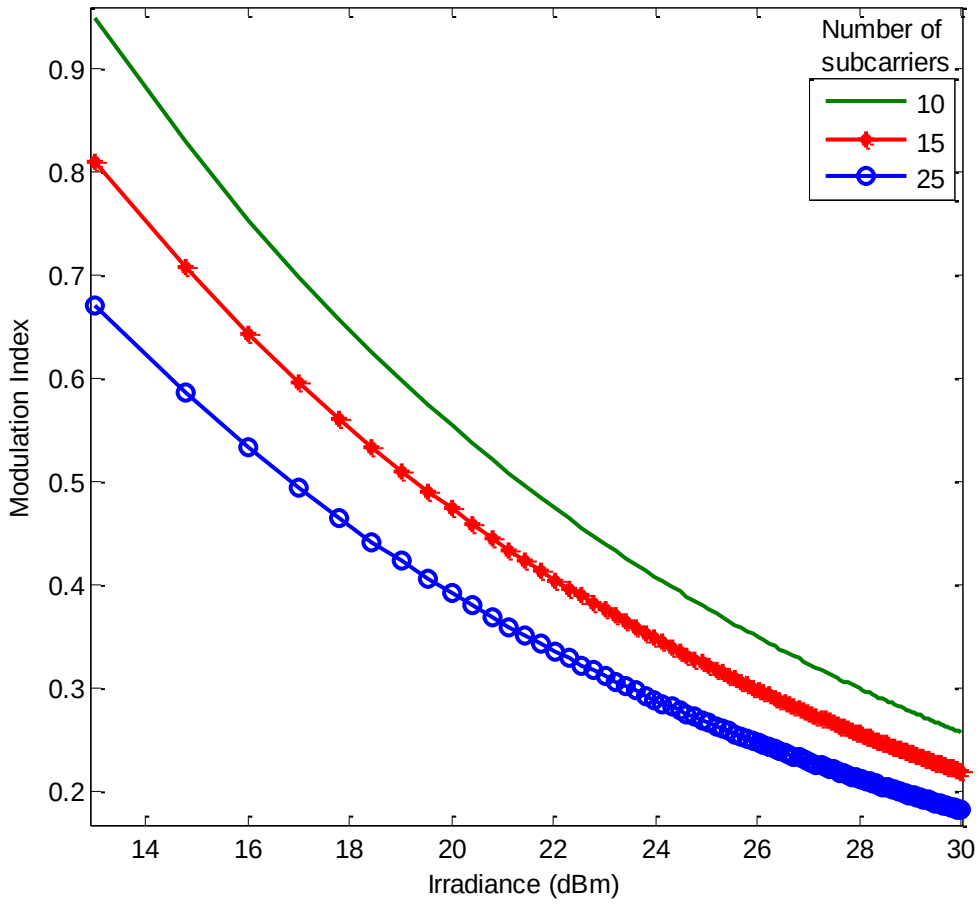

Fig. 6.19: Modulation index against the irradiance in the absence of atmospheric turbulence for N = [10, 15, 25].

Since (6.40) does not take into account the irradiance fluctuation, the resulting modulation index is referred to as the sub-optimum modulation index, ξ_{subopt}. In the presence of atmospheric turbulence, the irradiance level fluctuates and the average subcarrier signal to noise and distortion ratio, CINR_{ave}, is therefore defined as the average of $\mathrm{CINR}(\xi, I)$ over the scintillation statistics.

$$\mathrm{CINR}_{ave}(\xi) = \int_0^{\infty} \mathrm{CINR}(\xi, I) p(I)\, dI \tag{6.41}$$

In weak atmospheric turbulence modelled using the log-normal distribution, (6.41) becomes:

$$\mathrm{CINR}_{ave}(\xi) = \frac{\Re^2 \left[\xi + \frac{3}{4} a_3 \xi^3 (2N-1)\right]^2}{2\sqrt{2\pi}\sigma_l} \times \int_0^{\infty} \frac{I}{(\sigma^2 + \mathcal{K}_1 \xi^6 I^2)} \exp\left(-\frac{[\ln(I/I_0) + \sigma_l^2/2]^2}{2\sigma_l^2}\right) dI \tag{6.42}$$

where $\mathcal{K}_1 = 9\Re^2 a_3^2 \left(4N_{x+y-z} + N_{2x-y}\right)/32$ and the index 'j' in (6.39) has been equated to unity. The optimum modulation depth can therefore be obtained graphically from the plot of (6.42). As an illustration, this is plotted in Fig. 6.20 for N = 12, σ^2 = 10^{-2} and σ_l^2 = 0.25, from this, the modulation index when the CINR_{ave} is maximum is clearly seen to be at $\xi_{opt} \cong 0.42$.

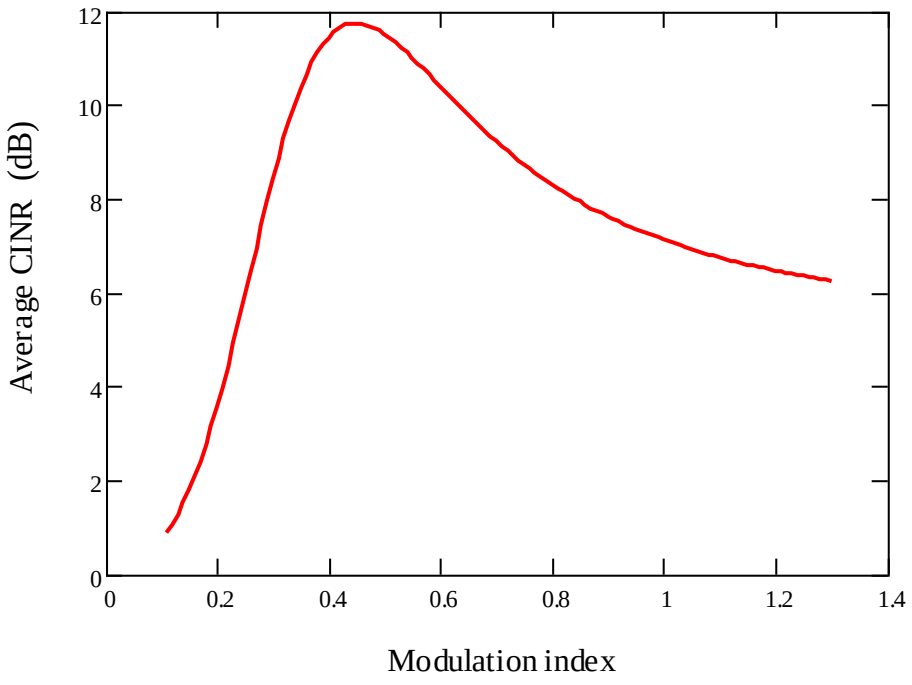

Fig. 6.20: CINR_{ave} (dB) against the modulation depth in atmospheric turbulence for σ^2 = 10^{-2}, σ_l^2 = 0.25, a_3 = 0.3, ℓ = k = 1 and N = 12.

For a BPSK pre-modulated multiple-SIM with IMD, the unconditional BER on any of the subcarriers is given by:

$$P_e(\xi) = \int_0^{\infty} \mathrm{Q}\left(\sqrt{\mathrm{CINR}(\xi, I)}\right) p(I)\, dI \tag{6.43}$$

The graph of this BER in weak scintillation is shown in Fig. 6.21 for N = 12, $\sigma^2 = 10^{-2}$ and σ_l^2 = 0.25 as an example. From this graph, the modulation depth ξ_{opt} that minimises the BER is obtained as 0.6 against 0.42 obtained previously (see Fig. 6.20) when the CINR_{ave} was used.

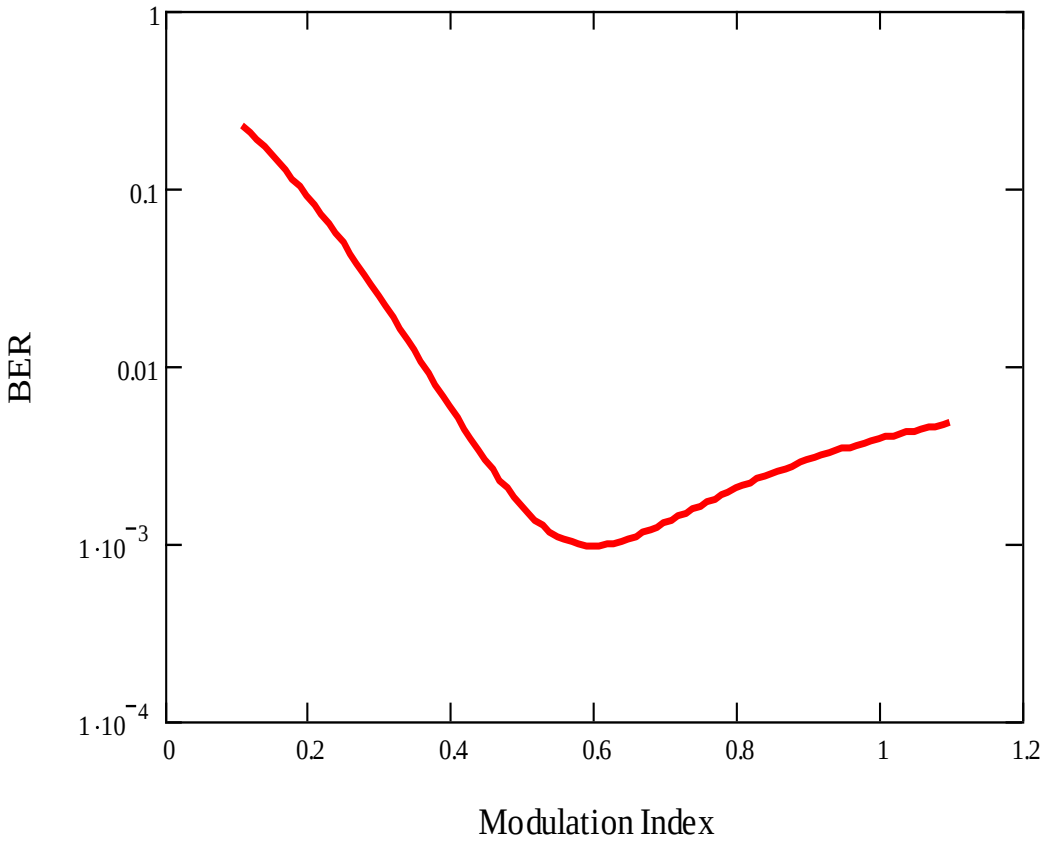

Fig. 6.21: Unconditional BER against the modulation depth in atmospheric turbulence for $\sigma^2 = 10^{-2}$, σ_l^2 = 0.25, a_3 = 0.3, $\ell = k$ = 1 and N = 12.

In Fig. 6.22, the optimum modulation index that results in the maximum $CINR_{ave}$ and which produces the minimum BER are plotted against the average irradiance I_0. It turns out that, increasing the average irradiance leads to a reduction in the optimum modulation depth. This is so in order to keep the subcarrier signal within the dynamic range of the optical source and prevent any signal clipping.

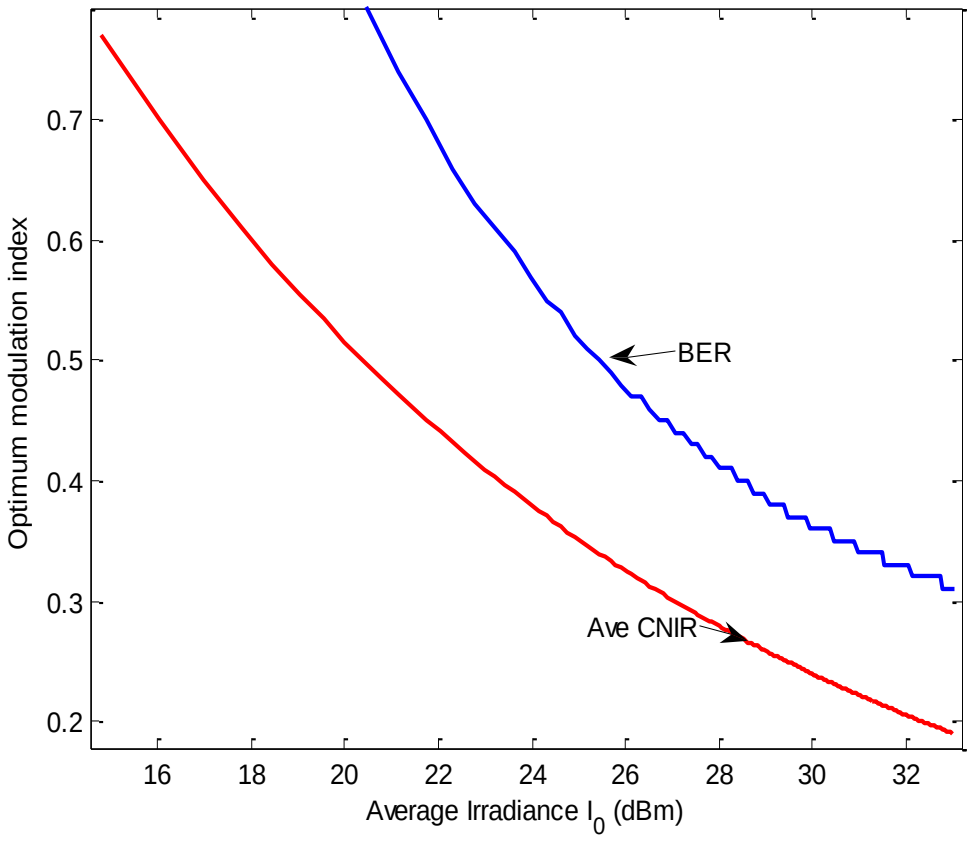

Fig. 6.22: Optimum modulation index based on minimum BER and maximum $CINR_{ave}$ against I_0 for $N = 12$, $a_3 = 0.3$, $\ell = k = 1$, $\sigma^2 = 10^{-3}$ and $\sigma_l^2 = 0.1$.

Furthermore, the unconditional BER using the optimum modulation index values from (6.43) and the suboptimum modulation index of (6.40) are plotted against I_0 in Fig. 6.23. From this figure, the BER performance that uses ξ_{opt} is superior to the case based on a fixed modulation index. From Section 6.2.1.4, when multiple subcarriers are

considered with $\xi = 1/N$, there is always a 10log$N$ (dB) penalty in I_0. But as shown in Fig. 6.23, this penalty is reduced by 7 dB and 4 dB, respectively with the use of ξ_{opt} and ξ_{subopt}, at a BER of 10^{-6}. The penalty is expected to increase as both a_3 and the channel fading strength increase. For a multiple-SIM system with different modulation techniques on each subcarrier, the average BER is described as $\sum_{i=1}^{N} P_{ei}/N$.

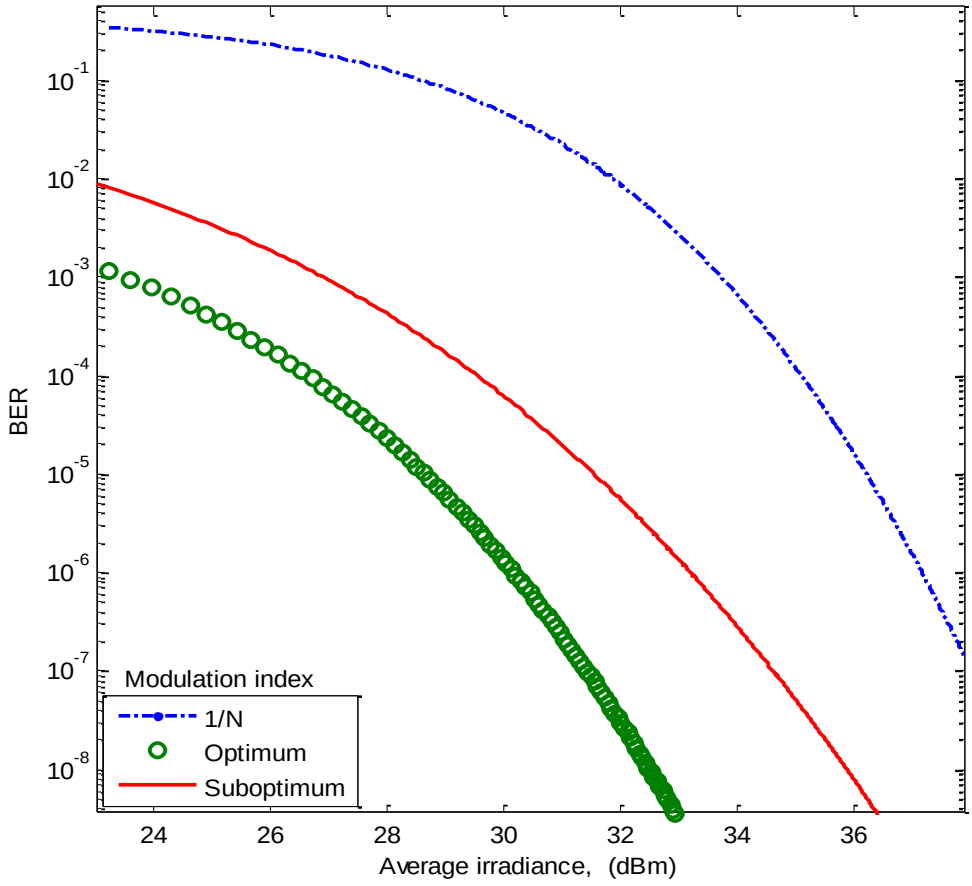

Fig. 6.23: BER of multiple SIM-FSO against I_0 in atmospheric turbulence for N = 12, a_3 = 0.3, $\ell = k = 1$, $\sigma^2 = 10^{-3}$ and $\sigma_l^2 = 0.1$ using optimum and suboptimum modulation index.

6.6 Summary

In this chapter, the BER and outage probability of subcarrier intensity modulated FSO have been presented across all turbulence regimes representing short to very long range systems. Based on the results presented, the SIM is recommended in atmospheric turbulence against the fixed threshold OOK modulated FSO currently used in commercial terrestrial FSO systems, primarily because it does not exhibit a BER floor like the fixed threshold OOK. Multiple SIM has also been studied as a means of increasing the system throughput/capacity but at an electrical SNR penalty of at least 20log$N$ dB. The multiple SIM-FSO should therefore only be considered when the quest to achieve a higher throughput outweighs the accompanying penalty. Also, the intermodulation effect due to the optical source non-linearity has been analysed and the in-band intermodulation products calculated. By choosing the subcarrier frequencies carefully, the number of in-band intermodulation products can be reduced. Expressions for the optimum modulation index based on average CNIR and unconditional BER have equally been derived. Using the optimum modulation index can potentially reduce the power penalty incurred due to IMD by up to 7 dB at a BER of 10^{-6}.

The atmospheric turbulence has been found to introduce power penalties in the system and to guarantee a reliable communication link in this condition, the penalties must be combated. This can be achieved by increasing the transmitted power but this is only effective in the very weak turbulence regime when $\sigma_l^2 < 0.1$. Beyond this regime, the technique fails and other methods will have to be adopted. In the next chapter, diversity techniques which exploit both the spatial and temporal variations in the characteristics of the turbulent atmospheric channel will be examined as means of ameliorating the fading effect of the channel.

Chapter Seven

SIM-FSO with Spatial and Temporal Diversity Techniques

7.1 Introduction

Fog, aerosols, rain and gases and other particles suspended in the atmosphere result in laser irradiance attenuation. The coefficient of attenuation typically ranges from a few dB/km in clear atmosphere to over 100 dB/km in a dense fog regime [20]. The huge attenuation suffered during dense fog restricts the carrier class FSO links to ~500 m [1, 15]; extending the link range in such conditions requires alternative schemes such as hybrid RF/FSO schemes [34, 125]. The thick fog which causes the most signal

attenuation is a short duration, localised event, which only occurs in few locations. Another factor that accounts for the FSO performance degradation in clear atmosphere is the irradiance and phase fluctuation. The signal fluctuation results from random index of refraction variations along the propagation path due to atmospheric turbulence as discussed in the preceding chapters. These phase and irradiance fluctuation suffered by the traversing beam makes optical coherent detection less attractive, because it is sensitive to both signal amplitude and phase. This informs the choice of direct detection in terrestrial FSO links as it is not sensitive to the signal phase as mentioned in chapter three. In direct detection systems, turbulence effects could result in deep irradiance fades that lasts up to ~1-100 μs [44, 71]. For a link operating at say 1 Gbps, this could result in a loss of up to 10^5 consecutive bits (burst error). To avoid this and reduce the turbulence induced power penalty highlighted in chapter six, atmospheric turbulence has to be mitigated.

Possible ways of reducing the fading duration and strength include the use of aperture averaging, adaptive optics, error control and spatial diversity. In aperture averaging, the receiver aperture needs to be far greater than the spatial coherence distance ρ_0 of the atmospheric turbulence in order to receive several uncorrelated signals. This condition is not always achievable in FSO as the spatial coherence distance is of the order of centimetres [29]. For coding to be effective in FSO, it must be robust enough to detect and correct not only random errors but also burst errors because the temporal coherence time, τ_0 of atmospheric turbulence is much greater than the typical symbol duration. To mitigate atmospheric turbulence effects, the use of convolution coding with hard-decision Viterbi decoding has been investigated in [126], while a more efficient Turbo code employing the maximum-likelihood decoding has been reported in [127]. In addition, the work reported in [69] explored the use of a much more powerful low

density parity codes (LDPC) to detect and correct the burst error that results from scintillation. In their work, the LDPC coded SIM in atmospheric turbulence was reported to achieve a coding gain of more than 20 dB compared with similarly coded OOK. It has also been reported in [70] that the use of space-time block code (STBC) with coherent and differential detection improves the error performance of SIM in atmospheric turbulence. However, invoking error control coding could introduce huge processing delays and efficiency degradation in view of the number of redundant bits that will be required [71].

The adaptive optics which is based on the phase conjugation principle is another viable option. It has been used in FSO as reported in [68, 128] to reverse the wavefront deformation effect of atmospheric turbulence. However, the complexity and cost of its implementation is prohibitive. This perhaps is the reason why its use has only been restricted to deep space FSO where the cost to benefit ratio is within acceptable limits. In this chapter, the performance of a SIM-FSO with temporal diversity in a turbulent atmospheric channel will be discussed. The spatial diversity analysis will be based on the following linear combining techniques: equal gain combining (EGC), maximum ratio combining (MRC) and selection combining (SelC). Subcarrier timed delay diversity will also be introduced as an alternative channel fading mitigation technique which can be used separately or with the spatial diversity. The receiver is assumed to comprise of identical PIN photodetectors and unity modulation index under spatial diversity. Inter-symbol interference will not be considered since terrestrial FSO is basically a line-of-sight technology with negligible delay spread.

7.2 Receiver Diversity in Log-normal Atmospheric Channels

The idea of spatial diversity is premised on the fact that for a given $\mathcal{N}$ separated photodetectors, the chance that all the photodetectors will experience deep fade (due to scintillation) simultaneously at any given instant is remote. An important consideration in spatial diversity is the amount of correlation that exists between the signals received by the different photodetectors. Apart from mitigating scintillation, the spatial diversity in an FSO communication link is also advantageous in combating temporary link blockage/outage due to birds or other small object flying cross the link path. It is also a good means of combating misalignment when combined with wide divergence optical sources, thereby circumventing the need for an active tracking. Moreover, it is much easier to provide independent aperture averaging with a multiple aperture system, than in a single aperture where the aperture size has to be far greater than the irradiance spatial coherence distance [71]. In dense fog regime however, an FSO link with spatial diversity offers limited advantage and an alternative configuration such as the hybrid FSO/RF should be considered. In the following analysis, both instances of correlated and uncorrelated received signals will be considered. Since the spatial coherence length of the atmospheric channel only measures a few centimetres, it follows therefore that the photodetectors only need to be separated by a few centimetres to achieve uncorrelated reception. At the receiver, the beam footprint covers the entire field of view (FOV) of all the $\mathcal{N}$ detectors. The photocurrents $\{i_i(t)\}_{i=1}^{\mathcal{N}}$, as shown in Fig. 7.1, are then linearly combined before being sent to the coherent demodulator that separates the composite signal into its constituent subcarriers and then demodulates each subcarrier. The linear combining techniques considered are: MRC, EGC and SelC.

Scintillation is a random phenomenon that changes with time, thereby making the received irradiance time variant and the coherence time τ_0, of the irradiance fluctuation in atmospheric turbulence is known to be in the order of milliseconds [71]. This implies that within a time duration $t < \tau_0$, the received signal is constant and time invariant. A typical data symbol duration $T \ll \tau_0$ (T = 1.6 ns when transmitting at a moderate 625 Mbps symbol rate), it follows therefore, that thought the channel is time varying, the received irradiance $\{I_i\}_{i=1}^{\mathcal{N}}$ is time invariant over one symbol duration.

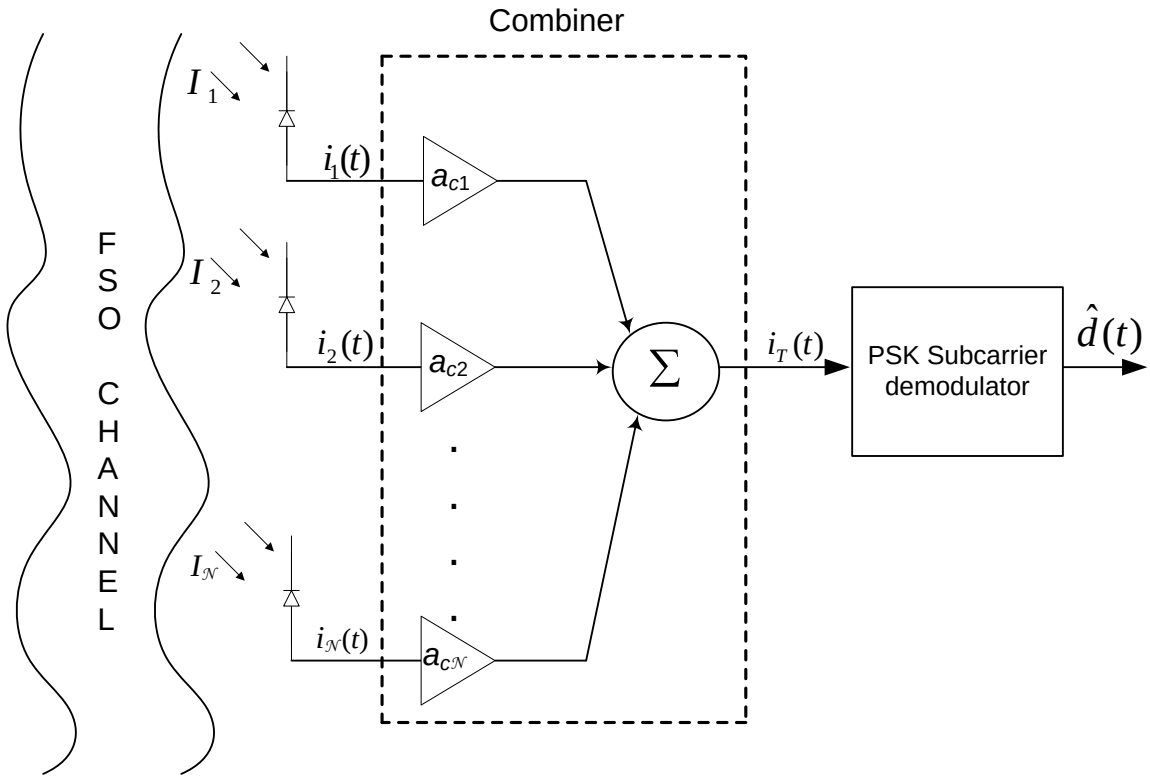

Fig. 7.1: Block diagram of a spatial diversity receiver with $\mathcal{N}$ detectors

To facilitate a fair comparison between an FSO link with and without spatial diversity, each detector aperture in the $\mathcal{N}$-detector system is assumed to have an area of $A_D/\mathcal{N}$, where A_D is the detector aperture area with no diversity. It follows therefore, that the background radiation noise on each branch with detector diversity is reduced by a factor of $\mathcal{N}$. Hence, on each branch the additive white Gaussian background noise variance

will be $\sigma^2/\mathcal{N}$. The thermal noise on each photodetector is however not reduced by a factor of $\mathcal{N}$. The output of the individual detector during a symbol duration is given as:

$$i_i(t) = \frac{\Re}{\mathcal{N}} I_i \left(1 + \sum_{j=1}^{N} A_j g(t) \cos(\omega_{cj} + \theta_j) \right) + n(t) \qquad i = 1,2 \ldots \mathcal{N} \qquad (7.1)$$

The combiner shown in Fig. 7.1 scales the signal from each photodetector by a gain factor, $\{a_{ci}\}_{i=1}^{\mathcal{N}}$, before adding them together. Since the photodetectors are required to be a few centimetres apart, and the link range a few kilometres, the difference in the propagation delay across the receiver array becomes negligible. The combiner's output thus become:

$$i_T(t) = \sum_{i=1}^{\mathcal{N}} a_{ci} i_i(t) \qquad (7.2)$$

7.2.1 Maximum ratio combining (MRC)

In the MRC linear combiner, the gain factor $\{a_{ci}\}_{i=1}^{\mathcal{N}}$ is proportional to the received irradiance. The weighted signals are then co-phased and summed coherently to obtain the combiner's output current given by (7.2). Without any interference, the MRC is optimal regardless of the fading statistics. This, according to [115], is because it results in a maximum-likelihood receiver structure. On the other hand, MRC requires the knowledge of the individual received irradiance and phase on each branch, making it unsuitable for non-coherent demodulated subcarriers, such as the DPSK-SIM.

By substituting (7.1) into (7.2) and suppressing the DC components via filtering, the MRC combiner output becomes:

$$i_{MRC}(t) = \sum_{i=1}^{\mathcal{N}} \left[\frac{\Re a_{ci}}{\mathcal{N}} I_i \sum_{j=1}^{N} A_j g(t) \cos\left(\omega_{cj} t + \theta_j\right) \right] + a_{ci} n_i(t) \tag{7.3}$$

The signal demodulation and the consequently extraction of the transmitted data is done separately for each subcarrier; as such, the photocurrent at a particular subcarrier frequency ω_c is given by:

$$i_{MRC}(t) = \sum_{i=1}^{\mathcal{N}} \left[\frac{\Re a_{ci}}{\mathcal{N}} I_i A g(t) \cos(\omega_c t + \theta) \right] + a_{ci} n_i(t) \tag{7.4}$$

Since the coherence time of the turbulent atmospheric $\tau_0 \gg T$, the branch irradiance I_i is therefore time invariant over a period T. This leads to the following expression for the signal power S_p, at the subcarrier frequency of interest:

$$\begin{aligned} S_p &= \left(\sum_{i=1}^{\mathcal{N}} a_{ci} I_i \right)^2 \frac{1}{T} \int_0^T \left[\frac{\Re A g(t) \cos(\omega_c t + \theta)}{\mathcal{N}} \right]^2 dt \\ &= \left(\frac{\Re A}{\mathcal{N}\sqrt{2}} \right)^2 \left(\sum_{i=1}^{\mathcal{N}} a_{ci} I_i \right)^2 \end{aligned} \tag{7.5}$$

The overall noise is Gaussian, with a zero mean and a variance $\sigma_{MRC}^2 = \sum_{i=1}^{\mathcal{N}} a_{ci}^2 \sigma_i^2 = \sigma_{sc}^2 \sum_{i=1}^{\mathcal{N}} a_{ci}^2$. The electrical SNR at the demodulator input conditioned on the received irradiance is thus derived as:

$$\gamma_{MRC}(\vec{I}) = \left(\frac{\Re A}{\mathcal{N}\sqrt{2}} \sum_{i=1}^{\mathcal{N}} a_{ci} I_i \right)^2 \Big/ \sigma_{MRC}^2 \tag{7.6}$$

Applying Cauchy inequality [118], $\left(\sum_{i=1}^{\mathcal{N}} a_{ci} I_i\right)^2 \leq \left(\sum_{i=1}^{\mathcal{N}} a_{ci}^2\right)\left(\sum_{i=1}^{\mathcal{N}} I_i^2\right)$, to (7.6) results in the following expression for the combiner's output SNR:

$$\gamma_{MRC}(\vec{I}) \leq \frac{\left(\frac{\Re A}{\mathcal{N}\sqrt{2}}\right)^2 \left(\sum_{i=1}^{\mathcal{N}} a_{ci}^2 \sigma_{sc}^2\right)\left(\sum_{i=1}^{\mathcal{N}} I_i^2/\sigma_{sc}^2\right)}{\left(\sum_{i=1}^{\mathcal{N}} a_{ci}^2 \sigma_{sc}^2\right)} \tag{7.7}$$

The left hand side of the Cauchy inequality is apparently equal to the right hand side when $a_{ci} \equiv I_i$. For a background noise limited FSO link, the noise variance on each branch is proportional to the pupil receiver aperture area, $A_D/\mathcal{N}$ and $\sigma_{sc}^2 = \sigma^2/\mathcal{N}$. It should be noted that in arriving at (7.7), the intermodulation distortion due to the inherent nonlinearity of the optical source discussed in section 6.3.3.1 has not been considered. For an ideal optical source with a modulation index of one, the subcarrier amplitude is constrained by the condition $A < 1/N$. The optimum electrical SNR for each subcarrier frequency ω_c now becomes:

$$\gamma_{MRC}(\vec{I}) = \left(\frac{\Re A}{\sqrt{2\mathcal{N}}}\right)^2 \left(\sum_{i=1}^{\mathcal{N}} I_i^2/\sigma^2\right) = \sum_{i=1}^{\mathcal{N}} \gamma_i(I_i) \tag{7.8}$$

where $\gamma_i(I_i) = \frac{(\Re A I_i)^2}{2\mathcal{N}\sigma^2}$ is the conditional SNR on each diversity branch. The average SNR, $\tilde{\gamma}_{MRC}$, obtained by averaging (7.8) over the scintillation statistics is given as:

$$\tilde{\gamma}_{MRC} = \int \gamma_{MRC}(\vec{I}) p(\vec{I})\, d\vec{I} \tag{7.9}$$

where $p(\vec{I})$ is the joint pdf of scintillation, given by $p(\vec{I}) = \prod_{i=1}^{\mathcal{N}} p(I_i)$ for $\mathcal{N}$ photodetectors receiving uncorrelated signals. Similarly, for a BPSK pre-modulated subcarrier, the unconditional BER for the subcarrier at frequency ω_c obtained by averaging the conditional error rate over the statistics of the intensity fluctuation across

all branches is given by:

$$P_{e(MRC)} = \int_0^{\infty} \mathrm{Q}\left(\sqrt{\gamma_{MRC}(\vec{I})}\right) p(\vec{I})\, d\vec{I} \tag{7.10}$$

Solving (7.10) involves $(\mathcal{N}+1)$ fold integrations if the classical definition of the Q-function is used, but by using the alternative form of the Q-function and the Gauss-Hermite quadrature integration described in section 6.2.1.1, this can be simplified to the form below:

$$P_{e(MRC)} = \frac{1}{\pi} \int_0^{\pi/2} [\mathrm{S}(\theta)]^{\mathcal{N}}\, d\theta \tag{7.11}$$

where $S(\theta) \approx \frac{1}{\sqrt{\pi}} \sum_{j=1}^{n} w_j \exp\left(-\frac{K_0^2}{2\sin^2\theta} \exp\left[2\left(x_j\sqrt{2}\sigma_l - \sigma_l^2/2\right)\right]\right)$ and $K_0 = \Re I_0 A/\sqrt{2\mathcal{N}}\,\sigma$. With $\mathcal{N} = 1$, expression (7.11) expectedly reduces to (6.12), which is the BER with no diversity.

7.2.2 Equal gain combining (EGC)

In implementing the EGC spatial diversity technique, the irradiance estimate on each branch is not required but an estimate of the phase of all subcarrier signals on each branch is still very much needed. The EGC combiner samples the photocurrents $\{i_i(t)\}_{i=1}^{\mathcal{N}}$ and sums them coherently with equal weights $\{a_{ci}\}_{i=1}^{\mathcal{N}} = 1$, to produce the decision statistics [115]. With the DC component suppressed via filtering, the photocurrent at the output of the EGC combiner is given by:

$$i_{EGC}(t) = \sum_{i=1}^{\mathcal{N}} \left[\frac{\Re}{\mathcal{N}} I_i \sum_{j=1}^{N} A_j g(t) \cos\left(\omega_{cj} t + \theta_j\right) \right] + n_i(t) \tag{7.12}$$

The conditional SNR at the output of the EGC combiner obtained is thus obtained as:

$$\gamma_{EGC}(\vec{I}) = \left(\frac{\Re A}{\sqrt{2}\mathcal{N}\sigma}\right)^2 \left(\sum_{i=1}^{\mathcal{N}} I_i\right)^2 < \left(\frac{\Re A}{\sqrt{2\mathcal{N}}}\right)^2 \left(\sum_{i=1}^{\mathcal{N}} \frac{I_i^2}{\sigma^2}\right) \tag{7.13}$$

From the foregoing, it is clear that $\gamma_{EGC}(\vec{I}) < \gamma_{MRC}(\vec{I})$. Since the noise variance is proportional to the individual receiver aperture area $\sigma_{EGC}^2 = \sum_{i=1}^{\mathcal{N}} \sigma_i^2 = \sum_{i=1}^{\mathcal{N}} \sigma^2/\mathcal{N} = \sigma^2$.

For a log normal distributed scintillation, the sum of moderate number of irradiances is known to be another log normal variable [71, 129]. That is, the sum of $\mathcal{N}$ independent irradiance $Z = \sum_{i=1}^{\mathcal{N}} I_i = \exp(\mathcal{U})$, where $\mathcal{U}$ is normally distributed with mean $\mu_{\mathcal{U}}$ and variance $\sigma_{\mathcal{U}}^2$. Equation (7.14) below gives the pdf of Z while its first and second moments derived in Appendix B are given by (7.15). The application of central limit is not appropriate here because the number of photodetectors $\mathcal{N}$ is too small to justify its use.

$$P(Z) = \frac{1}{\sqrt{2\pi}\sigma_{\mathcal{U}}} \frac{1}{Z} \exp\left(-\frac{(\ln Z - \mu_{\mathcal{U}})^2}{2\sigma_{\mathcal{U}}^2}\right) \tag{7.14}$$

$$\mu_{\mathcal{U}} = \ln(\mathcal{N}) - \frac{1}{2}\ln\left(1 + \frac{\exp(\sigma_l^2) - 1}{\mathcal{N}}\right) \tag{7.15a}$$

$$\sigma_{\mathcal{U}}^2 = \ln\left(1 + \frac{\exp(\sigma_l^2) - 1}{\mathcal{N}}\right) \tag{7.15b}$$

The average SNR and the unconditional BER for a BPSK pre-modulated subcarrier are then given by (7.16) and (7.17) respectively:

$$\tilde{\gamma}_{EGC} = \int_0^{\infty} \gamma_{EGC}(Z) p(Z)\, dZ \tag{7.16}$$

$$\begin{aligned} P_{e(EGC)} &= \int_0^{\infty} \mathrm{Q}\left(\sqrt{\gamma_{EGC}(Z)}\right) p(Z)\, dZ \\ &= \int_0^{\infty} \frac{1}{\pi} \int_0^{\pi/2} \exp\left(-\frac{K_1^2}{2\sin^2(\theta)} Z^2\right) p(Z)\, d\theta dZ \\ &= \frac{1}{\sqrt{\pi}} \sum_{i=1}^{n} w_i \mathrm{Q}\left(K_1 \exp\left[x_i \sqrt{2}\sigma_U + \mu_U\right]\right) \end{aligned} \tag{7.17}$$

where $K_1 = \Re I_0 A/\sqrt{2}\,\mathcal{N}\sigma$, w_i and x_i remain as previously defined in section 6.2.1.1. With one photodetector, (7.17) gives the same result as (6.12) for the case with no diversity.

7.2.3 Selection combining (SelC)

Both MRC and EGC spatial diversity techniques discussed thus far require the irradiance level and/or the subcarrier signals phase estimates, also a separate receiver chain is needed for each diversity branch thereby adding to the overall complexity of the receiver. The SelC linear combiner on the other hand samples all the received signal and selects the branch with the highest SNR or irradiance level, provided the photodetectors receive same dose of background radiation. The output is equal to the signal on only one of the branches and not the coherent sum of the individual photocurrents as is the case in MRC and EGC. This makes SelC suitable for differentially modulated, non-

coherent demodulated subcarrier signals. In addition, the SelC is of reduced complexity compared to the MRC and EGC and its conditional SNR is given by:

$$\gamma_{SelC}(I) = \frac{\Re^2 A^2 I_{max}^2}{2\mathcal{N}\sigma^2} \tag{7.18}$$

where $I_{max} = \max(I_1, I_2, \ldots I_{\mathcal{N}})$. The pdf of the received irradiance, $p(I_{max})$, given by (7.19), is obtained by first determining its cumulative density function (cdf) and then differentiating as detailed in Appendix C.

$$p(I_{max}) = \frac{2^{1-\mathcal{N}}\mathcal{N}\exp(-y^2)}{I\sigma_l\sqrt{2\pi}}[1 + \mathrm{erf}(y)]^{\mathcal{N}-1} \tag{7.19}$$

where $y = \frac{\ln(I/I_0) + \sigma_l^2/2}{\sqrt{2}\sigma_l}$. The average SNR and the unconditional BER, for a BPSK pre-modulated subcarrier in a turbulent atmospheric channel, are given by:

$$\tilde{\gamma}_{SelC} = \int_0^{\infty} \frac{\Re^2 A^2 I_{max}^2}{2\mathcal{N}\sigma^2} p(I_{max})\, dI_{max} \tag{7.20}$$

$$P_{e(SelC)} = \frac{2^{1-\mathcal{N}}\mathcal{N}}{\sqrt{\pi}} \sum_{i=1}^{n} w_i [1 + \mathrm{erf}(x_i)]^{\mathcal{N}-1} \mathrm{Q}\left(K_0 \exp\left[x_i\sigma_l\sqrt{2} - \sigma_l^2/2\right]\right) \tag{7.21}$$

where $K_0 = \Re I_0 A/\sqrt{2\mathcal{N}}\,\sigma$. For a binary DPSK pre-modulated SIM, the unconditional bit error obtained using the Gauss-Hermite quadrature integration approach is derived as:

$$P_{e(SelC)} = \int_0^{\infty} \frac{1}{2}\exp\left(-\frac{\gamma_{SelC}(I)}{2}\right) p(I_{max}) dI \tag{7.22}$$

$$\cong \frac{\mathcal{N}}{2^{\mathcal{N}}\sqrt{\pi}}\sum_{i=1}^{n} w_i[1+\mathrm{erf}(x_i)]^{\mathcal{N}-1}\exp\left(-K_2^2\exp\left(2x_i\sigma_l\sqrt{2}-\sigma_l^2\right)\right)$$

where $K_2 = \Re I_0 A/2\sigma\sqrt{\mathcal{N}}$.

7.2.4 Effect of received signal correlation on error performance

For a receiver array system in which the photodetectors are separated by a spatial distance, $\mathfrak{s}$, which is less than the spatial coherence distance of the channel at the receiver plane (i.e. $\mathfrak{s} < \rho_0$), the photodetectors will experience correlated irradiance fluctuations. This means that the multiple receivers can all experience similar irradiance fading at the same time. The effect of this on the system error performance will be investigated by considering the best case scenario with an optimum MRC combiner and only one subcarrier signal. The BER conditioned on the received irradiance is:

$$\begin{aligned} P_{ec} &= \mathrm{Q}\left(\sqrt{\gamma_{MRC}(\vec{I})}\right) \\ &= \frac{1}{\pi}\int_0^{\pi/2} \exp\left(-\frac{K_0^2}{2I_0^2\sin^2\theta}\sum_{i=1}^{\mathcal{N}} I_i^2\right)d\theta \end{aligned} \tag{7.23}$$

However in the presence of scintillation, the unconditional BER becomes $P_e = E[P_{ec}]$, which is the average of (7.23) over the joint pdf of the irradiance fluctuation. Based on Tatarski's [45] infinite power series expression for the correlation coefficient of an optical wave travelling through a turbulent atmosphere given by (7.24), and shown graphically in Fig. 7.2, it can be inferred that the correlation coefficient is inversely proportional to the spatial separation whenever $\frac{\mathfrak{s}}{\sqrt{\lambda L}} < 1$, where $\rho_0 \approx \sqrt{\lambda L}$.

$$\begin{aligned} \rho(\mathfrak{s}) = 1 - 2.36(2\pi\mathfrak{s}/\lambda L)^{5/6} + 1.71(2\pi\mathfrak{s}/\lambda L) - 0.024(2\pi\mathfrak{s}/\lambda L)^2 \\ + 0.00043(2\pi\mathfrak{s}/\lambda L)^4 + \ \ldots \end{aligned} \tag{7.24}$$

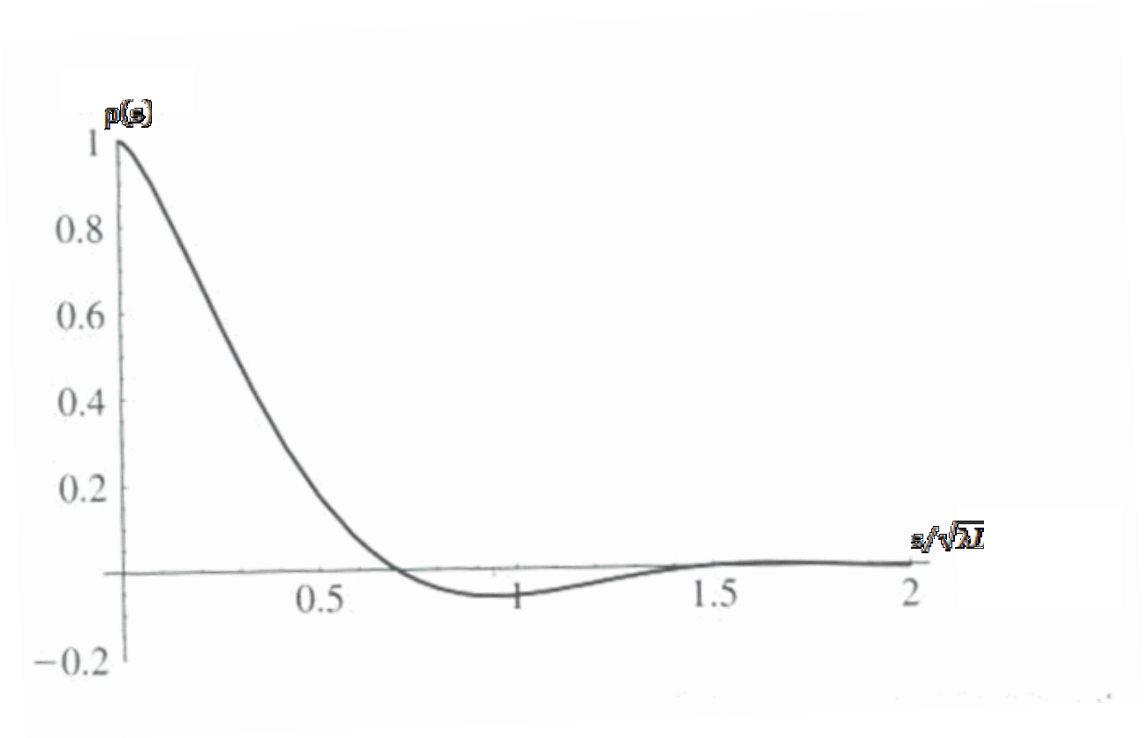

Fig. 7.2: Correlation coefficient for a weak turbulent field as a function of transverse separation. Reproduced from [45].

From the foregoing, the following expression is obtained for the covariance matrix:

$$C_{\mathcal{X}} = \begin{bmatrix} \sigma_{\mathcal{X}}^2 & \cdots & \rho\frac{\varsigma_{12}}{\varsigma_{1\mathcal{N}}}\sigma_{\mathcal{X}}^2 \\ \vdots & \ddots & \vdots \\ \rho\frac{\varsigma_{12}}{\varsigma_{\mathcal{N}1}}\sigma_{\mathcal{X}}^2 & \cdots & \sigma_{\mathcal{X}}^2 \end{bmatrix} \tag{7.25}$$

where ς_{ij} is the spatial separation between photodetectors *i* and *j* and ρ is the correlation coefficient between two photodetectors with a spatial separation ς_{12}. The joint pdf of the received irradiance is then given by:

$$p(I_1, I_2 \ldots I_{\mathcal{N}}) = \frac{\exp(-\mathbb{X}C_{\mathcal{X}}^{-1}\mathbb{X}^T/8)}{2^{\mathcal{N}}\prod_{i=1}^{\mathcal{N}} I_i\,(2\pi)^{\mathcal{N}/2}|C_{\mathcal{X}}|^{1/2}} \tag{7.26}$$

where $\mathbb{X} = [\ln I_1/I_0 \;\; \ln I_2/I_0 \;\; \ldots \;\; \ln I_{\mathcal{N}}/I_0]$ is a row matrix. The expression for the unconditional BER is then obtained as:

$$P_e = \int \mathrm{Q}\left(\sqrt{\gamma_{MRC}(\vec{I})}\right) p(I_1, I_2 \ldots I_{\mathcal{N}})\, d\vec{I} \tag{7.27}$$

7.2.5 Outage probability with receiver diversity in a log-normal atmospheric channel

Here, the outage probability of a SIM-FSO link with an array of photodetectors is presented. The emphasis in this section will be on the EGC linear combing because of its simplicity. The result can however be easily extended to other linear combining schemes in a similar manner. With an array of photodetectors, the outage probability becomes: $P_{Out} = P(P_{e(EGC)} > P_e^*) \equiv P\left(\gamma_{\mathrm{EGC}}(\vec{I}) < \gamma^*\right)$. If m_{EGC} represents the extra power margin required to achieve a given P_{Out} and γ^* is the SNR in the absence of atmospheric turbulence, then the outage probability is derived as:

$$P_{Out} = \mathrm{Q}\left(\frac{\ln(m_{EGC}/\mathcal{N}) + \mu_{\mathcal{U}}}{\sigma_{\mathcal{U}}}\right) \tag{7.28}$$

By applying the Chernoff bound $\mathrm{Q}(x) \leq 0.5\exp(-x^2/2)$, to (7.28), an approximate value of m_{EGC} to achieve a given P_{Out} is obtained as:

$$m_{EGC} \approx \mathcal{N} \exp\left(\sqrt{-2\sigma_{\mathcal{U}}^2 \ln(2P_{Out})} - \mu_{\mathcal{U}}\right) \tag{7.29}$$

Figure 7.3 shows how the upper bound of the outage probability given by (7.29) compares with the exact solution obtained from (7.28). The upper bound requires less than 0.5 dBm of power more than the exact solution and the upper bound appears to become tighter as the number of independent photodetector increases.

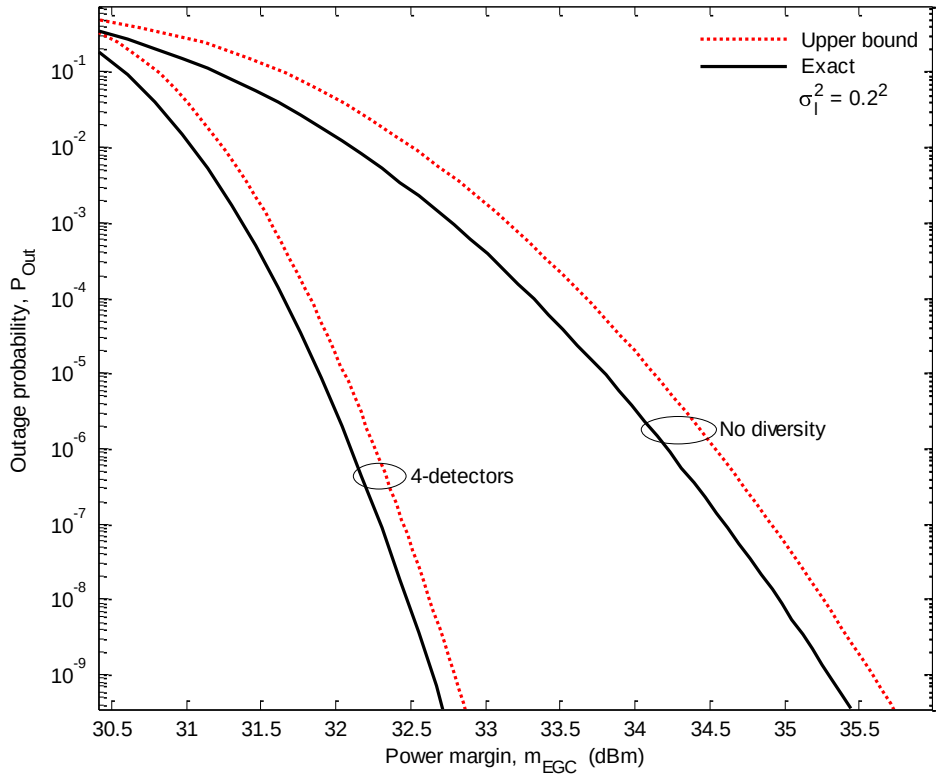

Fig. 7.3: The exact outage probability and its upper bound against the power margin with EGC spatial diversity in weak turbulent atmospheric channel for $\sigma_l^2 = 0.2^2$ and $\mathcal{N} = [1, 4]$.

Expression (7.30), which is the ratio of (6.22) to (7.29), gives the diversity gain based on the EGC linear combining for a given outage probability. The equation is the ratio of the link margin without spatial diversity to that with spatial diversity.

$$Gain = \frac{1}{\mathcal{N}} \exp\left(\sigma_l^2/2 + \mu_u + \sqrt{-2\sigma_l^2 \ln(2P_{out})} - \sqrt{-2\sigma_u^2 \ln(2P_{out})}\right) \qquad (7.30)$$

7.3 Transmitter Diversity in a Log-normal Atmospheric Channel

In this section, the error performance of a SIM-FSO with a multiple optical transmitter and a single photodetector (MISO) is discussed. The sources are assumed sufficiently

spaced so that the photodetector receives uncorrelated optical radiations. To ensure a fair comparison and to maintain a constant power requirement, it is assumed that the power available for a single-transmitter system is equally shared among $\mathcal{M}$-laser transmitters. This requirement is similar to that specified in the preceding section. As such, the irradiance from each optical source is reduced by a factor of $\mathcal{M}$ compared to a single transmitter system. An alternative approach will be for each source in the array to transmit the same power as in a single transmitter system, in this instance, the power requirement is increased by a factor of $\mathcal{M}$. Based on the former, the received signal is obtained as:

$$i(t) = \sum_{i=1}^{\mathcal{M}} \left[\frac{\Re}{\mathcal{M}} I_i \sum_{j=1}^{N} A_j g(t) \cos\left(\omega_{cj} t + \theta_j\right) \right] + n(t) \tag{7.31}$$

Since the optical sources in the array are only separated by few centimetres, the phase shift experienced by the received irradiance due to the path difference is therefore negligible. The SNR on each subcarrier, conditioned on the received irradiance is derived as:

$$\gamma_{MISO}\left(\vec{I}\right) = \left(\frac{\Re A}{\sqrt{2}\mathcal{M}\sigma}\right)^2 \left(\sum_{i=1}^{\mathcal{M}} I_i\right)^2 \tag{7.32}$$

From the obvious similarity between (7.13) and (7.32), it can then be concluded that the unconditional BER for a SIMO system is the same as that of single source with the EGC combined multiple photodetectors.

7.4 Transmitter-Receiver Diversity in a Log-normal Atmospheric Channel

Here, a multiple-source, multiple-photodetector (MIMO) SIM-FSO system will be examined. In consistency with the earlier assumptions, the total transmitted power is equal to the transmitted power when a single optical source is used with the same bit rate. In addition, the combined aperture area of the $\mathcal{N}$ photodetectors is the same as the no spatial diversity case. Moreover, the $\mathcal{M}$ optical sources and the $\mathcal{N}$ photodetectors are assumed well spaced to avoid any correlation in the received signals. First, the received signals are combined using the EGC, and from the preceding section, a MISO system with $\mathcal{M}$ laser sources is said to be identical to an EGC combined SIMO with $\mathcal{M}$ photodetectors, these combined lead to the following as the conditional SNR of the SIM-FSO in MIMO configuration:

$$\gamma_{MIMO}(\vec{I}) = \left(\frac{\Re A}{\sqrt{2}\mathcal{M}\mathcal{N}\sigma}\right)^2 \left(\sum_{i=1}^{\mathcal{N}}\sum_{j=1}^{\mathcal{M}} I_{ij}\right)^2 = \left(\frac{\Re A}{\sqrt{2}\mathcal{M}\mathcal{N}\sigma}\right)^2 \left(\sum_{i=1}^{\mathcal{M}\mathcal{N}} I_i\right)^2 \tag{7.33}$$

This expression is the same as that of an EGC combiner with a total of $\mathcal{M}\mathcal{N}$ photodetectors. Hence, the unconditional BER is obtained by replacing $\mathcal{N}$ in (7.17) by $\mathcal{M}\mathcal{N}$.

If however, the received signals are combined using the MRC linear combining scheme, the conditional SNR on each receiver branch will be:

$$\gamma_i(I_i) = \left(\frac{\Re A}{\sqrt{2\mathcal{N}}\mathcal{M}\sigma}\sum_{j=1}^{\mathcal{M}} I_{ij}\right)^2 \tag{7.34}$$

Considering the fact that the sum of independent lognormal random variables is another log-normal distribution [129], the unconditional BER becomes:

$$P_e = \frac{1}{\pi}\int_0^{\pi/2} [S(\theta)]^{\mathcal{N}}\, d\theta \tag{7.35}$$

where $S(\theta) \approx \frac{1}{\sqrt{\pi}}\sum_{j=1}^{n} w_j \exp\left(-\frac{K_2^2}{2\sin^2\theta}\exp\left[2\left(x_j\sqrt{2}\sigma_{\mathcal{U}} + \mu_{\mathcal{U}}\right)\right]\right)$ and $K_2 = \Re I_0 A/\sqrt{2\mathcal{N}}\,\mathcal{M}\sigma$, while $\sigma_{\mathcal{U}}^2$ and $\mu_{\mathcal{U}}$ are as previously defined by (7.15) with $\mathcal{N}$ replaced by $\mathcal{M}$.

7.5 Results and Discussions of SIM-FSO with Spatial Diversity in a Log-normal Atmospheric Channel

In order to analyse the results obtained so far, a 20th order Hermite polynomial is assumed while the log irradiance variance is assumed to vary between 0.2^2 and unity, (i.e. $0.2^2 \leq \sigma_l^2 \leq 1$). By plotting the BER expressions against the normalised $\text{SNR} = (\Re\xi E[I])^2/\sigma^2$, the link margin $m_{\mathcal{N},\sigma_l}$, defined as the ratio of required SNR with no diversity to that with $\mathcal{N}$ photodetectors at a BER of 10^{-6} and turbulence strength σ_l^2, is obtained. In Fig. 7.4, $m_{\mathcal{N},\sigma_l}$ for BPSK-SIM is plotted against $\mathcal{N}$ for the EGC and SelC techniques for various values of σ_l^2, while $m_{\mathcal{N},\sigma_l}$ for a DPSK pre-modulated SIM is plotted against the fading strength in Fig. 7.5.

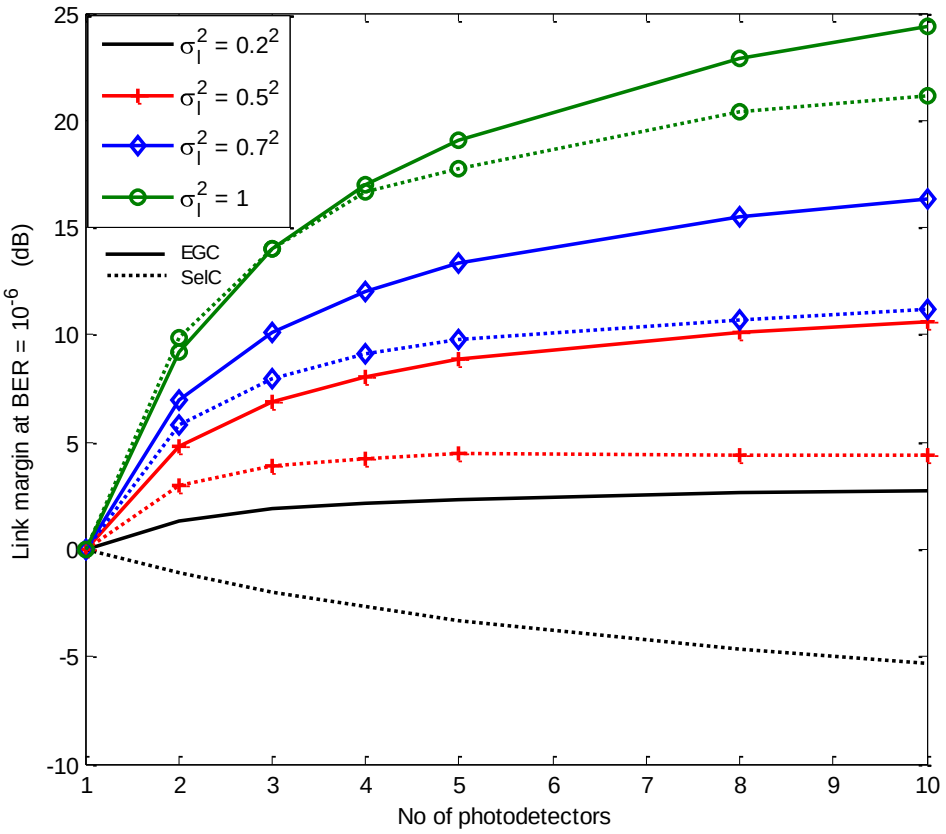

Fig. 7.4: BPSK-SIM link margin with EGC and SelC against number of photodetectors for various turbulence levels and a BER of 10^{-6}.

In both situations, the use of SelC in weak turbulence results in negative link margins. For instance, Fig. 7.5 shows that for $\sigma_l < 0.4$, SelC spatial diversity results in between -2 dB and -7 dB link margin for $2 \leq \mathcal{N} \leq 10$, similarly in Fig. 7.4, it results in a margin of up to -5 dB at $\sigma_l = 0.2$. The negative link margin experienced with SelC can be attributed to the fact that at a very low turbulence level, the effect of reducing the received intensity by a factor of $\mathcal{N}$ on each branch is dominant over the turbulence induced intensity fluctuation.

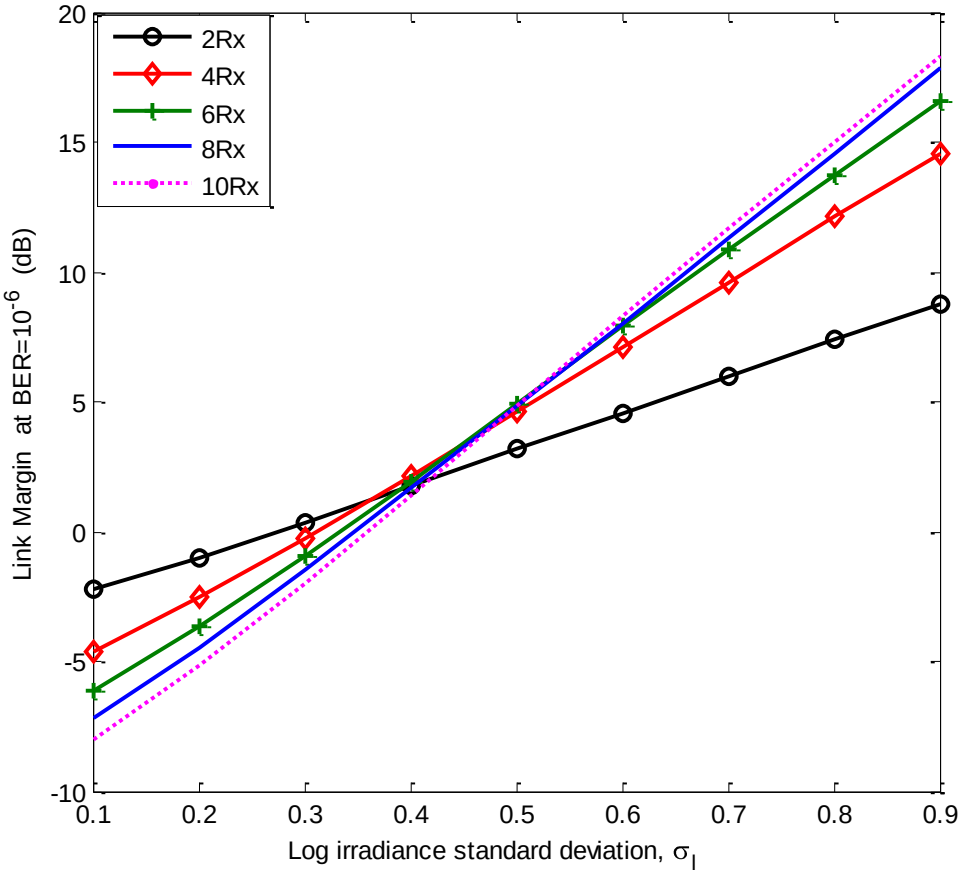

Fig. 7.5: DPSK-SIM with SelC spatial diversity link margin against turbulence strength for $\mathcal{N} = [2, 4, 6, 8, 10]$.

However, as the turbulence level increases beyond $\sigma_l = 0.4$, SelC spatial diversity starts to yield a positive link margin; producing up to 9 dB link margin with two photodetectors in a DPSK pre-modulated SIM link. And for $\sigma_l > 0.2$ in Fig. 7.4, SelC proves worthwhile with positive link margins but the gains are still lower than that obtainable from EGC by about ~1 to ~6 dB depending on the number of photodetectors used. Based on the foregoing, SelC spatial diversity will not be recommended for use on short link FSO experiencing weak irradiance fluctuation.

The performance of EGC and MRC linear combiners is compared in Fig. 7.6, this figure shows very clearly, that the link margin obtainable using the EGC is between 0 and ~2 dB (depending on the turbulence severity) lower than using the complex MRC.

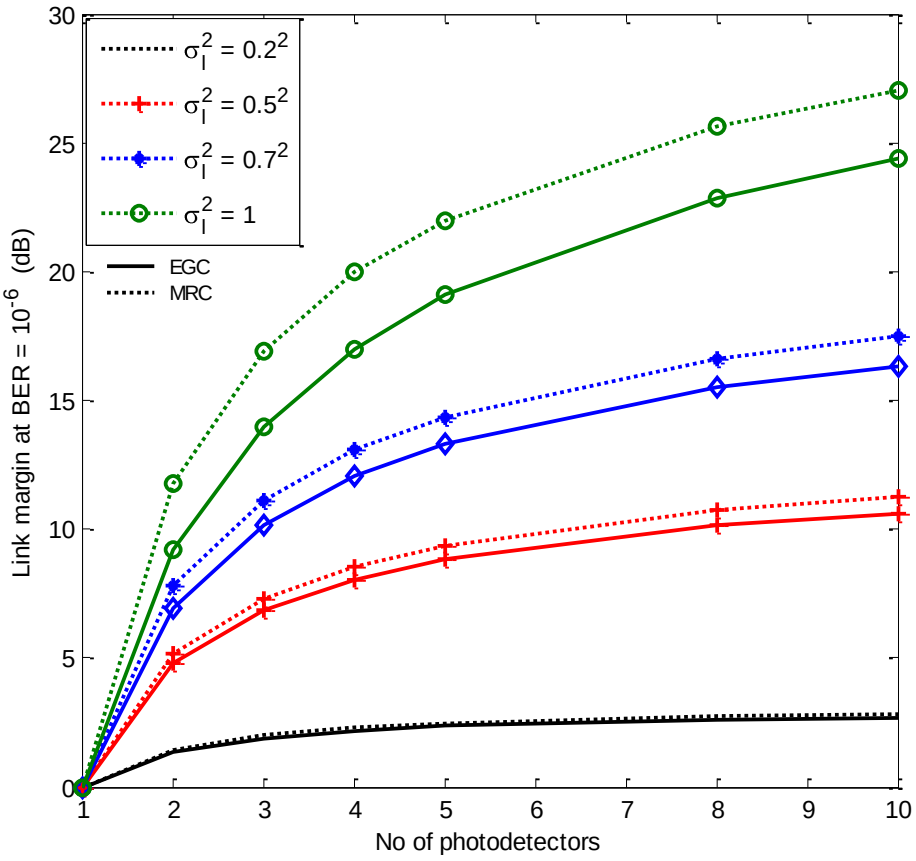

Fig. 7.6: BPSK-SIM diversity link margin with EGC and MRC against number of photodetectors for various turbulence levels and a BER of 10^{-6}.

Using two photodetectors with optimal MRC in atmospheric turbulence with $0.2^2 \leq \sigma_l^2 \leq 1$, has the potential to reduce the SNR required to achieve a BER of 10^{-6} by between ~2 and ~12 dB . With up to four independent photodetectors however, the theoretical link margin for the MRC combiner increases to ~20 dB as shown in Fig. 7.6. Another inference from this figure is that the spatial diversity gain (link margin) becomes more pronounced as scintillation increases; using two detectors with MRC at turbulence level, $\sigma_l = 0.2$ results in a link margin which is ~10 dB lower than at $\sigma_l = 1$.

Also for $\mathcal{N} \geq 4$, the marginal link margin per unit detector ($m_{\mathcal{N},\sigma_l} - m_{\mathcal{N}-1,\sigma_l}$) reduces drastically as the graphs begin to flatten out. For instance, increasing $\mathcal{N}$ from 4 to 10 with MRC across the turbulence levels $0.2^2 \leq \sigma_l^2 \leq 1$ only results in a meagre increase of between 0 and ~6 dB link margin, while increasing $\mathcal{N}$ from 1 to 4 over the same turbulence range results in between ~3 and ~22 dB diversity gain.

The plot of the diversity gain (7.30) at a P_{Out} of 10^{-6} is shown in Fig. 7.7 for different number of photodetectors and log intensity variance. This plot illustrates the gain based on the outage probability metric. From the plot, using two photodetectors result in ~4 dB gain at $\sigma_l^2 = 0.7^2$ and this rises to ~8 dB with $\mathcal{N} = 4$. Beyond four photodetectors, the graphs start to plateau, implying a reduction in the amount of gain recorded for each additional photodetector.

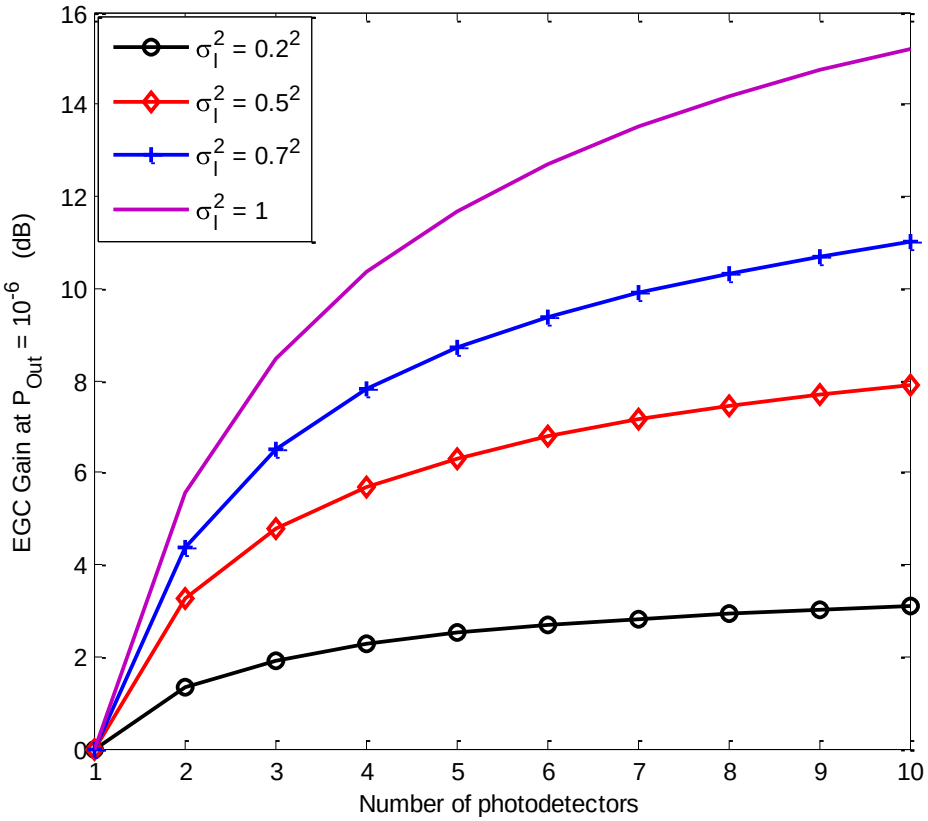

Fig. 7.7: EGC diversity gain in log-normal atmospheric channel against the number of photodetectors at P_{Out} of 10^{-6} and $\sigma_l^2 = [0.2^2, 0.5^2, 0.7^2, 1]$.

To illustrate the impact of signal correlation on the error performance, the combination of (7.25) (7.26) and (7.27) is plotted in Fig. 7.8 for $\mathcal{N} = [2, 3]$, $\rho = [0, 0.1, 0.3, 0.6]$ and $\sigma_l^2 = 0.5^2$. For instance at a BER of 10^{-6}, the use of two photodetectors with correlation coefficients $\rho = 0.3$ and 0.6 requires additional ~1.6 dB and ~3 dB of SNR, respectively compared to when $\rho = 0$. With three photodetectors, the additional SNR required to achieve the same BER of 10^{-6} is ~2.4 dB and ~4.6 dB for $\rho = 0.3$ and 0.6, respectively. This shows that the correlation effect results in a power penalty and this result, by extension, buttresses the need for the photodetector separation to be greater than the spatial coherence length ρ_0, in order to get the most of the spatial diversity technique.

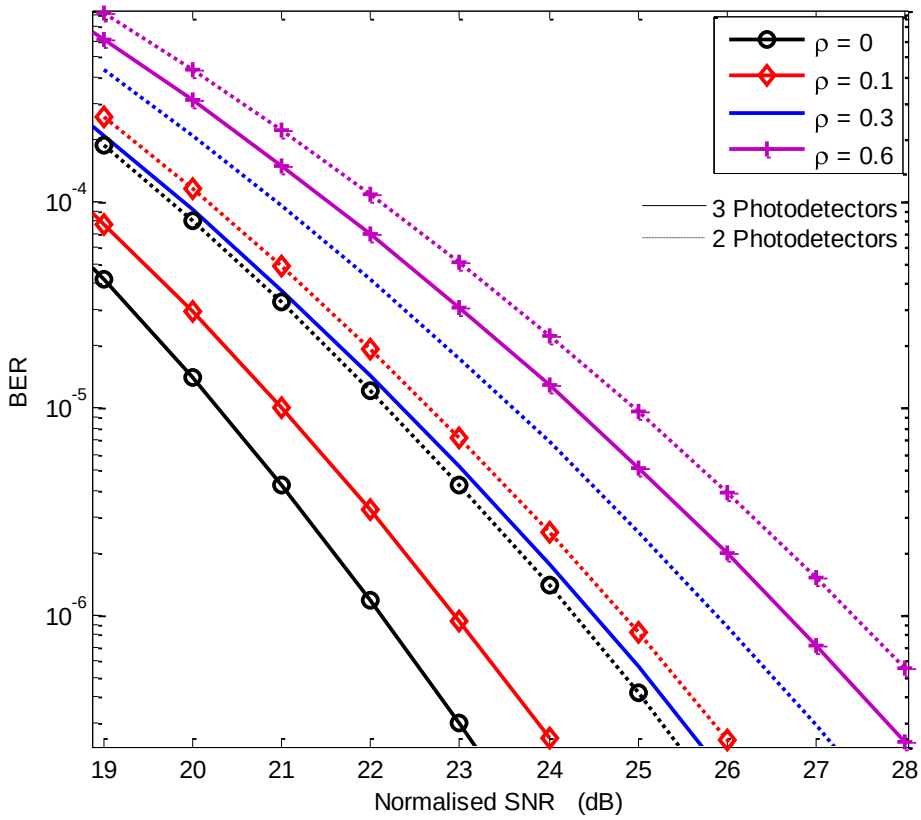

Fig. 7.8: Error performance of BPSK-SIM at different values of correlation coefficient for $\mathcal{N} = [2, 3]$ and $\sigma_l^2 = 0.5^2$.

Furthermore in Fig. 7.9, the plot of (7.35) against the normalised SNR is shown at a turbulence level $\sigma_l^2 = 0.3$ for different values of $\mathcal{N}$ and $\mathcal{M}$. It can be inferred from the plot that at a BER of 10^{-6}, using a 2 × 2 MIMO requires ~0.4 dB of SNR more than employing a 1 × 4-MIMO configuration. However, spacing four photodetectors to ensure that the received signals are uncorrelated is far more demanding and cumbersome than spacing two photodetectors. Also, to achieve a BER of 10^{-6}, the use of 4 × 4-MIMO system requires about ~4 dB and 1 dB less SNR compared with using a lone source with 4 and 8 photodetectors, respectively.

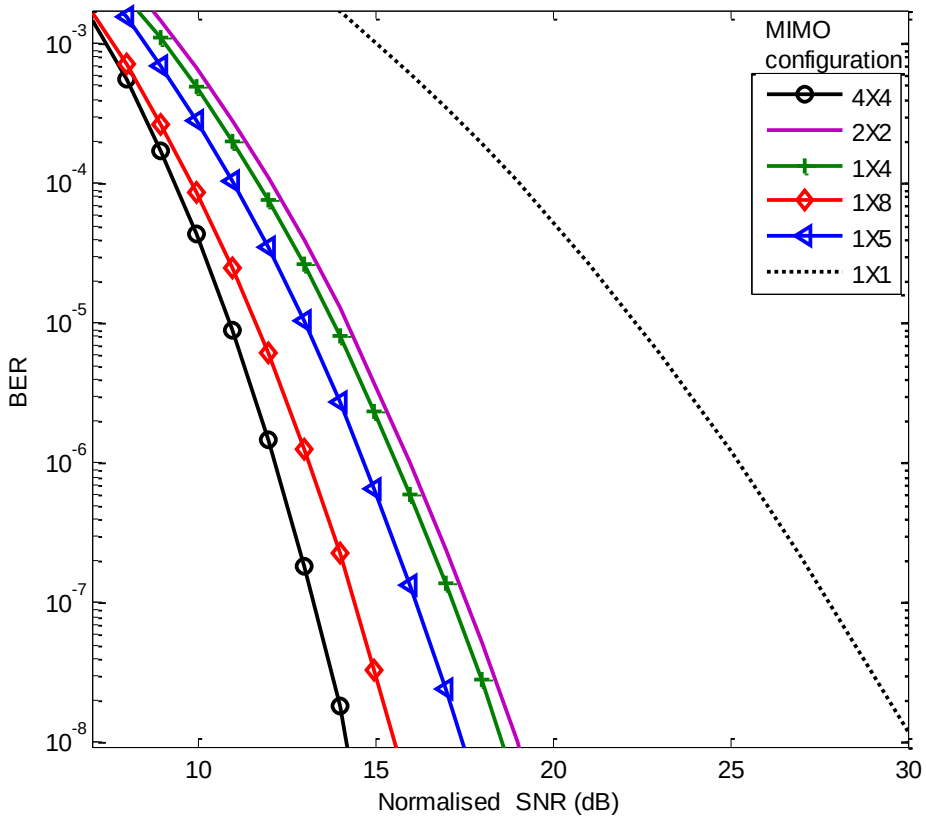

Fig. 7.9: Error performance of BPSK-SIM with MIMO configuration in turbulent atmospheric channel for $\sigma_l^2 = 0.3$.

7.6 SIM-FSO with Receiver Diversity in Gamma-gamma and Negative Exponential Atmospheric Channels

In this section, the performance of SIM-FSO will be analysed in terms of BER and the outage probability based on the gamma-gamma and negative exponential turbulence models. While the results of the previous sections are valid for short FSO links characterised by weak irradiance fluctuation only, the performance analysis of this section will capture the performance of short to very long FSO links.

7.6.1 BER and outage probability of BPSK-SIM with spatial diversity

Following on from section 7.2, the general expression for the unconditional BER of an FSO employing BPSK-SIM with an array of photodetectors can be written as:

$$P_e = \int_0^{\infty} \mathrm{Q}\left(\sqrt{\gamma(\vec{I})}\right) p(\vec{I}) d\vec{I} \tag{7.36}$$

where $\gamma(\vec{I})$ represents the post detection electrical SNR at the BPSK demodulator input and $p(\vec{I}) = \prod_{i=1}^{\mathcal{N}} p(I_i)$ is the joint pdf of the uncorrelated irradiance. In evaluating $\gamma(\vec{I})$, the EGC linear combining technique is considered because of its simplicity, but other linear combining schemes can be used as well. The total noise variance is given by $\sigma_{EGC}^2 = \mathcal{N}\sigma_{Th}^2 + \sigma_{Bg}^2$, using a narrow band optical bandpass filter combined with narrow field of view detectors, the background noise can be reduced considerably to make the thermal noise dominant. Therefore, $\sigma_{Bg}^2 < N\sigma_{Th}^2$ and $\sigma_{EGC}^2 \approx \mathcal{N}\sigma_{Th}^2$. The post detection $\gamma(\vec{I})$ for the thermal noise limited performance at the BPSK demodulator input is thus obtained as:

$$\gamma(\vec{I}) = \frac{\Re^2 A^2}{2\mathcal{N}^3\sigma^2}\left(\sum_{i=1}^{\mathcal{N}} I_i\right)^2 \tag{7.37}$$

The system performance analysis with spatial diversity in weak, moderate and strong turbulence regimes will be based on the gamma-gamma model introduced in chapter four. The gamma-gamma parameters representing each of the stated turbulence regimes are as previously presented in Table 6.3. From the numerical solution of (7.36), the BER can thus be obtained.

In the limit of strong turbulence however, the BER expression based on the simple EGC linear combining can be reduced to single integration as follow. Let the random variable Z represent the sum of $\mathcal{N}$ independent negative exponential variables, that is, $Z = \sum_{i=1}^{\mathcal{N}} I_i$, then the pdf of Z is obtained by adopting the characteristic function method as:

$$p(Z) = \frac{I_0^{-\mathcal{N}} Z^{\mathcal{N}-1} \exp(-Z/I_0)}{\Gamma(\mathcal{N})}, \qquad Z \geq 0 \tag{7.38}$$

The unconditional BER with receiver spatial diversity in a negative exponential turbulent atmospheric channel is now be derived as:

$$P_e = \frac{1}{\pi\Gamma(\mathcal{N})} \int_0^{\pi/2} \int_0^{\infty} Z^{\mathcal{N}-1} \exp(-K_1(\theta)Z^2 - Z) dZ d\theta \tag{7.39}$$

where $K_1(\theta) = (\Re A)^2/4\mathcal{N}^3\sigma^2 \sin^2(\theta)$. Expression (7.39) has no closed form but the multiple integral involved can be eliminated by invoking equation (3.462) reported in [118]. This leads the following equation for the BER of BPSK-SIM in a negative exponential fading channel.

$$P_e = \frac{1}{\pi} \int_0^{\pi/2} \frac{1}{\sqrt{\left(2K_1(\theta)\right)^{\mathcal{N}}}} \exp(1/8K_1(\theta)) D_{-\mathcal{N}}\left(1/\sqrt{2K_1(\theta)}\right) d\theta \tag{7.40}$$

Since (7.40) cannot be further simplified, its upper bound is obtained by maximising the integrand as:

$$P_e \leq \frac{1}{2\sqrt{(2K_1)^{\mathcal{N}}}} \exp(1/8K_1) D_{-\mathcal{N}}\left(1/\sqrt{2K_1}\right) \tag{7.41}$$

where $K_1 = (\Re A)^2/4\mathcal{N}^3\sigma^2$ and D_ρ is the parabolic cylinder function whose definition is available in [118].

The outage probability in the fully developed speckle regime is given by the following:

$$\begin{aligned} P_{Out} &= p\left(\frac{m_{EGC}}{\mathcal{N}}\left(\sum_{i=1}^{\mathcal{N}} I_i\right) < I_0\right) \\ &= p(Z < \mathcal{N}I_0/m_{EGC}) \end{aligned} \tag{7.42}$$

Expression (7.42) is the cumulative distribution function of Z at the specified point and by combining this with (7.38), the outage probability is obtained as:

$$\begin{aligned} P_{out} &= \int_0^{\mathcal{N}/m_{EGC}} p(Z)dZ \\ &= \int_0^{\mathcal{N}/m_{EGC}} Z^{\mathcal{N}-1}\exp(-Z)/\Gamma(\mathcal{N})dZ \end{aligned} \tag{7.43}$$

Equation (7.43) above can be expressed as an implicit function in terms of the incomplete gamma function $\gamma(a, x)$ [118] or as a series as:

$$\begin{aligned} P_{Out} &= \frac{\gamma(\mathcal{N}, \mathcal{N}/m_{EGC})}{\Gamma(\mathcal{N})} \\ &= \frac{1}{\Gamma(\mathcal{N})}\sum_{\ell=0}^{\infty}\frac{(-1)^\ell(\mathcal{N}/m_{EGC})^{\mathcal{N}+\ell}}{\ell!\,(\mathcal{N}+\ell)} \end{aligned} \tag{7.44}$$

where the incomplete gamma function is defined as, $\gamma(a,x) = \int_0^{\mathrm{x}} \exp(-t)t^{a-1}\,dt$.

7.6.1.1 *Results and discussions*

In Fig. 7.10, the BER of BPSK-SIM is plotted against the normalised SNR for two photodetectors under different turbulence regimes. When compared to the results obtained with no spatial diversity, the gain of spatial diversity in mitigating the effect of turbulence induced irradiance fluctuation becomes very clear. A summary of the resulting diversity gains, (i.e. reduction in the SNR), with two and three photodetectors at a BER of 10^{-6} is presented in Table 7.1. As expected, the impact of diversity is least in weak turbulence regime resulting in only 2.6 dB reductions in the SNR at a BER of 10^{-6}. Whereas in strong turbulence regime, the gain in SNR is ~12 dB, increasing to ~47 dB in the saturation regime.

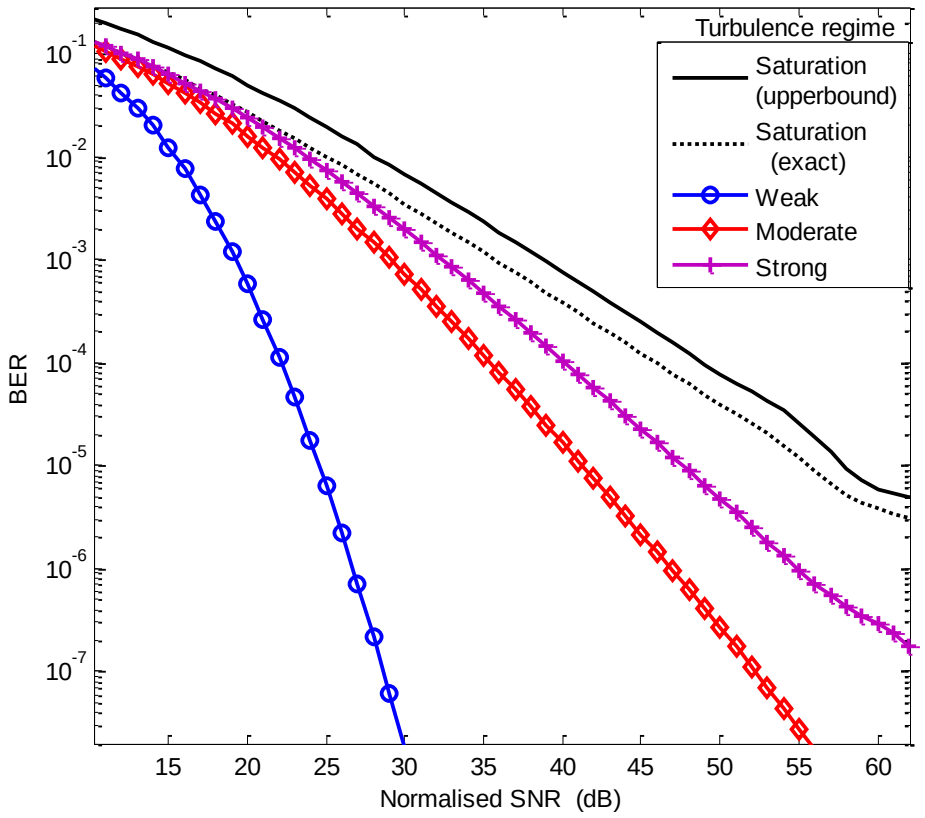

Fig. 7.10: BPSK-SIM error rate against the normalised SNR in gamma-gamma and negative exponential channels for two photodetectors.

As would be expected, the diversity gain is highest in extreme fading conditions since adding more branches will greatly reduce the chance of a catastrophic fading from happening

Table 7.1: Diversity gain at a BER of 10^{-6} in gamma-gamma and negative exponential channels.

Number of photodetectors	**Spatial Diveristy Gain (dB)**		
	Weak	Strong	Saturation
2	2.6	11.6	46.7
3	3.0	21.2	63.6

Figure 7.11 shows the extra power margin required to achieve a certain outage probability P_{Out} with and without spatial diversity in negative exponential atmospheric channels. The gain of employing diversity is apparent from the figure just as the case under the BER performance metric. For instance at a P_{Out} of 10^{-6}, a diversity gain of almost 30 dB is predicted and this increases to ~43 dB with four photodetectors. This significant gain is down to the fact that with multiple photodetectors, more independent irradiances are received.

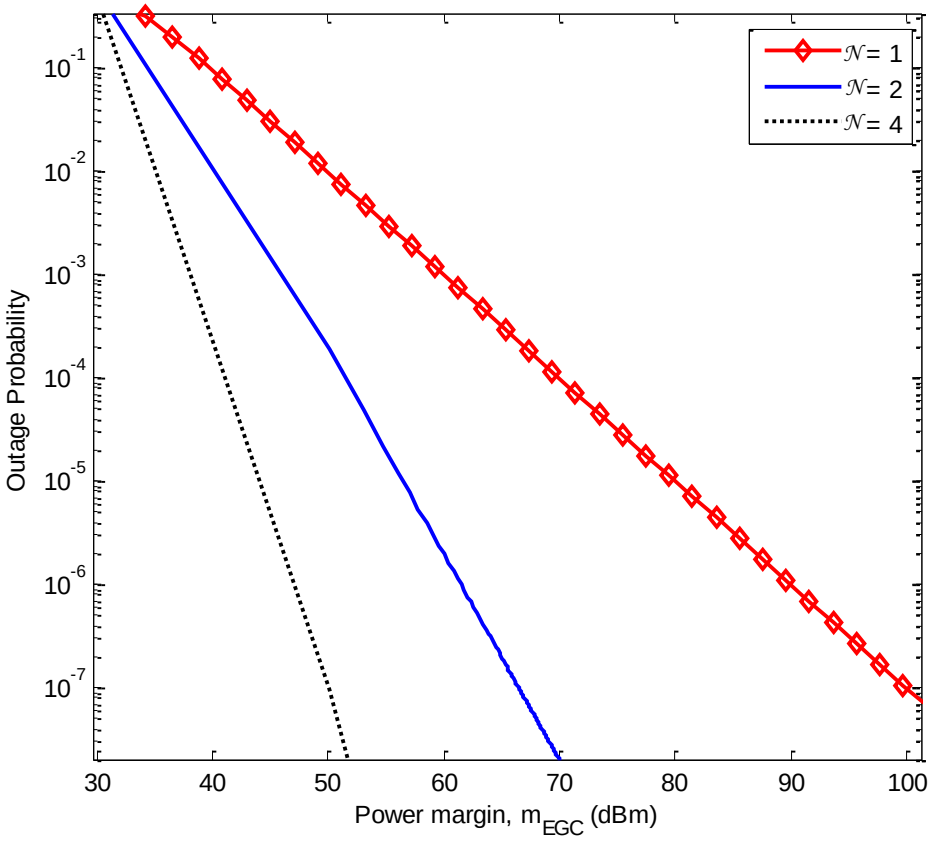

Fig. 7.11: The outage probability as a function of power margin m_{EGC} (dBm) for $\mathcal{N} = [1, 2, 4]$ in negative exponential channel.

For the sake of comparison, the predicted spatial diversity gains based on both metrics, (BER and outage probability), are shown in Fig. 7.12 as a function of the number of photodetectors. For both metrics, it is observed that as the number of photodetectors increases beyond four, the diversity gains start to plateau. Although P_{Out} and BER are different by definition, they both result in a similar conclusion. It should however be mentioned that using an array of photodetectors adds to the cost and design complexity.

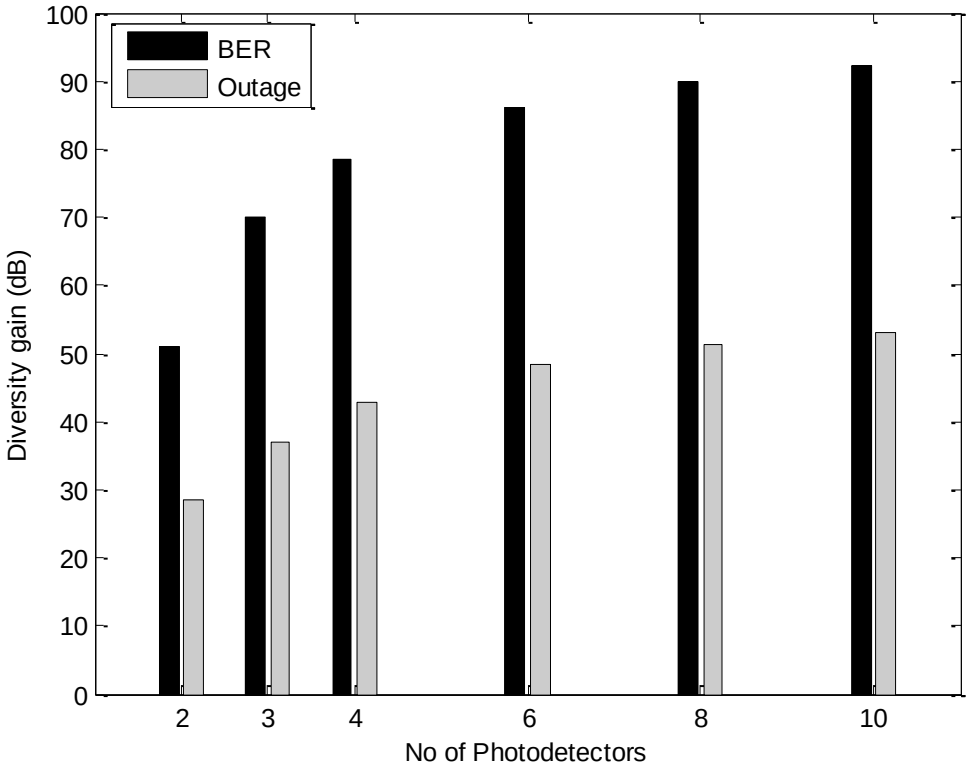

Fig. 7.12: Diversity gain against number of independent photodetectors at BER and P_{Out} of 10^{-6} in negative exponential atmospheric channel.

7.6.2 BER and outage probability of DPSK-SIM in negative exponential channels

For a DPSK pre-modulated subcarrier with an array of photodetectors, the most suitable linear combining scheme will be the SelC. This is because in DPSK demodulation, the absolute phase information of the subcarrier is not available and it is only the SelC that does not require the subcarrier phase information. The SNR for a SIM-FSO with SelC is given by (7.45) while the unconditional BER for a DPSK-SIM in a negative exponential channel is given by (7.46).

$$\gamma_{SelC}(I) = \frac{\Re^2 A^2 I^2}{2\mathcal{N}\left(\mathcal{N}\sigma_{Th}^2 + \sigma_{Bg}^2\right)} \tag{7.45}$$

$$P_{e(SelC)} = \int_0^{\infty} \frac{1}{2} \exp\left(-\frac{\gamma_{SelC}(I)}{2}\right) p(I_{max}) dI \tag{7.46}$$

The pdf, $p(I_{max}) = p\left(max\{I_i\}_{i=1}^{\mathcal{N}}\right)$ in a negative exponential channel model given by (7.47) is obtained by first finding the cumulative distribution function of I_{max} at an arbitrary point and then differentiating. The resulting pdf is given by (7.47) and the detailed proof presented in Appendix D.

$$p(I_{max}) = \frac{\mathcal{N}}{I_0} \exp\left(-\frac{I}{I_0}\right)\left(1 - \exp\left(-\frac{I}{I_0}\right)\right)^{\mathcal{N}-1} \tag{7.47}$$

The plot of the pdf of I_{max} is shown in Fig. 7.13 for different values of $\mathcal{N}$.

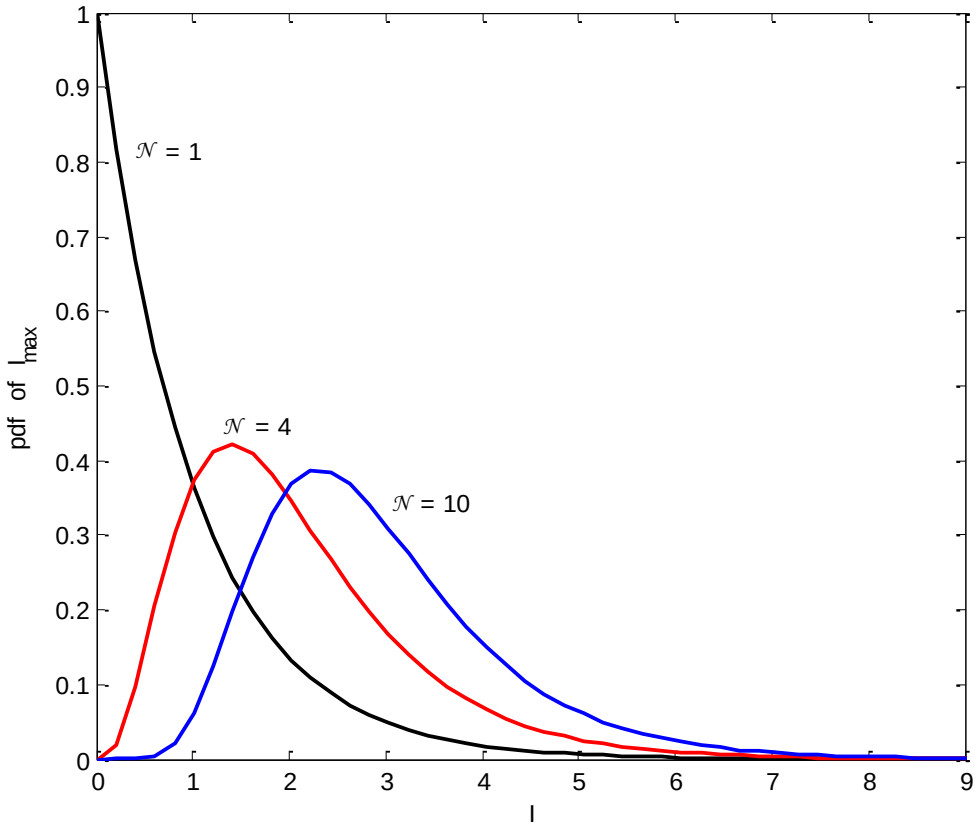

Fig. 7.13: The pdf, $p\left(max\{I_i\}_{i=1}^{\mathcal{N}}\right)$ for $\mathcal{N} = [1, 4, 10]$, and I_0 = 1 in a negative exponential channel.

From the combination of (7.45), (7.46) and (7.47), an expression for the error performance of a DPSK-SIM laser communication system in fully developed speckle atmospheric channel is obtained as:

$$P_{e(SelC)} = \int_0^\infty \frac{\mathcal{N}}{2I_0}\left(1 - \exp\left(-\frac{I}{I_0}\right)\right)^{\mathcal{N}-1} \exp\left(-\frac{I}{I_0} - \frac{\Re^2 A^2 I^2}{2\mathcal{N}\left(\mathcal{N}\sigma_{Th}^2 + \sigma_{Bg}^2\right)}\right) dI \qquad (7.48)$$

Now the received irradiance I_0 needed to attain an outage probability $P_{Out} = P(\gamma(I) < \gamma^*)$ in a negative exponential atmospheric channel without diversity is given by (7.49). In arriving at this equation, the threshold SNR has been taken as, $\gamma^* = (\Re A I^*)^2/2\sigma^2$ where I^* is the receiver sensitivity required to attain the threshold BER*.

$$I_0 = \frac{I^*}{\ln(1 - P_{Out})^{-1}} \qquad (7.49)$$

With an array of PIN photodetectors employing SelC in a negative exponential atmospheric channel, the received irradiance $I_{0(SelC)}$ needed to attain a given P_{Out} is derived from the combination of (7.45), and (7.47), as:

$$I_{0SelC} = \frac{I^*}{\ln\left(1 - \sqrt[\mathcal{N}]{P_{Out}}\right)^{-1}} \left(\frac{\mathcal{N}\left(\mathcal{N}\sigma_{Th}^2 + \sigma_{Bg}^2\right)}{\sigma_{Th}^2 + \sigma_{Bg}^2}\right)^{1/2} \qquad (7.50)$$

From the foregoing, the diversity gain I_0/I_{0SelC} can thus be obtained.

7.6.2.1 *Results and discussions*

The numerical simulations presented in this section are based on the parameters of Table 7.2. In Fig. 7.14, the error performance of DPSK-SIM in a negative exponential channel, obtained from (7.48), is shown as a function of the average irradiance. This plot brings to bear the potential gain of SelC in reducing the required sensitivity for a given BER under very strong fading conditions. For example, to achieve a BER of 10^{-6} with no diversity, about 23 dBm of received irradiance is required while with two photodetectors , about -1.7 dBm is needed to achieve the same level of performance. Moreover, as the number of photodetectors increases, the attained diversity gain per additional detector reduces. For instance, for $\mathcal{N} = 2$, the gain per detector at a BER of 10^{-6} is ~12 dB and this reduces to about 5 and 4 dB for $\mathcal{N} = 2$ and 10, respectively. These results are summarised in Table 7.3 for up to 10 photodetectors.

Table 7.2: Numerical simulation parameters

Parameter	**Value**
Symbol rate R_b	155 – 625 Mbps
Spectral radiance of the sky $N(\lambda)$	10^{-3} W/cm^{2}μmSr
Spectral radiant emittance of the sun $W(\lambda)$	0.055 W/cm^{2}μm
Optical band-pass filter bandwidth $\Delta\lambda$ @ λ = 850 nm	1 nm
PIN photodetector field of view FOV	0.6 rad
Radiation wavelength λ	850 nm
Number of Photodetectors $\mathcal{N}$	$1 \leq \mathcal{N} \leq 10$
Load resistance R_L	50 Ω
PIN photodetector responsivity $\Re$	1
Operating temperature T_e	300 K

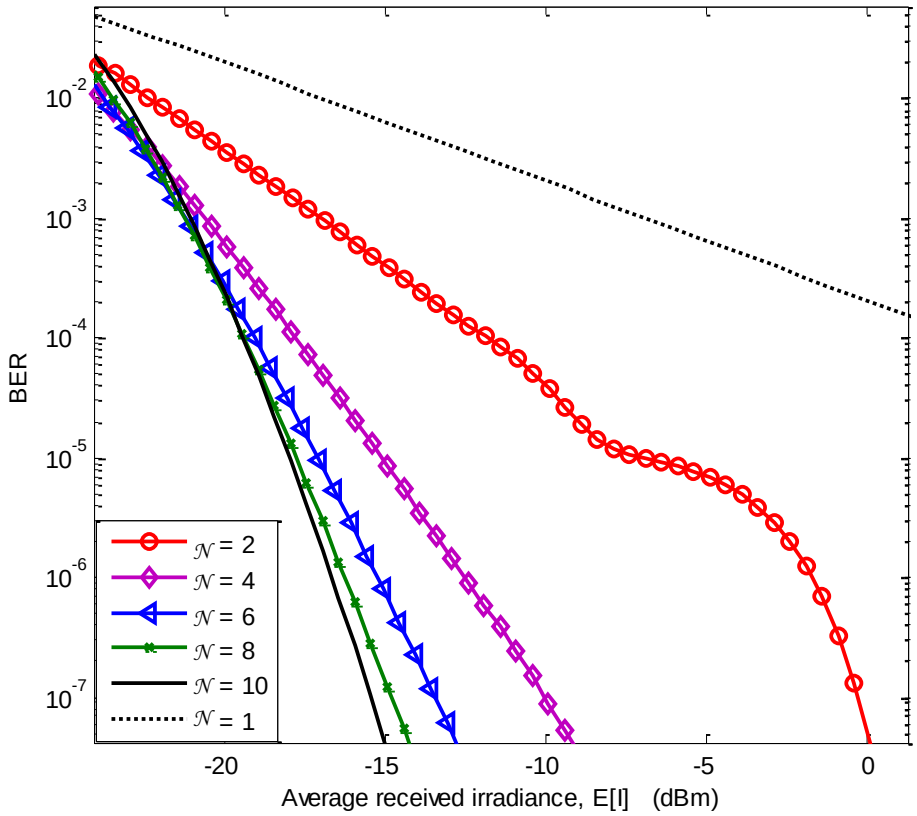

Fig. 7.14: Error rate of DPSK-SIM against the average received irradiance with spatial diversity in negative exponential channel for $\mathcal{N} = [2, 4, 6, 8, 10]$.

Table 7.3: Gain per photodetector at a BER of 10^{-6}

$\mathcal{N}$	1	2	4	6	8	10
Average Irradiance (dBm)	23.1	-1.7	-12.5	-15.2	-16.2	-16.7
Gain (dB) per $\mathcal{N}$	0	12.4	8.9	6.4	4.9	4.0

In discussing the outage probability in negative exponential fading channels, (7.50) is plotted in Fig. 7.15. In this plot, the threshold average irradiance I^* is assumed to be 0 dBm. This graph shows that for a very long SIM-FSO link, whose channel fading is modelled by the negative exponential distribution, achieving an outage probability of 10^{-6} or better will require a minimum of 60 dBm received irradiance without SelC.

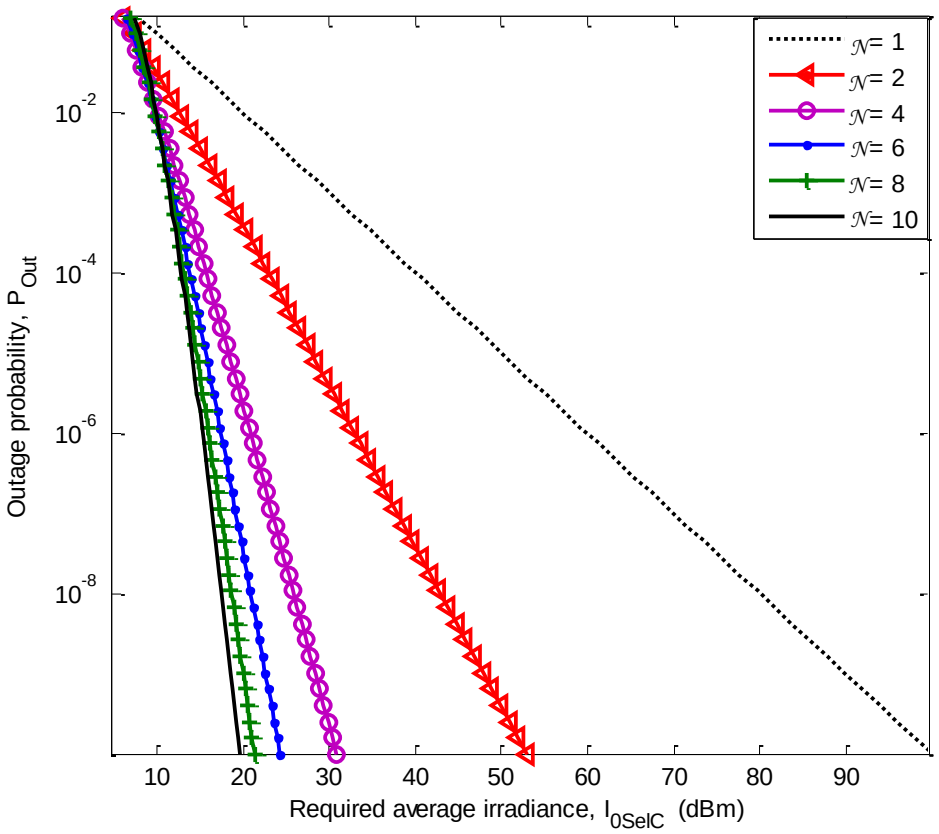

Fig. 7.15: Outage probability against the average irradiance with SelC spatial diversity in negative exponential channel for I^* = 0 dBm and $\mathcal{N} = [1, 2, 4, 6, 10]$.

This power requirement reduces to ~35 dBm and ~23 dBm, respectively, with 2 and 4 photodetectors that are combined using the SelC. To further illustrate the gain of using SelC in the saturation regime, Figs. 7.16 and 7.17 show the predicted diversity gain at different values of P_{Out} and $\mathcal{N}$. With 2 photodetectors and an outage probability of 10^{-6}, the maximum predicted gain per detector is about 14 dB. This predicted gain is even observed to be higher at lower values of P_{out}. This makes sense, as the use of diversity in a fading channel increases the received signal strength and by extension lowers the outage probability. And in Fig. 7.17, it is clearly shown that the gain (dB) per detector peaks at $\mathcal{N} = 2$ and then decreases very rapidly beyond $\mathcal{N} = 4$.

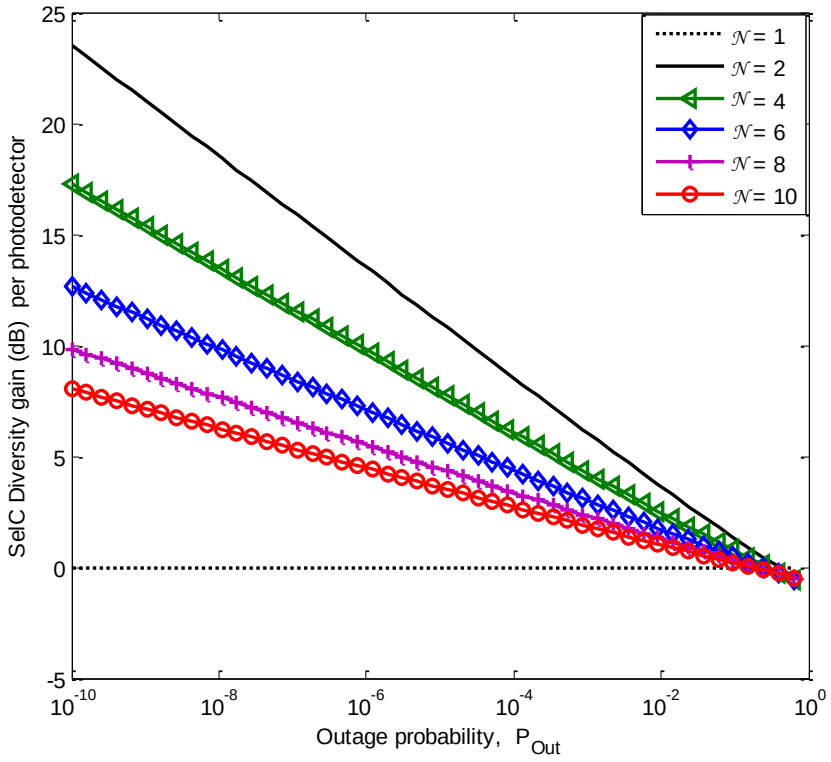

Fig. 7.16: Predicted SelC diversity gain per photodetector against P_{out} in saturation regime for $\mathcal{N} = [1, 2, 4, 6, 10]$.

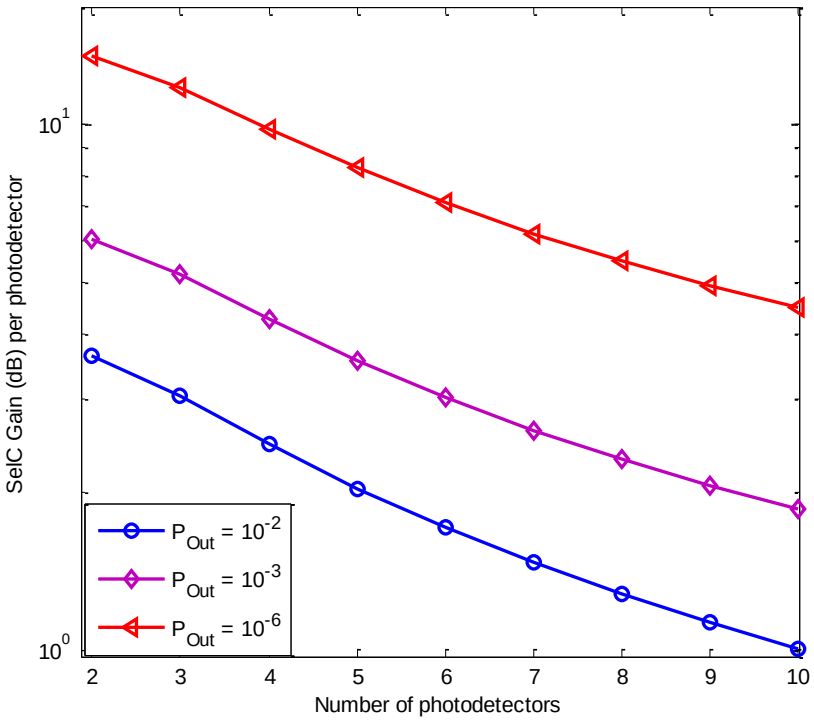

Fig. 7.17: Predicted SelC diversity gain (dB) per photodetector for P_{Out} = [10^{-6}, 10^{-3}, 10^{-2}] in saturation regime.

Although up to 10 photodetectors have been shown in the results above, this is mainly for illustration purpose. The use of such a large number of detectors will pose serious implementation difficulties, as they all have to be spaced beyond the spatial coherence distance in order to avoid any signal correlation. An interesting point to note from these results is that, in contrast to the short range links where the use of SelC is not worthwhile, it is highly recommended in very long range links, as it results in a significant reduction in the required receiver sensitivity especially when the photodetector is kept to a maximum of four. This is due to the fact that the irradiance fading experienced in a fully developed speckle regime is dominant over the reduction in the received irradiance due to the reduction in the receiver aperture area. Any scheme that mitigates this dominant irradiance fading will clearly result in improved performance. The predicted average irradiance and diversity gains presented above are valid for as long as the photodetectors received signals are uncorrelated. That is, $\rho_0 < s < \theta_s L$ where θ_s is the divergence angle of the optical source in milliradians and L is the link length in kilometres. For $s < \rho_0$, the received irradiances are correlated and diversity gain is lower as previously discussed in section 7.2.4.

7.7 SIM-FSO with Subcarrier Time Delay Diversity

In the previous sections, spatial diversity has been discussed as a means of ameliorating the deleterious impact of a turbulent atmosphere, an improvement of about 22 dB in electrical SNR has been reported from the use of a four-detector system in weak turbulence. But this gain is only achievable when the detectors are physically separated by a distance greater than the turbulence coherence length, whose value is in the order of centimetres and depends on the turbulence strength. Likewise, the use of aperture averaging requires the receiver aperture to be several times the turbulence coherence

length. This does not only make the system bulky, it is cumbersome and not always feasible.

In this section, subcarrier time delay diversity (TDD) is proposed as an alternative means of mitigating channel fading in SIM-FSO links. The subcarrier TDD can equally be used together with the spatial diversity techniques in order to achieve a more resilient system. The conventional use of multiple subcarriers is to increase throughput/capacity via subcarrier multiplexing. In the proposed TDD scheme however, dissimilar subcarriers are used to transmit delayed copies of the original data as shown in Fig. 7.18. The proposed subcarrier TDD scheme has an advantage of simplicity and low cost, to achieve a reasonable diversity gain compared to schemes such as the adaptive optics or forward error correction. In addition, reduction in the throughout associated with the temporal diversity scheme can be compensated for by employing subcarrier multiplexing.

The TDD scheme relies solely on the statistical temporal variation of the atmospheric turbulence induced fading. Turbulent eddies responsible for the fading are frozen in space and only move across the beam path by the wind speed component perpendicular to the propagation direction, this is according to Taylor frozen turbulence hypothesis [45]. Thus from the knowledge of the average wind speed transverse to the direction of beam propagation, the spatial statistics of turbulence can be translated into temporal statistics. Following which the temporal covariance function of the irradiance fluctuations can be obtained [130]. The temporal covariance is useful in determining the correlation time τ_0 defined as the e^{-1} point on the normalised covariance function. τ_0 for weak turbulence has been reported in various experiments to measure between 3 ms and 15 ms [130].

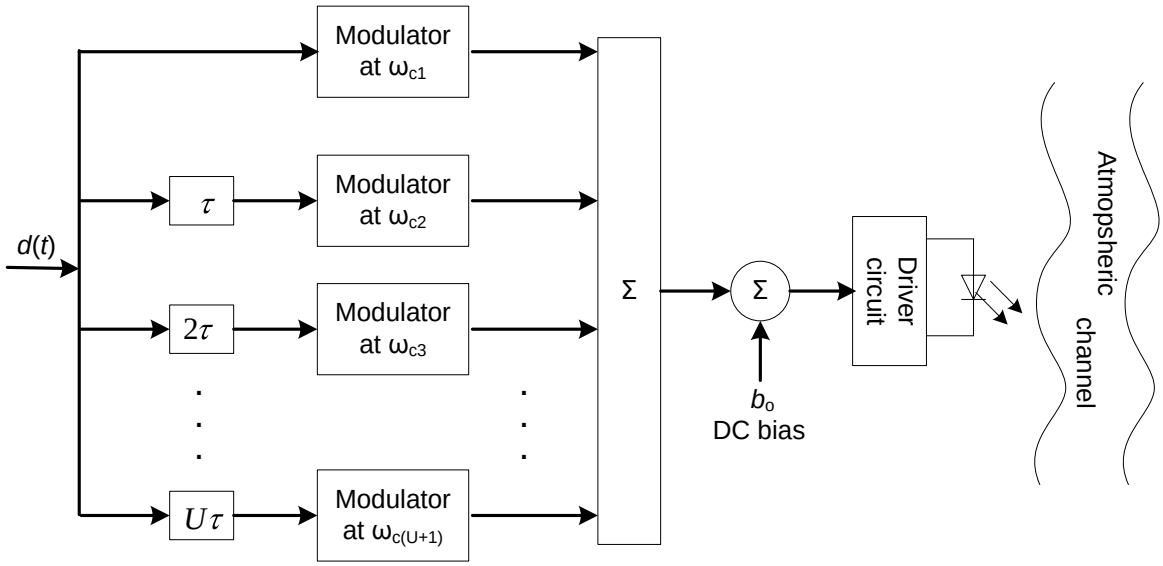

(a)

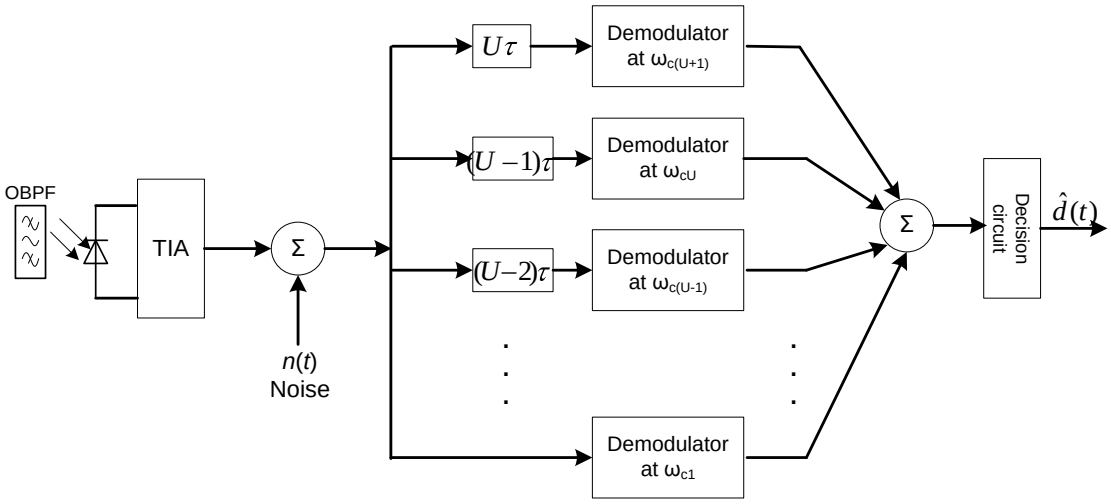

(b)

Fig. 7.18: Proposed subcarrier TDD block diagram: (a) transmitter, and (b) receiver

Apart from re-transmitting the delayed version of the original data on different subcarriers, other viable options include using different wavelengths or polarisations for the retransmission. These two options have previously been investigated and reported in [130-132].

7.7.1 Error performance with the subcarrier TDD

In the following analysis, it is assumed that $\tau \geq \tau_0$. The minimum required buffer size τR_b, which is now a part of the communication parameters, has to be determined prior to transmission. To illustrate the system error performance with the proposed TDD, the BPSK-SIM system with a single data carrying subcarrier and *U*-TDD paths will be considered and the turbulent atmosphere modelled using the log-normal distribution. During the j^{th} symbol, the received signal, prior to coherent demodulation on each branch is given by:

$$i_i = R\xi A d_j I_i \cos w_{cU+2-i}(t-(U+1-i)\tau) + n_i(t) \qquad i=1,2...U+1, \tag{7.51}$$

where $d_j \in \{-1, 1\}$. The standard RF coherent demodulator employed extracts the reference carrier needed to down convert the received signal to its base band equivalent from the incoming signal. The sum of the demodulator outputs is then fed into the decision circuit, see Fig. 7.18. The electrical SNR is then derived from the foregoing as:

$$\gamma(\vec{I}) = \frac{(\Re\xi)^2 P_m}{\sigma^2}\left(\sum_{i=1}^{U+1} I_i\right)^2 \tag{7.52}$$

where $P_m = \frac{A^2}{2T}\int_0^T g^2(t)\,dt$ and the noise variance $\sigma^2 = \sigma_{Bg}^2 + (U+1)\sigma_{Th}^2$, since there are now $(U+1)$ demodulation paths associated with one PIN photodetector. It should be noted that $\xi = 1/(U+1)A$ is the minimum modulation depth needed to avoid clipping distortions with the addition of *U*-TDD paths. With the sum of independent log-normal variables being another log-normal variable, replacing $\mathcal{N}$ by $(U+1)$ in (7.15) results in the following unconditional BER expression for the BPSK-SIM link with *U*-TDD:

$$P_e = \int_0^\infty \mathrm{Q}\left(\sqrt{\frac{(\Re\xi I_0)^2 P_m Z^2}{\sigma_{Bg}^2 + (U+1)\sigma_{Th}^2}}\right)\frac{1}{\sqrt{2\pi}\sigma_{\mathcal{U}}}\frac{1}{Z}\exp\left(-\frac{(\ln Z - \mu_{\mathcal{U}})^2}{2\sigma_{\mathcal{U}}^2}\right)dZ$$
$$= \frac{1}{\sqrt{\pi}}\sum_{i=1}^{n} w_i \mathrm{Q}\left(\sqrt{K_3}\exp\left[x_i\sqrt{2}\sigma_{\mathcal{U}} + \mu_{\mathcal{U}}\right]\right) \quad (7.53)$$

where $K_3 = \frac{(\xi\Re I_0)^2 P_m}{\sigma_{Bg}^2 + (U+1)\sigma_{Th}^2}$. The penalty due to atmospheric turbulence induced fading at a given BER with and without TDD can now be obtained from the plot of this equation. The TDD is simple to implement but at the cost of increased communication latency and an apparent reduction in throughput which is proportional to the number of additional delay paths used. The use of subcarrier multiplexing can however compensate for this reduction in throughput. A by-product of subcarrier TDD that is too grave to be ignored is the IMD due to laser transmitter inherent non-linearity. The impact of this on the error performance is discussed next.

7.7.2 Performance of multiple-SIM with TDD and intermodulation distortion

The effect of IMD when *U* additional subcarrier(s) is/are used per channel for retransmission of delayed version of the data is examined here. The proposed TDD technique apparently increases the amount of IMD, since the total number of subcarriers is now increased to $N(U+1)$. Also the CINR and indeed the BER per subcarrier are also impaired by the additional IMD from the *U*-delay paths, this is in contrast to the multiple-SIM of Section 6.5, in which IMD resulted from the use of *N* subcarrier channels only. Following the approach of section 6.5, the CINR with subcarrier TDD is then be derived as:

$$\mathrm{CINR}\left(\xi,\vec{I}\right)=\frac{\left(\Re\left(\xi+\frac{3}{4}\mathrm{a}_3\xi^3[2(U+1)N-1]\right)\sum_{i=1}^{U+1}I_i\right)^2}{2(U+1)\sigma^2+2\Re\mathrm{a}_3^2\xi^6\sum_{i=1}^{U+1}I_i^2\,\sigma_{IMD3i}^2} \tag{7.54}$$

In the above equation $\sigma^2 \approx \sigma_{Th}^2$. The average CINR and the unconditional BER can be obtained by substituting (7.54) in (6.41) and (6.43), respectively. An illustration of the behaviour of the $\mathrm{CINR}_{ave}(\xi)$ and BER as a function of the modulation depth is shown in Fig. 7.19(a) for a 12-subcarrier FSO link with and without TDD. From this figure, the optimum modulation index that either maximises the CINR_{ave} or minimises the BER metric can be obtained. This figure is then used to arrive at the optimum BER graph of Fig. 7.19(b), which shows very clearly the superiority of a SIM-FSO with TDD in terms of BER over a SIM-FSO link with no TDD.

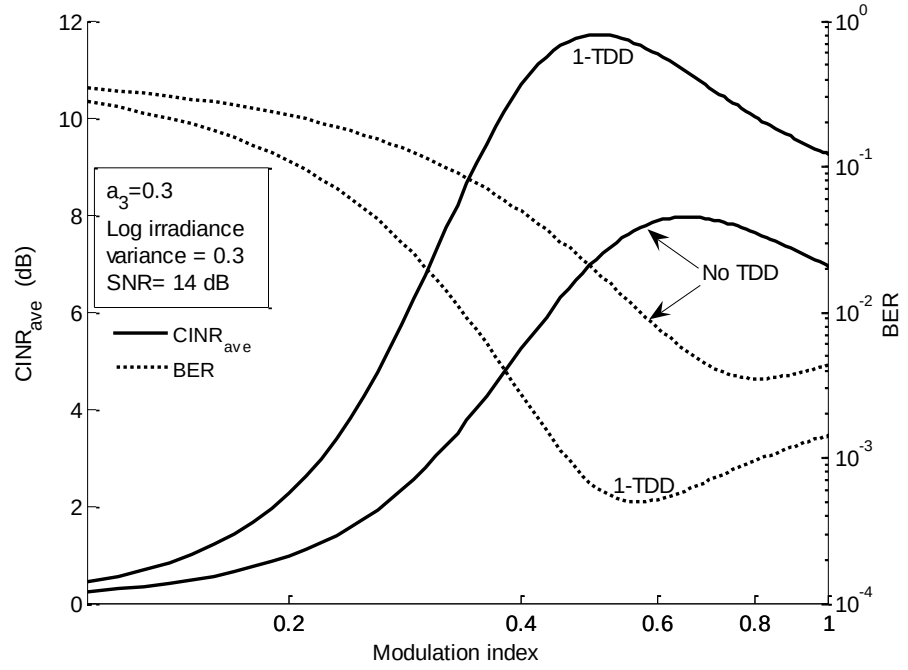

(a)

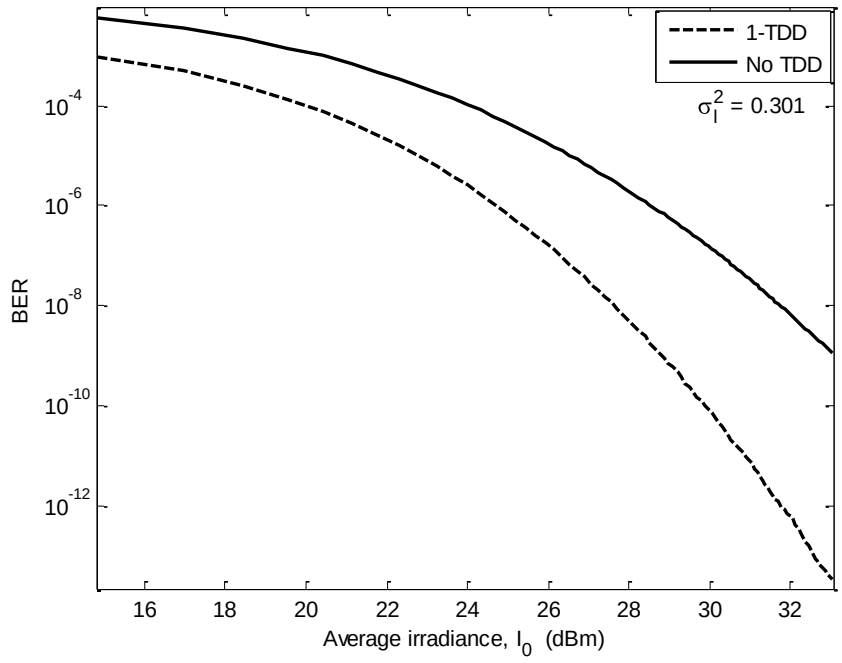

(b)

Fig. 7.19: Performance of 12-subcarrier FSO link with and without TDD (a) average CINR and BER as a function of modulation index at 14 dB SNR, and (b) optimum BER against I_0 for $\sigma_I^2 = 0.3$, $a_3 = 0.3$, and $\ell = k = 1$.

7.7.3 Subcarrier TDD results and discussions

Based on the same simulation parameters given in Table 7.2, the error performance with and without TDD as a function of the average irradiance I_0 is shown in Fig. 7.20. This plot shows that the required irradiance decreases as the number of temporal diversity paths increases. To determining the optimum number of diversity paths required, the diversity gain (difference in the average irradiance with and without TDD) and the fading penalties (difference in the average irradiance with and without fading) are summarised in Table 7.4. The table shows explicitly that at $\sigma_I^2 = 0.3$, the highest TDD gain per additional path of 2 dB is obtained with 1-TDD. It is interesting to note that the gain per unit path decreases as more paths are added.

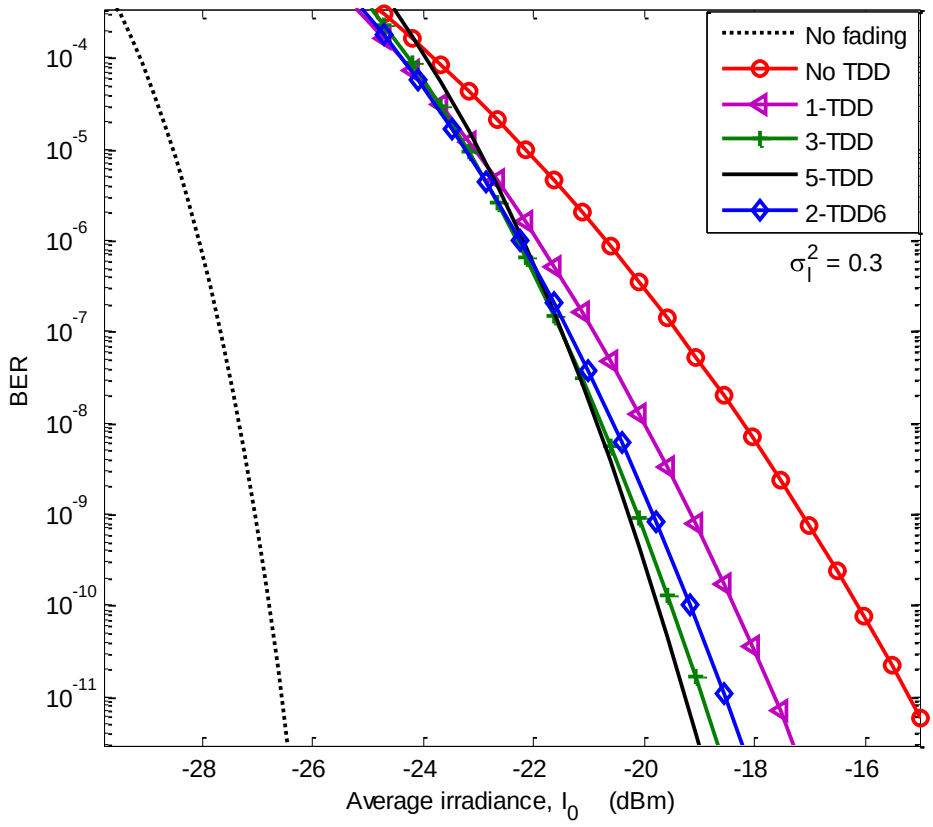

Fig. 7.20: Error performance of BPSK-SIM against I_0 at 155 Mbps and $\sigma_I^2 = 0.3$ with no fading and with/without TDD.

This makes sense, because the modulation index has to be reduced as more paths are added, in order to keep the laser within its dynamic range. The conclusion that single retransmission is the optimum seems to be independent of how the TDD scheme is implemented. A similar conclusion was previously reported when the delayed data was retransmitted on different polarizations/wavelengths [130, 132]. Henceforth, only 1-TDD will be considered because retransmitting a delayed copy of the data more than once is less efficient in fading channels.

Table 7.4: Fading penalty and TDD gain at BER = 10^{-9}, $\sigma_l^2 = 0.3$, $N = \xi = 1$.

	No TDD	**1-TDD**	**2-TDD**	**3-TDD**	**5-TDD**
I_0 **(dBm)** (no fading: -27.05)	-17.17	-19.17	-19.85	-20.13	-20.3
Fading penalty (dB)	9.88	7.88	7.2	6.92	6.75
Diversity gain (dB) (gain / unit path)	0 (0)	2 (2)	2.68 (1.34)	2.96 (0.99)	3.13 (0.63)

Based on (7.53) with $\xi = 1/(U+1)A$ and N = 1, it is shown in Fig. 7.21 that for a given level of error performance, the required average irradiance and indeed the diversity gain both increase as the fading strength increases. However, the fading penalties and diversity gains are independent of the data rate. For instance, at $\sigma_l^2 = 0.1$ the estimated gains and fading penalties with 1-TDD stand at 0.36 dB and ~4.2 dB respectively for both symbol rates 155 Mbps and 625 Mbps and these increase to 3 dB and ~11 dB at a fading strength of $\sigma_l^2 = 0.5$ irrespective of the data rate.

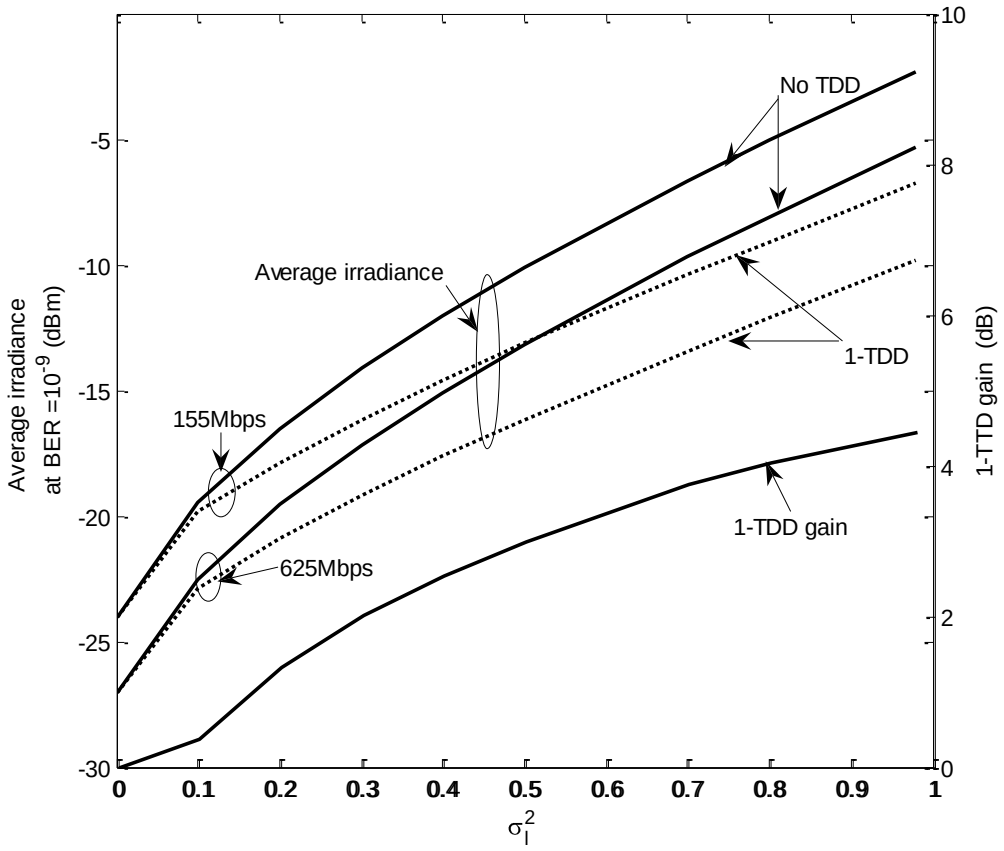

Fig. 7.21: Average irradiance and 1-TDD gain for different turbulence strength, $R_b = [155, 625]$ Mbps and $N = 1$.

With IMD, there exists a certain ξ_{opt} that produces an optimal BER performance as illustrated in Fig. 7.19, but evaluating this ξ_{opt} will require the system to be self adaptive. That is, it will have to track the channel parameters in demodulating every symbol. This will ultimately make the system more complex and less attractive, just as the optimum OOK, thereby negating a major justification of SIM. In order to illustrate the impact of IMD on the error performance with and without TDD, a fixed ξ will be considered. This leads to the result depicted in Fig. 7.22, from which it is observed that IMD imposes a floor on the error performance, thereby limiting the achievable level of performance.

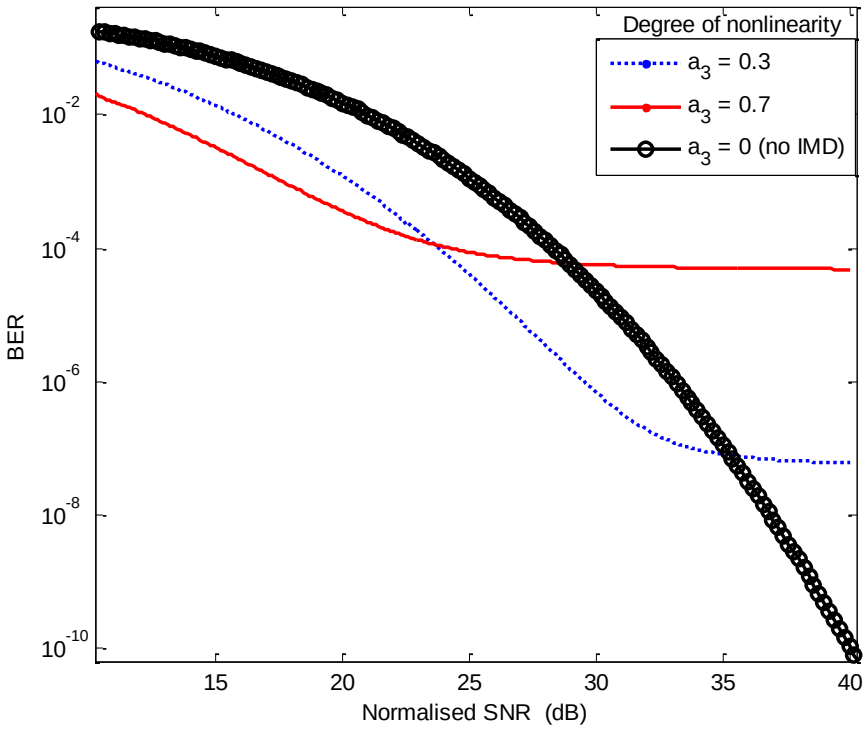

(a)

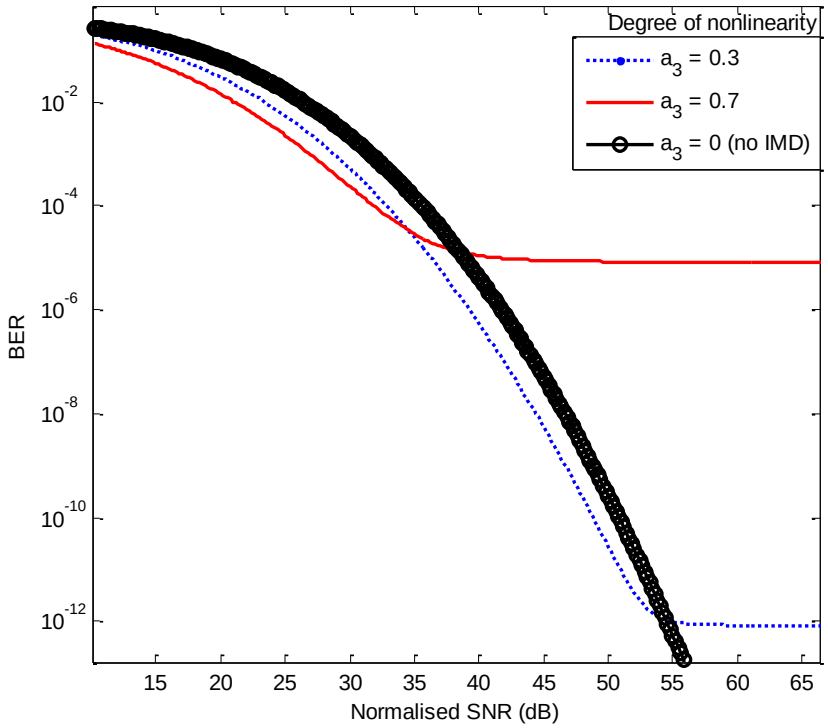

(b)

Fig. 7.22: Error performance against the normalised SNR for N = 12, $a_3 = [0.3, 0.7]$, $\sigma_i^2 = 0.3$ and $\xi = 0.3$ (a) with 1-TDD, and (b) with no TDD.

The value of the BER floor depends, expectedly, on the degree of nonlinearity of the optical source. For instance, with a nonlinearity degree $a_3 = [0.7]$ and N = 12, the BER floors for a link with 1-TDD and no TDD are ~10^{-4} and ~10^{-5}, respectively. These floor values reduce to ~10^{-7} and 10^{-12}, respectively with a much more linear source with $a_3 = [0.3]$. The BER floor for 1-TDD system under the influence of IMD is observed to be higher than with no TDD simply because of the increased IMD accompanying the TDD technique, although a SIM-FSO with 1-TDD still has higher CINR and lower BER than without TDD before the floor is reached. It can thus be concluded that IMD places a limit on the achievable link performance by imposing a BER floor on the system. This further emphasises the desire and need for a linear laser transmitter in a SIM-FSO system with multiple subcarriers.

7.8 Summary

In this chapter the error performance and outage probability of a SIM-FSO system employing spatial diversity to combat the channel fading have been presented. The following fading channel models have been considered: log-normal, gamma-gamma and negative exponential. An expression for the unconditional BER of $\mathcal{N}$x$\mathcal{M}$-MIMO FSO system that uses PSK subcarrier intensity modulation in turbulent atmosphere has equally been derived. The error performance and the obtainable link margin using three different linear combining techniques were also presented. Results showing clearly the effect of correlated received irradiance on the system error performance have also been given. In a single transmitter and 2-photodetector system at $\sigma_l^2 = 0.5^2$, a correlation coefficient of 0.6 between the received irradiances results in additional ~3 dB of SNR to achieve a BER of 10^{-6}. And this additional SNR increases as the correlation between the

received signals increases.

The use of SelC in a single source-multiple photodetector system in very weak turbulence ($\sigma_l^2 \leq 0.2^2$) has been shown to result in a negative link margin and therefore is not suggested as the sole means of mitigating scintillation. It has also been illustrated that a multiple transmitter-single photodetector system is in effect a single transmitter-multiple photodetector configuration employing EGC linear combining, and that a reasonable number of independent photodetectors to mitigate scintillation without overwhelming complexity can be put at between two and four. Using a 2 x 2-MIMO system requires ~0.5 dB of *SNR* more than using 4-photodetector with single transmitter at a BER of 10^{-6} but spacing an array of 4-photodetector sufficiently to ensure uncorrelated irradiance reception is far more demanding than spacing 2-photodetector. Also the use of 4 x 4-MIMO requires ~3 dB and ~0.8 dB of SNR less than using 4 and 8-photodetector, respectively with single optical transmitter at the same BER of 10^{-6}.

The subcarrier TDD as an alternative technique for ameliorating the channel fading has equally been introduced and its error performance analysed. It has been shown that up to 3 dB improvement in the receiver sensitivity can be achieved by re-transmitting the delayed copy of the data five times in a channel of turbulence strength $\sigma_l^2 = 0.3$. Retransmitting the delayed copy of the information just once is however found to be the optimum with a gain of up to 4.5 dB in weak atmospheric turbulence. Expectedly, the TDD gain was shown to be proportional to the fading strength but independent of the data rate. It has also been shown that the IMD, caused by the optical source nonlinearity, imposes a limit on the achievable BER of SIM-FSO. For SIM-FSO with multiple subcarriers therefore, a linear laser source (one with negligible nonlinearity) is much desired.

Chapter Eight

Link Budget Analysis

8.1 Introduction

The link budget is useful in estimating the theoretical power limited link range of a communication system. In doing this, the various loss mechanisms experienced in a terrestrial FSO link will be examined and discussed in this chapter. The principal source of power loss in an FSO system, which is due to the constituents of the atmosphere, will be discussed. Other losses mentioned in this chapter include the geometric loss, pointing loss and optical loss due to imperfections in the lenses used in the design of the system. Any other unforeseen power losses due to component ageing or component replacement

are catered for with the inclusion of link margin in the link budget analysis. Also the expected level of performance, based on the outage probability or the BER performance metrics, will be considered in determining the sensitivity of the receiver.

8.2 Power Loss

For optical radiation travelling through the atmospheric channel, the interaction between the photons and the molecular constituent of the atmosphere cause some of the photons to be extinguished while particulate constituents scatter the photons. These events ultimately result in a power loss mechanism otherwise described by the Beer-Lambert law. This law describes the transmittance of an optical field through the atmosphere as function of the propagation distance. In addition, optical radiation traversing the atmosphere spreads out due to diffraction, causing the size of the received beam to be greater than the receiver aperture. These factors, combined with others herein discussed are responsible for the difference between the transmitted and the received optical powers.

8.2.1 Atmospheric channel loss

The atmospheric channel attenuates the field traversing it as a result of absorption and scattering processes. The concentrations of matter in the atmosphere, which result in the signal attenuation, vary spatially and temporally, and will depend on the current local weather conditions. For a terrestrial FSO link transmitting an optical signal through the atmosphere, the received irradiance at a distance L from the transmitter is related to the transmitted irradiance by the Beer-Lambert's law as [79]:

$$\tau(\lambda, L) = \frac{P_R}{P_T} = \exp[-\gamma_T(\lambda)L] \tag{8.1}$$

where $\gamma_T(\lambda)$ and $\tau(\lambda, L)$ represent the total attenuation/extinction coefficient (m^{-1}) and the transmittance of the atmosphere at wavelength λ, respectively. The attenuation of the optical signal in the atmosphere is due to the presence of molecular constituents (gases) and aerosols. The aerosol is made up of tiny particles of various shapes ranging from spherical to irregular shapes suspended in the atmosphere. The attenuation coefficient is the sum of the absorption and the scattering coefficients from aerosols and molecular constituents of the atmosphere, it follows therefore that [20]:

$$\gamma_T(\lambda) = \alpha_m(\lambda) + \alpha_a(\lambda) + \beta_m(\lambda) + \beta_a(\lambda) \tag{8.2}$$

The first two terms represent the molecular and aerosol absorption coefficients, respectively while the last two terms are the molecular and aerosol scattering coefficients respectively.

a) *Absorption* – This takes place when there is an interaction between the propagating photons and molecules (present in the atmosphere) along its path. Some of the photons are extinguished and their energies converted into heat [32]. The absorption coefficient depends very much on the type of gas molecules and their concentration [79]. Absorption is wavelength dependent and therefore selective. This leads to the atmosphere having transparent zones – range of wavelengths with minimal absorptions – referred to as the transmission windows as shown in Fig. 8.1. Since it is not possible to change the physics of the atmosphere, the wavelengths used in FSO are basically chosen to coincide with

the atmospheric transmission windows [31]. The attenuation coefficient is therefore dominated by scattering and as such $\gamma_T(\lambda) \cong \beta_a(\lambda)$.

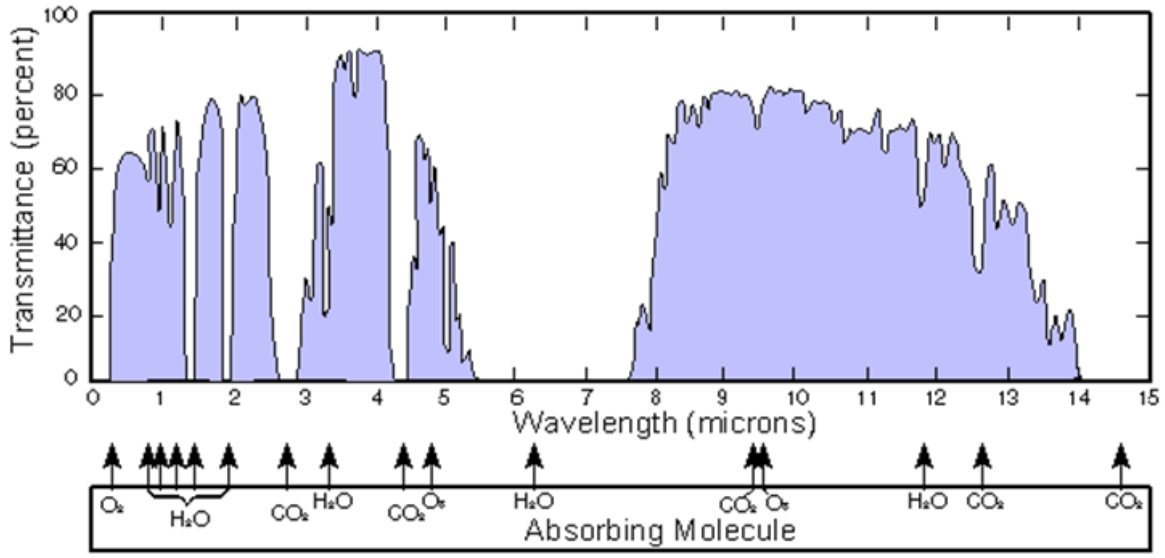

Fig. 8.1: Atmospheric absorption transmittance over a sea level 1820 m horizontal path [20].

b) *Scattering* – This results in angular redistribution of the optical field with and without wavelength modification. The scattering effect depends on the radius r of the particles (fog, aerosol) encountered during propagation. One way of describing this is to consider the size parameter $x_0 = 2\pi r/\lambda$. If $x_0 \ll 1$, the scattering process is classified as Rayleigh scattering [133]; if $x_0 \approx 1$ it is Mie scattering and for $x_0 \gg 1$, the scattering process can then be explained using the diffraction theory (geometric optics). The scattering process for different scattering particles present in the atmosphere is summarised in Table 8.1.

Table 8.1: Typical atmospheric scattering particles with their radii and scattering process at λ = 850 nm

Type	**Radius (μm)**	**Size Parameter x_0**	**Scattering Process**
Air molecules	0.0001	0.00074	Rayleigh
Haze particle	0.01 – 1	0.074 – 7.4	Rayleigh – Mie
Fog droplet	1 – 20	7.4 – 147.8	Mie – Geometrical
Rain	100 – 10000	740 – 74000	Geometrical
Snow	1000 – 5000	7400 –37000	Geometrical
Hail	5000–50000	37000 – 370000	Geometrical

8.2.1.1 *Rayleigh scattering*

A simplified expression describing Rayleigh scattering is given by [134]:

$$\beta_{Rayleigh}(\lambda) = 0.827 N_p A_p^3 \lambda^{-4} \tag{8.3}$$

where N_p is the number of particles per unit volume along the propagation path and A_p represents the cross-sectional area of scattering. The λ^{-4} proportionality of the Rayleigh scattering suggests that the shorter wavelengths get scattered more; this effect is what is responsible for the blue colour of the sky during the day.

8.2.2.1 *Mie scattering*

Mie scattering occurs when the particle size is comparable to the beam size and as the fog particle size compares very much with the wavelength band of interest in FSO (0.5 μm – 2 μm), this makes fog the major photon scatterer and Mie scattering the dominant scattering process in terrestrial FSO systems. Based on the assumptions that the scattered light has the same wavelength as the incident light, only single scattering occurs while the multiple scattering effects are neglected, and that the particles are spherical in shape and are acting independently with a complex refractive index in space, the following expression for the Mie scattering was derived in [6] as:

$$\gamma_T(\lambda) \cong \beta_a(\lambda) = 10^5 \int_0^\infty Q_d\left(\frac{2\pi r}{\lambda}, \acute{n}\right) \pi r^2 n(r) dr \tag{8.4}$$

where r is the particle (fog, aerosol etc.) radius in centimetres, Q_d is the Mie scattering efficiency, $\acute{n}$ is real part of the complex refractive index and $n(r)$ is the volume concentration that is the number of fog particles per unit volume per unit increment in radius. Here, $\beta_a(\lambda)$ is the specific attenuation measured in dB/km and is calculated by summing up the attenuation effect of all the individual fog droplets present per unit volume per unit increase in radius.

The particles encountered in the atmosphere have complex shapes and orientations and applying the theory of Mie scattering to these atmospheric particles is therefore very complicated. Henceforth, the description of attenuation due to scattering will be based on reported empirical formulae. These empirical equations are often expressed in terms of the visibility range V in km. The visibility range is the distance that a parallel luminous beam travels through in the atmosphere until its intensity drops to 2% of its original value [135]. It is measured with an instrument called the transmissiometer and a commonly used empirical model for Mie scattering is given by:

$$\beta_a(\lambda) = \frac{3.91}{V}\left(\frac{\lambda}{550}\right)^{-\delta} \tag{8.5}$$

where δ is given by (8.6) and Table 8.2 gives the international visibility range and attenuation in the visible waveband for different weather conditions.

Kim model

$$\delta = \begin{cases} 1.6 & V > 50 \\ 1.3 & 6 < V < 50 \\ 0.16V + 0.34 & 1 < V < 6 \\ V - 0.5 & 0.5 < V < 1 \\ 0 & V < 0.5 \end{cases}$$

Kruse model

$$\delta = \begin{cases} 1.6 & V > 50 \\ 1.3 & 6 < V < 50 \\ 0.585V^{1/3} & V < 6 \end{cases} \quad (8.6)$$

Table 8.2: International visibility range and attenuation coefficient in the visible waveband for various weather conditions [78].

International Visibility Code				
Weather conditions	**Precipitation**	**mm/hr**	**Visibility (m)**	**Attenuation (dB/km)**
			0	
Dense fog			50	315
Thick fog			200	75
Moderate fog			500	28.9
Light fog	Snow Storm	100	770	18.3
Very light fog			1,000	13.8
	Strong rain	25	1,900	6.9
Light mist			2,000	6.6
	Average rain	12.5	2,800	4.6
			4,000	3.1
Very light mist	Light rain	2.5	5,900	2
			10,000	1.1
Clear air	Drizzle	0.25	18,100	0.6
			20,000	0.54
Very clear air			23,000	0.47
			50,000	0.19

Recently, Al Naboulsi [36] in his work came up with equations 8.7(a-b) as a simple relationship for estimating the advection and radiation (or convection) fog attenuation in the 690 – 1550 nm wavelength band and 50 – 1000 m visibility range.

$$\alpha_{Advection}(\lambda) = \frac{0.11478\lambda + 3.8367}{V} \tag{8.7a}$$

$$\alpha_{Radiation}(\lambda) = \frac{0.18126\lambda^2 + 0.13709\lambda + 3.7502}{V} \tag{8.7b}$$

where λ is in nm and V is in metres. The power loss due to rain and snow are so low compared to that due to the Mie scattering, they still have to be accounted for in the link margin during the link budget analysis. A typical rainfall of 2.5 cm/hour could result in an attenuation of ~6 dB/km [125] while a typical value for attenuation due to light snow to blizzard is 3 dB/km to 30 dB/km [20]. In early 2008 in Prague, Czech Republic, the fog attenuation was measured and compared with the empirical fog attenuation models. This result is shown in Fig. 8.2, with a visibility of less than 200 m, corresponding to thick fog, the attenuation at the location is ~200 dB/km. The empirical models provide a reasonable fit to the measured values with a maximum of about $\pm$5 dB/km difference between any two empirical models.

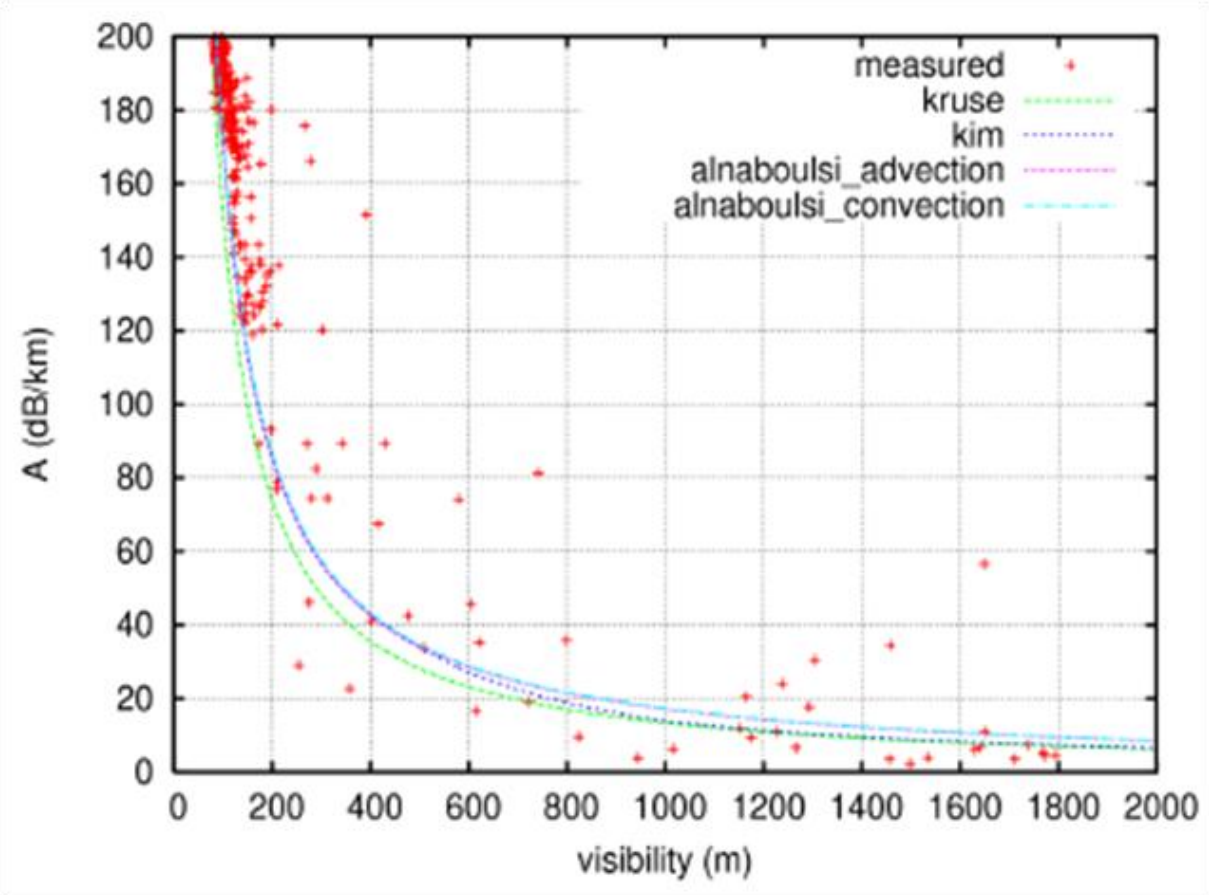

Fig. 8.2: Measured attenuation coefficient as a function of visibility range at $\lambda = 830$ nm in early 2008, Prague, Czech Republic,[136].

8.2.2 Beam divergence

One of the main advantages of FSO systems is the ability to transmit a very narrow optical beam, thus offering enhanced security, but due to diffraction, the beam spreads out. This results in a situation in which the receiver aperture is only able to collect a fraction of the beam and hence beam divergence loss.

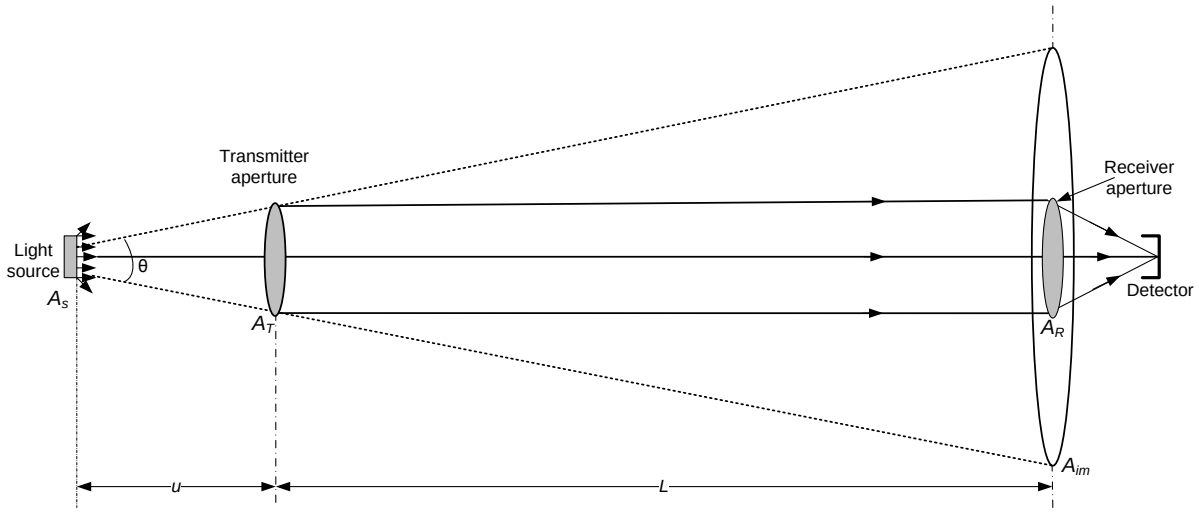

Fig. 8.3: Beam divergence

Considering the arrangement of a free-space optical communication link of Fig. 8.3, and by invoking the thin lens approximation to the diffuse optical source whose irradiance is represented by I_s, the amount of optical power focused on the detector is derived as [137]:

$$P_R = \frac{I_s A_T A_D}{L^2 A_s} \tag{8.8}$$

where A_T and A_D are the transmitter and receiver aperture areas, respectively while A_s is the area of the optical source. This clearly shows that a source with high radiance I_s/A_s and wide apertures are required in order to increase the received optical power.

For a non-diffuse, small source such as the laser, the size of the image formed at the receiver plane is no longer given by the thin lens approximation; it is determined by diffraction at the transmitter aperture. The diffraction pattern produced by a uniformly illuminated circular aperture of diameter d_T is known to consist of a set of concentric rings. The image size is said to be diffraction limited when the radius of the first

intensity minimum or dark ring of the diffraction pattern becomes comparable in size with the diameter d_{im} of the normally focussed image [137]. That is:

$$d_{im} = \frac{L}{u} d_s < 1.22 \frac{\lambda L}{d_T} \tag{8.9}$$

Therefore,

$$d_s < 1.22 \frac{\lambda u}{d_T} \approx 1.22 \frac{\lambda f}{d_T} \tag{8.10}$$

The equation above shows that for diffraction to be the sole cause of beam divergence (diffraction limited), the source diameter $d_s < 1.22 \frac{\lambda f}{d_T}$. A laser being inherently collimated and coherent normally produces a diffraction-limited image. The diffraction limited beam divergence angle in radians is thus given by $\theta_b \cong \frac{\lambda}{d_T}$. If the transmitter and receiver effective antenna gains are respectively given by:

$$G_T = \frac{4\pi}{\Omega_b} \tag{8.11a}$$

$$G_R = \frac{4\pi A_T}{\lambda^2} \tag{8.11b}$$

And the free-space path loss is given by:

$$\mathcal{L} = \left(\frac{\lambda}{4\pi L}\right)^2 \tag{8.12}$$

The received optical power then becomes:

$$P_R = P_T \mathcal{L} G_T G_R = P_T \frac{4A_D}{L^2 \Omega_b} \cong P_T \left(\frac{4}{\pi}\right)^2 \frac{A_T A_D}{L^2 \lambda^2} \tag{8.13}$$

where the radiation solid angle $\Omega_b \cong \frac{\pi \theta_b^2}{4}$. The diffraction limited beam spreading/geometric loss in dB is thus given by:

$$L_{Geom} = -10 \left[\log\left(\frac{A_T A_D}{L^2 \lambda^2}\right) + 2\log\left(\frac{4}{\pi}\right)\right] \tag{8.14}$$

The same result given by (8.14) can be obtained by substituting $A_{im} = \theta_b L$ for the image size in $P_R = P_T \frac{A_D}{A_{im}}$. In order to reduce the diffraction-limited beam divergence, a beam expander of the type shown in Fig. 8.4, in which the diffracting aperture has been increased, can then be used. The beam expander reduces the beam divergence loss and increases the received signal power in the process.

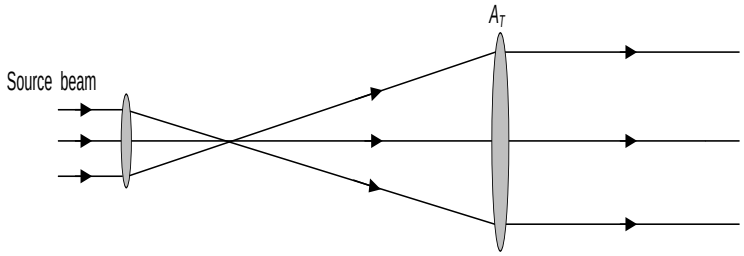

Fig. 8.4: Typical beam expander

For most practical sources, the beam divergence angle is usually greater than that dictated by diffraction and for a source with an angle of divergence θ_s, the beam size at a distance L away is $(d_T + \theta_s L)$. The fraction of the received power to the transmitted power is therefore given as:

$$\frac{P_R}{P_T} = \frac{A_D}{A_{Im}} = \frac{d_R^2}{(d_T + \theta_s L)^2} \tag{8.15}$$

The geometric loss in dB is thus:

$$L_{Geom} = -20 \log \left[\frac{d_R}{(d_T + \theta_s L)} \right] \tag{8.16}$$

The beam spreading loss for the diffraction limited source given by (8.14) is, expectedly, lower than that of the non-diffraction limited case represented by (8.16), this is because the image size is smaller by d_T in the diffraction limited case.

From the foregoing, it is clear that a source with a very narrow angle of divergence is preferable in terrestrial FSO systems. It should however be mentioned that, wide divergence angle sources are desirable in short range FSO links to ease the alignment requirement, compensate for building sway and eliminate the need for active tracking systems at the expense of increased geometric loss apparently. A typical FSO transceiver has optical beam divergence in the range of 2–10 mrad and 0.05–1.0 mrad (equivalent to a beam spread of 2–10 m, and 5 cm to 1 m, respectively at 1 km link range) for systems without and with tracking respectively.

8.2.3 Optical and window loss

This class of power loss includes losses due to imperfect lenses and other optical elements used in the design of both the transmitter and receiver. It accounts for the reflection, absorption and scattering due to the lenses in the system [20]. The value of the optical loss L_{op}, can be obtained from the component manufacturer. It apparently depends on the characteristics of the equipments and quality of the lenses used. For FSO transceivers installed behind windows within a building, there exists an additional optical power loss due the window glass attenuation. Although (glass) windows allow

optical signals to pass through them, they contribute to the overall power loss of the signal. Uncoated glass windows usually attenuate 4% per surface, because of reflection. Coated windows display much higher losses and its magnitude is wavelength dependent.

8.2.4 Pointing loss

Additional power penalty is usually incurred due lack of perfect alignment of the transmitter and receiver. The resulting power loss is catered for by including pointing/misalignment loss L_P in the link budget analysis. For short FSO links (< 1 km), this might not be an issue but for longer link ranges, this can certainly not be neglected. Misalignments could result from building sway or strong wind effect on the FOS link head stand.

8.3 The Link Budget

Based on the losses highlighted above, the received optical power in dBm can thus be obtained from the link budget equation as:

$$P_R(\lambda, L) = P_T(\lambda, 0) - 4.343L\beta_a(\lambda) - L_{Geom} - L_{op} - L_P - L_M \quad (8.17)$$

The link margin L_M is included in the link budget equation above to cater for other losses such as changes in specification when a faulty component is replaced, ageing of laser source, attenuation due to rain, snow and so on. One major importance of the link budget equation is for determining the achievable link range, for a given receiver sensitivity and link margin. The receiver sensitivity represents the minimum amount of optical power needed for the system to achieve a specified level performance, for

example a BER of 10^{-9}. The receiver sensitivity depends on the modulation technique in use, the noise level, fading/scintillation strength and the data rate. Higher data rates simply implies shorter optical pulse duration, hence fewer photons that can be detected. The noise could be from a combination of background radiation, the detection process/quantum shot noise and the thermal noise caused by the thermal agitation of electrons in the receiver electronic components. The receiver sensitivity for at any desired level of performance can then be obtained from the results of Chapters Six and Seven.

For a typical commercial FSO system whose specifications are given in Table 8.3, the achievable link range as a function of link margin is shown in Fig. 8.5 for different visibility values. The results in the figure are based on the Kim model of atmospheric attenuation and the specifications are for non-turbulent atmospheric channels. By operating the link at a 5 dB link margin in clear atmosphere, a range of about 3 km is attainable at the specified data rate; doubling the link margin reduces the link range to below 1.5 km.

Table 8.3: Typical link budget parameters

Parameter	**Typical Value**
Receiver aperture diameter, d_R	8 cm
Transmitter aperture diameter, d_T	2.5 cm
Beam divergence, θ_s	2 mrad
Modulation technique/Bit rate	On-Off keying/155Mbps
Transmitted power	14 dBm
Receiver sensitivity	-30 dBm
Optical loss, L_{op}	1 dB
Pointing loss, L_P	1 dB
Wavelength, λ	850 nm

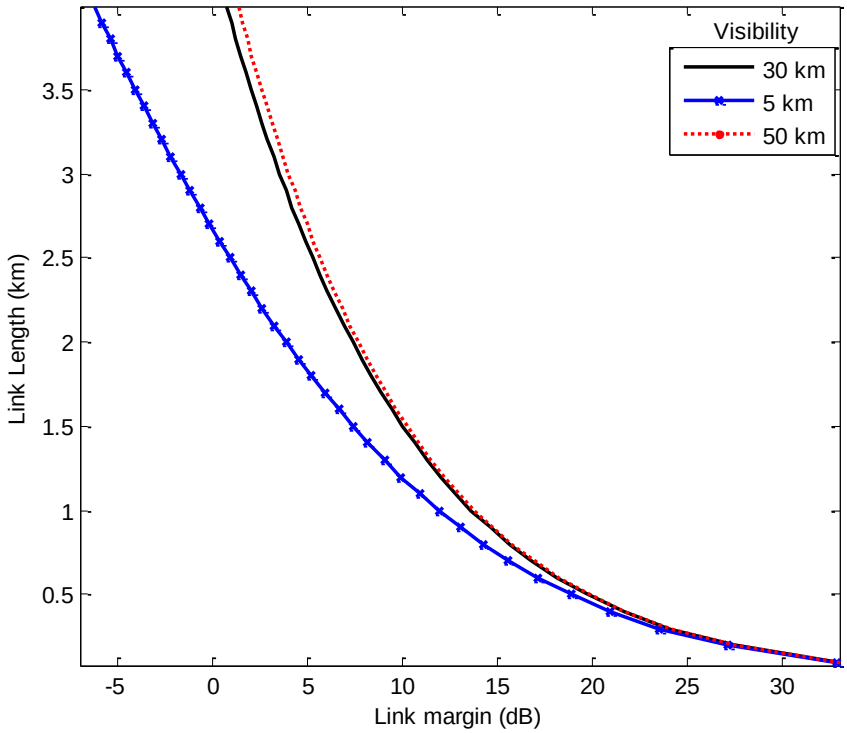

Fig. 8.5: Link length against the available link margin for OOK-FSO in a channel with visibility values 5, 30 and 50 km.

To illustrate the link budget analysis of a BPSK-SIM modulated FSO operating in turbulent atmosphere, the analysis and results of the previous chapter will be considered. For instance, from Figs. 7.9 and 7.20, the required average irradiance to achieve a BER of 10^{-9} with and without diversity can be obtained, these values are summarised in Table 8.4 below.

Table 8.4: Required irradiance to achieve a BER of 10^{-9} based on BPSK-SIM, R_b = 155 Mbps and $\sigma_l^2 = 0.3$.

	No diversity	1-TDD	4 × 4 - MIMO
I_0 (dBm)	-17.2	-19.2	-28.8

Using these values in Table 8.3 to replace the receiver sensitivity and in the link budget equation, the following plots, showing the link length as a function of link margin are obtained.

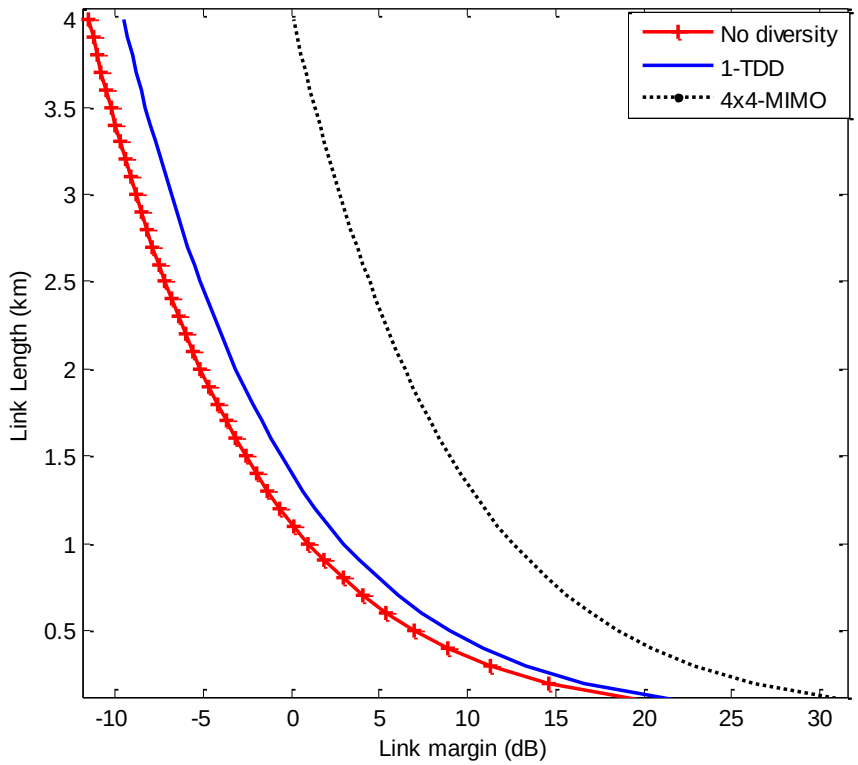

Fig. 8.6: Link length against the available link margin for SIM-FSO considering 1-TDD, 4×4-MIMO configuration and no diversity in clear turbulent atmospheric channel.

These plots show that, to attain a 4-km link range for example, an additional ~12 dB of power will be required if no diversity is used at the specified data rate and channel conditions. With a 4 × 4 – MIMO configuration, the same link length can be achieved with 0 dB link margin while using 1-TDD will require an extra 9 dB. If the link is however operated at a 5 dB link margin, the predicted link ranges are 2.5 km, 0.8 km and ~0.6 km for a 4 × 4 – MIMO, 1-TDD and no diversity configuration, respectively.

8.4 Summary

In this chapter, the link budget equation, from which the attainable link length of terrestrial FSO systems can be estimated, has been presented. In arriving at this equation, various sources of power loss encountered in terrestrial FSO systems have been discussed and accounted for. Out of all the losses, atmospheric scattering due to fog is the most deleterious. This is because the wavelengths of interest in FSO (0.5 μm – 2 μm) are approximately the size as the particles making up the fog. Also, the estimated link length is limited by the available power at the transmitter and the receiver sensitivity. The available transmitted power is limited by safety standards while the receiver sensitivity depends on the modulation type used, noise and atmospheric turbulence.

Chapter Nine

Experimental Demonstration of Scintillation Effect

9.1 Introduction

A turbulent atmospheric channel changes the power distribution profile, among other things, of an optical beam travelling through it. Different models for describing this phenomenon have been discussed in Chapter Four while theoretical analysis of its (atmospheric turbulence) impact on the error performance of an FSO link, including methods that can be used to mitigate its effects has already discussed in Chapters Five to Seven. In this chapter, an experimental demonstration of the scintillation effect on an FSO system will be discussed. The experiment involves the use of both OOK signalling

format and the BPSK-SIM modulation technique. A description of the experimental set-up, including the turbulence simulation chamber, will be presented and finally, results of the experiment will be discussed and inferences drawn.

9.2 Experimental Set-up

The block diagram of the experimental set-up is shown in

Fig. 9.1, each functional block in the set-up is here discussed under the following sub-headings:

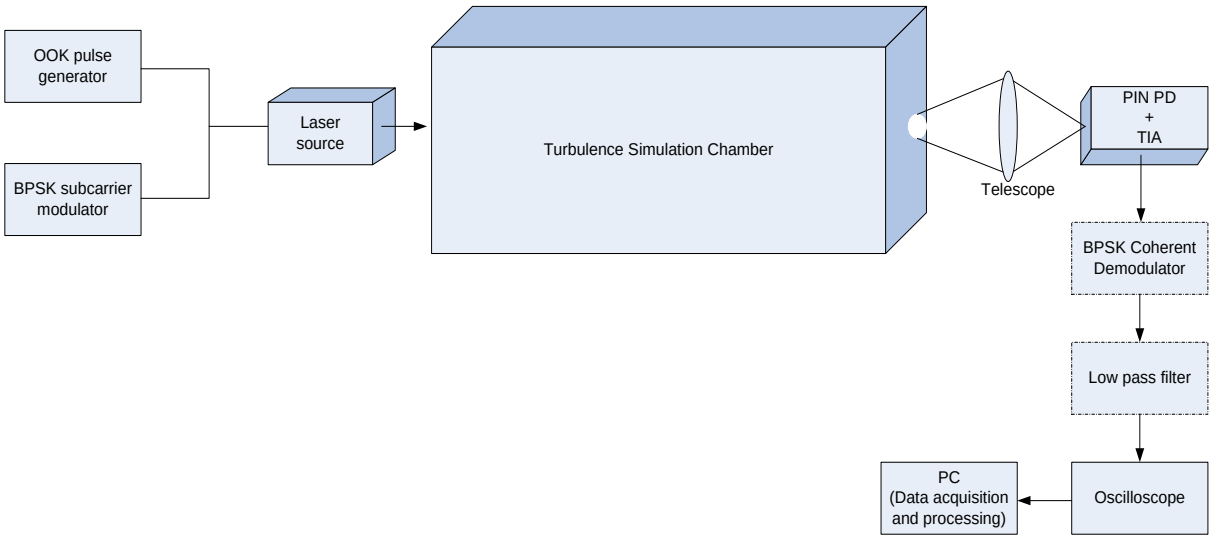

Fig. 9.1: An FSO experimental system block diagram to evaluate the turbulence effect

TIA – Trans-impedance amplifier, PD – Photodetector

9.2.1 The transmitter

The optical source used in the experiment is a 850 nm ‘modulatable Beta-Tx’ laser source with a maximum output power of 3 mW. Near-infrared wavelength is chosen because cheap matching photodetectors are readily available at this wavelength. The laser source has its biased point factory-set midway along the linear section of its output characteristic curve. In order for this laser source to operate within its linear region the peak-to-peak amplitude of the input electrical signal must not exceed 500 mV. With this in mind, the OOK signalling is generated by directly modulating the laser output with a bipolar square wave signal.

The BPSK modulated subcarrier on the other hand is generated by using a MC 1496 multiplier integrated circuit. The schematic diagram of the BPSK modulator is shown in Fig. 9.2, the subcarrier oscillator is a sinusoidal signal of a frequency 1MHz and an amplitude 150 mVp-p while the modulating signal is a bipolar binary data sequence. In this experiment, the aim is to investigate the scintillation effect on the symbol detection threshold level, as such, less emphasis will be place on the data rate. For fair comparison however, both modulation techniques under consideration will be operated at the same data rate. The output impedance of the BPSK modulator of Fig. 9.2 is over 100 kΩ at the 1 MHz centre frequency. This is far higher than the 50 Ω input impedance of the laser source. To ensure optimum power transfer therefore, an impedance matching network shown in Fig. 9.3 is inserted between the subcarrier BPSK modulator and the laser source as shown in Fig. 9.3.

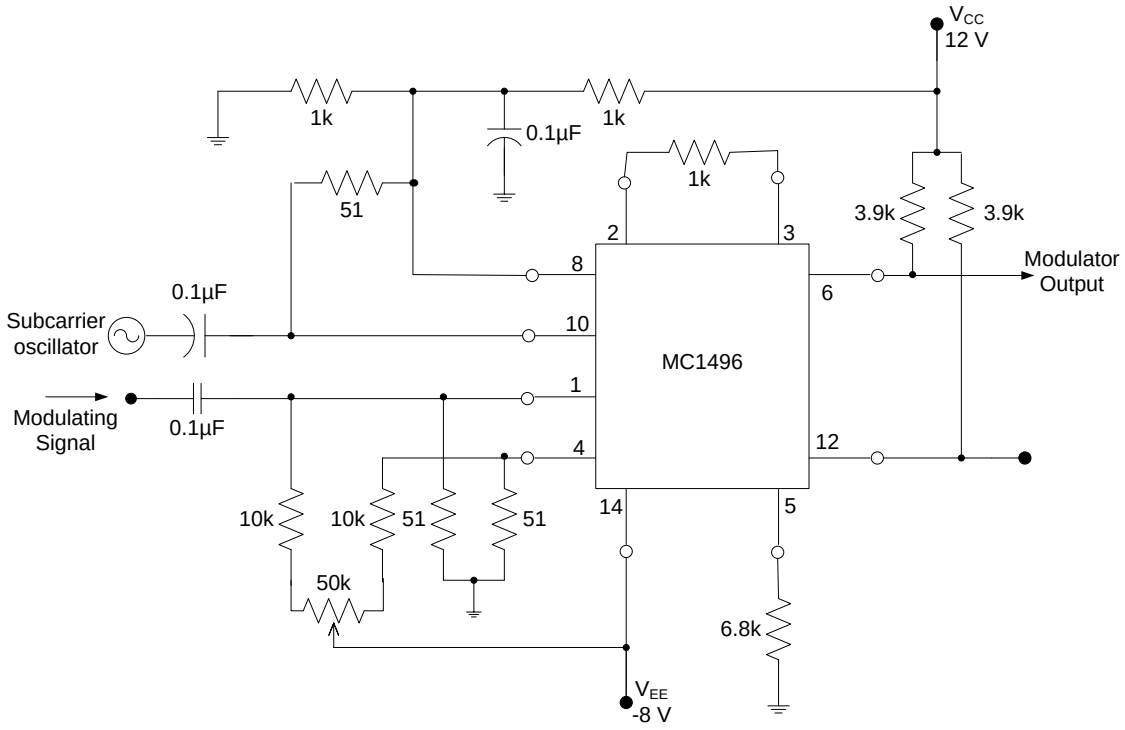

Fig. 9.2: Schematic diagram of the BPSK subcarrier modulator

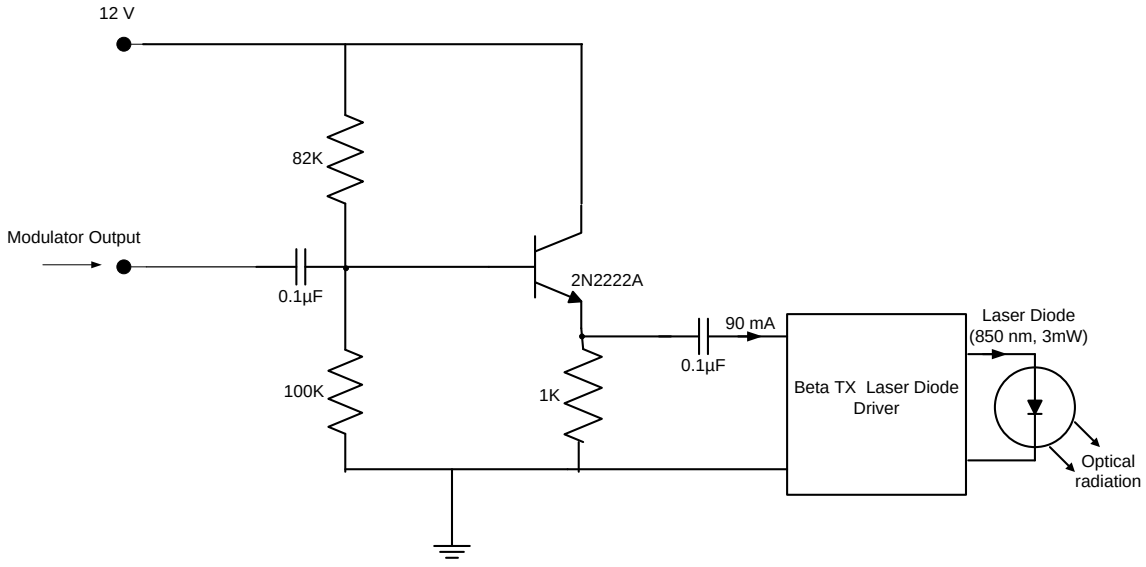

Fig. 9.3: Impedance matching network

9.2.2 Turbulence simulation chamber

The turbulence simulation, whose schematic diagram is shown in Fig. 9.4, has the following dimensions: 140 x 30 x 30 cm. The scintillation effect due to atmospheric turbulence is simulated by exploiting the dependence of the channel index of refraction on the temperature variations as earlier discussed in Chapter Four. The turbulence simulation process involves blowing cold and hot air into the chamber at different locations as shown in Fig. 9.4. The direction of the air is such that, it is transverse to the optical beam's direction of travel. The cold air is set at room temperature of ~ 25 °C and hot air covers a temperature range of 25 to 95 °C. Using a series of air vents, additional temperature control is achieved thus ensuring a constant temperature gradient between the source and the detector. Four temperature sensors are used to measure the instantaneous temperatures at different positions along the length of the chamber. The whole experiment is conducted in a dark room to reduce the effect of ambient light to a barest minimum. A similar approach for simulating turbulence has been reportedly used by other researchers [1, 2].

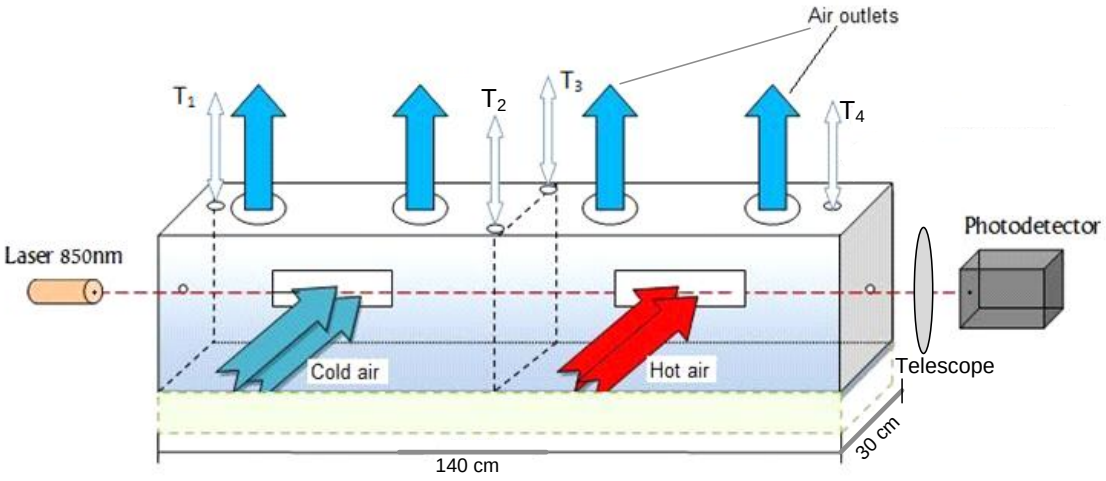

Fig. 9.4: Schematic diagram of the turbulence simulation chamber

T_1,T_2,T_3,T_4 – Temperature sensors

9.2.3 The receiver

The optical receiver is composed of a telescope which focuses the incoming radiation onto a SFH203PFA PIN photodiode. The photodiode has an in built optical band-pass filter with a spectral bandwidth of 750 - 1100 nm to limit the background radiation. The trans-impedance amplifier that follows uses the LT6202 operational amplifier and its schematic diagram is shown in Fig. 9.5.

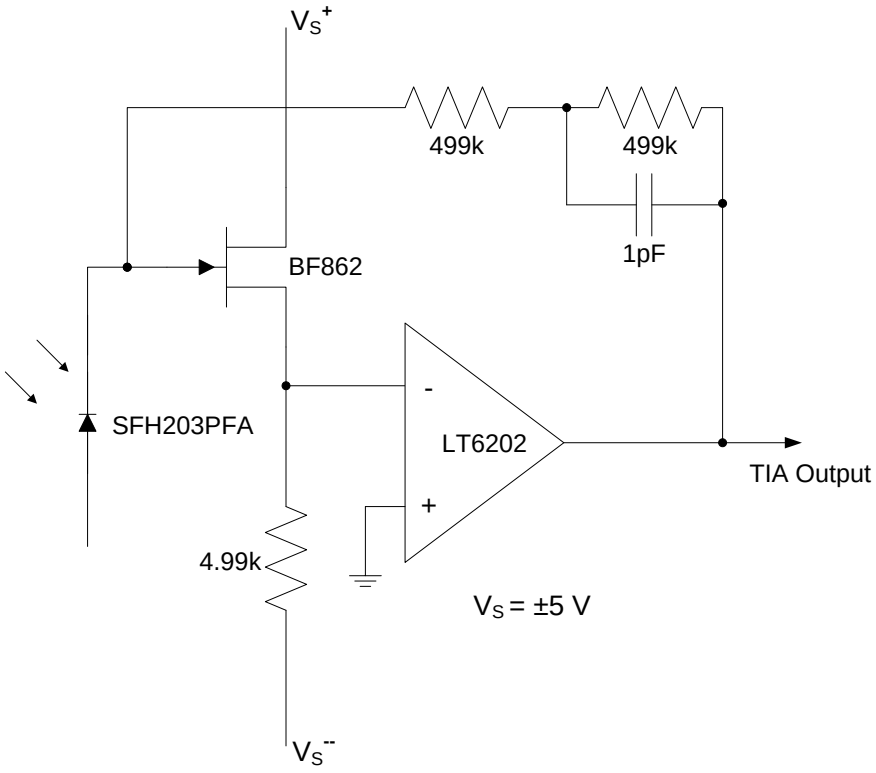

Fig. 9.5: LT6202 trans-impedance amplifier schematic diagram.

In the case of OOK modulated input signal, the output of the TIA is directly fed into an oscilloscope and then to the computer for processing using the 'LabView SignalExpress' data logging software. For the BPSK-SIM case, a coherent demodulator which is based on the same MC1496 multiplier of Fig. 9.2 is used and it shares the same oscillator with the BPSK modulator. The TIA output is here used as the modulating signal input signal to the multiplier. In order to remove the out of band signals, the output of the coherent demodulator is fed into a 10^{th} order low-pass filter shown in Fig. 9.6. The filter is a root raised cosine response low-pass filter with a 3 dB bandwidth of 128 kHz. The output of the filter is then captured, logged and processed by using the oscilloscope with the data logging software.

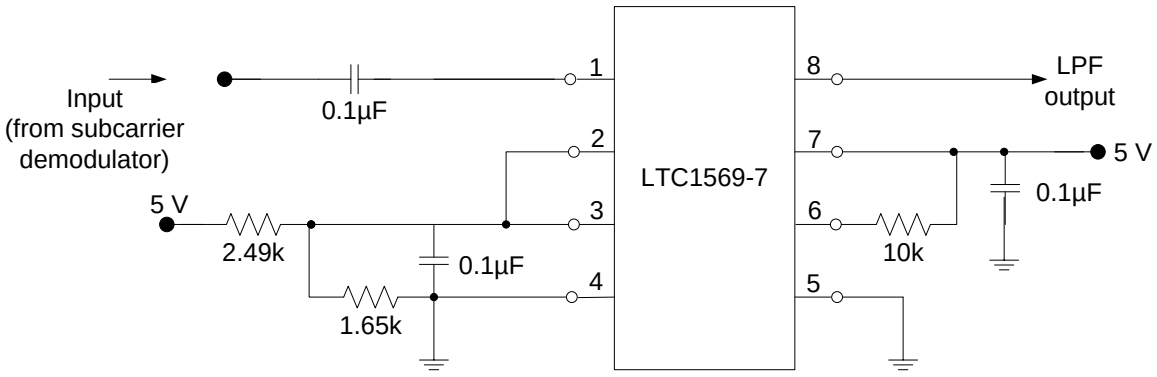

Fig. 9.6: 10^{th} order low-pass filter with root raised cosine response

Since the emphasis in this experiment is on threshold level position rather than data rate, the constraint imposed on the achievable data rate by the filter will hence have no impact on the result of the experiment. In Fig. 9.7, the input and output signal waveforms for the OOK modulated laser without turbulence are shown while Fig. 9.8 gives the input and the received signal waveforms for the BPSK subcarrier modulated laser. The simulation parameters used to obtain these results are summarised in Table 9.1 and the picture of the experimental set-up is given in Fig. 9.9.

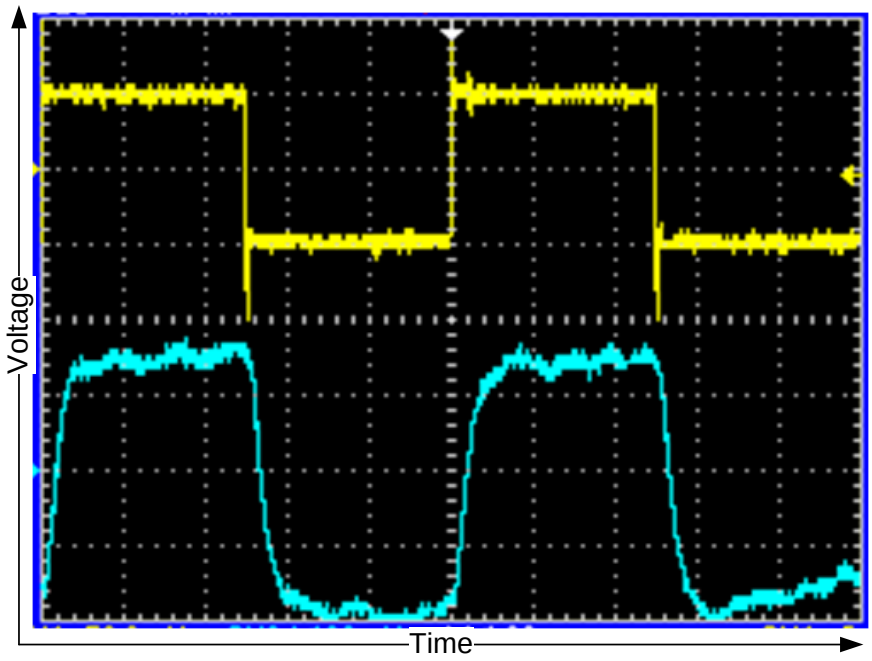

y-axis	100 mV/division	50 mV/division
x-axis	10 µs/division	10 µs/division

Fig. 9.7: OOK modulated laser input and received signal waveforms without turbulence, input signal 100 mV p-p, 40 kHz.

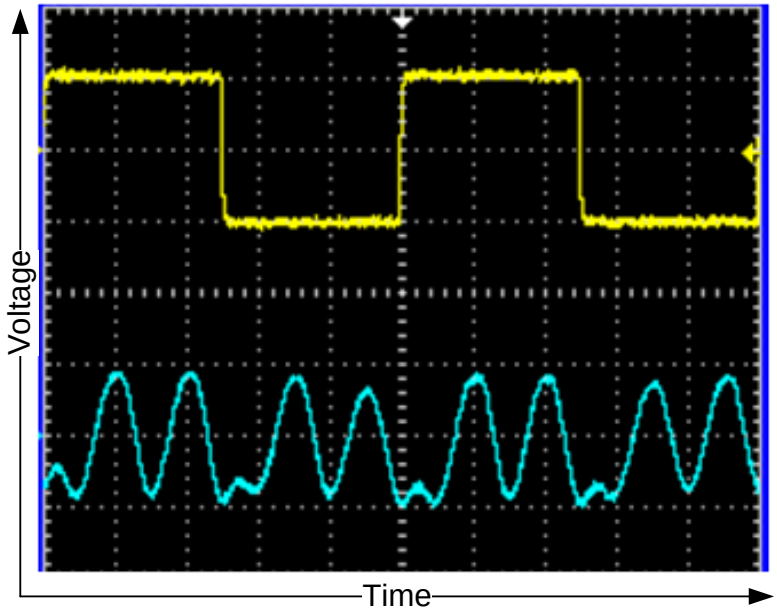

Input modulating electrical signal 100 mV p-p.

Received BPSK modulated subcarrier at the TIA output,

y-axis x-axis	200 mV/division 10 µs/division	50 mV/division 10 µs/division

(a)

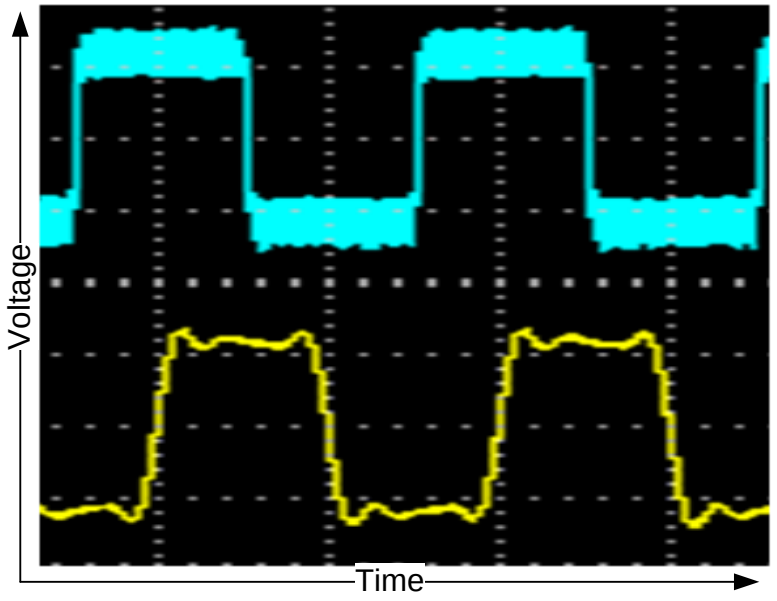

Received signal waveform at the output of the coherent demodulator.

Received signal waveform at the output of the low-pass filter ~400 mV p-p.

y-axis x-axis	200 mV/division 25 µs/division	200 mV/division 25 µs/division

(b)

Fig. 9.8: BPSK subcarrier modulated laser: (a) input and received signal waveforms before demodulation in the absence of turbulence (b) received signals after demodulation. Carrier signal input: 150 mV p-p, 1MHz, modulating signal: 100 mVp-p, 40 kHz.

Fig. 9.9: Turbulence simulation set-up picture

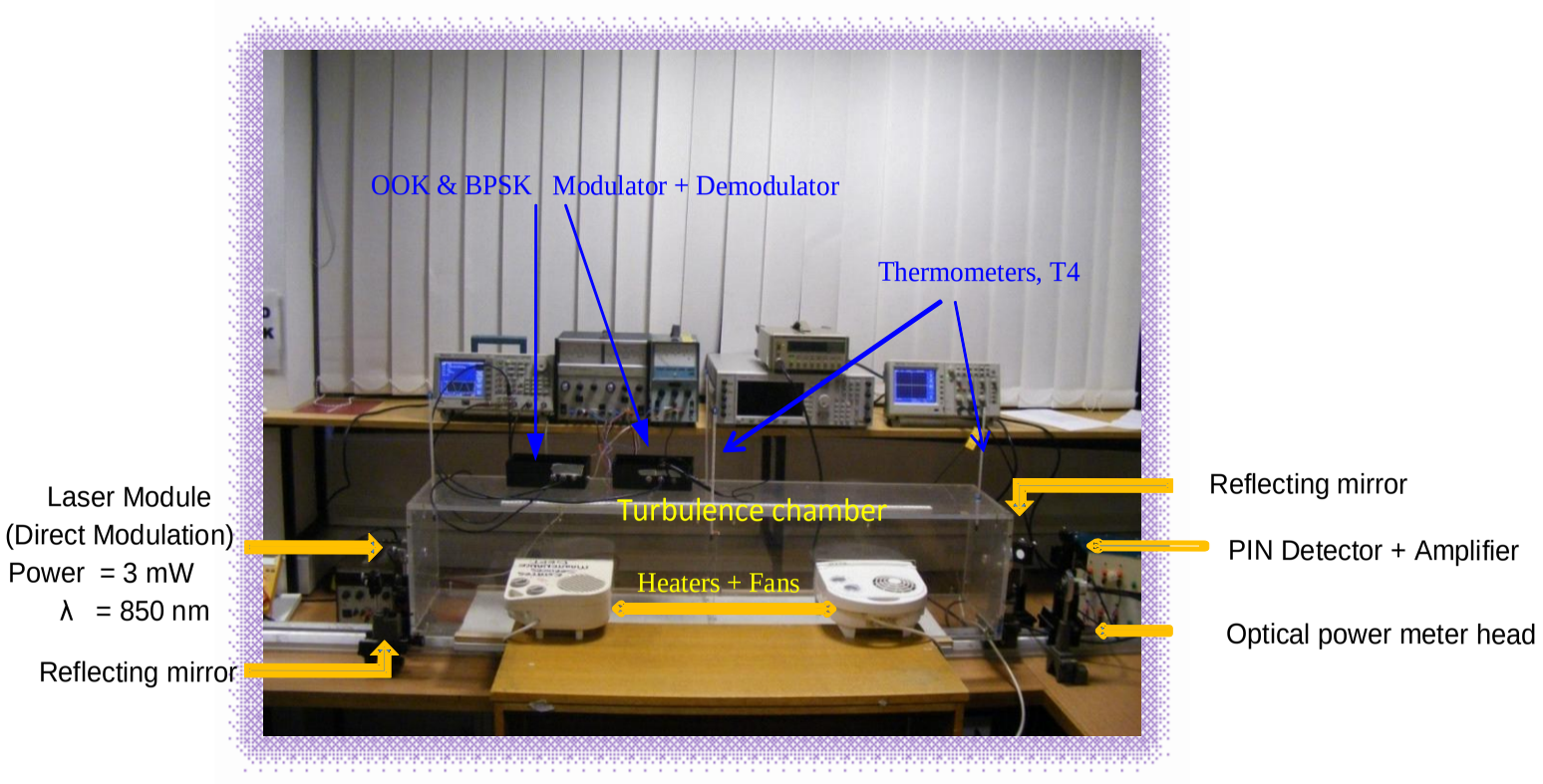

BPSK modulator

- Carrier 1.0 MHz
- Data rate A few kHz

Turbulence chamber

- Dimension 140 x 30 x 30 cm
- Temp. range 25 ^{o} C – 90 ^{o} C

Table 9.1: Parameters for the OOK and BPSK subcarrier modulation experiment.

Parameters	**Value**
Laser type	Modulatable Beta-Tx
Laser diode wavelength	850 nm
Laser maximum output power	3 mW
Laser beam size at aperture	5 mm × 2 mm
PIN detector (SFH203PFA) switching time	0.5 μs
PIN detector responsivity @ 850 nm	0.59 A/W
Modulation type	OOK and BPSK-SIM
Optical band-pass filter	750 - 1100 nm
Turbulence simulation chamber	140×30×30 cm
Carrier signal (sinusoidal) frequency	1 MHz
Carrier signal (sinusoidal) amplitude	150 mV p-p
Modulating signal (square wave) amplitude	100 mV p-p
Modulating signal (square wave) pulse duration	25 μs
Ambient temperature	25 °C

9.3 Characterisation of Simulated Turbulence

To evaluate the strength of the turbulence generated via this set-up, the intensity of laser is directly modulated by a 1 MHz 200 mV peak to peak sinusoidal signal and the mean values of the received signal without the locally generated turbulence logged over a period of time. The process is then repeated with the turbulence simulator in operation and the mean values acquired as well. While doing the experiment without turbulence, the temperature across the turbulence simulation chamber is same as the ambient temperature. With turbulence, the temperature at four different positions, T_1 to T_4 in Fig. 9.4, are constantly changing, typical values are given in Table 9.2.

Table 9.2: Turbulence simulation chamber temperature at four different positions

T_1 °C	T_2 °C	T_3 °C	T_4 °C
26.1	26.1	26.1	26.1
41.5	34.2	31.8	35.3
58.6	42.9	38.2	44.1
71.1	49.9	43.0	49.5
79.8	55.6	46.8	52.9
85.7	60.2	50.4	55.3
90.3	63.6	53.2	56.9

The histogram shown in Fig. 9.10 gives the distribution of the received mean values without the simulated turbulence. The variation observed in the received signal under no scintillation is down to the innate noise (shot and thermal) associated with photodetection process. By fitting the experimental data to a Gaussian curve, the detection noise variance is found to be approximately 5×10^{-5} (V^2). Figure 9.11 shows the mean value distribution with the simulated turbulence. In order to estimate the strength of the simulated scintillation effect, the log-normal distribution introduced in Chapter Four is fitted onto the histogram as shown in Fig. 9.11. From this fit, the log intensity variance σ_I^2 is obtained to be 9×10^{-3} (V^2). As discussed in Chapter Four, when the log intensity variance is in the range $0 < \sigma_I^2 \leq 1$, the turbulence is generally classified to be in the weak regime, the simulated turbulence is thus very weak.

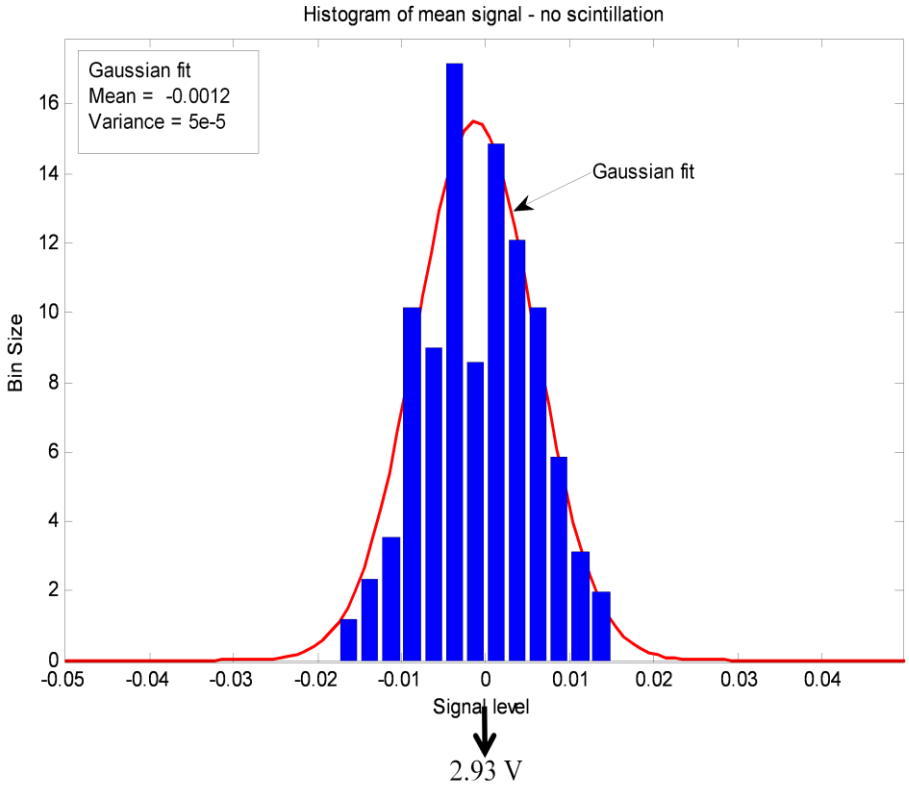

Fig. 9.10: Received mean signal distribution in the absence of turbulence

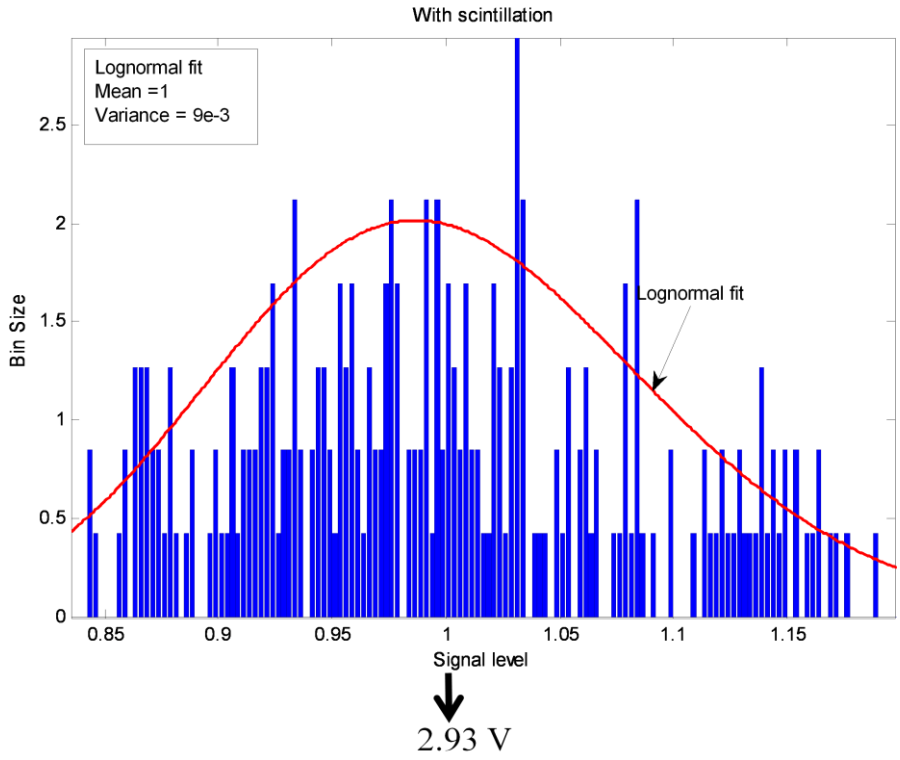

Fig. 9.11: Received mean signal distribution with simulated turbulence and photodetection noise.

9.4 Experimental Results

9.4.1 Scintillation effect on OOK signalling

To demonstrate the effect of the weak scintillation on an OOK modulated FSO link, a stream of low (bit ‘0’) and high (bit ‘1’) bipolar signal is used to directly modulate the laser whose output is then transmitted through the turbulence simulation chamber. In order to recover a faithful replica of the transmitted pulse and avoid pulse shape distortion due to the rise and fall times of the devices, the transmitted electrical square pulses are each of duration 25μs. This data rate restriction is down to the limited bandwidth of the components used in the experiment. To demonstrate the impact of turbulence on the threshold and input signal levels ,three modulating signal amplitudes 50, 100 and 200 mVp-p were used and the corresponding received signal amplitude in the absence of turbulence are ~150, ~300, ~600 mVp-p, respectively at the output of the trans-impedance amplifier. The received signal waveforms and distributions (histograms) with and without scintillation are shown in Figs. 12-14.

From Fig. 9.11(a), it is observed that without turbulence, bits ‘1’ and ‘0’ are clearly distinguishable from the signal distribution. The signal profiles for both bits are similar and are equally spaced on both sides of the zero mark. The decision threshold point can therefore be set at the zero mark. But in the presence of turbulence, the signal waveform becomes heavily distorted and the signal distributions are no longer distinguishable. The signal profiles for bits ‘1’ and ‘0’ have now merged to become one as illustrated Fig. 9.12(b), making it very difficult to locate the threshold level from the signal distributions.

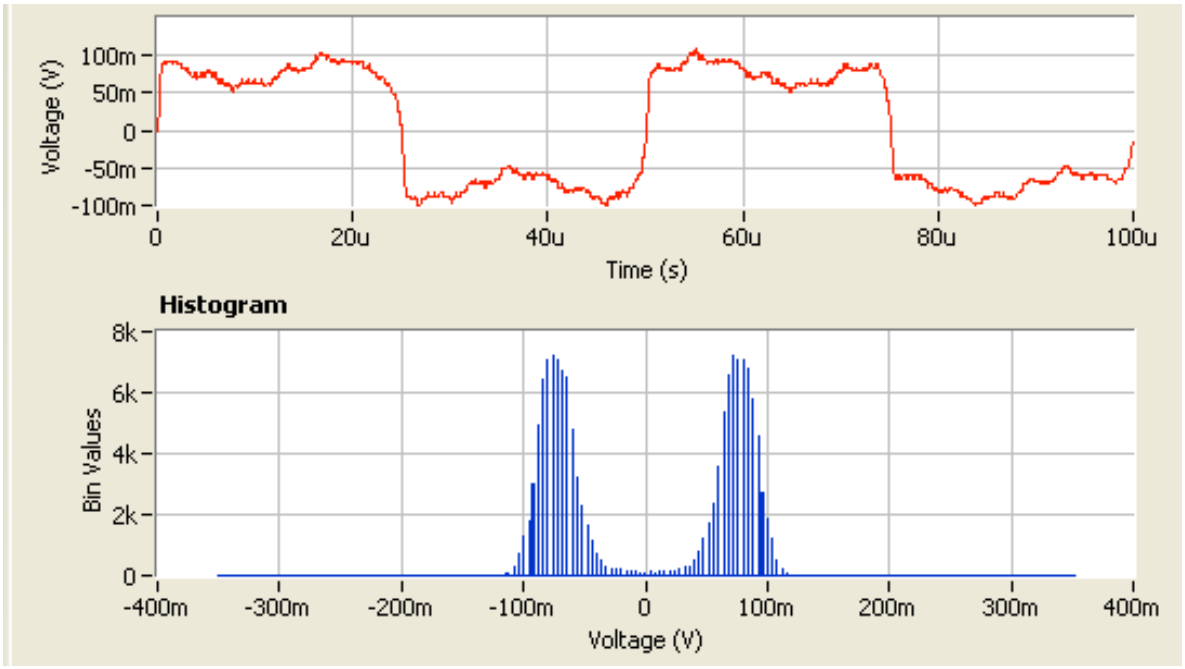

(a)

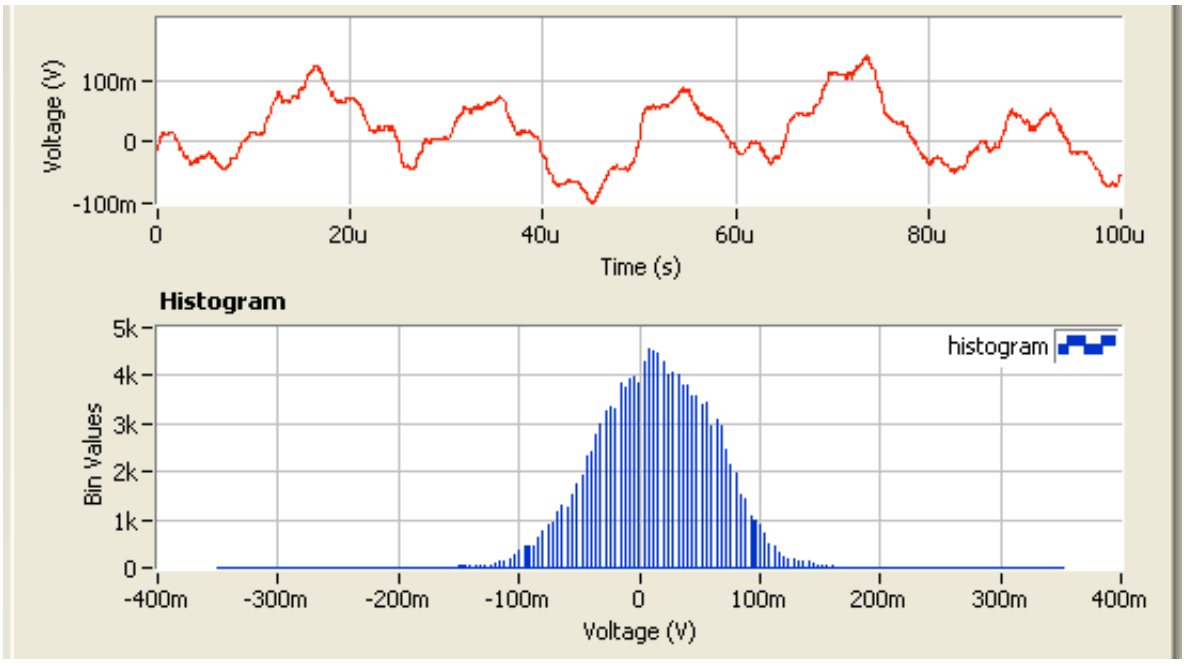

(b)

Fig. 9.12: OOK modulated laser received signal waveform and its distribution for 50 mV p-p input signal: (a) without turbulence, and (b) with turbulence.

Increasing the input signal by a factor of two and keeping the turbulence strength the same does not make any difference in terms of the threshold level position in the absence of turbulence, the zero mark as seen in Fig. 9.13(a) remains the obvious threshold position. During turbulence, the signal distributions for bits ‘1’ and ‘0’ are though distinguishable as shown in Fig. 9.13(b), there exists and overlap in the distribution. From the distributions, the threshold position that will result in minimum detection error cannot be said to be fixed at the zero, it lies between -50 mV and +50 mV and the overlap in the distributions signifies increased error detection possibilities compared with no turbulence case.

With the input signal level increased four folds to 200 mV p-p, the Gaussian-like signal distributions without turbulence shown in Fig. 9.14(a), are still very much similar to the ones shown in Figs. 12 and 13 with the threshold level best positioned at the zero mark. In the presence of turbulence, the signal distributions for bits ‘1’ and ‘0’ become more separated, broadened with some overlap. Compared to the case with no turbulence, the overlap indicates higher likelihood of detection error.

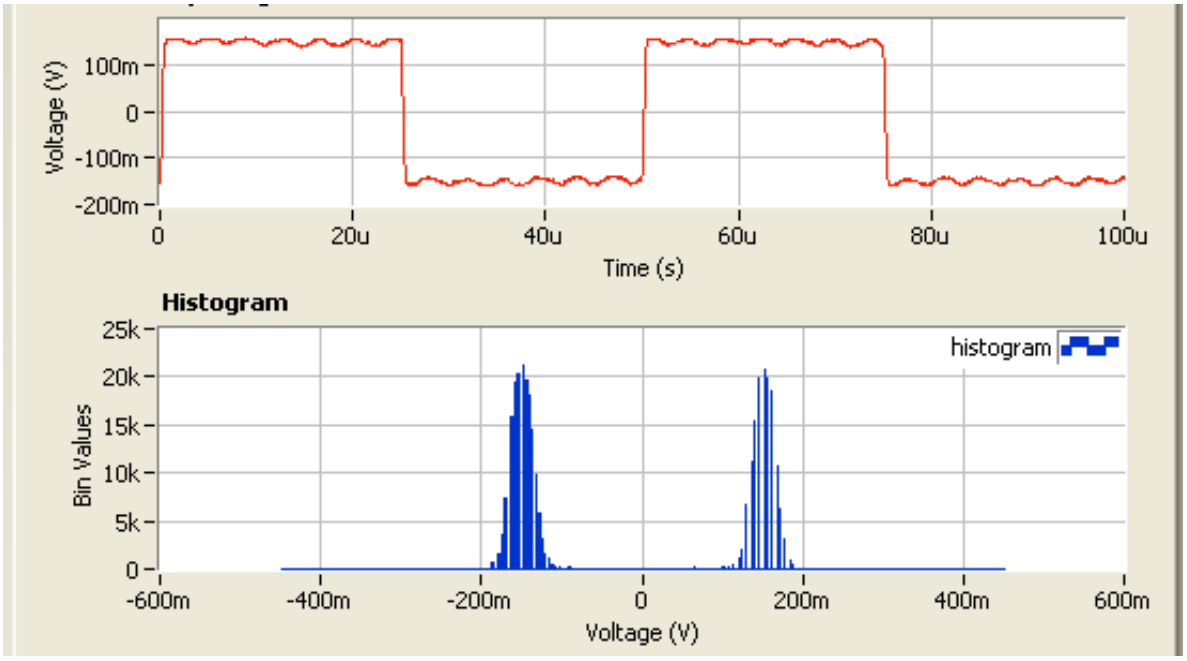

(a)

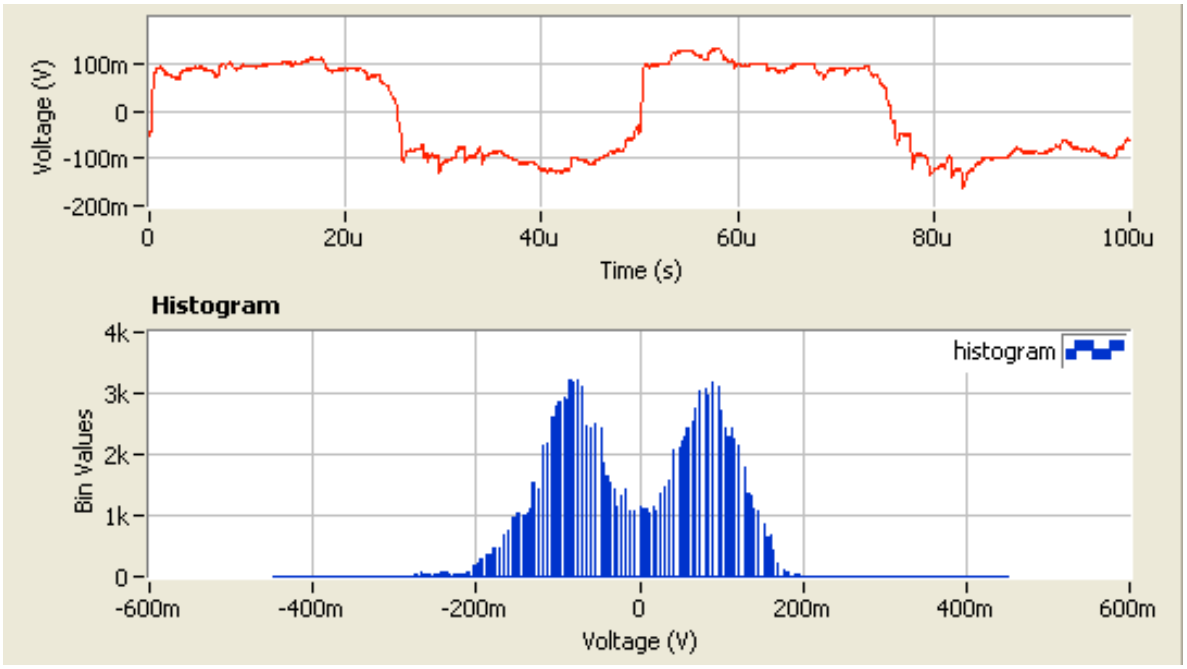

(b)

Fig. 9.13: OOK modulated laser received signal waveform and its distribution for 100 mV p-p input signal: (a) without turbulence and (b) with turbulence.

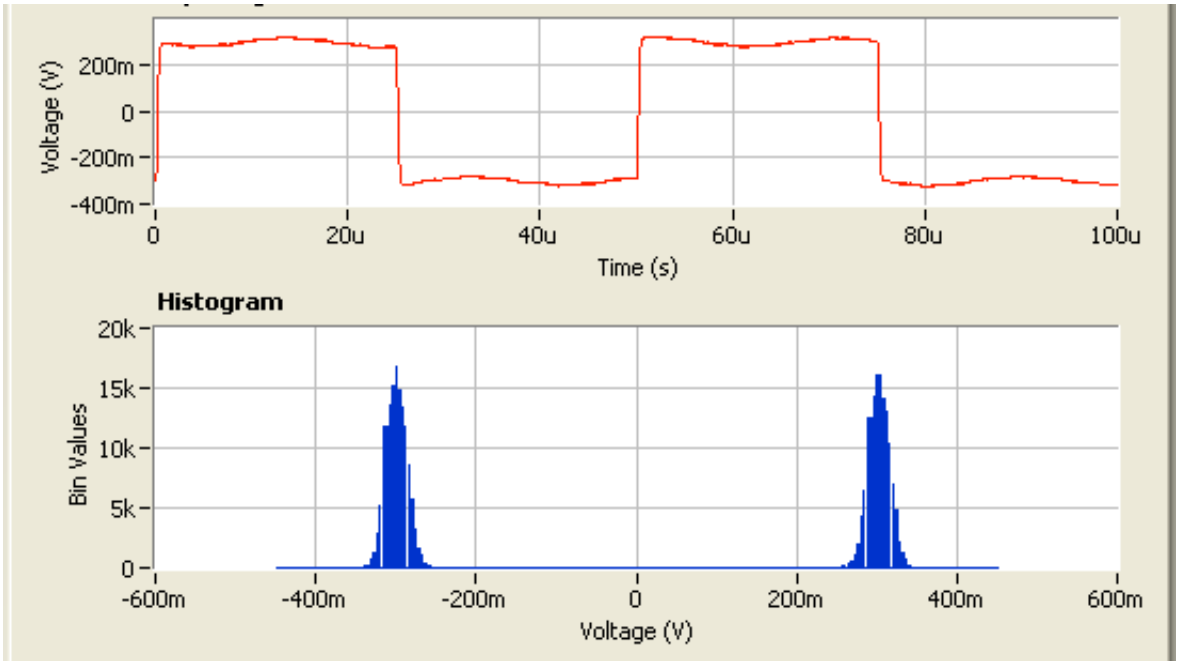

(a)

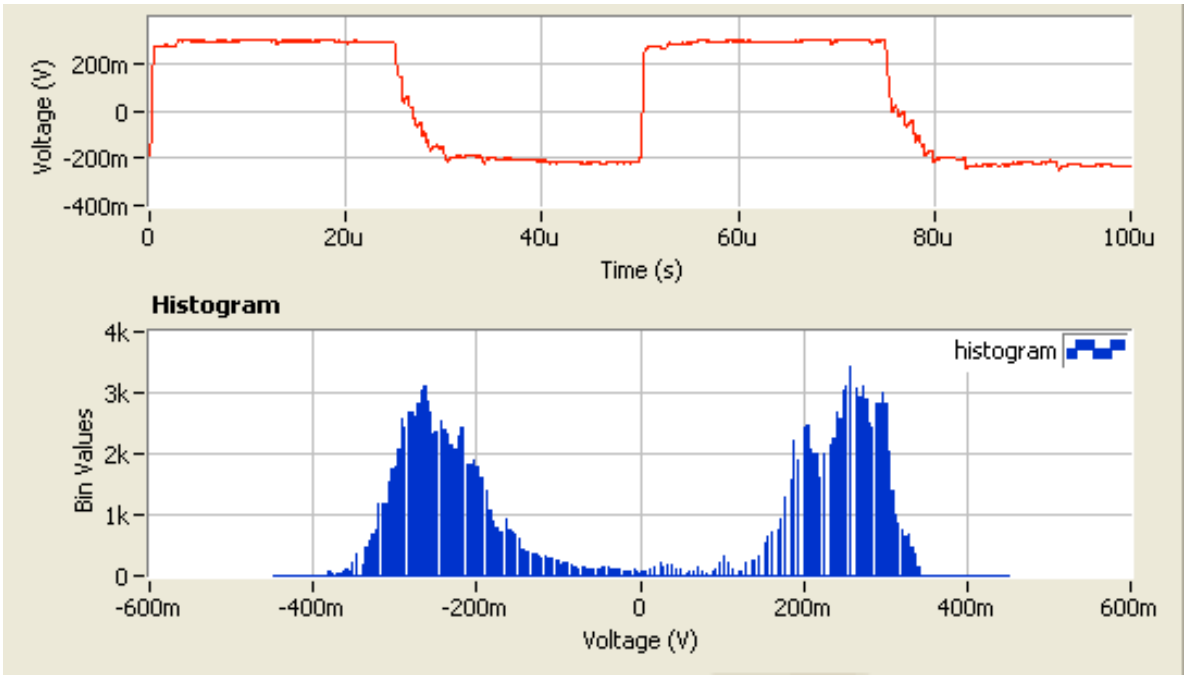

(b)

Fig. 9.14: OOK modulated laser received signal waveform and its distribution for 200 mV p-p input signal: (a) without turbulence, and (b) with turbulence.

From the foregoing, it can be said that in the absence of turbulence, the threshold level can be fixed at the zero signal level but this is no longer the case as soon as turbulence sets in. During turbulence, finding the exact decision threshold level that will minimize detection error will require the knowledge of the turbulence strength. What this means in essence is that, an adaptive threshold will be required for the OOK modulated FSO system to perform optimally. The practical implementation of such an FSO system with the adaptive threshold is not trivial, as the design will involve a continual tracking of both the scintillation and noise levels. This conclusion has previously been theoretically arrived at in Chapter Five. Also from the results, increasing the input signal/transmitted power level can be used to combat the effect of very weak turbulence on the position of the symbol detection threshold level. Increasing the transmitted power will work fine for short range FSO links, for long range systems (> 1 km), this approach will have a limited impact as highlighted in Chapter Six. Moreover, the fact that the transmitted power is premium and the existence of a limit on the amount of power can be safely transmitted through the atmosphere (as discussed in Chapter Two) further limits the use of increased power as a way of mitigating atmospheric turbulence effect.

9.4.2 Scintillation effect on BPSK-SIM modulation

In this section, the same experiment described above is performed for BPSK subcarrier intensity modulation. The modulating signal amplitude levels at the transmitter are the same as that used under OOK modulation and the carrier signal amplitude adjusted such that the electrical signal amplitude at the output of the low pass filter, that follows the BPSK demodulator, is approximately the same as that under the OOK signalling. The

waveforms and distributions of the received signals are then shown in Figs. 15-17 for the three different input signal levels.

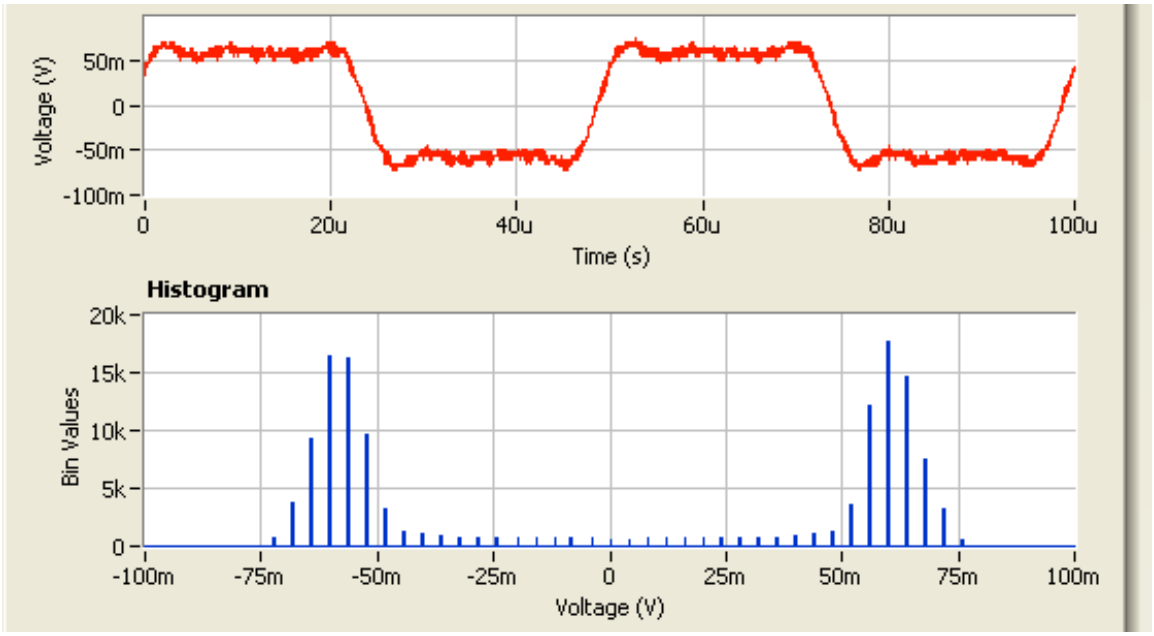

(a)

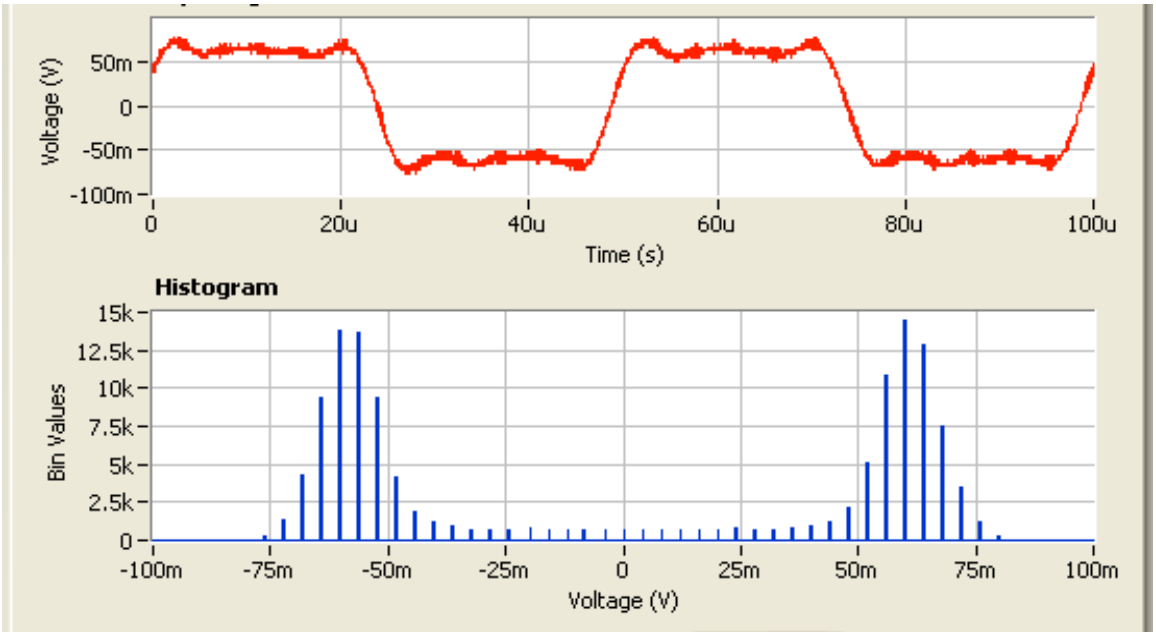

(b)

Fig. 9.15: Received signal waveform for BPSK-SIM modulated laser and its distribution for 50 mV p-p modulating signal: (a) without turbulence, and (b) with turbulence.

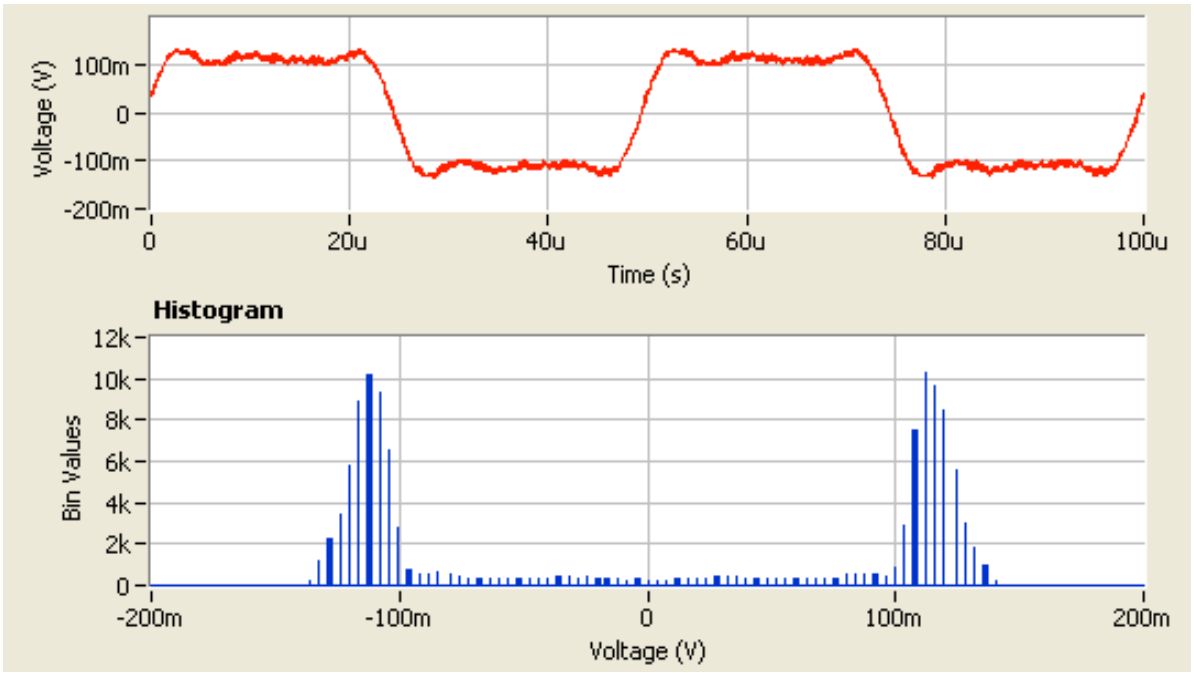

(a)

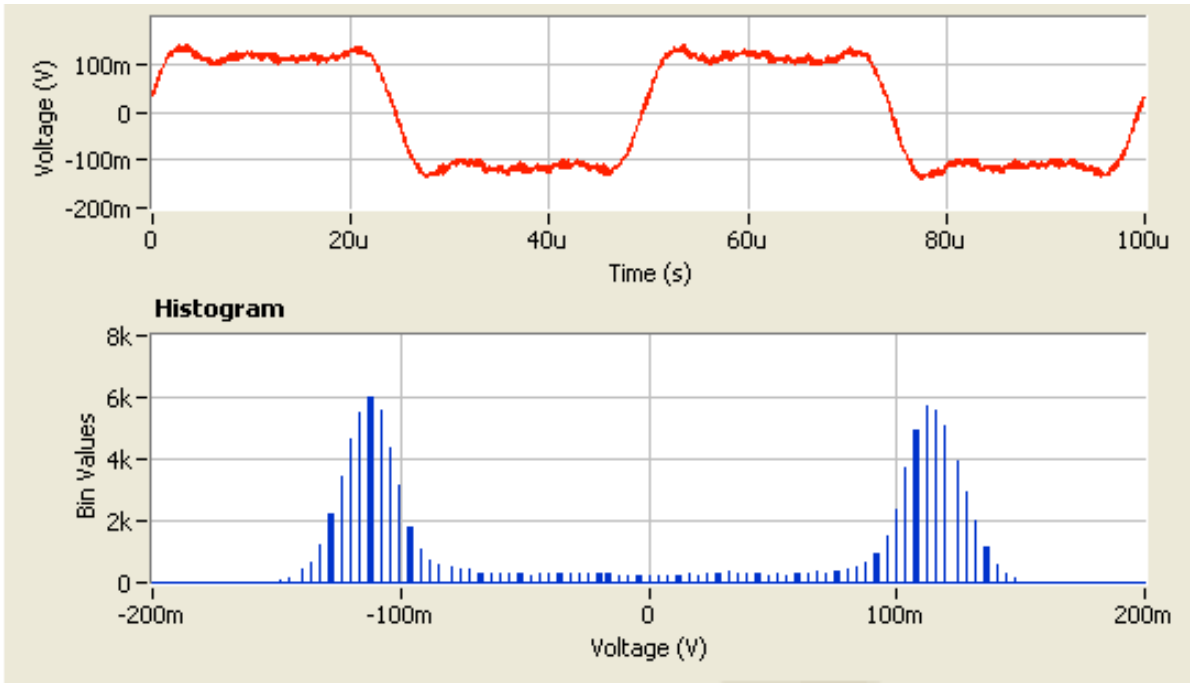

(b)

Fig. 9.16: BPSK-SIM modulated laser received signal waveform and its distribution for 100 mV p-p modulating signal: (a) without turbulence, and (b) with turbulence.

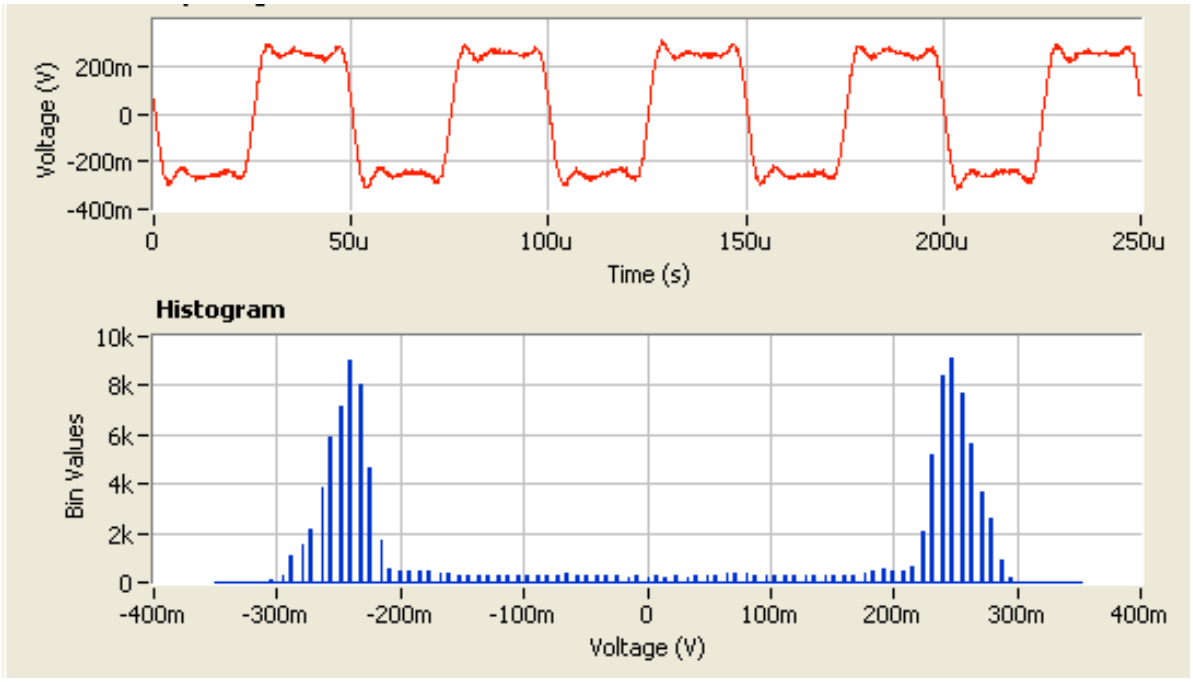

(a)

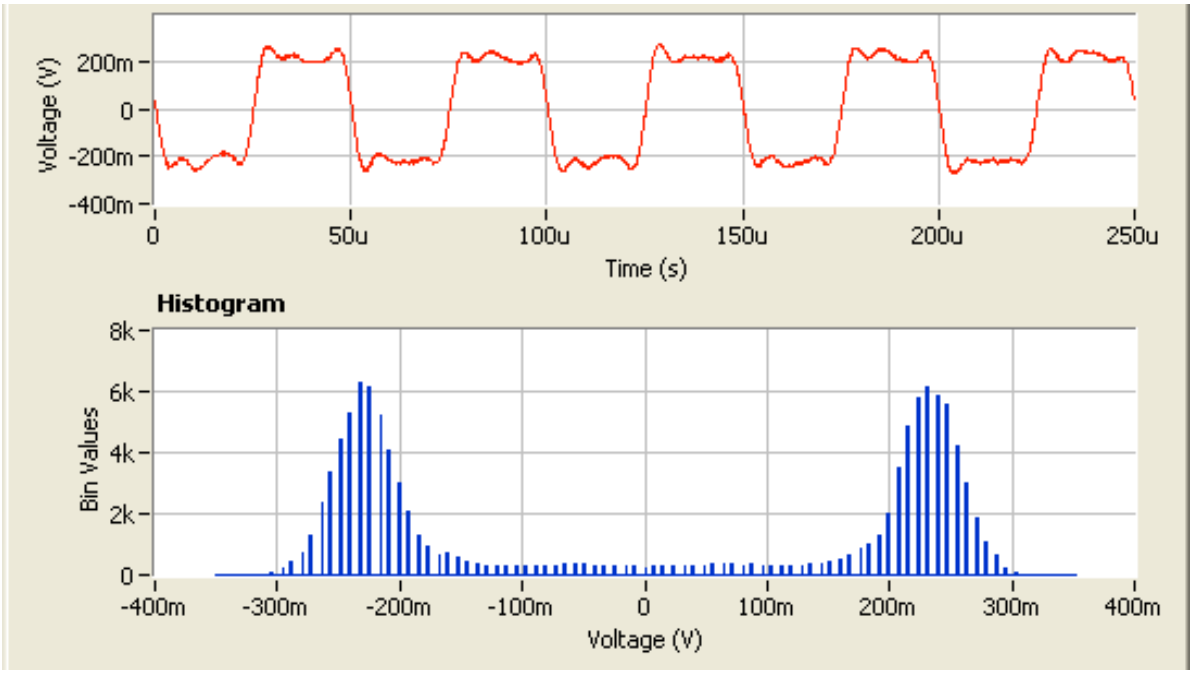

(b)

Fig. 9.17: Received signal waveform for BPSK-SIM modulated laser and its distribution for 200 mV p-p modulating signal: (a) without turbulence, and (b) with turbulence.

With or without turbulence, it is observed from the figures that signal distribution for bits '1' and '0' are similar and are equally spaced on either sides of the zero mark. This is in contrast to when OOK signalling is used. The threshold position can therefore be

fixed at the zero mark and it is not affected by scintillation. This is a clear advantage of BPSK-SIM over the simple OOK signalling. The results of this experiment can also be explained in the spectral domain by noting that the scintillation noise power is concentrated in very low frequencies below 100 Hz [3, 4]. This makes the OOK, which has a significant portion of its power distribution within the low frequency, susceptible to scintillation as demonstrated by the experiment. The SIM-BPSK based FSO on the other hand does not suffer this same fate because its signal spectral distribution is shifted away from the low frequency region to the frequency of the subcarrier, which is 1 MHz in this experiment.

It can therefore be inferred from the experiment and the analysis of Chapters Five and Six that in turbulent atmospheric channels, an FSO system with the data directly impressed on the intensity of the laser irradiance, as is the case in OOK, will suffer from symbol decision difficulties which will eventually lead to detection errors. An alternative approach will be to consider modulation schemes that will require no prior knowledge of turbulence in deciding what symbol has been received. These schemes include : i) PSK pre-modulated SIM, in which the information is not directly on the laser intensity but on the phase of the subcarrier signal, ii) polarisation shift keying, in which the information is placed on the polarization state of the optical beam, iii) or pulse time modulation techniques, such as pulse position modulation, pulse width modulation and pulse frequency modulation; in which the information is also not directly on the beam intensity but on the pulse position, pulse width and the pulse frequency respectively. The summary of key challenges, including atmospheric turbulence, associated with optical wireless communication systems as a whole (indoor and outdoor) are presented in Table 9.3.

Table 9.3: Challenges in optical wireless communications

Challenge	Cause(s)	Effects	Mitigation Approach	Channel
Inter symbol interference (ISI)	Multipath Propagation	Poor transmission quality (high BER) Multipath distortion or dispersion Reduced date rates	Channel equalization Forward error control (FEC) Spread spectrum techniques Multiple subcarrier Modulation (*More bandwidth efficient than a single-carrier system*) OFDM Multi-beam transmitter Field of view controlling	Indoor
Safety	Laser Radiation	Damage to eyes and skin	Power efficient modulation schemes: PPM, DPIM, etc. Use LED, Class 1 lasers, and 1550 nm wavelength	Both
Noise	Dark current noise Shot noise Background noise Thermal noise Relative intensity noise Excess noise (with APD) ASE (only if optical amplifier is used)	Low Signal-to-noise ratio and high BER	Optical and electrical filtering Pre-amplification FEC Low noise post detection amplifier Small field of view optical sources Optical filter	Both
Turbulence	Random refractive index variation	Phase and intensity fluctuations (scintillation) Image dancing Spatial coherence degradation Beam spreading	FEC (LDPC, Turbo codes) Robust modulation: SIM, PPM MIMO Diversity reception (temporal and spatial) Adaptive optics	Outdoor
Reflection index	Different materials	Higher losses due to reflection on surfaces	Higher transmit power	Indoor
Blocking	Furniture Moving objects Walls Birds	Temporary link outage	Diffuse link Cellular system Multi-beam Hybrid FSO/RF	Both
Weather effects	Fog, Rain, Gases, Smoke, Aerosols	Attenuations, Scattering Link outage	Higher transmit power Hybrid FSO/RF	Outdoor
Pointing, Acquisition and Tracking (PAT)	Mobile link heads Building sway	Temporary/permanent link outage Power loss	Hybrid FSO/RF Active tracking Adaptive optics (beam steering and tracking)	Outdoor

9.5 Summary

For an FSO system operating in a turbulent atmospheric channel, the effect of scintillation on the receiver decision circuit – the circuit which decides what bit has been received – has been experimentally verified. In the experiment, a turbulence simulation chamber is used to mimic a turbulent atmospheric channel. The results of the experiment show that for an FSO system operating in a turbulent atmospheric channel, the prior knowledge of the channel fading strength or its statistics is not required in demodulating and recovering the transmitted data in a BPSK-SIM based FSO system. This is however not the case for an OOK-FSO, as the signal fluctuation caused by turbulence affects the position of the symbol detection threshold level. To minimise detection error in such systems will require increasing in the transmitted power or using a complex decision circuit that can continually monitor and estimate the channel fading and noise strengths.

It should be mentioned that in the experiment, the method used to simulate atmospheric turbulence does not account for signal attenuation due to the molecular constituents of the atmospheric channel. Also the short length (140 cm) of the turbulence simulation chamber means that only very weak turbulence could be simulated.

Chapter Ten

Conclusions and Future work

10.1 Conclusions

The main objective for studying the terrestrial FSO communication system is to harness its potential in addressing the 'access network bottle-neck'. The research reported in this thesis supports this fundamental objective by investigating and analysing the use of subcarrier intensity modulation for terrestrial FSO systems as against the prevailing OOK signalling technique. The motivation behind this is the performance limitation of OOK modulated FSO in atmospheric turbulence channels. The SIM-FSO has been proven to overcome this limitation but not without its own shortcomings, which include

poor power efficiency and possibility of signal distortion due to intermodulation distortion.

To be able to carry out the objectives of this research, the fundamental principles of FSO and its building blocks had to be reviewed and discussed in Chapter Two. Following this, optical detection was reviewed in Chapter Three, this is important in understanding the statistical behaviour of transmitted photons. This chapter also highlighted the process of converting photons to their corresponding electrical signals, from which the transmitted data can then be extracted. Also, the different types of noise encountered during optical detection were discussed with the view to understanding the limit imposed on the system performance by each of them. The review work revealed that the transmitted photons obey the Poisson distribution and this can be adequately approximated as the tractable Gaussian distribution for large photoelectron counts as is the case in terrestrial FSO systems.

A turbulent atmospheric channel causes the intensity of an optical beam travelling through it to fluctuate randomly due to random changes in refractive index along the beam's path. In Chapter Four, this atmospheric turbulence induced signal fluctuation was reviewed and three most reported models (log-normal, Gamma-gamma and negative exponential) were described and their respective pdfs presented. These models were later used to model the statistical behaviour of the received signal for short to very long range FSO systems.

In accordance with the research objectives, this thesis has focused on optimising the system performance during atmospheric turbulence with the use of the phase shift keying pre-modulated-SIM and in order to reduce the turbulence induced fading

penalty, spatial and subcarrier time delay diversity techniques have been explored. From the BER performance analysis of terrestrial OOK-FSO in the presence of noise and atmospheric turbulence, it was inferred that atmospheric turbulence: i) causes increased SNR, which translates into increased transmitted optical power and ii) implies that an adaptive threshold will be required for optimum performance, as the use of fixed threshold resulted in a BER floor and sub-optimal error performance. This study also revealed that in very weak turbulence situations ($\sigma_l^2 < 0.1$), increasing the transmitted power could be used to combat the channel fading. This approach does not work beyond the very weak regime and alternative techniques will have to be sought.

In order to circumvent the performance limitation of OOK-FSO in turbulent atmospheric channels and the poor spectral efficiency/requisite slot and symbol synchronisation requirements of the PPM modulated systems, the SIM-FSO was proposed and its error performance analysis presented in Chapter Six. The BER and the outage probability of SIM-FSO across all turbulence regimes, representing short to very long range systems, were presented in Chapter Seven. On the evidence of the results, the SIM has been recommended in turbulent channels against the fixed threshold OOK modulated FSO currently used in commercial terrestrial FSO systems. A SIM-FSO system does not suffer from BER floor and its decision circuit does not need to track the channel fading and noise levels continually in order to perform optimally. It has been found that the turbulent atmosphere does impose power penalties on the system. For instance, in weak atmospheric turbulence, a BPSK pre-modulated SIM-FSO system will incur a power penalty of about 5 dB at a BER of 10^{-6}, and this penalty will rise to ~10 dB when the link error performance level is raised to a BER of 10^{-9}, this will continue to rise as the error requirement level is raised. This suggests that the channel fading has to be mitigated in order to reduce the penalty.

This led to the study of diversity techniques in Chapter Seven where the bit error and outage probabilities of a SIM-FSO system employing spatial diversity to combat the turbulence induced channel fading were presented. An expression for the BER of an $\mathcal{N}\times\mathcal{M}$-MIMO FSO system operating in a turbulent atmospheric channel was derived. The error performance and the obtainable link margin using three different linear combining techniques (MRC, EGC and SelC) were also presented. The use of SelC linear combining technique in a multiple photodetector system operating in a very weak turbulent atmospheric channel ($\sigma_l^2 \leq 0.2^2$) would result in negative link margins and is therefore not suggested as a way of mitigating fading in short range (< 1 km) FSO links. The MRC technique is optimum but complex to implement while the EGC is simpler to implement. The diversity gain attainable with the EGC technique is less than 3 dB inferior compared to the complex MRC. Hence in a photodetector array system, the EGC is proposed as the preferred linear combining method.

With a turbulence induced fading of strength $\sigma_l^2 = 0.3$ and a BER of 10^{-6}, using a 4 × 4 receiver/transmitter array reduced the required SNR from 25 dB to about 12 dB, resulting in a gain of 13 dB. This gain will increase with the fading strength and as the required bit error level is lowered. A reasonable number of independent photodetectors, appropriate to mitigate scintillation without an overwhelming complexity, is between two and four based on results presented in this thesis. Using a 2 × 2-MIMO system required ~0.5 dB of SNR more than using four photodetectors with single transmitter at BER of 10^{-6} but spacing an array of 4 photodetectors sufficiently to ensure uncorrelated irradiance reception is far more demanding than spacing two photodetectors. Also the use of 4 × 4-MIMO required ~3 dB and ~0.8 dB lower SNR than using four and eight photodetectors, respectively with single optical transmitter at the same BER of 10^{-6}.

In strong atmospheric fading channels, using 1 × 2-MIMO configuration was predicted to result in ~12 dB diversity gain and as the turbulence strength increases into the saturation regime, the gain in electrical SNR exceeds 40 dB at the same BER of 10^{-6}. However the diversity gain thus depends on the performance metric used, when the outage probability metric is considered, the gain is generally lower. At a P_{out} of 10^{-6} during the saturation regime, the predicted gain was ~28 dB for a similar 1 × 2-MIMO configured SIM-FSO but the general trend of the gain, with respect to the turbulence strength and source/detector configuration, are the same for both the BER and P_{out} metrics.

In the spatial diversity technique, whenever the photodetectors are closer together than the spatial correlation distance of the field travelling through the turbulent channel, the received signals become correlated. This raises the possibility of all the photodetectors in the array experiencing deep fades simultaneously, thereby jeopardising the primary aim of using spatial diversity. This effect has been verified and reported in chapter seven, in a single transmitter and two photodetectors system at $\sigma_l^2 = 0.5^2$, a correlation coefficient of 0.6 between the received signals was predicted to cause a 3 dB reduction in the expected diversity gain at a BER of 10^{-6}. The reduction in the diversity gain increased to over 4 dB in a SIM-FSO with 1 × 3-MIMO configuration and this penalty is bound to increase as the received signals become more correlated.

The subcarrier TDD as an alternative/complementary technique for ameliorating the channel fading was proposed in Chapter Seven. The idea is to retransmit delayed copies of the data/information on different subcarriers. The results showed that up to 3 dB improvement in receiver sensitivity can be achieved by retransmitting the delayed copy of the data five times in a channel of turbulence strength $\sigma_l^2 = 0.3$. However,

retransmitting just once, on a different subcarrier frequency, was found to be the optimum approach with a gain of up to 4.5 dB in weak atmospheric turbulence. Expectedly, the TDD gain is proportional to the fading strength but independent of the data rate.

In order to increase the system throughput/capacity, multiple SIM was also studied. This however comes at a price, the SNR required to achieve say a BER of 10^{-6} with five subcarriers is about 40 dB in a channel with a fading strength σ_l^2 of 0.3. This increases to about 46 dB with 10 subcarriers under the same conditions, depicting a $20\log N$ (dB) increment over the SNR required to attain the same level of error performance with a single subcarrier. The multiple SIM-FSO should therefore only be considered when the quest to achieve a higher throughput outweighs its accompanying power penalty.

In addition, the intermodulation effect due to the optical source non-linearity was studied and the number of in-band intermodulation products calculated. This investigation is particularly helpful in subcarrier frequency planning. The results of the analysis can be used in leaving-out certain subcarrier frequencies (out of a range of frequencies) that have high numbers of in-band intermodulation products. Also presented were criteria that could be used to optimise the optical modulation index, this is with the view to improving the system performance in the face of intermodulation distortion and multiple subcarriers. It has been found out that IMD, caused by optical source nonlinearity, imposes a limit on the achievable BER of a SIM-FSO. It should hence be ensured that a linear laser source (one with negligible nonlinearity) is used to transmit a multiple subcarrier multiplexed signal.

From the error performance analyses presented, the power required to achieve a given level of performance could be obtained. These were then used in Chapter Nine to estimate the power limited link range of a SIM-FSO. The results predicted that, achieving a 4 km SIM-FSO link length with no diversity technique will require about 12 dB of power more than using a 4 × 4 – MIMO configured system with the same data rate and channel conditions. If the link is however operated at a 5 dB link margin in clear atmosphere, the predicted link ranges are 2.5 km, 0.8 km and 0.6 km for a 4 × 4 – MIMO, 1-TDD and no diversity configuration respectively.

In Chapter Nine, a turbulence simulating chamber was used to demonstrate the atmospheric turbulence effect on symbol detection with both OOK and BPSK-SIM modulated FSO systems. From the experimental results for an OOK-FSO system, it was observed that in the absence of turbulence, the threshold level can be fixed at the zero signal level but this is no longer the case as soon as turbulence sets in. During turbulence, finding the exact decision threshold level that will minimize detection error will require knowledge of the turbulence strength. What this means in essence is that an adaptive threshold will be required for the OOK modulated FSO system to perform optimally. The practical implementation of such an FSO system with adaptive threshold is not trivial, as the design will involve a continual tracking of both the scintillation and noise levels. A similar inference was theoretically arrived at in Chapter Five. Moreover, increasing the input signal/transmitted power level can be used to combat the effect of very weak turbulence on the position of the symbol detection threshold level. Increasing the transmitted power will work fine for short range FSO links, for long range systems (> 1 km), this approach will have a limited impact and the fact that the transmitted power is premium and the existence of a limit on the amount of power that can be safely transmitted through the atmosphere further limits the use of increased power as a way of

mitigating atmospheric turbulence effect. For a BPSK pre-modulated SIM-FSO system on the other hand, the experimental results confirmed that the position of the threshold level is indeed independent of fading strength of the turbulent atmosphere. This is a clear advantage of BPSK-SIM over an OOK modulated FSO link.

In conclusion, the performance of PSK pre-modulated SIM-FSO systems has been investigated in the presence of atmospheric turbulence and its error rate/outage probability expressions derived for different channel conditions. The SIM-FSO system has been experimentally and theoretically compared with the classical OOK based FSO systems in the presence of atmospheric turbulence. The SIM-FSO is advantageous in that its decision circuit, unlike the OOK-FSO, does not require knowledge of the atmospheric turbulence strength or its statistics to perform optimally. For FSO systems spanning over 1 km, the effect of channel fading caused by atmospheric turbulence becomes significant and can be mitigated (via diversity techniques) to prevent loss of data, excessive power requirements, increased error rate and link outage.

10.2 Recommendations for Future Work

Although the objectives listed in chapter one of this thesis have been achieved, the work was never envisaged to be self contained and comprehensive to cover the entire optical wireless communications research areas. Since the amount of work and time required to do so is beyond the scope of this thesis, the author will now be recommending further works, which can be carried out to extend the work reported here.

Radio over FSO (RoFSO): As a straight forward progression of the work presented here, the study and experimental demonstration of RoFSO could prove very useful.

This, potentially, will provide interesting findings regarding the integration of FSO with radio over fibre signals and cable television networks. This RoFSO experiment, which is in principle a multiple subcarrier system, can further prove the suitability/viability of subcarrier modulated FSO as a tool for increasing communication systems capacity and/or throughput.

Pulse interval modulated FSO: As an alternative solution to one of the findings reported in this thesis - that encoding the data directly on the intensity of an optical source, as is the case in OOK signalling technique, is sub-optimum in fading channels - an investigation of pulse interval modulated FSO systems in turbulent channels will be recommended. In pulse interval modulation, the data is encoded on the interval between pulses, this technique might provide an alternative solution for the complex symbol decision circuit needed for an optimum OOK-FSO system in turbulent atmospheric channels.

Polarisation shift keying modulated FSO: It has been reported in this thesis that a turbulent atmospheric channel does not result in change of polarisation state of a traversing field. This fact can be explored by encoding data on the polarisation state of an optical beam. The polarisation modulation technique has been studied in fibre communication systems but is not very attractive in that area because an optical fibre causes random changes in the polarisation state of an optical beam travelling through it.

Hybrid FSO/RF communication: The availability of FSO, especially links longer than 1 km, depends so much on the atmospheric weather conditions. The attainment of 99.99 % availability during thick fog is still a challenge and to address this, one option will be to combine an FSO link with an RF system as a back-up at reduced data rate. Since the frequency range used in FSO is not licensed, it will be suggested that a licence

free frequency should be used for the RF back-up. This is to ensure the whole system remains free from licence fee and bureaucracy.

Appendix A: Zeros and Weights of Gauss-Hermite Integration with n = 20

$$\int_{-\infty}^{\infty} f(x)dx = \int_{-\infty}^{\infty} e^{-x^2}\left[e^{x^2}f(x)\right]dx \approx \sum_{i=1}^{n} w(x_i)e^{-x_i^2}f(x_i)$$

i	Zeros, x_i	Weight, $w(x_i)$	Total Weight, $w(x_i)e^{x_i^2}$
1	-5.38748089001	2.22939364554E-013	0.898591961453
2	-4.60368244955	4.39934099226E-010	0.704332961176
3	-3.94476404012	1.08606937077E-007	0.62227869619
4	-3.34785456738	7.8025564785E-006	0.575262442852
5	-2.78880605843	0.000228338636017	0.544851742366
6	-2.25497400209	0.00324377334224	0.524080350949
7	-1.73853771212	0.0248105208875	0.509679027117
8	-1.2340762154	0.10901720602	0.499920871336
9	-0.737473728545	0.286675505363	0.493843385272
10	-0.245340708301	0.462243669601	0.490921500667
11	0.245340708301	0.462243669601	0.490921500667
12	0.737473728545	0.286675505363	0.493843385272
13	1.2340762154	0.10901720602	0.499920871336
14	1.73853771212	0.0248105208875	0.509679027117
15	2.25497400209	0.00324377334224	0.524080350949
16	2.78880605843	0.000228338636017	0.544851742366
17	3.34785456738	7.8025564785E-006	0.575262442852
18	3.94476404012	1.08606937077E-007	0.62227869619
19	4.60368244955	4.39934099226E-010	0.704332961176
20	5.38748089001	2.22939364554E-013	0.898591961453

Appendix B: Mean and variance of the sum of log-normal distribution

By definition a log-normal distributed variable is given by $I = I_0 \exp(l)$, where l obeys normal distribution. Let sum of independent log normal distributed irradiance be another log normal distribution [129], that is:

$$\sum_{i=1}^{\mathcal{N}} I_i = \exp(\mathcal{U}) = Z \tag{B1}$$

For identically distributed log normal random variable [129], $E[Z] = \mathcal{N}E[I]$ and $\sigma_Z^2 = \sigma_I^2$.

From [47],

$$E[\exp(ar)] = \exp\left(a\mu_r + \frac{a^2\sigma_r^2}{2}\right) \tag{B2}$$

Substituting (B2) into (B1) results in:

$$E[Z] = E[\exp(\mathcal{U})] = \exp\left(\mu_{\mathcal{U}} + \frac{\sigma_{\mathcal{U}}^2}{2}\right) \tag{B3}$$

The expectation of log normal random variable I is given by:

$$E[I] = I_0 \exp\left(\mu_l + \frac{\sigma_l^2}{2}\right) \tag{B4}$$

Note that $E[I] = I_0$, therefore $\exp\left(\mu_l + \frac{\sigma_l^2}{2}\right) = 1$ from which the log intensity mean, μ_l, is found as:

$$\mu_l = -\frac{\sigma_l^2}{2} \tag{B5}$$

It follows from the foregoing that:

$$\exp\left(\mu_{\mathcal{U}} + \frac{\sigma_{\mathcal{U}}^2}{2}\right) = \mathcal{N}E[I] \tag{B6}$$

And having normalising $E[I] = I_0 = 1$ equation (B6) reduces to:

$$\mu_{\mathcal{U}} = \ln(\mathcal{N}) - \frac{\sigma_{\mathcal{U}}^2}{2} \tag{B7}$$

The second central moment of a log-normal random variable *I* is given by:

$$\sigma_I^2 = \exp(\sigma_I^2 + 2\mu_{\mathcal{U}})\,[\exp(\sigma_I^2) - 1] \tag{B8}$$

Substituting equation (B5) into (B8) and invoking the relation given by (B2) results in:

$$E[\exp(2\mathcal{U})] - (E[\exp(\mathcal{U})])^2 = \mathcal{N}\left[\exp\left(\sigma_I^2\right) - 1\right] \tag{B9}$$

$$\exp\left(2\mu_{\mathcal{U}} + 2\sigma_{\mathcal{U}}^2\right) - \exp\left(2\mu_{\mathcal{U}} + \sigma_{\mathcal{U}}^2\right) = \mathcal{N}\left[\exp\left(\sigma_I^2\right) - 1\right] \tag{B10}$$

This implies that:

$$\exp\left(\sigma_{\mathcal{U}}^2\right) = \left\{\mathcal{N}\exp(-2\ln(\mathcal{N}))\left[\exp\left(\sigma_I^2\right) - 1\right]\right\} + 1 \tag{B11}$$

Hence:

$$\sigma_{\mathcal{U}}^2 = \ln\left(1 + \frac{\left[\exp\left(\sigma_I^2\right) - 1\right]}{\mathcal{N}}\right) \tag{B12}$$

And

$$\begin{aligned} \mu_U &= \ln(\mathcal{N}) - \frac{\sigma_U^2}{2} \\ &= \ln(\mathcal{N}) - \frac{1}{2}\ln\left(1 + \frac{\left[\exp\left(\sigma_I^2\right) - 1\right]}{\mathcal{N}}\right) \end{aligned} \tag{B13}$$

Appendix C: Probability density function of $I_{\max} = \max\{I_i\}_{i=1}^{\mathcal{N}}$ for log-normal distributed variables

$$I_{\max} = \max\{I_i\}_{i=1}^{\mathcal{N}} \tag{C1}$$

and

$$p(I_{\max}) = p\left(\max\{I_i\}_{i=1}^{\mathcal{N}}\right) \tag{C2}$$

Considering an arbitrary received irradiance I, it follows therefore that: $p(I_{\max} < I) = p(I_1 < I, I_2 < I, \ldots I_{\mathcal{N}} < I)$. Since none of the $\{I_i\}_{i=1}^{\mathcal{N}}$ is greater than $I_{\max}$. The following therefore gives the cumulative distribution function (cdf) of $I_{\max}$ for $\mathcal{N}$ independent and identically distributed irradiances:

$$p(I_{\max} < I) = \int_0^I \ldots \int_0^I \int_0^I p(I_1)p(I_2)\, dI_1\, dI_2 \ldots dI_{\mathcal{N}} = \prod_{i=1}^{\mathcal{N}} \int_0^I p(I_i)\, dI_i \tag{C3}$$

Assuming the received irradiance are independent and all obey log-normal statistics, then:

$$\begin{aligned} p(I_{\max} < I) &= \left[\frac{1}{\sqrt{2\pi}\sigma_l}\int_0^I \frac{1}{I}\exp\left\{-\frac{\left(\ln(I/I_0) + \sigma_l^2/2\right)^2}{2\sigma_l^2}\right\} dI\right]^{\mathcal{N}} \\ &= \frac{1}{2^{\mathcal{N}}}\left[1 + \operatorname{erf}\left(\frac{2\ln(I/I_0) + \sigma_l^2}{2\sqrt{2}\sigma_l}\right)\right]^{\mathcal{N}} \end{aligned} \tag{C4}$$

From $(I_{\max}) = \frac{d(\mathrm{cdf})}{dI}$, then:

$$p(I_{\max}) = \frac{\mathcal{N}2^{1-\mathcal{N}}\exp(-y^2)}{I\sigma_l\sqrt{2\pi}}[1 + \operatorname{erf}(y)]^{\mathcal{N}-1} \tag{C5}$$

where $y = \frac{\ln(I/I_0)+\sigma_l^2/2}{\sqrt{2}\sigma_l}$. With $\mathcal{N} = 1$ equation (C5) returns the log-normal distribution as would be expected.

Appendix D: Probability density function of $I_{\max} = \max\{I_i\}_{i=1}^{\mathcal{N}}$ for negative exponential distributed variables

$$I_{\max} = \max\{I_i\}_{i=1}^{\mathcal{N}} \tag{D1}$$

and

$$p(I_{\max}) = p\left(\max\{I_i\}_{i=1}^{\mathcal{N}}\right) \tag{D2}$$

Considering an arbitrary received irradiance I, it follows therefore that: $p(I_{\max} < I) = p(I_1 < I, I_2 < I, \ldots I_{\mathcal{N}} < I)$. Since none of the $\{I_i\}_{i=1}^{\mathcal{N}}$ is greater than $I_{\max}$. The following therefore gives the cumulative distribution function (cdf) of $I_{\max}$ for $\mathcal{N}$ independent and identically distributed irradiances:

$$p(I_{\max} < I) = \int_0^I \ldots \int_0^I \int_0^I p(I_1)p(I_2)\, dI_1\, dI_2 \ldots dI_{\mathcal{N}} = \prod_{i=1}^{\mathcal{N}} \int_0^I p(I_i)\, dI_i \tag{D3}$$

Assuming the received irradiance are independent and all obey negative exponential statistics, then:

$$\begin{aligned} p(I_{\max} < I) &= \left[\frac{1}{I_0}\int_0^I \exp\left(-\frac{I}{I_0}\right) dI\right]^{\mathcal{N}} \\ &= \left[1 - \exp\left(-\frac{I}{I_0}\right)\right]^{\mathcal{N}} \end{aligned} \tag{D4}$$

From $(I_{\max}) = \frac{d(\text{cdf})}{dI}$, then:

$$p(I_{\max}) = \frac{\mathcal{N}}{I_0}\exp\left(-\frac{I}{I_0}\right)\left(1 - \exp\left(-\frac{I}{I_0}\right)\right)^{\mathcal{N}-1} \tag{D5}$$

With $\mathcal{N} = 1$ equation (D5) returns the negative exponential distribution as would be expected.

References

[1] D. Killinger, "Free space optics for laser communication through the air," *Optics & Photonics News,* vol. 13, pp. 36-42, Oct. 2002.

[2] A. G. Bell, "On the production and reproduction of sound by light," *American Journal of Sciences,* vol. Series 3, pp. 305 - 324, Oct. 1880.

[3] F. E. Goodwin, "A review of operational laser communication systems," *Proceedings of IEEE,* vol. 58, pp. 1746-1752, Oct. 1970.

[4] H. Hemmati, "Interplanetary laser communications," *Optics and Photonics News,* vol. 18, pp. 22-27, Nov. 2007.

[5] S. Zoran, F. Bernhard, and L. Hanspeter, "Free-space laser communication cctivities in Europe: SILEX and beyond," *IEEE Lasers and Electro-Optics Society (LEOS) 19th Annual Meeting* pp. 78-79, Oct. 2006.

[6] H. Hemmati, "Deep Space Optical Communications," in *Deep space communications and navigation series* Canifornia: Wiley-Interscience, 2006.

[7] S. Hardy, "Free-space optics systems are finding their niches," *Lightwave* pp. 33-36, Dec. 2005.

[8] C. P. Colvero, M. C. R. Cordeiro, G. V. de Faria, and J. P. von der Weid, "Experimental comparison between far- and near infrared wavelenghts in free space optical systems," *Microwave and Optical Technology Letters,* vol. 46, pp. 319-323, Aug. 2005.

[9] R. Dennis, L. Mark, G. Ganesh, P. Bruce, and N. Gerald, "Optical wireless propagation, theory vs eperiment," *Proceedings of SPIE: Optical Wireless Communications III,* vol. 4214, pp. 38-45, 2001.

[10] E. Korevaar, I. I. Kim, and B. McArthur, "Atmospheric propagation characteristics of highest importance to commercial free space optics," *Proceeding of SPIE,* vol. 4976, pp. 1-12, 2003.

[11] D. Song, et al., "4 × 10 Gb/s terrestrial optical free space transmission over 1.2 km using an EDFA preamplifier with 100 GHz channel spacing," *Optics Express,* vol. 7, pp. 280-284, Oct. 2000.

[12] B. Flecker, E. Leitgeb, S. Sheikh Muhammad, C. Chlestil, E. Duca, and V. Carrozzo, "Measurement of light attenuation in fog and snow conditions for terrestrial FSO links," *15th IST Mobile and Wireless Communications Summit,* June 2006.

[13] M. D'Amico, A. Leva, and B. Micheli, "Free-space optics communication systems: first results from a pilot field-trial in the surrounding area of Milan, Italy," *IEEE Microwave and Wireless Components Letters,* vol. 13, pp. 305-307, Aug. 2003.

[14] J. D. Montgomery, "Free-space optics seen as viable alternative to cable," *Lightwave (Analyst Corner),* pp. 43-44, April 2004.

[15] Isaac I. Kim, Bruce McArthur, and E. Korevaar, "Comparison of laser beam propagation at 785 nm and 1550 nm in fog and haze for optical wireless communications," *SPIE Proceeding: Optical Wireless Communications III,* vol. 4214, pp. 26-37, 2001.

[16] M. Bettayeb and S. F. A. Shah, "State of the art ultra-wideband technology for communication systems: a review," *Proceedings of the 10th IEEE International*

Conference on Electronics, Circuits and Systems, (ICECS), vol. 3, pp. 1276 - 1279, 2003.

[17] J. N. Pelton, "Global satellite communications technology and systems," International Technology Research Institute, World Technology (WTEC) Division, Baltimore Dec. 1998.

[18] I. Kim, "10 G FSO systems position technology for the future," *Lightwaveonline* pp. 19-21, July 2009.

[19] K. Kazaura, K. Omae, T. Suzuki, M. Matsumoto, E. Mutafungwa, T. Murakami, K. Takahashi, H. Matsumoto, K. Wakamori, and Y. Arimoto, "Performance evaluation of next generation free-space optical communication system," *IEICE Transaction of Electronics*, vol. E90-C, pp. 381-388, Feb. 2007.

[20] H. Willebrand and B. S. Ghuman, *Free Space Optics: Enabling Optical Connectivity in today's network*. Indianapolis: SAMS publishing, 2002.

[21] BuddeComm, "Global - Broadband - FTTH overview & statistics," May 2009.

[22] C.-H. Cheng, "Signal processing for optical communication," *IEEE Signal Processing Magazime*, pp. 88-94, Jan. 2006.

[23] C. C. Davis, I. I. Smolyaninov, and S. D. Milner, "Flexible optical wireless links and networks," *IEEE Communications Magazine*, vol. 41, pp. 51-57, March 2003.

[24] A. Nordbotten, "LMDS systems and their application," *IEEE Communications Magazine*, vol. 38, pp. 150 -154, 2000.

[25] R. C. Qiu, H. Liu, and X. Shen, "Ultra-wideband for multiple access communications," *IEEE Communications Magazine*, vol. 43, pp. 80-87, 2005.

[26] D. Kedar and S. Arnon, "Optical wireless communication through fog in the presence of pointing errors," *Applied Optics*, vol. 42, pp. 4946-4954, Aug. 2003.

[27] T. Kamalakis, T. Sphicopoulos, S. Sheikh Muhammad, and E. Leitgeb, "Estimation of power scintillation statistics in free space optical links using the multi canonical monte carlo method," *IEEE International Symposium on Communication Systems, Networks and Digital Signal Processing (CSNDSP)* pp. 629-633, July 2006.

[28] D. Kedar and S. Arnon, "Urban optical wireless communication networks: the main challenges and possible solutions," *IEEE Communications Magazine*, vol. 42, pp. s2-s7, May 2004.

[29] X. Zhu and J. M. Kahn, "Free-space optical communication through atmospheric turbulence channels," *IEEE Transactions on Communications*, vol. 50, pp. 1293-1300, Aug. 2002.

[30] S. Karp, R. M. Gagliardi, S. E. Moran, and L. B. Stotts, *Optical Channels: fibers, clouds, water and the atmosphere*. New York: Plenum Press, 1988.

[31] S. Bloom, E. Korevaar, J. Schuster, and H. Willebrand, "Understanding the performance of free-space optics," *Journal of Optical Networking*, vol. 2, pp. 178-200, June 2003.

[32] W. K. Pratt, *Laser Communication Systems*, 1st ed. New York: John Wiley & Sons, Inc., 1969.

[33] D. Kedar and S. Arnon, "Optical wireless communication through fog in the presence of pointing errors," *Applied Optics*, vol. 42, pp. 4946-4954, Aug. 2003.

[34] S. Bloom and W. S. Hartley, "The last-mile solution: Hybrid FSO radio," in *AirFiber, Inc. White paper*, http://www.freespaceoptic.com/WhitePapers/Hybrid_FSO.pdf, last visited: 16th July 2007.

[35] B. Flecker, M. Geghart, E. Leitgeb, S. Sheikh Muhammad, and C. Chlestil, "Results of attenuation-measurements for optical wireless channels under dense

fog conditions regarding different wavelengths " *Prococeeding of SPIE* vol. 6303, pp. 1-11, 2006.
[36] M. al Naboulsi and H. Sizun, "Fog attenuation prediction for optical and infrared waves," *Optical Engineering*, vol. 23, pp. 319-329, 2004.
[37] E. Leitgeb, S. Sheikh Muhammad, B. Flecker, C. Chlestil, M. Geghart, and T. Javornik, "The influence of dense fog on optical wireless systems, analysed by measurements in Graz for improving the link-reliability," *IEEE- ICTON Conference*, pp. 154-159, June 2006.
[38] E. J. McCartney, *Optics of The Atmosphere*. New York: J. Wiley and Sons, 1976.
[39] P. P. Smyth, P. L. Eardley, K. T. Dalton, D. R. Wisely, P. Mckee, and D. Wood, "Optical wireless - a prognosis," *Wireless Data Transmission, Proceeding of SPIE*, vol. 2601, pp. 212-225, 1995.
[40] J. T. Li and M. Uysal, "Optical wireless communications: System model, capacity and coding," *Vehicular Technology Conference*, vol. 1, pp. 168-172, 2003.
[41] I. Hossein, E. Tamer, K. Vikas, D. Frank, and R. B. K, "High-availability free space optical and RF hybrid wireless networks," *IEEE Wireless Communications* vol. 10, pp. 45-53, April 2003.
[42] I. I. Kim, M. Mitchell, and E. J. Korevaar, "Measurement of scintillation for free-space laser communication at 785 nm and 1550 nm," *Optical Wireless Communications II, Proceedings of SPIE*, vol. 3850, pp. 49-52, 1999.
[43] I. I. Kim, J. Koontz, H. Hakakha, P. Adhikari, R. Stieger, C. Moursund, M. Barclay, A. Stanford, R. Ruigrok, J. J. Schuster, and E. J. Korevaar, "Measurement of scintillation and link margin for the TerraLink laser communication system," *Wireless Technology and Systems: Millimeter Wave and Optical, Proceedings of SPIE*, vol. 3232, pp. 100-118, 1997.
[44] V. W. S. Chan, "Free-space optical communications," *IEEE Journal of Lightwave Technology*, vol. 24, pp. 4750-4762, Dec. 2006.
[45] G. R. Osche, *Optical Detection Theory for Laser Applications*. New Jersey: Wiley, 2002.
[46] S. Karp, E. L. O'Neill, and R. M. Gagliardi, "Communication theory for the free-space optical channel," *Proceedings of the IEEE*, vol. 58, pp. 1626-1650, 1970.
[47] J. W. Goodman, *Statistical Optics*. New York: John Wiley, 1985.
[48] M. Uysal, J. T. Li, and M. Yu, "Error rate performance analysis of coded free-space optical links over gamma-gamma atmospheric turbulence channels," *IEEE Transactions on Wireless Communications*, vol. 5, pp. 1229-1233, June 2006.
[49] L. C. Andrews, R. L. Phillips, and C. Y. Hopen, *Laser beam scintillation with applications*. Bellingham: SPIE, 2001.
[50] L. C. Andrews and R. L. Phillips, *Laser beam propagation through random media*, second ed. Washington: SPIE Press, 2005.
[51] X. Zhu and J. M. Kahn, "Performance bounds for coded free-space optical communications through atmospheric turbulence channels," *IEEE Transaction on Communications*, vol. 51, pp. 1233-1239, Aug. 2003.
[52] X. Zhu and J. M. Kahn, "Mitigation of turbulence-induced scintillation noise in free-space optical links using temporal-domain detection techniques " *IEEE Photonics Technology Letters*, vol. 15, pp. 623-625, 2003.
[53] I. B. Djordjevic, B. Vasic, and M. A. Neifeld, "Multilevel coding in free-space optical MIMO transmission with Q-ary PPM over the atmospheric turbulence channel," *IEEE Photonics Technology Letters*, vol. 18, pp. 1491-1493, 2006.

[54] K. Kiasaleh, "Performance of APD-based, PPM free-space optical communication systems in atmospheric turbulence," *IEEE Transactions on Communications,* vol. 53, pp. 1455-1461, Sept. 2005.

[55] S. G. Wilson, M. Brandt-Pearce, Q. Cao, and J. H. Leveque, "Free-space optical MIMO transmission with Q-ary PPM," *IEEE Transactions on Communications,* vol. 53, pp. 1402-1412, Aug. 2005.

[56] S. Sheikh Muhammad, T. Javornik, I. Jelovcan, Z. Ghassemlooy, and E. Leitgeb, "Comparison of hard-decision and soft-decision channel coded M-ary PPM performance over free space optical links," *European Transaction on Telecommunications,* pp. 12, DOI: 10.1002/ett.1343, 2008.

[57] M. A. Al-Habash, L. C. Andrews, and R. L. Phillips, "Mathematical model for the irradiance probability density function of a laser beam propagating through turbulent media," *Optical Engineering,* vol. 40, pp. 1554-1562, 2001.

[58] A. Garcia-Zambrana, "Error rate performance for STBC in free-space optical communications through strong atmospheric turbulence," *IEEE Communication Letters,* vol. 11, pp. 390-392, May 2007.

[59] M. Uysal, S. M. Navidpour, and J. T. Li, "Error rate performance of coded free-space optical links over stong turbulence channels," *IEEE Communication Letters,* vol. 8, pp. 635-637, 2004.

[60] X. Zhu and J. M. Kahn, "Pairwise codeword error probability for coded free-space optical communication through atmospheric turbulence channels," *IEEE International Conference on Communications (ICC),* vol. 1, pp. 161-164, 2001.

[61] M. Razavi and J. H. Shapiro, "Wireless optical communications via diversity reception and optical preamplification," *IEEE Transaction on Communications,* vol. 4, pp. 975-983, 2005.

[62] S. M. Navidpour, M. Uysal, and L. Jing, "BER performance of MIMO free-space optical links," *60th IEEE Vehicular Technology Conference,* vol. 5, pp. 3378-3382, 2004.

[63] Q. Cao, M. Brandt-Pearce, S. G. Wilson, and L. C. Brown, "Free-space optical MIMO system using an optical pre-amplifier," *IEEE Global Telecommunications Conference* pp. 1-5, Nov. 2006.

[64] S. M. Navidpour, M. Uysal, and M. Kavehrad, "BER performance of free-space optical transmission with spatial diversity," *IEEE Transaction on Communications,* vol. 6, pp. 2813-2819, 2007.

[65] I. I. Kim, H. Hakakha, P. Adhikari, E. Korevaar, and A. K. Majumdar, "Scintillation reduction using multiple transmitters," *Proceeding of SPIE,* vol. 2990, pp. 102-113, 1997.

[66] S. Rosenberg and M. C. Teich, "Photocounting array receivers for optical communication through the lognormal atmospheric channel: error bound for M-ary equal energy orthogonal signalling," *IEEE Transaction on Information Theory,* vol. IT-19, pp. 807-809, Nov. 1973.

[67] M. Abtahi, P. Lemieux, W. Mathlouthi, and L. A. Rusch, "Supprression of turbulence-induced scintillation in free-space optical communication systems using saturated optical amplifiers," *Journal of Lightwave Technology,* vol. 24, pp. 4966-4973, Dec. 2006.

[68] J. Elon Grave and S. Drenker, "Advancing Free space Optical communication with Adaptive optics," *Lightwaveonline,* vol. 19, pp. 105-113, Sept. 2002.

[69] I. B. Djordjevic, B. Vasic, and M. A. Neifeld, "LDPC coded OFDM over the atmospheric turbulence channel," *Optical Express,* vol. 15, pp. 6336-6350, 2007.

[70] H. Yamamoto and T. Ohtsuki, "Atmospheric optical subcarrier modulation systems using space-time block code," in *IEEE Global Telecommunications Conference, (GLOBECOM '03)* vol. 6, New York, pp.3326-3330, 2003.

[71] E. J. Lee and V. W. S. Chan, "Optical communications over the clear turbulent atmospheric channel using diversity," *IEEE Journal on Selected Areas in Communications*, vol. 22, pp. 1896-1906, Nov. 2004.
[72] D. Rockwell, A. and S. Mecherle, G., "Optical wireless: Low-cost, broadband, optical access," www.freespaceoptic.com/WhitePapers/optical_wireless.pdf, last visited 11 Sept. 2009.
[73] A. K. Majumdar and J. C. Ricklin, *Free-Space Laser Communications: Principles and Advances*. New York: Springer, 2008.
[74] A. Pavelchek, R. G. Trissel, J. Plante, and S. Umbrasas, "Long-wave infrared (10-μm) free-space optical communication system " *Free-Space Laser Communication and Active Laser Illumination III*, vol. 5160, pp. 247-252, Jan. 2004.
[75] A. McCuaig, "Free-space optics: LEDs vs lasers," in *Lightwaveonline*: PennWell, 2009.
[76] Practel, "Free space optics - from wireless fiber to visible light communications," Practel, Inc. July 2009.
[77] G. Keiser, *Optical Communications Essentials* 1st ed. New York: McGraw-Hill Professional, 2003.
[78] O. Bouchet, H. Sizun, C. Boisrobert, F. De Fornel, and P. Favennec, *Free-Space Optics: Propagation and Communication*. London: ISTE Ltd, 2006.
[79] R. M. Gagliardi and S. Karp, *Optical Communications*, 2nd ed. New York: John Wiley, 1995.
[80] AFGL, "AFGL Atmospheric Constituent Profiles (0–120 km), ," AFGL-TR-86-0110, Air Force Geophysics Laboratory, Hanscom Air Force Base, Massachusetts, 1986.
[81] M. Jeganathan and P. Ionov, "Multi-gigabits-per-second optical wireless communications," Optical Crossing, http://www.freespaceoptic.com/WhitePapers/Jeganathan%20%20(Optical%20Crossing).pdf , last visited 20th May 2009.
[82] S. Betti, G. De marchis, and E. Iannone, *Coherent Optical Communication Systems*, 1st ed. Canada: John Wiley and Sons Inc., 1995.
[83] S. Hranilovic, *Wireless Optical Communication Systems* vol. 1st. Boston: Springer, 2005.
[84] IEC, "Safety of laser products - Part 1: Equipment classification and requirements," 2nd ed: International Electrotechnical Commission, 2007.
[85] D. J. T. Heatley, D. R. Wisely, I. Neild, and P. Cochrane, "Optical wireless: The story so far," *IEEE Communications Magazine*, vol. 36, pp. 72-82, Dec. 1998.
[86] K. Schröder, "Handbook on Industrial laser safety ": Technical University of Vienna, 2000.
[87] J. M. Senior, *Optical Fiber Communications Principles and Practice*, 3rd ed. Essex: Pearson Education Limited, 2009.
[88] G. Keiser, *Optical Fiber Communications*, 3rd ed. New York: McGraw-Hill 2000.
[89] N. S. Kopeika and J. Bordogna, "Background noise in optical communication systems," *Proceedings of the IEEE*, vol. 58, pp. 1571-1577, 1970.
[90] S. F. Clifford, "The classical theory of wave propagation in a turbulent medium," in *Laser Beam Propagation in the Atmosphere*, J. W. Strobehn, Ed.: Springer-Verlag, 1978.
[91] A. Kolmogorov, "Turbulence," in *Classic Papers on Statistical Theory*, S. K. Friedlander and L. Topper, Eds. New York: Wiley-Interscince, 1961.

[92] A. Kolmogorov, "The local structure of turbulence in incompressible viscous fuid for very large Reynold numbers," *Proceeding of Royal Society of London Series A- Mathematical and Physical,* vol. 434, pp. 9-13, 1991.
[93] V. I. Tatarski, *Wave propagation in a turbulent medium*. (Translated by R.A. Silverman) New York: McGraw-Hill 1961.
[94] A. Ishimaru, "The beam wave case and remote sensing," in *Topics in Applied Physics: Laser Beam Propagation in the Atmosphere*. vol. 25 p.134 New York: Springer-Verlag, 1978.
[95] H. Hodara, "Laser wave propagation through the atmosphere," *Proceedings of the IEEE,* vol. 54, pp. 368-375, March 1966.
[96] J. W. Strohbehn, "Line-of-sight wave propagation through the turbulent atmosphere," *Proceedings of the IEEE,* vol. 56, pp. 1301-1318, Aug. 1968.
[97] J. W. Strobehn and S. F. Clifford, "Polarisation and angle of arrival fluctuations for a plane wave propagated through turbulent medium," *IEEE Transaction on Antennas Propagation,* vol. AP-15, p. 416, 1967.
[98] H. D.H., "Depolarisation of laser beam at 6328 Angstrom due to atmospheric transmission," *Applied Optics,* vol. 8, p. 367, Feb. 1969.
[99] W. O. Popoola, Z. Ghassemlooy, and E. Leitgeb, "Free-space optical communication using subcarrier modulation in gamma-gamma atmospheric turbulence," *9th International Conference on Transparent Optical Networks (ICTON '07)* vol. 3, pp. 156-160, July 2007.
[100] J. H. Churnside and S. F. Clifford, "Log-normal Rician probability density function of optical scintillations in the turbulent atmosphere," *Journal of Optical Society of America,* vol. 4, pp. 1923-1930, Oct. 1987.
[101] L. C. Andrews and R. L. Phillips, "I-K distribution as a universal propagation model of laser beams in atmospheric turbulence," *Journal of optical society of America A,* vol. 2, p. 160, Feb. 1985.
[102] G. Parry and P. N. Pusey, "K distributions in atmopsheric propagation of laser light," *Journal of Optical Society of America,* vol. 69, pp. 796-798, 1979.
[103] S. F. Clifford and R. J. Hill, "Relation between irradiance and log-amplitude variance for optical scintillation described by the *K* distribution," *Journal of Optical Society of America,* vol. 71, pp. 112-114, 1981.
[104] S. Sheikh Muhammad, W. Gappmair, and E. Leitgeb, "PPM channel capacity evaluation for terrestrial FSO links," *International Workshop on Satellite and Space Communications,* pp. 222-226, Sept. 2006.
[105] W. O. Popoola, Z. Ghassemlooy, M. S. Awan, and E. Leitgeb, "Atmospheric channel effects on terrestrial free space optical communication links," *3rd International Conference on Computers and Artificial Intelligence (ECAI 2009),* pp. 17-23, July 2009.
[106] W. O. Popoola, Z. Ghassemlooy, J. I. H. Allen, E. Leitgeb, and S. Gao, "Free-space optical communication employing subcarrier modulation and spatial diversity in atmospheric turbulence channel," *IET Optoelectronic,* vol. 2, pp. 16-23, 2008.
[107] T. Ohtsuki, "Multiple-subcarrier modulation in optical wireless communications," *IEEE Communications Magazine,* pp. 74-79, March 2003.
[108] I. B. Djordjevic and B. Vasic, "100-Gb/s transmission using orthogonal frequency -division multiplexing," *IEEE Photonics Technology Letters,* vol. 18, pp. 1576-1578, Aug. 2006.
[109] G. P. Agrawal, *Fiber-Optic Communication Systems,* 3rd ed. New york: Wiley-Interscience, 2002.

[110] H. Rongqing, Z. Benyuan, H. Renxiang, T. A. Christopher, R. D. Kenneth, and R. Douglas, "Subcarrier multiplexing for high-speed optical transmission," *Journal of Lightwave Technology,* vol. 20, pp. 417-424, 2002.
[111] R. You and J. M. Kahn, "Average power reduction techniques for multiple-subcarrier intensity-modulated optical signals," *IEEE Transaction on Communications,* vol. 49, pp. 2164-2171, 2001.
[112] S. Teramoto and T. Ohtsuki, "Multiple-subcarrier optical communication systems with peak reduction carriers," in *IEEE Global Telecommunications Conference (GLOBECOM)* vol. 6, pp. 3274-3278, 2003.
[113] S. Teramoto and T. Ohtsuki, "Multiple-subcarrier optical communication systems with subcarrier signal-point sequence," *IEEE Transactions on Communications,* vol. 53, pp. 1738-1743, 2005.
[114] J. G. Proakis, *Digital Communications*. New York: McGraw-Hill, 2004.
[115] M. K. Simon and M.-S. Alouini, *Digital Communication Over Fading Channels*, 2nd ed. New York: John Wiley & Sons Inc., 2004.
[116] M. Abramowitz and I. S. Stegun, *Handbook of Mathematical functions with formulars, graphs and mathematical tables*: Dover, 1977.
[117] W. O. Popoola, Z. Ghassemlooy, and E. Leitgeb, "BER performance of DPSK subcarrier modulated free space optics in fully developed speckle," in *6th International Symposium on Communication Systems, Networks and Digital Signal Processing, (CNSDSP),* Graz, Austria, pp. 273-277, 2008.
[118] I. S. Gradshteyn and I. M. Ryzhik, *Table of integrals, series, and products*, 5th ed. London: Academic Press, Inc., 1994.
[119] W. Huang and M. Nakagawa, "Nonlinear effect of direct-sequence CDMA in optical transmission," *Global Telecommunications Conference, GLOBECOM, San Francisco,* vol. 2, pp. 1185-1189, 1994.
[120] J. Daly, "Fiber optics intermodulation distortion," *IEEE Transaction on Communications,* vol. COM-30, pp. 1954-1958, 1982.
[121] M. Abuelma'atti, "Carrier-to-intermodulation performance of multiple FM/FDM carriers through a GaA1As hetrojunction laser diode," *IEEE Transactions on Communications,* vol. 33, pp. 246-248, 1985.
[122] K. Stubkjaer and M. Danielsen, "Nonlinearities of GaAlAs lasers-Harmonic distortion," *IEEE Journal of Quantum Electronics,* vol. QE-16, pp. 531-537, 1980.
[123] T. L. Paoli, "Nonlinearities in the emission characteristics of stripe-geometry (AlGa)As double heterostructure junction lasers," *IEEE Journal of Quantum Electronics,* vol. QE-12, pp. 770-776, 1976.
[124] J. Buus, "Multimode field theory explanation of kinks in the characteristics of DH lasers," *IEE Electronic Letters,* vol. 14, pp. 127-128, 1978.
[125] I. I. Kim and E. Korevaar, "Availability of free space optics and hybrid FSO/RF systems," *Proceedings of SPIE: Optical Wireless Communications IV,* vol. 4530, pp. 84-95, 2001.
[126] J. P. Kim, K. Y. Lee, J. H. Kim, and Y. K. Kim, "A performance analysis of wireless optical communication with convolutional code in turbulent atmosphere," in *International Technical Conference on Circuits Systems, Computers and Communications (ITC-CSCC '97),* Okinawa, pp.15-18, 1997.
[127] T. Ohtsuki, "Turbo-coded atmospheric optical communication systems," in *IEEE International Conference on Communications (ICC)* New York, pp.2938-2942, 2002.
[128] R. K. Tyson, " Bit-error rate for free-space adaptive optics laser communications " *Optical Society of America Journal,* vol. 19, pp. 753-758 2002.

[129] R. L. Mitchell, "Permanence of the log-normal distribution," *Journal of the Optical Society of America,* vol. 58, pp. 1267-1272, 1968.
[130] S. Trisno, I. I. Smolyaninov, S. D. Milner, and C. C. Davis, "Characterization of time delayed diversity to mitigate fading in atmopheric turbulence channels," *Proceeding of SPIE* vol. 5892, pp. 589215.1-589215.10, 2005.
[131] S. Trisno, I. I. Smolyaninov, S. D. Milner, and C. C. Davis, "Delayed diversity for fade resistance in optical wireless communications through turbulent media," *Proceedings of SPIE,* vol. 5596, pp. 385-394, 2004.
[132] C. H. Kwok, R. V. Penty, and I. H. White, "Link reliability improvement for optical wireless communication systems with temporal domain diversity reception," *IEEE Photonics Technology Letters,* vol. 20, pp. 700-702, 2008.
[133] D. R. Bates, "Rayleigh scattering by air," *Planetary space Science,* vol. 32, pp. 785-790, 1984.
[134] H. C. van de Hulst, *Light scattering by small particles,* (also Dover Publications, Jan1, 1982) ed. New York: Wiley, 1957
[135] E. Leitgeb, M. Geghart, and U. Birnbacher, "Optical networks, last mile access and applications," *Journal of Optical and Fibre Communications Reports,* vol. 2, pp. 56-85, 2005.
[136] M. Grabner and V. Kvicera, "Experimental study of atmospheric visibility and optical wave attenuation for free-space optics communications," *http://ursi-france.institut-telecom.fr/pages/pages_ursi/URSIGA08/papers/F06p5.pdf,* last visited 2nd Sept. 2009.
[137] J. Gowar, *Optical Communication Systems,* 2nd ed.: Prentice Hall, 1993.